



**UNIVERSIDADE TÉCNICA DE LISBOA
INSTITUTO SUPERIOR TÉCNICO**

**ON THE MODELLING OF THE POTENTIAL FLOW
ABOUT WINGS AND MARINE PROPELLERS
USING A BOUNDARY ELEMENT METHOD**

João Manuel Ribeiro da Costa Baltazar
(Mestre)

Dissertação para obtenção do Grau de Doutor em
Engenharia Mecânica

Orientador: Doutor José Alberto Caiado Falcão de Campos
Co-Orientador: Doutor Luís Rego da Cunha de Eça

Júri:

Presidente: Reitor da Universidade Técnica de Lisboa
Vogais:
Doutor Ir Hendrik Willem Marie Hoeijmakers
Doutor António Franco de Oliveira Falcão
Doutor Heitor Lobato Girão Pina
Doutor José Alberto Caiado Falcão de Campos
Doutor Luís Rego da Cunha de Eça
Doutor Nuno Miguel Magalhães Duque da Fonseca

Setembro de 2008

Resumo

Apresenta-se um método de painel de ordem baixa para o cálculo do escoamento potencial estacionário incompressível em torno de asas e hélices propulsores marítimos. São considerados três modelos de esteira: esteira rígida com condição de Kutta linear e iterativa de pressão, relaxamento parcial da esteira e relaxamento total da esteira com enrolamento. Descrevem-se as técnicas para a geração de malhas estruturadas sobre as superfícies da asa, pá do hélice, tubeira, cubo e folhas de vórtice. Este estudo pretende contribuir para uma maior compreensão dos métodos de painel na modelação do escoamento potencial incompressível em torno de superfícies sustentadoras. Primeiro, são apresentados estudos de convergência de malha e comparações com outros métodos de painel e resultados experimentais. Segundo, estuda-se o comportamento da solução potencial na extremidade da superfície sustentadora. Testam-se diferentes técnicas por forma a obter-se uma solução admissível na extremidade. Por fim, a modelação da separação de folhas de vórtice é investigada com o presente método. São apresentados resultados para uma asa delta e um hélice propulsor marítimo com separação de vorticidade de bordo de ataque, e para o escoamento na folga entre a superfície da tubeira e a extremidade da pá do hélice.

Palavras-chave:

Asas, Hélices Propulsores Marítimos, Método de Elementos de Fronteira, Escoamento Potencial, Escoamento na Extremidade, Separação de Folhas de Vórtice.

Abstract

A low-order potential-based panel method for the calculation of the incompressible steady potential flow around wings and marine propellers is presented. Three wake models are considered: rigid wake with linear and iterative pressure Kutta condition, partial wake relaxation and full wake relaxation with roll-up. The techniques for the generation of structured grids on the surfaces of the wing, propeller blade, duct, hub and vortex sheet are described. The purpose of the present study is to contribute to a better understanding of panel methods in the modelling of the incompressible potential flow around lifting surfaces. First, grid convergence studies and comparison with other panel methods and experimental measurements are presented. Second, the potential flow solution behaviour in the vicinity of the tip is studied. Different techniques are tested to obtain a more reliable solution at the tip. Finally, the modelling of separated vortex flows with the present method is investigated. Results are presented for a delta wing and a marine propeller with leading edge vortex sheet separation, and for the gap flow between the duct inner side and the propeller blade tip.

Key-words:

Wings, Marine Propellers, Boundary Element Method, Potential Flow, Tip Flow, Vortex Sheet Separation.

Acknowledgements

First of all, I am very much indebted to my supervisors Prof. Falcão de Campos and Prof. Luís Eça. I would like to express my great thanks to Prof. Falcão de Campos for his encouragement and constant guidance for the realisation of this thesis. The fundamental and theoretical discussions about Boundary Element Methods and the practical discussions about marine propellers were very important for me to have a more clear understanding of these topics. I would like to thank Prof. Luís Eça for his contributions and suggestions on numerical methods and grid generation techniques. The discussions with him were very important for the development and improvement of the panel method.

I would also express my thanks to Ir. Johan Bosschers and Dr. Guilherme Vaz for their discussions, instructions and important remarks to the present work. My thanks to Ir. Johan Bosschers for his coordination and guidance in the IST-MARIN cooperative project, who helped me in my research work. Dr. Guilherme Vaz was also very important in this project, not only during our meetings at MARIN but also as a host in the Netherlands.

I enjoyed very much the time and the fun I had together with my roommates, colleagues and friends during these four years at IST. They were: Afonso Tiago, Douglas Cemin, Henrique Borralho, João Henriques, Lúcia Moreira, Miguel Lopes, Pedro Martins, Ricardo Pascoal and Rui Gomes.

I also acknowledge the financial support granted by Fundação para a Ciência e a Tecnologia, Ph.D. grant SFRH/BD/14334/2003.

I dedicate my thesis to my parents Avelina Baltazar and Dinis Baltazar, for their constant support, advices, encouragement and patience that made it possible for me to finish this thesis.

Nomenclature

A	Wing planform area
a	Helical axial pitch per unit radian
$\vec{a}_\xi, \vec{a}_\eta$	Vectors tangent to the panel surface
C_{D_i}	Induced drag coefficient
C_L	Lift coefficient
C_p	Pressure coefficient
C_{pn}	Pressure coefficient based on rotational speed
C_x, C_y, C_z	Force coefficients in x , y and z direction
C_0	Maximum chord
c	Blade section chord length
D	Propeller diameter
D_i	Induced drag
D_{ij}	Dipole influence coefficient matrix
d	Largest diagonal of the panel
$\vec{e}_x, \vec{e}_r, \vec{e}_\theta$	Unit vectors of the cylindrical coordinate system
$\vec{e}_x, \vec{e}_y, \vec{e}_z$	Unit vectors of the Cartesian coordinate system
\vec{e}_1, \vec{e}_2	Orthogonal unit vectors on the surface
f	Local blade section camber
f_M	Blade section maximum camber
f_V	Vinokur stretching function
I, J	Parametric coordinates
i, j	Grid panel strips
i_T	Local blade rake
K	Number of propeller blades; number of body sectors
K_Q	Propeller torque coefficient
K_{T_D}	Duct thrust coefficient
K_T	Propeller thrust coefficient
K_{T_T}	Total thrust coefficient
L	Lift; duct length
N	Total number of panels in the body sector
N_{blade}	Total number of panels for one propeller blade
N_C	Number of panels in the chordwise direction on each section side
N_{CP}	Number of panels in the chordwise direction
N_{Dt}	Number of duct panels in the circumferential direction

N_{Dx}	Number of duct panels in the axial direction
N_{duct}	Total number of panels for one duct sector
N_{Ht}	Number of hub panels in the circumferential direction
N_{Hx}	Number of hub panels in the axial direction
N_{hub}	Total number of panels for one hub sector
N_K	Number of wake dipole strengths
N_{LR}	Number of leading edge wake panels in the spanwise direction
N_{LW}	Number of leading edge wake panels in the streamwise direction
N_R	Number of panels in the spanwise direction
N_{TW}	Number of trailing edge wake panels in the streamwise direction
N_W	Number of wake panels in the streamwise direction
N_{wing}	Total number of wing panels
n	Propeller rate of revolutions
\vec{n}	Unit normal
P	Pitch
P_{ij}	Jacobian matrix
p	Static pressure
p_∞	Undisturbed static pressure
Q	Propeller torque
\vec{Q}_i	Position vector of panel corner points
R	Propeller radius
Re	Reynolds number
$R(P, Q)$	Distance between point P and Q
S	Semi-span
\mathcal{S}	Boundary domain
$\mathcal{S}_{\mathcal{B}}$	Body surfaces
S_{blades}	Propeller blade surfaces
S_{duct}	Duct surface
S_e	Element surface
\mathcal{S}_{FW}	Far wake surface
S_{hub}	Hub surface
\mathcal{S}_{LW}	Leading edge wake surface
\mathcal{S}_{TW}	Trailing edge wake surface
\mathcal{S}_w	Wake surfaces
S_{wing}	Wing surface
S_{ij}	Source influence coefficient matrix
s, t	Parametric coordinates
s_1, s_2	Parametric coordinates of the surface definition
T	Propeller thrust
T_D	Duct thrust
t	Local blade section thickness
t_M	Blade section maximum thickness
U	Propeller advance speed
U_∞	Undisturbed velocity in the moving frame

u, v	Parametric coordinates
\vec{u}_μ	Velocity induced by a dipole distribution
\vec{u}_σ	Velocity induced by a source distribution
u_1, u_2	Local orthogonal coordinates
\vec{V}	Total fluid velocity
\vec{V}_t	Total velocity tangent to the surface
\vec{V}_m	Mean velocity on the wake surface
\vec{V}_w	Velocity of the vortex sheet surface
\vec{v}_t	Perturbation velocity tangent to the surface
W_{ij}	Wake influence coefficient matrix
\vec{x}	Position vector
x, r, θ	Cylindrical coordinates in the moving frame
x, y, z	Cartesian coordinates in the moving frame
x_W	Axial wake length
α	Angle of attack; stretching parameter
β	Perturbation parameter
Γ	Circulation
$\vec{\gamma}$	Vorticity vector
$\Delta \vec{V}$	Velocity discontinuity across the wake surface
$\Delta \phi$	Potential-jump on the wake surface
θ_s	Local blade skew angle
Λ	Wing aspect-ratio
μ	Dipole strength
ξ, η	Panel local coordinate system; computational domain
ρ	Fluid density
σ	Source strength
ϕ	Perturbation potential
φ	Phase angle
$\hat{\psi}_i$	Panel base functions
Ω	Propeller angular speed

Subscripts and Superscripts

B	Blade
D	Dipole; duct
H	Hub
h, t	Hub, tip radius, respectively
i, o	Inner and outer sides of the duct, respectively
le, te	Leading and trailing edges, respectively
(n)	Iteration step
S	Source
VF	Vortex filament
$+, -$	Suction and pressure sides, respectively

Acronyms

BEM	Boundary Element Methods
DTNSRDC	David Taylor Naval Ships Research & Development Center
DTRC	David Taylor Research Center
GRAPE	Grids about Aircrafts by Poisson's Equation
IGES	Initial Graphics Exchange Specification
IST	Instituto Superior Técnico
ITTC	International Towing Tank Conference
MARIN	Maritime Research Institute Netherlands
NACA	National Advisory Committee for Aeronautics
NSMB	Netherlands Ship Model Basin

Contents

1	Introduction	1
2	Mathematical Formulation	7
2.1	Description of the Problem	7
2.2	Potential Flow Problem	8
2.3	Integral Equation	9
2.4	Boundary Conditions on the Wake Surface	11
2.5	Velocity, Pressure and Forces	13
3	Panel Method	17
3.1	Discretisation of the Integral Equation	17
3.2	Wake Models	18
3.2.1	Rigid Wake	18
3.2.2	Partial Wake Relaxation	20
3.2.3	Full Wake Relaxation	22
3.3	Calculation of Influence Coefficients	23
3.3.1	Panel Definition	23
3.3.2	Potential Influence Coefficients	24
3.3.3	Velocity Influence Coefficients	26
3.4	Numerical Surface Differentiation	29
3.5	Calculation of Forces	31
4	Grid Generation	33
4.1	Introduction	33
4.2	Surface Definition	33
4.2.1	Analytical Surface Definition	34
4.2.2	Bi-Cubic Splines Surface Definition	35
4.3	Geometry Discretisation	36
4.3.1	Wing Panelling	37
4.3.2	Blade Panelling	37
4.3.3	Duct Panelling	38
4.3.4	Wake Panelling	41
4.3.5	Hub Panelling	43
4.4	Algebraic Quasi-Orthogonal Grids	46

5 Potential Flow Calculations for Wings and Marine Propellers	51
5.1 Introduction	51
5.2 Wings	52
5.2.1 Elliptical Wing	52
5.2.2 Rectangular Wing	57
5.3 Open Propellers	63
5.3.1 DTRC P4119	63
5.3.2 DTRC P4842M	68
5.4 Ducted Propellers	72
5.4.1 NSMB Duct 19A	72
5.4.2 Propeller K_a 4-70 Inside Duct NSMB 19A	75
5.5 Discussion of the Results	81
6 Tip Flow Modelling	83
6.1 Introduction	83
6.2 Influence of the Wake Model	84
6.3 Panel Arrangements With “Hydrodynamic Tip”	87
6.4 Sensitivity to Blade Tip Geometry	94
6.5 Discussion of the Results	98
7 Vortex Sheet Separation Modelling	99
7.1 Introduction	99
7.2 Leading Edge Vortex Flow About Delta Wings	100
7.2.1 Numerical Method	100
7.2.2 76 Degrees Swept Delta Wing at 20 Degrees Incidence	104
7.2.3 Solution for the 76 Degrees Swept Delta Wing for Different Angles of Attack	111
7.3 Leading Edge Vortex Sheet Separation on Open Propellers	121
7.4 Tip Leakage Modelling in Ducted Propellers	126
8 Conclusions	135
Bibliography	137
A Dynamic Boundary Condition on the Wake	143
B Iterative Solution of the System of Equations With Pressure Kutta Condition	145
C Propeller Geometries	149
C.1 DTRC Propeller P4119	149
C.2 DTRC Propeller P4842M	151
C.3 NSMB Duct 19A	153
C.4 NSMB Propeller K_a 4-70	154
C.5 DTNSRDC Propeller P4498	156

Chapter 1

Introduction

Marine propellers have been widely used for propulsion applications of maritime structures. Calculation of the pressure distribution on the blade surfaces is fundamental for the design and analysis of marine propellers. An accurate pressure distribution is important, not only for thrust and torque calculations, but also for cavitation inception prediction and cavitation extent modelling. Moreover, prediction of pressure fluctuations on the propeller blades is essential for the assessment of induced vibrations on the ship hull.

Traditionally, the hydrodynamic design of marine propellers has made use of empirical, lifting line and lifting surface methods, as well as model testing in towing basins. However, these methods involve a number of physical and geometrical simplifications. The disadvantage of model testing is that it is both time consuming and expensive. Moreover, extrapolation of the model results to full-scale requires an accurate estimation of the scale effects. The geometry of propeller blades can be rather complex, especially for blades with high skew, rake and pitch. Therefore, a reliable numerical method for the design and analysis of marine propellers is desirable.

Boundary Element Methods (BEM), also known as panel methods, have been used for the calculation of the incompressible potential flow around marine propellers. Panel methods allow a more precise representation of the marine propeller geometry in comparison to lifting line and lifting surface methods.

In the sixties, Hess and Smith [1] developed a panel method for non-lifting bodies with arbitrary geometry. In his method, the body surface was represented by flat quadrilateral elements with constant source distributions. Hess [2] extended the method for lifting bodies by including vorticity. Since then, panel methods have undergone numerous developments and became a widely used tool in analysis and design problems in many aerodynamic and hydrodynamic applications.

The first application of a panel method to propellers is due to Hess and Valarezo [3] with a velocity integral formulation in which the boundary condition on the body surface is satisfied through the direct computation of the velocity.

1. Introduction

Morino and Kuo [4] introduced a panel method based on Green's second identity to the perturbation potential with a Dirichlet boundary condition for the potential inside the body. This formulation implements hyperboloidal quadrilateral panels with constant source and constant normal dipole distributions on the body surface. This results in a Fredholm integral equation of the second kind for the surface perturbation potential since the source distribution becomes known from the Neumann boundary condition on the body surface.

Maskew [5] presented a piecewise constant singularity panel method for the calculation of subsonic aerodynamic characteristics on wings. Two forms of the internal Dirichlet boundary condition were discussed: internal flow equal to onset flow which implies the condition that the perturbation potential is zero inside the body, and the zero flow inside. The zero internal perturbation potential formulation is more accurate when dealing with unmatched panelling.

Youngren *et al.* [6] performed a comparison between the panel method formulations of Hess [2] and Morino and Kuo [4]. The internal Dirichlet boundary condition makes the Morino's formulation nearly insensitive to changes in panel size and allows to overcome the difficulties encountered in Hess's formulation when applied to heavily loaded thin lifting surfaces.

Morino's method has been successfully applied to marine propeller problems by many researchers. Kerwin *et al.* [7], Lee [8] and Hoshino [9] developed methods for the steady propeller problem in uniform flow and Kinnas *et al.* [10], Hsin [11] and Hoshino [12] for the unsteady flow problem of a propeller in a non-uniform inflow.

Another advantage of the potential-based panel method is that it is easier to extend to sheet cavitation prediction on propellers, because the dynamic boundary condition is easier to enforce on the cavity surface by prescribing the potential than by prescribing the velocity. Fine [13] was the first author to apply a potential-based panel method for the analysis of cavitating propellers subjected to non-axisymmetric inflows. Recently, Vaz [14] presented a panel method for the modelling of wetted and cavitating flows around hydrofoils and marine propellers. The method is able to predict with good accuracy the sheet cavity extent when using appropriate grids.

In 1993, in a workshop organised by the “20th ITTC Propulsor Committee” [15], various panel methods were assessed for the steady propeller problem in a uniform flow by means of comparative calculations and comparison with experimental results for two representative propellers. In general, the results of comparative calculations were in good agreement with the experimental data. However, differences in the pressure distribution were observed near the root, tip, leading edge and trailing edge.

The problem of predicting the pressure distribution near propeller blade tips with a panel method contains a number of considerable difficulties. These are basically of two kinds: firstly, of modelling nature related to the definition of an adequate potential flow model

for lifting blades with vorticity shedding devoid of internal inconsistencies. Secondly, of numerical nature related to the specification of blade and wake grids suitable for a particular blade tip. Usually, both problems are solved together.

A grid oriented along constant radii, the so-called conventional grid, has been previously employed with BEM. This grid arrangement results in high aspect-ratio of the panels at the propeller tip. Pyo [16], among others, showed that using the conventional grid arrangement, convergence of the iteration required to enforce a pressure Kutta condition at the trailing edge in the tip region may be difficult to obtain. In addition, for fine discretisations of the tip region the pressure distribution exhibits an irregular behaviour when approaching the tip. This is seen to occur both for blades with wide blade tip of vanishing chord and for highly skewed propellers with zero or finite chord tips, see Kinnas [17].

Hsin *et al.* [18] showed that the use of an orthogonal panel arrangement improves the prediction of velocities for the non-lifting case of an ellipsoid and the convergence with the number of panels of the circulation distribution of circular wings. To avoid the irregular behaviour of the pressure distribution at the tip, the flow adapted grid arrangement was introduced by Kinnas *et al.* [19], which is orthogonal at the leading edge and aligned with the resulting mean flow at the trailing edge.

Further improvements on the circulation distribution and flow velocity predictions near the tip were reported by Pyo [16] both for wings and marine propellers using the flow adapted grid arrangement. In particular, the application of the iterative pressure Kutta condition, which upon convergence produces large pressure peaks at the trailing edge with the conventional grid arrangement, has been considerably improved by the use of a flow adapted grid, Pyo [16]. However, although the velocities in the last chordwise strips are less singular at the trailing edge with the flow adapted grid arrangement than with the conventional one, it is not clear whether a reliable pressure distribution is obtained up to the blade tip.

In a previous work, Baltazar [20], the behaviour of the potential flow solution near the tip for an elliptical wing with conventional and quasi-orthogonal grids using a rigid wake model was investigated. Both with the conventional and quasi-orthogonal grids, the pressure distributions near the tip of the elliptical wing showed unrealistic pressure peaks at the trailing edge, when the iterative pressure Kutta condition was applied. From these studies it became clearer that the lack of wake alignment with the flow near the tip should be responsible for the occurrence of the unrealistic pressure peaks at the trailing edge.

There have been many attempts to predict vortex roll-up behind three-dimensional lifting bodies. A full alignment of a marine propeller wake according to the flow velocity was carried out by Maitre and Rowe [21] using a panel method. A similar method for heavily loaded marine propellers was also used by Takinaci [22]. In Pyo [16], an iterative process for the complete wake alignment, including roll-up, was introduced and implemented in a propeller panel method. Hyperboloidal panels with a bi-quadratic dipole distribution

1. Introduction

over the trailing vortex sheet are used. This method was also coupled with the flow adapted grid, Kinnas *et al.* [19]. These methods are able to model sheet roll-up and wake contraction. However, a rough description of the rolled-up regions, especially near the blade tip, is obtained.

Since the wake alignment is also important for the modelling of sheet cavitation and tip vortex cavitation, several wake alignment models were developed. Dang [23] used a low-order panel method with iterative alignment with time step of the wake sheet using a predictor-corrector Euler scheme, for the modelling of unsteady partial cavity flows. In Lee [24], the modelling of unsteady wake alignment and developed tip vortex cavitations was studied. A finite core tip vortex is introduced at the tip of the wake sheet. The trailing wake surface and the trajectory of the tip vortex cavity core are determined by aligning the wake surface with the flow velocity in an iterative manner. By applying the finite core at the tip, a rather smooth geometry of the rolled-up region is obtained.

Panel methods can also handle difficult flow conditions such as off-design conditions. It is well known from experiments that when a propeller is operating in a heavy-load condition, vortex sheet separation can occur from the leading edge. A similar phenomenon can be observed on low-aspect-ratio wings or wings with highly swept leading edges. A strong interaction between the separated vortex sheet and the flow over the surface can occur, changing considerably the local pressure distribution and the overall characteristics of the lifting body.

References to this leading edge separation phenomena and its modelling can be found in Greeley and Kerwin [25] for a highly skewed propeller and in Hoeijmakers [26] for delta-like wings. A lifting surface method for the performance analysis of marine propellers at design and off-design operating conditions is presented by Greeley and Kerwin [25]. Hoeijmakers [26] modelled the potential flow around delta wings with leading edge vortex sheet separation by a second-order panel method. In addition, vortex sheet separation can also occur along the chord at the tip of the blade of a ducted propeller, due to the gap flow between the blade tip and the duct inner side surface. An iterative method coupling a lifting surface method and a finite volume method was introduced by Gu [27]. The separated vortex sheet is composed of horseshoes vortices placed along the chord at the tip of the propeller blade.

In 1996, the development of a panel code which implements a low-order potential-based panel method for the calculation of the incompressible potential flow around marine propellers was initiated at IST by Falcão de Campos [28]. The code is able to calculate the three-dimensional wetted potential flow around wings and marine propellers. A verification study of the code was performed by a grid convergence study for the flow past an ellipsoid with conventional and quasi-orthogonal grids, Falcão de Campos *et al.* [29].

The purpose of the present study is to contribute to a better understanding of panel methods in the modelling of the incompressible potential flow around wings and marine

propellers. The analysis is restricted to steady wetted flow. The panel method is presented and compared with other panel methods and with available experimental data. Then, two problems are considered: the potential flow solution behaviour in the vicinity of the tip and the modelling of separated vortex flows with BEM.

The thesis is organised as follows: in Chapter 2 the mathematical model for the three-dimensional potential flow about wings and marine propellers is given. Chapter 3 presents the numerical details of the panel method. Three wake models are considered: a rigid wake model with linear and iterative pressure Kutta condition applied at the trailing edge of the lifting surface, a partial wake relaxation model where the dipole strengths are calculated in order to have zero-pressure-jump on the wake surface, and a full wake relaxation model where the vortex lines are aligned with the local fluid velocity. Chapter 4 describes the techniques for the generation of structured grids on the surfaces of the wing, propeller blade, duct, hub and vortex sheet. Conventional and quasi-orthogonal panel arrangements are considered for the propeller blade. Results of the three-dimensional potential flow model about wings and marine propellers are presented in Chapter 5. Results of the present method are compared with other panel methods and experimental measurements available from the literature. Chapter 6 is centred on the numerical modelling of wing and propeller tip flows. Different techniques are tested to obtain a more reliable solution at the tip. In Chapter 7 the present method is used to model the vortex sheet separation. First, results of leading edge separation about delta wings at high incidence are presented. Second, the leading edge separation modelling for marine propellers is addressed. Finally, the gap flow between the blade tip and the duct inner surface is considered. In this case, vortex sheet separation is assumed along the blade tip. Chapter 8 contains the main conclusions of the present study.

Chapter 2

Mathematical Formulation

2.1 Description of the Problem

Let us consider the general case of one or more bodies that are moving at constant speed U in an incompressible ideal fluid otherwise at rest in a domain extending to infinity in all directions. These moving bodies may be: a wing of span $2S$, Figure 2.1-right, or a screw propeller of radius R consisting of K blades symmetrically distributed around an axisymmetric hub, Figure 2.1-left, (which can be inside a duct) rotating at constant angular velocity Ω .

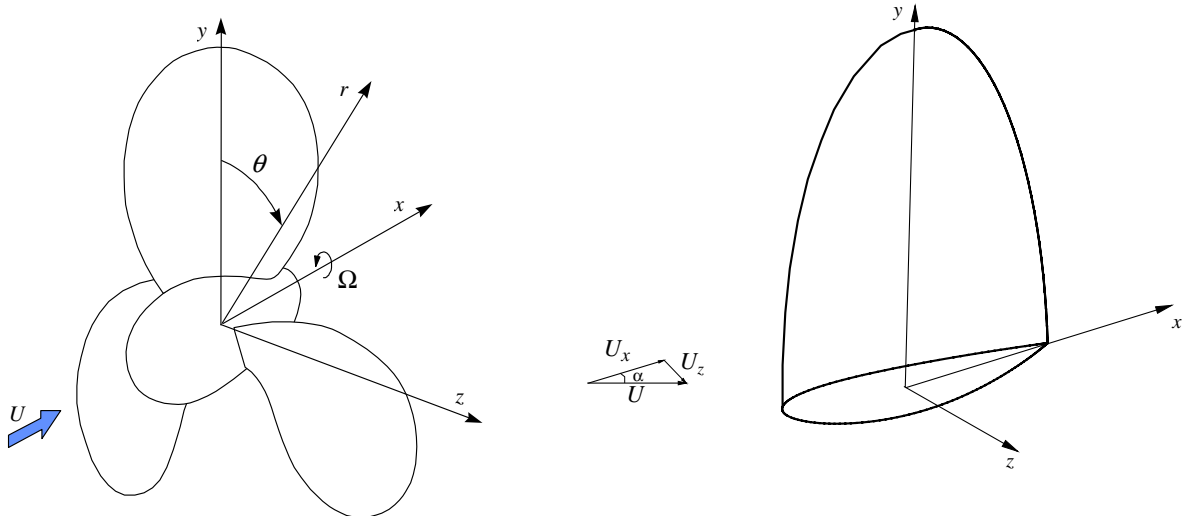


Figure 2.1: Coordinate reference systems for propeller and wing.

For the wing case, we define a Cartesian coordinate system (x, y, z) with unit vectors $(\vec{e}_x, \vec{e}_y, \vec{e}_z)$ moving with the wing. The x -axis is aligned with the chord direction at the wing mid-span plane, the y -axis is along the span of the wing and z completes the right-hand system. The undisturbed onset velocity in the moving frame is written as:

$$\vec{U}_\infty = \vec{U}, \quad (2.1)$$

2.2. Potential Flow Problem

with magnitude $|\vec{U}| = U$ equal to the wing speed, where $|\vec{U}|$ denotes the Euclidian norm of the vector \vec{U} . Although not required, for the present study we will assume that the onset flow velocity has zero spanwise component $U_y = 0$, so that

$$\vec{U} = U_x \vec{e}_x + U_z \vec{e}_z, \quad (2.2)$$

with

$$U_x = U \cos \alpha, \quad U_z = U \sin \alpha, \quad (2.3)$$

and α is the angle of attack.

For the propeller case, we define the Cartesian coordinate system (x, y, z) with unit vectors $(\vec{e}_x, \vec{e}_y, \vec{e}_z)$ rotating with the propeller blades, with the positive x -axis direction opposite to the propeller axial motion, the y -axis coincident with the propeller reference line, passing through the reference point of the root section of the blade $k = 1$, and the z -axis completing the right-hand system. We use a cylindrical coordinate system (x, r, θ) which is related to the Cartesian system by the transformation

$$y = r \cos \theta, \quad z = r \sin \theta. \quad (2.4)$$

The undisturbed onset velocity in the rotating frame is

$$\vec{U}_\infty = U \vec{e}_x + \Omega r \vec{e}_\theta, \quad (2.5)$$

where $(\vec{e}_x, \vec{e}_r, \vec{e}_\theta)$ are the unit vectors of the cylindrical coordinate system.

2.2 Potential Flow Problem

In the coordinate system moving with the body the flow is steady and the flow field velocity $\vec{V}(x, y, z)$ may be described by the undisturbed onset velocity plus a perturbation potential $\phi(x, y, z)$ in the form

$$\vec{V} = \vec{U}_\infty + \nabla \phi. \quad (2.6)$$

The perturbation potential satisfies the Laplace equation

$$\nabla^2 \phi = 0. \quad (2.7)$$

The boundary of domain consists of the body surfaces \mathcal{S}_B . The perturbation potential must satisfy the following boundary conditions:

$$\nabla \phi \rightarrow 0, \quad \text{if } |\vec{x}| \rightarrow \infty \text{ and } x \neq +\infty \quad (2.8)$$

at infinity, where $\vec{x} = x\vec{e}_x + y\vec{e}_y + z\vec{e}_z$ is the Cartesian distance to the origin, and a Neumann boundary condition

$$\frac{\partial \phi}{\partial n} \equiv \vec{n} \cdot \nabla \phi = -\vec{n} \cdot \vec{U}_\infty \text{ on } \mathcal{S}_{\mathcal{B}}, \quad (2.9)$$

where $\partial/\partial n$ denotes differentiation along the normal and \vec{n} is the unit vector normal to the surface directed outward from the body.

The body surfaces $\mathcal{S}_{\mathcal{B}}$ can be either lifting surfaces, like the wing, the propeller blades and the duct, or non-lifting surfaces, like the hub. For a lifting surface we allow for the existence of circulation. In this case, a vortex sheet is shed from the trailing edge of the lifting surface. From continuity and momentum considerations across a surface of velocity discontinuity, Saffman [30], two boundary conditions apply on the vortex sheet or vortex wake surface $\mathcal{S}_{\mathcal{W}}$: the normal component of the fluid velocity is continuous and equal to the normal velocity of the sheet

$$\vec{V}_w \cdot \vec{n} = \vec{V}^+ \cdot \vec{n} = \vec{V}^- \cdot \vec{n} \text{ on } \mathcal{S}_{\mathcal{W}}, \quad (2.10)$$

and the pressure is continuous across the vortex wake

$$p^+ = p^- \text{ on } \mathcal{S}_{\mathcal{W}}, \quad (2.11)$$

where \vec{V} is the fluid velocity, \vec{V}_w the velocity of the points on the vortex sheet surface $\mathcal{S}_{\mathcal{W}}^1$, p is the pressure and the indices $+$ and $-$ denote the two sides of the vortex sheet, arbitrarily chosen on the upper side and lower side of the lifting surface at the trailing edge, respectively. The unit vector normal to the vortex sheet is defined pointing from the lower $-$ to the upper $+$ side of the sheet.

In order to specify uniquely the circulation around the lifting surface it is necessary to impose the Kutta condition at the trailing edge. Various forms of the Kutta condition have been used, see, for instance Morino [31]. In its most general form, the Kutta condition requires the velocity to remain bounded

$$|\nabla \phi| < \infty \quad (2.12)$$

at a sharp trailing edge.

2.3 Integral Equation

Applying Green's second identity, we obtain the representation for the perturbation potential at a field point $P(x, y, z)$ in the fluid domain outside the body in terms of source and dipole distributions on its boundary $\mathcal{S} = \mathcal{S}_{\mathcal{B}} \cup \mathcal{S}_{\mathcal{W}}$ as

¹It should be noted that for a sufficiently smooth vortex sheet surface with well defined normal, the motion of the sheet is fully specified by its velocity in the normal direction.

2.3. Integral Equation

$$4\pi\varepsilon\phi(P) = - \iint_{\mathcal{S}} \mu(Q) \frac{\partial}{\partial n_Q} \left(\frac{1}{R(P,Q)} \right) dS - \iint_{\mathcal{S}} \sigma(Q) \frac{1}{R(P,Q)} dS, \quad (2.13)$$

where

$$\varepsilon = \begin{cases} 0 & \Leftarrow P \in \text{int } \{\mathcal{S}\} \\ 1/2 & \Leftarrow P \in \text{bound } \{\mathcal{S}\} \\ 1 & \Leftarrow P \in \text{out } \{\mathcal{S}\} \end{cases} \quad (2.14)$$

$R(P,Q)$ is the distance between the field point $P(x_P, y_P, z_P)$ and the point $Q(x_Q, y_Q, z_Q)$ on the boundary \mathcal{S} , and $\partial/\partial n_Q$ denotes the derivative normal to the boundary at the point Q . A detailed derivation of Equation (2.13) may be found in Batchelor [32].

The strength of the dipole distributions is given by the discontinuity of the potential across the surface \mathcal{S}

$$\mu(Q) = -(\phi(Q) - \bar{\phi}(Q)) \text{ on } \mathcal{S}, \quad (2.15)$$

and the strength of the source distributions is given by

$$\sigma(Q) = \frac{\partial\phi}{\partial n_Q} - \frac{\partial\bar{\phi}}{\partial n_Q} \text{ on } \mathcal{S}, \quad (2.16)$$

in which $\bar{\phi}$ represents the potential on the other side of the surface \mathcal{S} . On the body surfaces \mathcal{S}_B , $\bar{\phi}$ represents the potential in the domain inside the body. Since we are only interested in the domain outside the body, the potential inside the body may be chosen arbitrarily. In the so-called Morino formulation, Morino and Kuo [4], we take $\bar{\phi} = 0$ inside the body surfaces \mathcal{S}_B . Therefore, we have

$$\mu(Q) = -\phi(Q) \text{ on } \mathcal{S}_B, \quad (2.17)$$

and

$$\sigma(Q) = \frac{\partial\phi}{\partial n_Q} \text{ on } \mathcal{S}_B. \quad (2.18)$$

On the wake surface \mathcal{S}_W , since $\vec{V}_w \cdot \vec{n}$ and \vec{U}_∞ are continuous across the sheet, the boundary condition (2.10) on both sides of the wake surface gives

$$\sigma(Q') = \frac{\partial\phi^+}{\partial n} - \frac{\partial\phi^-}{\partial n} = 0, \text{ if } Q' \in \mathcal{S}_W, \quad (2.19)$$

which means that the wake surface is represented only by a dipole layer,

$$\mu(Q') = -(\phi^+(Q') - \phi^-(Q')) \equiv -\Delta\phi(Q'). \quad (2.20)$$

On the body surfaces \mathcal{S}_B , the boundary condition (2.9), together with Equation (2.18), determine the strength of the source distribution. Application of Equation (2.13) on \mathcal{S}_B leads to

$$2\pi\phi(P) - \iint_{\mathcal{S}_B} \phi(Q) \frac{\partial}{\partial n_Q} \left(\frac{1}{R(P, Q)} \right) dS - \iint_{\mathcal{S}_W} \Delta\phi(Q') \frac{\partial}{\partial n_{Q'}} \left(\frac{1}{R(P, Q')} \right) dS = \\ \iint_{\mathcal{S}_B} (\vec{n} \cdot \vec{U}_\infty) \frac{1}{R(P, Q)} dS, \quad P \in \mathcal{S}_B. \quad (2.21)$$

Equation (2.21) is a Fredholm integral equation of the second kind in the dipole distribution $\mu(Q) = -\phi(Q)$ on the body surfaces \mathcal{S}_B . The Kutta condition (2.12) yields the additional relationship between the dipole strength $\mu(Q') = -\Delta\phi(Q')$ in the wake and the surface dipole strength at the trailing edge.

2.4 Boundary Conditions on the Wake Surface

The two boundary conditions on the wake are:

- The normal component of the fluid velocity is continuous and equal to the normal velocity of the wake surface, Equation (2.10).
- The pressure must be continuous across the wake surface, Equation (2.11).

The first condition, Equation (2.10), implies that the vortex sheet moves with the fluid. In the reference system moving with the body, the flow is steady and the normal velocity of the wake surface is zero:

$$\vec{V}_w \cdot \vec{n} = 0 \text{ on } \mathcal{S}_W, \quad (2.22)$$

and taking the average of Equation (2.10), we obtain

$$\vec{V}_m \cdot \vec{n} = 0 \text{ on } \mathcal{S}_W, \quad (2.23)$$

where $\vec{V}_m = \frac{1}{2}(\vec{V}^+ + \vec{V}^-)$ denotes the mean velocity. Outside of the vortex sheet the Bernoulli equation for incompressible steady potential flow applies

$$\frac{p}{\rho} + \frac{1}{2}|\vec{V}|^2 = \frac{p_\infty}{\rho} + \frac{1}{2}|\vec{U}_\infty|^2, \quad (2.24)$$

where p_∞ is the pressure of the undisturbed inflow and ρ the fluid density. Applying consecutively the Bernoulli equation at a given point on each side of the vortex sheet and subtracting, we obtain

$$\frac{\Delta p}{\rho} = -\frac{1}{2} \left(|\vec{V}^+|^2 - |\vec{V}^-|^2 \right), \quad (2.25)$$

2.4. Boundary Conditions on the Wake Surface

where $\Delta p = p^+ - p^-$ is the pressure-jump across the sheet. From the boundary condition (2.11), the pressure-jump is zero and by noting that

$$\left| \vec{V}^+ \right|^2 - \left| \vec{V}^- \right|^2 = (\vec{V}^+ + \vec{V}^-) \cdot (\vec{V}^+ - \vec{V}^-), \quad (2.26)$$

we obtain

$$\vec{V}_m \cdot \Delta \vec{V} = 0 \text{ on } \mathcal{S}_{\mathcal{W}}, \quad (2.27)$$

where $\Delta \vec{V} = \vec{V}^+ - \vec{V}^-$ denotes the velocity discontinuity on the wake surface. It may be shown, see Appendix A, that the velocity discontinuity may be written as the surface gradient of the potential discontinuity,

$$\vec{V}_m \cdot \nabla_S(\Delta \phi) = 0 \text{ on } \mathcal{S}_{\mathcal{W}}, \quad (2.28)$$

where $\nabla_S = -\vec{n} \times (\vec{n} \times \nabla)$ denotes the surface gradient. Equation (2.28) shows that the potential-jump remains constant following a fluid particle moving on the wake with the velocity \vec{V}_m .

The exact modelling of the wake, i.e., the fulfillment of the exact boundary conditions (2.23) and (2.28) on the wake surface, requires solving for both the position $\mathcal{S}_{\mathcal{W}}(\vec{x})$ and the strength of the dipole singularity distribution $\mu(\vec{x})$ on the wake, together with the singularity distributions on the body. This is not an easy task to accomplish due to the highly non-linear character of the boundary conditions. The main difficulty is that the wake geometry is not known at the outset, and a successful initial guess to be input in the procedure that solves the system of equations may be difficult to find. Often, one relies on the use of a hierarchical “wake relaxation” procedure, in which, one starts with a rigid wake, next the vortex lines are aligned with the local velocity, giving a new estimate of the wake surface, and the iterative procedure is repeated until some convergence criteria are met. This is essentially the method followed in the so-called “full wake relaxation” procedures applied by Pyo [16] and Dang [23]. In these methods the simulation of the roll-up of the vortex sheet near the blade tip is attempted. We note that the resulting integral equations for $\mu(\vec{x})$ and $\mathcal{S}_{\mathcal{W}}(\vec{x})$ in the general formulation are highly non-linear in \vec{x} , and this iterative scheme may diverge. In such cases a simultaneous solution for the position and singularity strength would be needed, Hoeijmakers [33].

A simple linearisation of the boundary conditions with respect to the undisturbed flow leads to the classical “rigid wake” approximation. This results in vortex lines aligned with the undisturbed velocity \vec{U}_∞ , where the wake strips have constant dipole strength equal to the value of μ at the trailing edge. The dipole strength at the wake surface may be related to the potential discontinuity at the trailing edge of the lifting surface. If the dipole strength is made equal to (minus) the potential-jump at the trailing edge, no discrete vortex will be present along the trailing edge. This is the so-called Morino Kutta condition, Morino and Kuo [4], which can be written in the form

$$\Delta\phi = \phi^+ - \phi^-, \quad (2.29)$$

in which ϕ^+ and ϕ^- denote the values of the potentials at the trailing edge, respectively on the upper and lower sides of the lifting surface.

A simplification of the “full wake relaxation”, is the “partial wake relaxation”, where the wake surface is split in a near wake and a far wake, both specified by the user. In the near wake, the vortex lines are allowed to move freely on that prescribed surface, in a way that the zero-pressure-jump condition, Equation (2.28), is satisfied on the near wake. The far wake is made by vortex lines of asymptotic shape that start from the end-points of the near wake. For a wing they should be straight lines and for a propeller in uniform flow helicoidal lines. The resulting equations in the near wake are only weakly non-linear in $\mu(\vec{x})$, Hoeijmakers [33].

In order to fulfill the zero-pressure-jump condition, the mean velocity on the vortex sheet has to be perpendicular to $\nabla_S(\mu)$. However, the normal velocity condition is not satisfied and the wake is not exactly force-free. The mean velocity vector \vec{V}_m and the surface vorticity vector $\vec{\gamma} = -\vec{n} \times \nabla_S(\mu)$ are not parallel to each other, resulting in a force on the wake, tangential to its surface. This force is proportional to $\vec{V}_m \times \vec{\gamma}$. Figure 2.2 illustrates this.

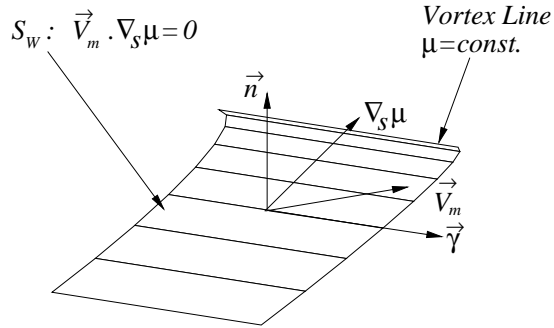


Figure 2.2: Partial wake relaxation - force on wake.

2.5 Velocity, Pressure and Forces

The solution of the integral equation (2.21) gives the perturbation potential $\phi(Q)$ on the body surfaces \mathcal{S}_B . The perturbation velocity tangent to the surface can be obtained by differentiation of the surface distribution of the potential $\phi(Q)$. Let (u_1, u_2) be orthogonal curvilinear coordinates on the surface and (\vec{e}_1, \vec{e}_2) be the unit vectors along the coordinate lines $u_2 = \text{const.}$ and $u_1 = \text{const.}$, respectively. The perturbation velocity tangent to the surface is

$$\vec{v}_t = \frac{\partial \phi}{\partial u_1} \vec{e}_1 + \frac{\partial \phi}{\partial u_2} \vec{e}_2. \quad (2.30)$$

The total velocity tangent to the surface \vec{V}_t is obtained by adding to the component tangent to the surface of the perturbation velocity, Equation (2.30), the component tangent to the surface of the undisturbed onset flow velocity

$$\vec{V}_t = \vec{U}_\infty - (\vec{U}_\infty \cdot \vec{n}) \vec{n} + \vec{v}_t, \quad (2.31)$$

with \vec{U}_∞ given by Equation (2.1) for the wing case, and by Equation (2.5) for the propeller case. In terms of the two orthogonal components along (\vec{e}_1, \vec{e}_2) , \vec{V}_t becomes

$$\vec{V}_t = \left[(\vec{U}_\infty \cdot \vec{e}_1) + \frac{\partial \phi}{\partial u_1} \right] \vec{e}_1 + \left[(\vec{U}_\infty \cdot \vec{e}_2) + \frac{\partial \phi}{\partial u_2} \right] \vec{e}_2. \quad (2.32)$$

The pressure on the surface is obtained from the Bernoulli equation (2.24). We introduce the pressure coefficient

$$C_p = \frac{p - p_\infty}{1/2\rho U_\infty^2}, \quad (2.33)$$

with $U_\infty = |\vec{U}_\infty|$. For a propeller it is usual to define the pressure coefficient

$$C_{pn} = \frac{p - p_\infty}{1/2\rho n^2 D^2}, \quad (2.34)$$

in which $n = \Omega/(2\pi)$ is the propeller rate of revolutions and D its diameter.

The components of the inviscid force acting on the propeller are obtained by integration of the pressure distribution on the body surfaces. Let (n_x, n_y, n_z) be the Cartesian components of the outward unit normal \vec{n} . The integrated force is

$$\vec{F} = - \iint_{S_B} p \vec{n} dS, \quad (2.35)$$

and the moment is

$$\vec{M} = - \iint_{S_B} p(\vec{n} \times \vec{x}) dS. \quad (2.36)$$

Due to symmetry the only non-zero components of the force and moment acting on the propeller are in the axial direction x , respectively, the inviscid thrust of the propeller blades and hub T :

$$T = \iint_{S_{blades} \cup S_{hub}} p n_x dS, \quad (2.37)$$

and the inviscid torque of the propeller blades and hub Q :

$$Q = \iint_{S_{blades} \cup S_{hub}} p(n_y z - n_z y) dS. \quad (2.38)$$

We introduce the non-dimensional advance coefficient J :

$$J = \frac{U}{nD}, \quad (2.39)$$

and express the force and moment in terms of the non-dimensional thrust coefficient K_T and the torque coefficient K_Q :

$$K_T = \frac{T}{\rho n^2 D^4}, \quad K_Q = \frac{Q}{\rho n^2 D^5}. \quad (2.40)$$

For the ducted propeller case, we have also to consider the inviscid thrust of the duct T_D :

$$T_D = \iint_{S_{duct}} p n_x dS. \quad (2.41)$$

The non-dimensional duct thrust coefficient K_{T_D} is

$$K_{T_D} = \frac{T_D}{\rho n^2 D^4}. \quad (2.42)$$

Then, the non-dimensional total thrust of the propeller with the duct is given by

$$K_{T_T} = \frac{T + T_D}{\rho n^2 D^4}. \quad (2.43)$$

For the wing case, we introduce the non-dimensional coefficients C_x , C_y , C_z for each component of the force,

$$C_x = \frac{F_x}{1/2 \rho U_\infty^2 A}, \quad C_y = \frac{F_y}{1/2 \rho U_\infty^2 A}, \quad C_z = \frac{F_z}{1/2 \rho U_\infty^2 A}, \quad (2.44)$$

where A is the planform or projected area. F_x , F_y and F_z are obtained by pressure integration and the lift and induced drag forces are given by

$$\begin{aligned} L &= F_z \cos \alpha - F_x \sin \alpha \\ D_i &= F_x \cos \alpha + F_z \sin \alpha, \end{aligned} \quad (2.45)$$

or, in terms of the lift coefficient C_L and the induced drag coefficient C_{D_i} :

$$\begin{aligned} C_L &= C_z \cos \alpha - C_x \sin \alpha \\ C_{D_i} &= C_x \cos \alpha + C_z \sin \alpha. \end{aligned} \quad (2.46)$$

Chapter 3

Panel Method

3.1 Discretisation of the Integral Equation

For the numerical solution of the integral equation (2.21) a low-order panel method is used. The body surfaces \mathcal{S}_B and the wake surfaces \mathcal{S}_W are discretised in quadrilateral panels. The quadrilateral panels are defined by four points on the surface, which are not necessarily in the same plane. The boundary of each element consists of the four straight-line elements joining the four corner points of the quadrilateral panel. The surface of the panel, which approximates the exact surface, has a hyperboloidal shape. The advantage of using these type of panels in comparison with the use of flat panels as in the original work of Hess and Smith [1], is that the approximating surface is fully closed due to coincidence of the boundaries of the panel with the boundaries of adjacent panels.

In the numerical solution of the integral equation (2.21) the integrals over the body and wake surfaces are approximated by the summation of the integrals on the panels discretising the surfaces, assuming a constant strength of the dipole and source distributions on each panel. From flow symmetry considerations, the body and wake surfaces are divided in K identical sectors. In the wing case, the symmetry with respect to the central symmetric plane is enforced by considering $K = 2$ wing surface sectors.

Let $\mu_j = -\phi_j$ be the values of the dipole strength of the panel S_B^{jk} on the surface of the k^{th} body sector, with $k = 1, \dots, K$, $j = 1, \dots, N$, and N being the number of panels on each body sector; let $\Delta\mu_j = -\Delta\phi_j$ be the values of the dipole strengths of the panel S_W^{jk} on the surface of the k^{th} wake sector, with $j = 1, \dots, N_K$, and N_K being the number of wake dipole strengths that have to be determined from the wake model; let $(\vec{n}_j \cdot \vec{U}_\infty)$ be evaluated on the centre point of the panel S_B^{jk} on the surface of the k^{th} body sector. If Equation (2.21) is satisfied on the centre points P_i , $i = 1, \dots, N$, of the N panels of the $k = 1$ body sector, the so-called collocation points, we obtain a system of algebraic equations in the form

$$\sum_{j=1}^N (\delta_{ij} - D_{ij}) \phi_j - \sum_{j=1}^{N_K} W_{ij} \Delta\phi_j = \sum_{j=1}^N S_{ij} (\vec{n}_j \cdot \vec{U}_\infty), \quad i = 1, \dots, N, \quad (3.1)$$

3.2. Wake Models

in which δ_{ij} is the Kronecker delta and D_{ij} , W_{ij} and S_{ij} are the influence coefficients given by

$$\begin{aligned} D_{ij} &= \sum_{k=1}^K \left[\frac{1}{2\pi} \iint_{S_B^{jk}} \frac{\partial}{\partial n_Q} \left(\frac{1}{R(P_i, Q)} \right) dS \right] \\ W_{ij} &= \sum_{k=1}^K \left[\frac{1}{2\pi} \iint_{S_W^{jk}} \frac{\partial}{\partial n_Q} \left(\frac{1}{R(P_i, Q)} \right) dS \right]. \\ S_{ij} &= \sum_{k=1}^K \left[\frac{1}{2\pi} \iint_{S_B^{jk}} \frac{1}{R(P_i, Q)} dS \right] \end{aligned} \quad (3.2)$$

The algebraic system of equations (3.1) can be written in the matrix form as follows

$$[A] \{\phi\} - [W] \{\Delta\phi\} = \{B\}, \quad (3.3)$$

where $[A]$ is a $N \times N$ matrix with elements

$$A_{ij} = \delta_{ij} - D_{ij}, \quad i, j = 1, \dots, N, \quad (3.4)$$

$[W]$ is a $N \times N_K$ matrix with elements W_{ij} , $\{B\}$ is a N vector with elements

$$B_i = \sum_{j=1}^N S_{ij} (\vec{n}_j \cdot \vec{U}_\infty), \quad i = 1, \dots, N, \quad (3.5)$$

$\{\phi\}$ is the vector of N unknowns and $\{\Delta\phi\}$ is the vector of N_K wake dipole strengths that have to be determined from the wake model.

3.2 Wake Models

Three wake models are considered: a rigid wake model with linear and iterative pressure Kutta condition applied at the trailing edge of the lifting surface, a partial wake relaxation model where the wake is split in a near wake and a far wake and the dipole strengths are calculated in order to have zero-pressure-jump on the near wake, and a full wake relaxation model where the vortex lines are aligned with the local fluid velocity.

3.2.1 Rigid Wake

If the linear Morino Kutta condition (2.29) is applied assuming constant dipole strength along the streamwise direction, the number of unknown wake dipole strengths is equal to the number of panels along the trailing edge of the lifting surface, $N_K = N_R$. Then, the matrix equation (3.3) becomes

$$[A] \{\phi\} - [W]^{LK} \{\Delta\phi\}^{LK} = \{B\}, \quad (3.6)$$

where $[W]^{LK}$ is a $N \times N_R$ matrix with elements

$$W_{ij}^{LK} = \sum_{l=1}^{N_W} W_{i,(j-1)N_W+l}, \quad i = 1, \dots, N, j = 1, \dots, N_R, \quad (3.7)$$

$\{\Delta\phi\}^{LK}$ is a N_R vector with elements

$$\Delta\phi_j^{LK} = \Delta\phi_{(j-1)N_W+l}, \quad j = 1, \dots, N_R, l = 1, \dots, N_W, \quad (3.8)$$

and N_W is the number of wake panels along the streamwise direction. Then

$$[\bar{A}]^{LK} \{\bar{\phi}\}^{(0)} = \{\bar{B}\}^{LK}, \quad (3.9)$$

where $\{\bar{\phi}\}^{(0)}$ is a $(N + N_R)$ unknown vector with elements

$$\{\bar{\phi}\}^{(0)} : \begin{cases} \bar{\phi}_i^{(0)} = \phi_i & i = 1, \dots, N \\ \bar{\phi}_{N+j}^{(0)} = \Delta\phi_j^{LK} & j = 1, \dots, N_R \end{cases}, \quad (3.10)$$

$[\bar{A}]^{LK}$ is a $(N + N_R) \times (N + N_R)$ augmented matrix with

$$[\bar{A}]^{LK} : \begin{cases} \bar{A}_{ij}^{LK} = A_{ij} & i = 1, \dots, N; j = 1, \dots, N \\ \bar{A}_{ij}^{LK} = -W_{il}^{LK} & i = 1, \dots, N; j = N + l; l = 1, \dots, N_R \\ \bar{A}_{ij}^{LK} = 1 & i = N + l; j = (l - 1)N_{CP} + 1; l = 1, \dots, N_R \\ \bar{A}_{ij}^{LK} = -1 & i = N + l; j = lN_{CP}; l = 1, \dots, N_R \\ \bar{A}_{ij}^{LK} = 1 & i = N + l; j = N + l; l = 1, \dots, N_R \\ \bar{A}_{ij}^{LK} = 0 & \text{otherwise} \end{cases}, \quad (3.11)$$

$\{\bar{B}\}^{LK}$ is a $(N + N_R)$ vector with elements

$$\{\bar{B}\}^{LK} : \begin{cases} \bar{B}_i^{LK} = B_i & i = 1, \dots, N \\ \bar{B}_i^{LK} = 0 & i = N + l; l = 1, \dots, N_R \end{cases}, \quad (3.12)$$

and N_{CP} is the number of blade panels along the chordwise direction.

An alternative condition in the rigid wake formulation, is the implementation of an iterative pressure Kutta condition, which replaces the linear Kutta condition (2.29) by

3.2.2. Partial Wake Relaxation

imposing equal pressure on both sides of the lifting surface at the trailing edge. Due to the non-linear character of the pressure, the application of the condition for the pressure equality on the control points on the panels adjacent to the trailing edge gives origin to a non-linear system of equations. In the present work, its solution is obtained by the method of Newton-Raphson.

Let $(\Delta C_p)_i$, $i = 1, \dots, N_R$ be the pressure difference of the two control points on the panels adjacent to the trailing edge on the i^{th} blade strip. The pressure condition writes

$$(\Delta C_p)_i = (C_p^+)_i - (C_p^-)_i = 0, \quad i = 1, \dots, N_R. \quad (3.13)$$

According to the method of Newton-Raphson the values at the iteration level $(n + 1)$ of the dipole strength on the wake strips can be obtained from the solution of the system of equations

$$\sum_{j=1}^{N_R} P_{ij} \left(\Delta\phi_j^{(n+1)} - \Delta\phi_j^{(n)} \right) = -(\Delta C_p)_i^{(n)}, \quad i = 1, \dots, N_R, \quad (3.14)$$

where $\Delta\phi_i^{(n)}$ and $(\Delta C_p)_i^{(n)}$ denote the potential-jump on the wake strips and the pressure difference of the two control points of the panels adjacent to the trailing edge on the i^{th} strip in the iteration level (n) , respectively. P_{ij} is the Jacobian matrix defined by

$$P_{ij} = \frac{\partial (\Delta C_p)_i}{\partial (\Delta\phi)_j}, \quad i, j = 1, \dots, N_R. \quad (3.15)$$

The first approximation $\Delta\phi_i^{(0)}$ is obtained from the linear Kutta condition (2.29), which corresponds to the system of equations (3.9). The iterative solution of the system of equations (3.14) with the application of the pressure Kutta condition (3.13), including the calculation of the Jacobian matrix P_{ij} is described in the Appendix B.

3.2.2 Partial Wake Relaxation

The rigid wake model does not ensure the equality of the pressure on both sides of the wake surface. To address this problem a partial wake relaxation model is implemented. In this model the wake surface is split in a near wake and a far wake. We apply the condition of pressure equality on the control points of the near wake. This will give $N_W \times N_R$ conditions. Then, in the partial wake relaxation model $N_K = N_W \times N_R$, which means that the number of wake dipole strengths is equal to the total number of panels of the near wake. The N_R dipole strengths in the far wake are set equal to the dipole strengths of the adjacent wake panels of the near wake.

Again, due to the non-linear character of the pressure, the application of a zero-pressure-jump condition on the control points on the near wake leads to a non-linear system of

equations and its solution can be obtained by the method of Newton-Raphson. In the partial wake relaxation model, the pressure condition is

$$(\Delta C_p)_i = (C_p^+)_i - (C_p^-)_i = 0, \quad i = 1, \dots, N_W \times N_R. \quad (3.16)$$

Then, the values at the iteration level $(n + 1)$ of the dipole strength on the near wake can be obtained from the solution of the system of equations,

$$\sum_{j=1}^{N_W \times N_R} P_{ij} \left(\Delta\phi_j^{(n+1)} - \Delta\phi_j^{(n)} \right) = -(\Delta C_p)_i^{(n)}, \quad i = 1, \dots, N_W \times N_R, \quad (3.17)$$

where $\Delta\phi_i^{(n)}$ and $(\Delta C_p)_i^{(n)}$ denote the potential-jump and the pressure-jump on the near wake in the iteration level (n) , respectively. The Jacobian matrix is defined by

$$P_{ij} = \frac{\partial (\Delta C_p)_i}{\partial (\Delta\phi)_j}, \quad i, j = 1, \dots, N_W \times N_R. \quad (3.18)$$

A similar procedure, in comparison to the rigid wake model, is used for the solution of the system of equations (3.17), see Appendix B.

The pressure on the wake surface is obtained from the Bernoulli equation, applied consecutively at a given point on each side of the vortex sheet, Equation (2.25). From Equation (2.26) and considering the pressure coefficient, Equation (2.33), the zero-pressure-jump boundary condition can be written as

$$\Delta C_p = C_p^+ - C_p^- = -\frac{2}{U_\infty^2} \left(\vec{V}_m \cdot \Delta \vec{V} \right), \quad (3.19)$$

in which the $+$ and $-$ denote the upper side and the lower side of the wake surface, respectively.

$\vec{V}_m = \frac{1}{2}(\vec{V}^+ + \vec{V}^-)$ is the total mean velocity on the wake surface, which includes the contributions due to the undisturbed velocity and the singularity distributions on the body surfaces \mathcal{S}_B and wake surfaces \mathcal{S}_W . The mean velocity can be written as the sum of the various contributions

$$\vec{V}_m = \vec{U}_\infty + \vec{u}_\mu + \vec{u}_\sigma, \quad (3.20)$$

with

$$\begin{aligned} \vec{u}_\mu(P) &= \frac{1}{4\pi} \iint_{\mathcal{S}_B \cup \mathcal{S}_W} \mu(Q) \left[3 \left(\vec{R} \cdot \vec{n}_Q \right) \frac{\vec{R}}{|\vec{R}|^2} - \vec{n}_Q \right] \frac{1}{|\vec{R}|^3} dS, \\ \vec{u}_\sigma(P) &= \frac{1}{4\pi} \iint_{\mathcal{S}_B} \sigma(Q) \frac{\vec{R}}{|\vec{R}|^3} dS, \quad P \in \mathcal{S}_W, \end{aligned} \quad (3.21)$$

3.2.3. Full Wake Relaxation

where \vec{u}_μ is the velocity induced by the dipole distribution on the body and wake surfaces, \vec{u}_σ the velocity induced by the source distribution on the body surfaces and $\vec{R} \equiv \vec{R}(P, Q)$ as short-hand notation.

Alternatively, the mean velocity \vec{V}_m can be evaluated by differentiating the perturbation potential on the wake surface. However, surface numerical differentiation of the perturbation potential may be inaccurate for non-smooth wake grids as the ones produced by the wake alignment method near the rolled-up region. Therefore, in the present study the mean velocity on the wake surface is calculated directly from Equations (3.20) and (3.21).

Finally, the velocity discontinuity $\Delta\vec{V}$ is calculated by surface differentiation of the potential-jump on the wake surface,

$$\Delta\vec{V} = \nabla_S(\Delta\phi). \quad (3.22)$$

3.2.3 Full Wake Relaxation

A full wake relaxation model which predicts the roll-up of the vortex sheet behind the lifting surface is presented. The method aligns the vortex lines with the local fluid velocity by displacing the corner points of the wake grid panels with the mean velocity. A discretised form of the streamline equation is applied to find the new location of the wake surface which is aligned with local mean velocities:

$$\frac{V_m^x}{\Delta x} = \frac{V_m^y}{\Delta y} = \frac{V_m^z}{\Delta z} = \text{const.} = \frac{|\vec{V}_m|}{\Delta s}, \quad (3.23)$$

where $V_m^{x,y,z}$ denotes the Cartesian components of the mean velocity, and $\Delta x, \Delta y, \Delta z$ are the differences between the coordinates of two adjacent panel corners along the streamwise direction. The method is iterative. If Δs is defined as the distance between two adjacent panel corner points i and $i + 1$ at a given wake strip:

$$\Delta s = \sqrt{\left(x_{i+1}^{(n)} - x_i^{(n)}\right)^2 + \left(y_{i+1}^{(n)} - y_i^{(n)}\right)^2 + \left(z_{i+1}^{(n)} - z_i^{(n)}\right)^2} \quad (3.24)$$

at the iteration level (n) , then the new coordinates at the $(n + 1)^{\text{th}}$ iteration level are determined as follows:

$$\begin{aligned} x_{i+1}^{(n+1)} &= x_i^{(n)} + \frac{V_m^x}{|\vec{V}_m|} \Delta s \\ y_{i+1}^{(n+1)} &= y_i^{(n)} + \frac{V_m^y}{|\vec{V}_m|} \Delta s, \\ z_{i+1}^{(n+1)} &= z_i^{(n)} + \frac{V_m^z}{|\vec{V}_m|} \Delta s \end{aligned} \quad (3.25)$$

where $V_m^{x,y,z}$ is calculated by taking the average of the mean velocity between two adjacent panel corners:

$$V_m^{x,y,z} = \frac{1}{2} \left[V_m^{x,y,z}|_i^{(n)} + V_m^{x,y,z}|_{i+1}^{(n)} \right]. \quad (3.26)$$

The mean velocities at the panel corner points are obtained by linear interpolation from the values calculated at the mid points along each spanwise strip, except at the tip where the velocity is calculated at the corner point. A scheme is applied to accelerate the roll-up of the wake, which consists in updating all the nodes downstream of the current node along a streamwise grid line simultaneously with the displacement of the current node.

3.3 Calculation of Influence Coefficients

3.3.1 Panel Definition

Consider a quadrilateral panel defined by the straight-line elements joining four points in space, which are not necessarily in the same plane, as shown in Figure 3.1. The panel surface is curved and its boundary coincides with the four straight-line elements joining the four corners of the quadrilateral panel.

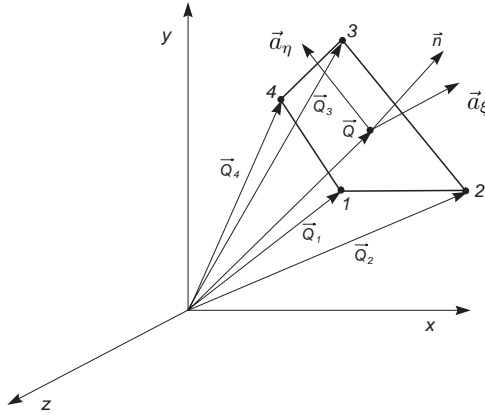


Figure 3.1: Definition of a hyperboloidal panel.

Let \vec{Q}_i , ($i = 1, \dots, 4$), be the position vectors of the corner points. We introduce curvilinear coordinates (ξ, η) on the surface of the panel. The surface is defined by

$$\vec{Q}(\xi, \eta) = \hat{\psi}_1(\xi, \eta) \vec{Q}_1 + \hat{\psi}_2(\xi, \eta) \vec{Q}_2 + \hat{\psi}_3(\xi, \eta) \vec{Q}_3 + \hat{\psi}_4(\xi, \eta) \vec{Q}_4, \quad (3.27)$$

where

$$\begin{aligned} \hat{\psi}_1(\xi, \eta) &= \frac{1}{4}(1-\xi)(1-\eta) & \hat{\psi}_2(\xi, \eta) &= \frac{1}{4}(1+\xi)(1-\eta), \\ \hat{\psi}_3(\xi, \eta) &= \frac{1}{4}(1+\xi)(1+\eta) & \hat{\psi}_4(\xi, \eta) &= \frac{1}{4}(1-\xi)(1+\eta) \end{aligned}, \quad (3.28)$$

3.3.2. Potential Influence Coefficients

and $-1 \leq \xi \leq 1, -1 \leq \eta \leq 1$. By convention the four panel corner points \vec{Q}_i , ($i = 1, \dots, 4$) correspond to the following pairs of variables (ξ, η) by the same order: $(-1, -1)$, $(1, -1)$, $(1, 1)$, $(-1, 1)$. We define two vectors tangent to the surface of the panel

$$\vec{a}_\xi = \frac{\partial \vec{Q}}{\partial \xi}, \quad \vec{a}_\eta = \frac{\partial \vec{Q}}{\partial \eta}. \quad (3.29)$$

The unit normal to the panel surface is

$$\vec{n}(\xi, \eta) = \frac{\vec{a}_\xi \times \vec{a}_\eta}{|\vec{a}_\xi \times \vec{a}_\eta|}. \quad (3.30)$$

The collocation point is chosen as the centre point of the panel at $\xi = 0, \eta = 0$:

$$\vec{Q}(0, 0) = \frac{1}{4} (\vec{Q}_1 + \vec{Q}_2 + \vec{Q}_3 + \vec{Q}_4). \quad (3.31)$$

If the four panel corner points lie on the same plane, the surface defined by Equations (3.27)-(3.28) coincides with the plane. Otherwise, the surface (3.27)-(3.28) coincides with a general hyperboloidal surface.

3.3.2 Potential Influence Coefficients

The potential influence coefficients D_{ij} , W_{ij} and S_{ij} are calculated by performing the integrations over the panel surface indicated in Equation (3.2). The influence coefficients are calculated analytically following the formulation of Morino and Kuo [4]. The formulas can be found in Morino *et al.* [34] and were slightly modified for computational purposes.

The induced potential at a field point $P(x, y, z)$ by a distribution of normal dipoles of constant strength -4π over the element surface S_e is given by

$$\phi_D(P) = \iint_{S_e} \frac{\partial}{\partial n_Q} \left(\frac{1}{R(P, Q)} \right) dS. \quad (3.32)$$

The analytical formulation for the calculation of the induced potential by a distribution of normal dipoles is given by the contribution of each panel corner to the solid angle of the element centred in P . The potential due to the dipole distribution over the quadrilateral element can be obtained by:

$$\phi_D(P) = \alpha_1 - \alpha_2 + \alpha_3 - \alpha_4, \quad (3.33)$$

with

$$\tan \alpha_i = \frac{\left| \vec{R}_i \right| \left| \vec{R}_i \cdot (\vec{a}_{\xi_i} \times \vec{a}_{\eta_i}) \right|}{\left(\vec{R}_i \times \vec{a}_{\xi_i} \right) \cdot \left(\vec{R}_i \times \vec{a}_{\eta_i} \right)}, \quad i = 1, \dots, 4, \quad (3.34)$$

where the function \tan^{-1} is defined in the domain $-\pi \leq \alpha_i \leq \pi$, $\vec{R}_i = \vec{R}(P, Q_i)$ is the vector from the field point P to the corner point Q_i , and $\vec{a}_{\xi_i}, \vec{a}_{\eta_i}$ are the tangent vectors to the panel evaluated at the corner point Q_i . Note that the definition of the function \tan^{-1} is different from the one in Morino *et al.* [34].

We remark that formula (3.33) only gives the value of the potential when the denominator of expression (3.34) has the same sign for all the vertices of the panel. Otherwise, it is necessary to subtract from expression (3.33) the sum of the discontinuities of the function \tan^{-1} from the vertices where the change of sign occurred.

The induced potential at a field point $P(x, y, z)$ by a source distribution of constant strength -4π over the element surface S_e is given by

$$\phi_S(P) = \iint_{S_e} \frac{1}{R(P, Q)} dS. \quad (3.35)$$

The potential due to the source distribution over the quadrilateral element can be obtained by considering the contributions of each panel corner:

$$\phi_S(P) = I_1^{(S)} - I_2^{(S)} + I_3^{(S)} - I_4^{(S)} + (\vec{R} \cdot \vec{n})_0 \phi_D(P). \quad (3.36)$$

The contribution of each panel corner is given by

$$I_i^{(S)} = -\frac{(\vec{R}_i \times \vec{a}_{\xi_i}) \cdot \vec{n}_i}{|\vec{a}_{\xi_i}|} \sinh^{-1} \left(\frac{\vec{R}_i \cdot \vec{a}_{\xi_i}}{|\vec{R}_i \times \vec{a}_{\xi_i}|} \right) + \frac{(\vec{R}_i \times \vec{a}_{\eta_i}) \cdot \vec{n}_i}{|\vec{a}_{\eta_i}|} \sinh^{-1} \left(\frac{\vec{R}_i \cdot \vec{a}_{\eta_i}}{|\vec{R}_i \times \vec{a}_{\eta_i}|} \right), \quad (3.37)$$

where $i = 1, \dots, 4$, \vec{n}_i denotes the normal at the corner point and the coordinate $\zeta = -(\vec{R} \cdot \vec{n})_0$ is calculated at the centre of the panel.

Equation (3.36) is exact for flat panels, but approximate for general hyperboloidal panels. The original formulation, Morino *et al.* [34], considers the normal at each panel corner. Consistent with the flat panel assumption, the normal may be considered constant over the panel. Therefore, Equations (3.36) and (3.37) can be derived for flat panels by employing the formulation of Newman [35], also described by Katz and Plotkin [36]:

3.3.3. Velocity Influence Coefficients

$$\begin{aligned}
\phi_S(P) = & - \left[(\vec{R}_1 \times \vec{a}_{\xi_1}) \cdot \frac{\vec{n}_0}{|\vec{a}_{\xi_1}|} \ln \left(\frac{|\vec{R}_1| + |\vec{R}_2| + 2|\vec{a}_{\xi_1}|}{|\vec{R}_1| + |\vec{R}_2| - 2|\vec{a}_{\xi_1}|} \right) \right] \\
& - \left[(\vec{R}_2 \times \vec{a}_{\eta_2}) \cdot \frac{\vec{n}_0}{|\vec{a}_{\eta_2}|} \ln \left(\frac{|\vec{R}_2| + |\vec{R}_3| + 2|\vec{a}_{\eta_2}|}{|\vec{R}_2| + |\vec{R}_3| - 2|\vec{a}_{\eta_2}|} \right) \right] \\
& + \left[(\vec{R}_3 \times \vec{a}_{\xi_3}) \cdot \frac{\vec{n}_0}{|\vec{a}_{\xi_3}|} \ln \left(\frac{|\vec{R}_3| + |\vec{R}_4| + 2|\vec{a}_{\xi_3}|}{|\vec{R}_3| + |\vec{R}_4| - 2|\vec{a}_{\xi_3}|} \right) \right], \quad (3.38) \\
& + \left[(\vec{R}_4 \times \vec{a}_{\eta_4}) \cdot \frac{\vec{n}_0}{|\vec{a}_{\eta_4}|} \ln \left(\frac{|\vec{R}_4| + |\vec{R}_1| + 2|\vec{a}_{\eta_4}|}{|\vec{R}_4| + |\vec{R}_1| - 2|\vec{a}_{\eta_4}|} \right) \right] \\
& + (\vec{R} \cdot \vec{n})_0 \phi_D(P)
\end{aligned}$$

where \vec{n}_0 is the normal vector at the collocation point.

When the distance of the field point P_i to the panel (say to the panel collocation point Q_j) is much larger than the typical dimension of the panel, the use of multipole expansions about the panel centre or numerical integration rules are more efficient than the use of analytical formulas. In our case, we have implemented a 4-point Gauss-Legendre integration rule for the intermediate field and a 1-point rule for the far field. We considered the intermediate and far fields when the distance $R(P_i, Q_j)$ of the field point to the panel collocation point is, respectively, between

$$\begin{aligned}
\text{Intermediate field} & \Rightarrow 3.0d \leq R(P_i, Q_j) < 6.5d, \\
\text{Far field} & \Rightarrow R(P_i, Q_j) \geq 6.5d
\end{aligned} \quad (3.39)$$

where d is the largest diagonal of the panel. The intermediate and far fields were defined based on the work of Vaz [14].

3.3.3 Velocity Influence Coefficients

The induced velocities \vec{u}_μ and \vec{u}_σ are calculated by performing the integrations over the discretised surfaces, as indicated in Equation (3.21).

The velocity potential induced at a field point $P(x, y, z)$ by a distribution of normal dipoles of constant strength -4π over the element surface S_e is given by

$$\vec{u}_D(P) = - \iint_{S_e} \left[3(\vec{R} \cdot \vec{n}_Q) \frac{\vec{R}}{|\vec{R}|^2} - \vec{n}_Q \right] \frac{1}{|\vec{R}|^3} dS. \quad (3.40)$$

The velocity potential induced at a field point $P(x, y, z)$ by a source distribution of constant strength -4π over the element surface S_e is given by

3.3.3. Velocity Influence Coefficients

$$\vec{u}_S(P) = - \iint_{S_e} \frac{\vec{R}}{|\vec{R}|^3} dS. \quad (3.41)$$

For a planar quadrilateral panel, analytical formulas are available to compute the influence coefficients for the dipole induced velocity (3.40) and source induced velocity (3.41). The dipole formulation is exact for both, planar and hyperboloidal elements. The source formulation is exact for planar panels, but just approximate for hyperboloidal elements. These formulas have been obtained by Hess and Smith [1], and can be found, for instance, in Katz and Plotkin [36].

The influence coefficient for the dipole induced velocity (3.40) can be calculated by considering the equivalence between a dipole panel and a vortex ring. In Katz and Plotkin [36], the derivation of the equivalence between the dipole panel and the vortex filaments of circulation Γ along the curve bounding the panel is described. It is seen that the velocity of the bounding curve is identical to the velocity of the dipole panel if $\Gamma = \mu$.

The velocity induced by a vortex filament of circulation $\Gamma = -4\pi$ from point 1 to point 2 at an arbitrary point P is

$$\vec{u}_{VF}(P) = -\frac{\vec{R}_1 \times \vec{R}_2}{|\vec{R}_1 \times \vec{R}_2|^2} \vec{R}_0 \cdot \left(\frac{\vec{R}_1}{|\vec{R}_1|} - \frac{\vec{R}_2}{|\vec{R}_2|} \right), \quad (3.42)$$

where $\vec{R}_0 = \vec{R}_2 - \vec{R}_1$. The velocity induced by a rectilinear vortex ring can be computed by calculating the induced velocities of the four vortex filaments that compose the boundary curve

$$\vec{u}_D(P) = \sum_{i=1}^4 \vec{u}_{VF}^{(i)}(P). \quad (3.43)$$

The derivation of the influence coefficient for the source induced velocity (3.41) is more easily done in the reference frame of the element and the final formulas are given in terms of quantities in that reference frame. Let $(\bar{x}, \bar{y}, \bar{z})$ be the cartesian coordinates of a reference frame with origin at the centroid of a planar quadrilateral panel located on the (\bar{x}, \bar{y}) plane and $(\vec{e}_{\bar{x}}, \vec{e}_{\bar{y}}, \vec{e}_{\bar{z}})$ be the unit vectors of the reference frame ($\vec{e}_{\bar{z}}$ coincide with the unit normal to the panel and points in the positive \bar{z} direction). Let the corner points of the quadrilateral panel be $\vec{Q}_i \equiv (\bar{x}_i, \bar{y}_i, 0)$, $i = 1, 2, 3, 4$, given in the counterclockwise sense.

Using the notation of Hess and Smith [1], the influence coefficients for the components of the source induced velocity at a point with coordinates $(\bar{x}, \bar{y}, \bar{z})$ in the panel reference frame are:

3.3.3. Velocity Influence Coefficients

$$u_{\bar{x}} = \left(\frac{\bar{y}_2 - \bar{y}_1}{d_{12}} \ln \frac{r_1 + r_2 - d_{12}}{r_1 + r_2 + d_{12}} + \frac{\bar{y}_3 - \bar{y}_2}{d_{23}} \ln \frac{r_2 + r_3 - d_{23}}{r_2 + r_3 + d_{23}} + \right. \\ \left. \frac{\bar{y}_4 - \bar{y}_3}{d_{34}} \ln \frac{r_3 + r_4 - d_{34}}{r_3 + r_4 + d_{34}} + \frac{\bar{y}_1 - \bar{y}_4}{d_{41}} \ln \frac{r_4 + r_1 - d_{41}}{r_4 + r_1 + d_{41}} \right) \quad (3.44)$$

$$u_{\bar{y}} = \left(\frac{\bar{x}_2 - \bar{x}_1}{d_{12}} \ln \frac{r_1 + r_2 - d_{12}}{r_1 + r_2 + d_{12}} + \frac{\bar{x}_3 - \bar{x}_2}{d_{23}} \ln \frac{r_2 + r_3 - d_{23}}{r_2 + r_3 + d_{23}} + \right. \\ \left. \frac{\bar{x}_4 - \bar{x}_3}{d_{34}} \ln \frac{r_3 + r_4 - d_{34}}{r_3 + r_4 + d_{34}} + \frac{\bar{x}_1 - \bar{x}_4}{d_{41}} \ln \frac{r_4 + r_1 - d_{41}}{r_4 + r_1 + d_{41}} \right) \quad (3.45)$$

$$u_{\bar{z}} = \left[\tan^{-1} \left(\frac{m_{12}e_1 - h_1}{\bar{z}r_1} \right) - \tan^{-1} \left(\frac{m_{12}e_2 - h_2}{\bar{z}r_2} \right) \right. \\ \left. + \tan^{-1} \left(\frac{m_{23}e_2 - h_2}{\bar{z}r_2} \right) - \tan^{-1} \left(\frac{m_{23}e_3 - h_3}{\bar{z}r_3} \right) \right. \\ \left. + \tan^{-1} \left(\frac{m_{34}e_3 - h_3}{\bar{z}r_3} \right) - \tan^{-1} \left(\frac{m_{34}e_4 - h_4}{\bar{z}r_4} \right) \right. \\ \left. + \tan^{-1} \left(\frac{m_{41}e_4 - h_4}{\bar{z}r_4} \right) - \tan^{-1} \left(\frac{m_{41}e_1 - h_1}{\bar{z}r_1} \right) \right] \quad (3.46)$$

where

$$d_{12} = \sqrt{(\bar{x}_2 - \bar{x}_1)^2 + (\bar{y}_2 - \bar{y}_1)^2} \\ d_{23} = \sqrt{(\bar{x}_3 - \bar{x}_2)^2 + (\bar{y}_3 - \bar{y}_2)^2} \\ d_{34} = \sqrt{(\bar{x}_4 - \bar{x}_3)^2 + (\bar{y}_4 - \bar{y}_3)^2} \\ d_{41} = \sqrt{(\bar{x}_1 - \bar{x}_4)^2 + (\bar{y}_1 - \bar{y}_4)^2} \quad (3.47)$$

and

$$m_{12} = \frac{\bar{y}_2 - \bar{y}_1}{\bar{x}_2 - \bar{x}_1} \\ m_{23} = \frac{\bar{y}_3 - \bar{y}_2}{\bar{x}_3 - \bar{x}_2} \\ m_{34} = \frac{\bar{y}_4 - \bar{y}_3}{\bar{x}_4 - \bar{x}_3} \\ m_{41} = \frac{\bar{y}_1 - \bar{y}_4}{\bar{x}_1 - \bar{x}_4} \quad (3.48)$$

and

$$r_k = \sqrt{(\bar{x} - \bar{x}_k)^2 + (\bar{y} - \bar{y}_k)^2 + \bar{z}^2} \\ e_k = (\bar{x} - \bar{x}_k)^2 + \bar{z}^2 \\ h_k = (\bar{x} - \bar{x}_k)(\bar{y} - \bar{y}_k), \quad k = 1, 2, 3, 4 \quad (3.49)$$

The numerical evaluation of the integrals (3.40) and (3.41) is only performed in the far field region ($R(P_i, Q_j) \geq 6.5d$), where a 4-point Gauss-Legendre integration rule is applied.

3.4 Numerical Surface Differentiation

On the body the perturbation velocity tangent to the surface, Equation (2.30), is obtained by numerical differentiation.

Let us consider the calculation of the derivatives $\partial\phi/\partial u_1$ and $\partial\phi/\partial u_2$ at the collocation point of the panel (i, j) on the surface, $i = 1, \dots, N_1$, $j = 1, \dots, N_2$, where N_1 and N_2 are the number of panels in the directions 1 and 2, respectively. Let s_1 and s_2 be the distances along the surface coordinate lines passing through the collocation points of the panels $(i-1, j)$, (i, j) , $(i+1, j)$ and $(i, j-1)$, (i, j) , $(i, j+1)$, respectively. The variation of the potential along each one of the two directions on the panel (i, j) is approximated by a parabola through the values of the potential on the three collocation points corresponding to that direction

$$\phi(s_m) = a_m s_m^2 + b_m s_m + c_m, \quad m = 1, 2. \quad (3.50)$$

A central difference scheme is used inside the domain, $i = 2, \dots, N_1 - 1$, $j = 2, \dots, N_2 - 1$. One-sided difference schemes are used at the boundaries of the domain, $i = 1, N_1$ and $j = 1, N_2$.

In general s_1 and s_2 will not be orthogonal. Let \vec{t}_1 and \vec{t}_2 be the unit vectors in the s_1 and s_2 directions, respectively, evaluated at the collocation point of the panel (i, j) . We introduce the unit vectors forming an orthogonal system

$$\begin{aligned} \vec{e}_1 &= \vec{t}_1 \\ \vec{e}_2 &= \vec{n} \times \vec{e}_1, \end{aligned} \quad (3.51)$$

where \vec{n} is the normal to the panel at the collocation point. We have

$$\begin{aligned} \frac{\partial\phi}{\partial u_1} &= \frac{\partial\phi}{\partial s_1} \\ \frac{\partial\phi}{\partial u_2} &= \frac{1}{(\vec{t}_2 \cdot \vec{e}_2)} \left[\frac{\partial\phi}{\partial s_2} - (\vec{t}_2 \cdot \vec{e}_1) \frac{\partial\phi}{\partial s_1} \right]. \end{aligned} \quad (3.52)$$

For the calculation of the derivatives $\partial\phi/\partial u_1$ and $\partial\phi/\partial u_2$ it is required to evaluate on each collocation point the arc lengths s_1 and s_2 , and the vectors \vec{t}_1 , \vec{t}_2 , \vec{e}_1 , \vec{e}_2 . To evaluate the arc lengths on the surface and the tangent vectors, we will consider the geometric description of a general hyperboloidal panel, Equations (3.27)-(3.28). The unit vectors in the s_1 and s_2 directions on an arbitrary panel are given by

$$\vec{t}_1 = \frac{\vec{a}_\xi(0, 0)}{|\vec{a}_\xi(0, 0)|}, \quad \vec{t}_2 = \frac{\vec{a}_\eta(0, 0)}{|\vec{a}_\eta(0, 0)|}. \quad (3.53)$$

The vectors \vec{a}_ξ and \vec{a}_η are given by

3.4. Numerical Surface Differentiation

$$\begin{aligned}\vec{a}_\xi(0,0) &= \sum_{i=1}^4 \vec{Q}_i \frac{\partial \hat{\psi}}{\partial \xi} \Big|_{(0,0)} = \frac{1}{4} (\vec{Q}_2 - \vec{Q}_1 + \vec{Q}_3 - \vec{Q}_4) \\ \vec{a}_\eta(0,0) &= \sum_{i=1}^4 \vec{Q}_i \frac{\partial \hat{\psi}}{\partial \eta} \Big|_{(0,0)} = \frac{1}{4} (\vec{Q}_4 - \vec{Q}_1 + \vec{Q}_3 - \vec{Q}_2)\end{aligned}. \quad (3.54)$$

The lines $\xi = 0$ and $\eta = 0$ through the panel collocation point are straight lines and their lengths are

$$\begin{aligned}s_\xi &= \int_{-1}^1 \sqrt{\left(\frac{\partial x}{\partial \xi}\right)_{\eta=0}^2 + \left(\frac{\partial y}{\partial \xi}\right)_{\eta=0}^2 + \left(\frac{\partial z}{\partial \xi}\right)_{\eta=0}^2} d\xi = 2 |\vec{a}_\xi(0,0)| \\ s_\eta &= \int_{-1}^1 \sqrt{\left(\frac{\partial x}{\partial \eta}\right)_{\xi=0}^2 + \left(\frac{\partial y}{\partial \eta}\right)_{\xi=0}^2 + \left(\frac{\partial z}{\partial \eta}\right)_{\xi=0}^2} d\eta = 2 |\vec{a}_\eta(0,0)|\end{aligned}. \quad (3.55)$$

Let $s_1^{(-1)}$ denote the arc length on the surface between the collocation points $(i-1, j)$ and (i, j) , and $s_1^{(1)}$ denote the arc length on the surface between the collocation points (i, j) and $(i+1, j)$. $s_2^{(-1)}$ and $s_2^{(1)}$ will denote the arc lengths between the collocation points $(i, j-1)$ and (i, j) , and (i, j) and $(i, j+1)$, respectively. Then, according to Equation (3.55) the arc lengths for the panel (i, j) become

$$\begin{aligned}s_1^{(-1)} &= |\vec{a}_\xi(0,0)|_{(i-1,j)} + |\vec{a}_\xi(0,0)|_{(i,j)} \\ s_1^{(1)} &= |\vec{a}_\xi(0,0)|_{(i,j)} + |\vec{a}_\xi(0,0)|_{(i+1,j)} \\ s_2^{(-1)} &= |\vec{a}_\eta(0,0)|_{(i,j-1)} + |\vec{a}_\eta(0,0)|_{(i,j)} \\ s_2^{(1)} &= |\vec{a}_\eta(0,0)|_{(i,j)} + |\vec{a}_\eta(0,0)|_{(i,j+1)}\end{aligned}. \quad (3.56)$$

In the partial wake relaxation model the velocity discontinuity is also calculated by numerical surface differentiation of the potential-jump at the wake surface, Equation (3.22). The zero-pressure-jump condition states that the tangential component of the mean velocity on the vortex sheet be parallel to the surface vorticity vector $\vec{\gamma}$. Nevertheless, the use of a central difference scheme in order to solve Equation (3.19) originates a stability problem, Hoeijmakers [33]. In this sense, a biased difference scheme is introduced.

The derivatives $\partial \Delta \phi / \partial s_1$ and $\partial \Delta \phi / \partial s_2$ are calculated using a backward difference scheme. The procedure for the calculation of the derivatives is similar to the previous case of the tangential perturbation velocity. However, in the present case the variation of the potential-jump on the panel (i, j) along the directions s_1 and s_2 is approximated by a parabola through the values of the potential-jump on the collocation points $(i-2, j)$, $(i-1, j)$, (i, j) and $(i, j-2)$, $(i, j-1)$, (i, j) , respectively.

3.5 Calculation of Forces

In the calculation of the inviscid thrust and torque of the propeller we separate the contributions from the propeller blades and the hub. In terms of the non-dimensional coefficients, Equation (2.40), we have

$$K_T = K_T^{(blades)} + K_T^{(hub)}, \quad K_Q = K_Q^{(blades)} + K_Q^{(hub)}, \quad (3.57)$$

where

$$K_T^{(blades)} = \frac{1}{8} \iint_{S_{blades}} C_{pn} n_x dS^*, \quad K_T^{(hub)} = \frac{1}{8} \iint_{S_{hub}} C_{pn} n_x dS^*, \quad (3.58)$$

and

$$K_Q^{(blades)} = \frac{1}{16} \iint_{S_{blades}} C_{pn} (n_y z^* - n_z y^*) dS^*, \quad K_Q^{(hub)} = \frac{1}{16} \iint_{S_{hub}} C_{pn} (n_y z^* - n_z y^*) dS^*, \quad (3.59)$$

with C_{pn} given by Equation (2.34), $y^* = y/R$ and $z^* = z/R$ are non-dimensional Cartesian coordinates and $dS^* = dS/R^2$ is the non-dimensional area of the element. We must have $K_Q^{(hub)} = 0$, because the hub is assumed axisymmetric and can not exert any tangential force on the flow. The numerical evaluation of the integrals (3.58) and (3.59) assuming constant pressure on the panels (i.e., a mid-point rule) gives

$$K_T^{(blades)} = \frac{K}{8} \sum_{j=1}^{N_{blade}} (C_{pn} n_x)_j \Delta S_j^*, \quad K_T^{(hub)} = \frac{K}{8} \sum_{j=1}^{N_{hub}} (C_{pn} n_x)_j \Delta S_j^*, \quad (3.60)$$

and

$$K_Q^{(blades)} = \frac{K}{16} \sum_{j=1}^{N_{blade}} (C_{pn})_j (n_y z^* - n_z y^*)_j \Delta S_j^*, \quad K_Q^{(hub)} = \frac{K}{16} \sum_{j=1}^{N_{hub}} (C_{pn})_j (n_y z^* - n_z y^*)_j \Delta S_j^*, \quad (3.61)$$

where N_{blade} is the total number of panels in one propeller blade, N_{hub} is the total number of panels in one hub sector, and ΔS_j^* is the non-dimensional area of the panel j .

For the ducted propeller case, the inviscid duct coefficient is given by

$$K_{T_D} = \frac{1}{8} \iint_{S_{duct}} C_{pn} n_x dS^*. \quad (3.62)$$

$K_{Q_D} = 0$ since the duct is also assumed to be axisymmetric. The numerical evaluation of the integral (3.62) gives

3.5. Calculation of Forces

$$K_{T_D} = \frac{K}{8} \sum_{j=1}^{N_{duct}} (C_{pn} n_x)_j \Delta S_j^*, \quad (3.63)$$

where N_{duct} is the total number of panels in one duct sector.

For the wing case, the non-dimensional coefficients $C_{x,y,z}$, Equation (2.44), for each force component become

$$C_{x,y,z} = \frac{F_{x,y,z}}{1/2\rho U_\infty^2 A} = -\frac{S^2}{A} \iint_{S_{wing}} C_p n_{x,y,z} dS^* = -\frac{\Lambda}{4} \iint_{S_{wing}} C_p n_{x,y,z} dS^* \quad (3.64)$$

where $\Lambda = 4S^2/A$ is the wing aspect-ratio and $dS^* = ds/S^2$. The numerical evaluation of the integral (3.64) gives

$$C_{x,y,z} = -\frac{\Lambda}{4} \sum_{j=1}^{N_{wing}} (C_p n_{x,y,z})_j \Delta S_j^*, \quad (3.65)$$

where N_{wing} is the total number of wing panels.

Chapter 4

Grid Generation

4.1 Introduction

For the numerical solution of the integral equation (2.21) we discretise the body surfaces \mathcal{S}_B and the wake surfaces \mathcal{S}_W in quadrilateral panels. The quadrilateral panels are defined by four corner points on the surface, which are not necessarily on the same plane. The definition of the panel corner points on the surface can be obtained from the points of a structured grid. In this way, the specification of the panel corner points requires the generation of surface grids.

The generation of a structured grid on a surface with arbitrary geometry is not a trivial problem. In general, two parametric coordinates are used for the definition of the surface geometry. In this way, the parametric coordinates may be used as the dependent variables of the grid generation procedure. Consequently, the two coordinate transformations are:

1. The surface definition which includes the relation between the physical coordinates (x, y, z) and two parametric coordinates, (s_1, s_2) .
2. A two-dimensional grid generation procedure that relates the parametric coordinates of the surface (s_1, s_2) with the independent variables of the computational domain, (ξ, η) .

4.2 Surface Definition

The geometrical definition of a surface is made from the relations between the physical Cartesian coordinates (x, y, z) and two parametric coordinates (s_1, s_2) :

$$\begin{aligned} x &= x(s_1, s_2) \\ y &= y(s_1, s_2) \\ z &= z(s_1, s_2) \end{aligned} . \quad (4.1)$$

Frequently, the parametric domain is normalised by $(s_1)_{\min} = (s_2)_{\min} = 0$ and $(s_1)_{\max} = (s_2)_{\max} = 1$. Nevertheless, the (s_1, s_2) limits are arbitrary. Two types of surface definitions are considered:

4.2.1. Analytical Surface Definition

1. Equations (4.1) are defined by analytical expressions.
2. Interpolation by bi-cubic splines from a set of discrete grid nodes on the surface.

4.2.1 Analytical Surface Definition

To illustrate the analytical surface definition, one of the cases of application is selected: a wing with elliptical planform of span $2S$ and maximum chord C_0 . The wing planform is given by

$$\frac{x^2}{(C_0/2)^2} + \frac{y^2}{S^2} = 1. \quad (4.2)$$

The chord c , for any position y , is

$$\frac{c(y)}{S} = \frac{C_0}{S} \sqrt{1 - \left(\frac{y}{S}\right)^2}. \quad (4.3)$$

Introducing the parametric coordinates (u, v) ,

$$\begin{aligned} u &= \frac{2x}{c(y)}, \\ v &= \frac{y}{S} \end{aligned}, \quad (4.4)$$

where $-1 \leq u \leq 1$ and $0 \leq v \leq 1$, and the non-dimensional thickness $t(u)$ and camber $f(u)$ functions, we obtain

$$\frac{z}{S} = \begin{cases} [f(u) + \frac{1}{2}t(u)] c(v) & \text{upper side} \\ [f(u) - \frac{1}{2}t(u)] c(v) & \text{lower side} \end{cases}, \quad (4.5)$$

Therefore, we can write the relations between the Cartesian coordinates (x, y, z) and the parametric coordinates (u, v)

$$\begin{aligned} \frac{x}{S} &= \frac{c(v)}{2S} u \\ \frac{y}{S} &= v \\ \frac{z}{S} &= \begin{cases} [f(u) + \frac{1}{2}t(u)] c(v) & \text{upper side} \\ [f(u) - \frac{1}{2}t(u)] c(v) & \text{lower side} \end{cases} \end{aligned}. \quad (4.6)$$

The expression for the chord in parametric coordinates is

$$\frac{c(v)}{S} = \frac{C_0}{S} \sqrt{1 - v^2}. \quad (4.7)$$

The definition of the parametric coordinates (u, v) , Equation (4.6), poses a problem for the generation of a grid, since there are two z values with the same parametric coordinates (u, v) . Therefore, we introduce a linear transformation between (u, v) and the new parametric coordinates (s_1, s_2) , which includes an unambiguous definition of the upper and lower sides of the wing surface,

$$\begin{aligned} u &= \begin{cases} -4s_1 + 1 & 0 \leq s_1 \leq 0.5 \\ 4s_1 - 3 & 0.5 < s_1 \leq 1 \end{cases} . \\ v &= s_2 \end{aligned} \quad (4.8)$$

Substituting (u, v) by the parametric coordinates (s_1, s_2) in Equation (4.6), we obtain the analytical definition of the surface with a normalised parametric domain, since $0 \leq s_1 \leq 1$ and $0 \leq s_2 \leq 1$.

4.2.2 Bi-Cubic Splines Surface Definition

In several practical cases there is no analytical description of the surface, but only a set of cross-sections defined by a given number of points. In this way, the surface is represented by a set of $N_{TX} \times N_{TY}$ grid nodes defined along two families of grid lines, designated by i and j , where the Cartesian coordinates (x, y, z) are known. Therefore, the surface definition requires an interpolation technique.

Bi-cubic spline interpolation can be used to interpolate the Cartesian coordinates (x, y, z) for any position on the surface. Usually, the interpolation can be easily performed using the indices (i, j) as independent variables, Pina [37]. However, the distribution of points (i, j) available by the discrete geometrical definition may not be regular. This may introduce oscillations in the bi-cubic spline description of the surface, Eça [38]. Therefore, we introduce independent variables (s_1, s_2) that represent the distance between the nodes along two boundaries of the domain:

$$\begin{aligned} s_1(i) &= \frac{\sqrt{(x_{i,1} - x_{i-1,1})^2 + (y_{i,1} - y_{i-1,1})^2 + (z_{i,1} - z_{i-1,1})^2}}{N_{TX}} + s_1(i-1) \\ &\quad \sum_{i=2}^{N_{TX}} \sqrt{(x_{i,1} - x_{i-1,1})^2 + (y_{i,1} - y_{i-1,1})^2 + (z_{i,1} - z_{i-1,1})^2} , \quad (4.9) \\ s_2(j) &= \frac{\sqrt{(x_{1,j} - x_{1,j-1})^2 + (y_{1,j} - y_{1,j-1})^2 + (z_{1,j} - z_{1,j-1})^2}}{N_{TY}} + s_2(j-1) \\ &\quad \sum_{j=2}^{N_{TY}} \sqrt{(x_{1,j} - x_{1,j-1})^2 + (y_{1,j} - y_{1,j-1})^2 + (z_{1,j} - z_{1,j-1})^2} \end{aligned}$$

where $s_1(1) = 0$ and $s_2(1) = 0$. In this case, the independent variables s_1 and s_2 are calculated along $j = 1$ and $i = 1$, respectively. Nevertheless, the selection of the lines for the definition of the independent variables is arbitrary.

A variable ε , which may be x , y or z is given by:

4.3. Geometry Discretisation

$$\begin{aligned}
\varepsilon(s_1, s_2) = & f_1(\lambda_1) (f_1(\lambda_2)\varepsilon_{i_0,j_0} + f_2(\lambda_2)\varepsilon_{i_0,j_1}) \\
& + f_2(\lambda_1) (f_1(\lambda_2)\varepsilon_{i_1,j_0} + f_2(\lambda_2)\varepsilon_{i_1,j_1}) \\
& + f_1(\lambda_1) \left\{ f_3(\lambda_2) \frac{\partial \varepsilon}{\partial s_2} \Big|_{i_0,j_0} + f_4(\lambda_2) \frac{\partial \varepsilon}{\partial s_2} \Big|_{i_0,j_1} \right\} S_y \\
& + f_2(\lambda_1) \left\{ f_3(\lambda_2) \frac{\partial \varepsilon}{\partial s_2} \Big|_{i_1,j_0} + f_4(\lambda_2) \frac{\partial \varepsilon}{\partial s_2} \Big|_{i_1,j_1} \right\} S_y , \\
& + f_3(\lambda_1) \left\{ f_1(\lambda_2) \frac{\partial \varepsilon}{\partial s_1} \Big|_{i_0,j_0} + f_2(\lambda_2) \frac{\partial \varepsilon}{\partial s_1} \Big|_{i_0,j_1} \right\} S_x \\
& + f_4(\lambda_1) \left\{ f_1(\lambda_2) \frac{\partial \varepsilon}{\partial s_1} \Big|_{i_1,j_0} + f_2(\lambda_2) \frac{\partial \varepsilon}{\partial s_1} \Big|_{i_1,j_1} \right\} S_x
\end{aligned} \tag{4.10}$$

where

$$\begin{aligned}
s_1(i_0) &\leq s_1 \leq s_1(i_1) \\
s_2(j_0) &\leq s_2 \leq s_2(j_1) \\
S_x &= s_1(i_1) - s_1(i_0) \\
S_y &= s_2(j_1) - s_2(j_0) , \\
\lambda_1 &= \frac{s_1 - s_1(i_0)}{S_x} \\
\lambda_2 &= \frac{s_2 - s_2(j_0)}{S_y}
\end{aligned} \tag{4.11}$$

and f_1, f_2, f_3, f_4 are the cubic Hermite polynomials:

$$\begin{aligned}
f_1(\lambda) &= 2\lambda^3 - 3\lambda^2 + 1 \\
f_2(\lambda) &= -2\lambda^3 + 3\lambda^2 \\
f_3(\lambda) &= \lambda^3 - 2\lambda^2 + \lambda \\
f_4(\lambda) &= \lambda^3 - \lambda^2
\end{aligned} . \tag{4.12}$$

The derivatives of x, y and z with respect to s_1 and s_2 at the $N_{TX} \times N_{TY}$ nodes are computed in the standard way of a spline representation to ensure that the second derivatives along the two families of grid lines $i = \text{const.}$ and $j = \text{const.}$ are continuous. The first and second derivatives with respect to s_1 and s_2 are easily derived from Equation (4.10), because they involve only the cubic Hermite polynomials, its derivatives with respect to λ and the scaling factors S_x and S_y . At the boundaries, the second derivatives of x, y and z with respect to s_1 and s_2 are set equal to zero. These conditions correspond to a $N_{TX} + N_{TY}$ tri-diagonal linear system of equations which can be easily solved by the Thomas algorithm, Pina [37].

4.3 Geometry Discretisation

For the generation of the wing and propeller blade grids, a conventional panel arrangement is first considered for the discretisation of the surface. The conventional grids are characterised by lines of constant parametric coordinates $s_1 = \text{const.}$ and $s_2 = \text{const.}$. Different parametric coordinates are defined for each geometry. The duct surface is discretised according to a helicoidal pattern. The wake grid is discretised in the trailing edge direction

with the same number of panel strips of the corresponding lifting body. For the generation of the hub grid, special care must be taken into account in the region between the blades, particularly near the leading and trailing edges, in order to avoid irregular or unacceptable panel distributions. To circumvent this difficulty an elliptical grid generator is used for the generation of the surface grid.

4.3.1 Wing Panelling

Let us first consider the discretisation of the wing surface. The grid is defined by lines of constant spanwise coordinate $s_2 = \text{const.}$ and lines of constant chordwise coordinate $s_1 = \text{const.}$ in the parametric domain. Since we are considering the conventional panel arrangement, we can use the coordinates (u, v) instead of the parametric coordinates (s_1, s_2) , Equation (4.8).

To generate the grid only half of the wing is considered. Different stretching functions may be used to distribute the points on the $u = \text{const.}$ and $v = \text{const.}$ lines. In the present work, we implemented a cosine distribution. We introduce the change of variables

$$\begin{aligned} u &= \cos \varphi, \quad 0 \leq \varphi \leq \pi \\ v &= \cos \psi, \quad 0 \leq \psi \leq \pi/2, \end{aligned} \quad (4.13)$$

and use an equidistant distribution in φ and ψ

$$\begin{aligned} \varphi_i &= i \frac{\pi}{N_C}, \quad i = 0, 1, \dots, N_C \\ \psi_j &= j \frac{\pi}{2N_R}, \quad j = 0, 1, \dots, N_R, \end{aligned} \quad (4.14)$$

where N_C represents the number of panels along the chordwise direction on each side of the wing and N_R the number of panels along the spanwise direction. The total number of panels along the chordwise direction is $N_{CP} = 2N_C$.

4.3.2 Blade Panelling

A grid can be generated on the propeller blade based on the conventional description of the blade geometry by sections on cylinders of constant radius. In this way, the blade is discretised in the spanwise radial direction by a number of strips, extending chordwise from the blade leading edge to the trailing edge.

We use radial coordinates made non-dimensional by the propeller radius R . Let r_h be the non-dimensional hub radius. The interval $r_h \leq r \leq r_t$ is divided into N_R strips. The radii of the panel corner points are given by a modified cosine distribution

$$r_j = \frac{1}{\cos \alpha_h + \cos \alpha_t} [(r_h \cos \alpha_t + r_t \cos \alpha_h) - (r_t - r_h) \cos \varphi_j], \quad (4.15)$$

4.3.3. Duct Panelling

with

$$\varphi_j = \alpha_h + j \frac{(\pi - \alpha_t - \alpha_h)}{N_R}, \quad j = 0, 1, \dots, N_R, \quad (4.16)$$

where r_t is the maximum radius or tip radius, and α_h , α_t are two parameters controlling the radial size of the panels close to the hub and tip, respectively. The maximum radius is chosen as the propeller radius $r_t = 1$, unless specified otherwise.

The distribution of coordinates s_{ij}/c_j of the panel corner points along the chord of the strip j is given by the modified cosine distribution

$$\frac{s_{ij}}{c_j} = \frac{\cos \alpha_{le} - \cos \varphi_i}{\cos \alpha_{le} + \cos \alpha_{te}}, \quad i = 0, 1, \dots, N_C, \quad j = 0, 1, \dots, N_R, \quad (4.17)$$

where

$$\varphi_i = \alpha_{le} + i \frac{(\pi - \alpha_{te} - \alpha_{le})}{N_C}, \quad i = 0, 1, \dots, N_C, \quad (4.18)$$

$c_j = c(r_j)$ and N_C is the number of panels along the chord. The parameters α_{le} and α_{te} control the panel size in the chordwise direction close to the leading edge and trailing edge, respectively.

Often, in the definition of the propeller geometry the functions are given at discrete points and interpolation is required. Also, the blade section geometry is often specified by camber and thickness distributions.

4.3.3 Duct Panelling

Each angular sector with amplitude $2\pi/K$ on the surface of revolution of the duct is discretised in $2N_{Dx}$ panels in the axial direction and $2N_{Dt}$ panels in the circumferential direction. The complete duct is discretised with a total number of $2N_{Dx} \times 2KN_{Dt}$ panels.

Axisymmetric Duct

Let us consider the discretisation of the surface of an axisymmetric duct. The coordinates of the panel corner points follow a helicoidal pattern with pitch ratio a_D (per unit radian):

$$\begin{aligned} x_{ij} &= \frac{1}{2} (x_{D0} + x_{D3}) - \frac{1}{2} (x_{D3} - x_{D0}) \cos \left(i \frac{\pi}{N_{Dx}} \right) \\ \theta_{ij} &= \frac{x_{ij} - x_{D0}}{a_D} \pm j \frac{\pi}{KN_{Dt}} \\ r_{ij}^{(i,o)} &= r_D^{(i,o)}(x_{ij}), \quad i = 0, 1, \dots, N_{Dx}, \quad j = 0, 1, \dots, N_{Dt} \end{aligned}, \quad (4.19)$$

where $r_D^{(i,o)}$ represents the radial coordinate of the inner side i and outer side o of the duct. x_{D0} and x_{D3} are the axial coordinates of the duct extreme point upstream and of the duct extreme point downstream, respectively.

Ducted Propeller With Gap

Let us consider now the case of a propeller inside the duct. In this case, we divide the duct surface into three distinct regions: the region between the blades, the region upstream of the blades and the region downstream of the blades, as shown in Figure 4.1.

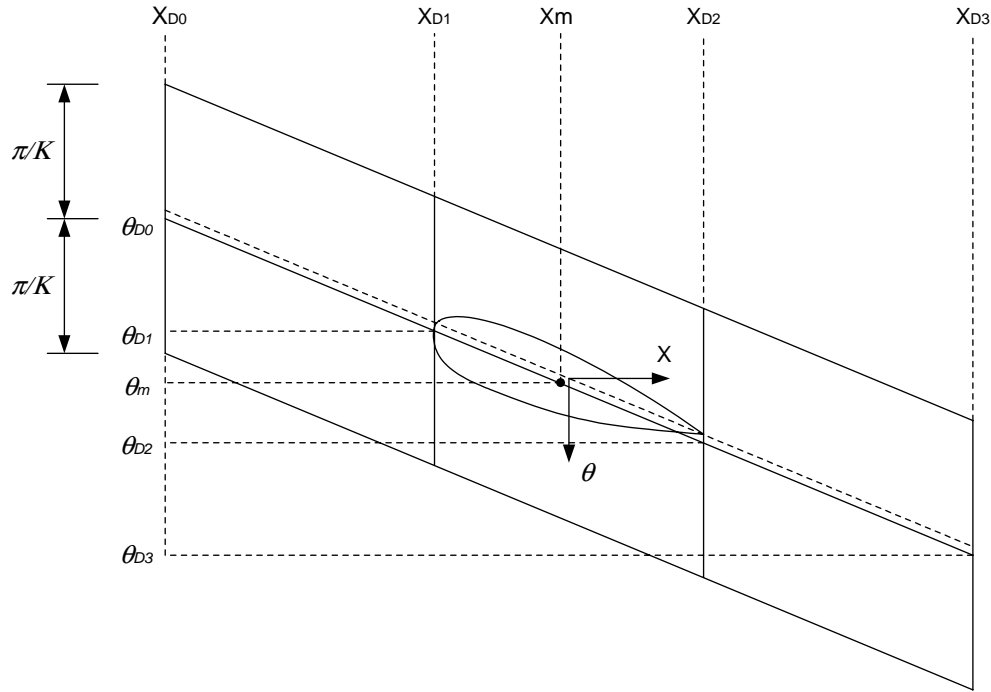


Figure 4.1: Definitions of regions for the panel discretisation of a duct sector surface.

The region on the duct surface between the blade leading and trailing edges, $x_{D1} \leq x \leq x_{D2}$, is discretised with N_C panels in the axial direction for each side of the duct, and $2N_{Dt}$ panels in the circumferential direction, according to a helicoidal pattern. The coordinates of the panel corner points in this region follow a helicoidal pattern centred at the point (x_m, θ_m) and with pitch ratio a_D equal to the pitch of the blade tip section. The axial coordinate x of the panel corner points are coincident with the axial coordinate x of the meanline corresponding to the blade tip section. In this way, we have

$$\begin{aligned} x_{ij} &= \frac{1}{2} \left(x_B^{(-)}(i) + x_B^{(+)}(i) \right) \\ \theta_{ij} &= \theta_m + \frac{x_{ij} - x_m}{a_D} \pm j \frac{\pi}{KN_{Dt}} \\ r_{ij}^{(i,o)} &= r_D^{(i,o)}(x_{ij}), \quad i = 0, 1, \dots, N_C, \quad j = 0, 1, \dots, N_{Dt} \end{aligned} \quad (4.20)$$

with

$$x_m = \frac{1}{2} \left(x_B^{(-)}\left(\frac{N_C}{2}\right) + x_B^{(+)}\left(\frac{N_C}{2}\right) \right), \quad \theta_m = \frac{1}{2} \left(\theta_B^{(-)}\left(\frac{N_C}{2}\right) + \theta_B^{(+)}\left(\frac{N_C}{2}\right) \right), \quad (4.21)$$

4.3.3. Duct Panelling

where the $-$ and $+$ superscripts correspond to the face (pressure side) and back (suction side) of the blade, respectively.

The region upstream of the blades, $x_{D0} \leq x < x_{D1}$, is discretised with N_{D1} panels in the axial direction using a two-sided Vinokur stretching function f_V , Vinokur [39], for each side of the duct. In the circumferential direction, the region upstream of the blades is discretised with $2N_{Dt}$ panels. The coordinates of the panel corner points in this region follow a helicoidal pattern with pitch ratio a_D :

$$\begin{aligned} x_{ij} &= x_{D0} + (x_{D1} - x_{D0}) f_V(i) \\ \theta_{ij} &= \theta_{D0} + \frac{x_{ij} - x_{D0}}{a_D} \pm j \frac{\pi}{KN_{Dt}} \\ r_{ij}^{(i,o)} &= r_D^{(i,o)}(x_{ij}), \quad i = 0, 1, \dots, N_{D1}, \quad j = 0, 1, \dots, N_{Dt} \end{aligned}, \quad (4.22)$$

where x_{D0} and x_{D1} are the axial coordinates of the duct extreme point upstream and of the blade leading edge, respectively. θ_{D0} and θ_{D1} are the circumferential coordinates of the points on the pitch line of the tip blade section at $x = x_{D0}$ and $x = x_{D1}$, respectively.

Finally, the region downstream of the blade trailing edge, $x_{D2} < x \leq x_{D3}$, is discretised with N_{D3} panels in the axial direction using a two-sided Vinokur stretching function f_V , Vinokur [39], for each side of the duct. In the circumferential direction, the region downstream of the blades is discretised with $2N_{Dt}$ panels according to a helicoidal pattern with pitch ratio a_D . Hence, the coordinates of the panel corner points in this region are given by

$$\begin{aligned} x_{ij} &= x_{D2} + (x_{D3} - x_{D2}) f_V(i) \\ \theta_{ij} &= \theta_{D2} + \frac{x_{ij} - x_{D2}}{a_D} \pm j \frac{\pi}{KN_{Dt}} \\ r_{ij}^{(i,o)} &= r_D^{(i,o)}(x_{ij}), \quad i = 0, 1, \dots, N_{D3}, \quad j = 0, 1, \dots, N_{Dt} \end{aligned}, \quad (4.23)$$

where x_{D2} and x_{D3} are the axial coordinates of the blade trailing edge and of the duct extreme point downstream, respectively. θ_{D2} and θ_{D3} are the circumferential coordinates of the points on the pitch line of the tip blade section at $x = x_{D2}$ and $x = x_{D3}$, respectively.

The slopes of the Vinokur stretching functions are chosen in order to have the same grid stretching along the axial direction at the leading edge and trailing edge of the blade. $2\pi a_D$ is the geometric pitch of the propeller blade tip section. In the axial direction the total number of panels on the duct for each side is $N_{Dx} = N_{D1} + N_C + N_{D3}$.

Ducted Propeller With Zero Gap Width

For the duct propeller with zero gap width, the coordinates (x, θ) at the region between blades are obtained using linear transfinite interpolation from its values at the boundaries. In this case, the boundaries in the region between the blade leading and trailing edges, $x_{D1} \leq x \leq x_{D2}$, coincide with the corner points of the blade at the tip. Thus, the

coordinates of the panel corner points at the boundary coincident with the pressure side of the blade are given by

$$\begin{aligned} x &= x_B^{(-)} \\ \theta &= \theta_B^{(-)} \quad , \\ r &= r_D(x_B^{(-)}) \end{aligned} \quad (4.24)$$

and the coordinates of the panel corner points at the boundary coincident with the suction side of the blade are given by

$$\begin{aligned} x &= x_B^{(+)} \\ \theta &= \theta_B^{(+)} \quad . \\ r &= r_D(x_B^{(+)}) \end{aligned} \quad (4.25)$$

4.3.4 Wake Panelling

In order to allow for the existence of circulation, wake surfaces are shed from the trailing edge of the lifting bodies: wing, propeller blade and duct.

Wing

The wing wake is discretised in the spanwise direction into N_R panel strips, which extend downstream from the trailing edge of the corresponding strips on the wing. Each strip is discretised with N_W panels in the streamwise direction. We allow for a gradual variation of the panel dimensions by adopting a half-cosine distribution in the axial coordinate. The coordinates of the panel corner points on the wing wake are given by

$$\begin{aligned} x_{ij} &= x_{0j} + \left[1 - \cos \left(i \frac{\pi}{2N_W} \right) \right] x_W \\ y_{ij} &= y_{0j} \\ z_{ij} &= 0 \\ i &= 0, 1, \dots, N_W, \quad j = 0, 1, \dots, N_R \end{aligned} \quad . \quad (4.26)$$

In Equation (4.26), (x_{0j}, y_{0j}) are the coordinates of the points on the wing trailing edge and x_W is the wake axial length. In addition, we observe that the wake strips are on the plane $z = 0$.

Propeller Blade

The helicoidal blade wake is discretised in the spanwise direction into N_R panel strips. The blade wake is divided into two regions: the transition wake region and the ultimate wake region. Contraction and variation of the pitch of the helicoidal lines, where the panel corner points are located, are considered in the transition wake region. On the

4.3.4. Wake Panelling

other hand, the radial position and the pitch of the helicoidal lines are kept constant in the ultimate region. The coordinates of the panel corner points on the blade wake are given by

$$\begin{aligned} x_{ij} &= x_{0j} + \left[1 - \cos \left(i \frac{\pi}{2N_W} \right) \right] x_W \\ r_{ij} &= r(\xi) \\ \theta_{ij} &= \theta_{0j} + \frac{1}{a(\xi)} \left[1 - \cos \left(i \frac{\pi}{2N_W} \right) \right] x_W \\ i &= 0, 1, \dots, N_W, \quad j = 0, 1, \dots, N_R \end{aligned} \quad (4.27)$$

The variations of both radial coordinate and pitch of the helicoidal lines in the transition wake region can be approximated by

$$\begin{aligned} r(\xi) &= r_{0j} - (r_u - r_{0j}) \cdot f(\xi) \\ a(\xi) &= a_{0j} - (a_u - a_{0j}) \cdot f(\xi), \end{aligned} \quad (4.28)$$

where $f(\xi)$ is a polynomial function. In the present study, the polynomial expression given by Hoshino [40] is considered:

$$f(\xi) = \sqrt{\xi} + 1.013\xi - 1.920\xi^2 + 1.228\xi^3 - 0.321\xi^4, \quad (4.29)$$

with

$$\xi = \frac{x - x_{0j}}{x_u - x_{0j}}. \quad (4.30)$$

x_{0j}, r_{0j}, a_{0j} represent the axial coordinate, the radial coordinate and the pitch at the trailing edge of the blade, respectively. x_u, r_u, a_u represent the axial coordinate, the radial coordinate and the pitch at the position where the ultimate wake region starts. The radial position and the pitch of the helicoidal lines in the ultimate wake region are $r(\xi) = r_u$ and $a(\xi) = a_u$, respectively.

Duct

The helicoidal duct wake is discretised in the circumferential direction into $2KN_{Dt}$ panel strips. Contraction and variation of the helicoidal lines are not considered. A half-cosine distribution is implemented along the axial direction. The coordinates of the panel corner points on the duct wake are given by

$$\begin{aligned} x_{ij} &= x_{0j} + \left[1 - \cos \left(i \frac{\pi}{2N_W} \right) \right] x_W \\ r_{ij} &= r_{0j} \\ \theta_{ij} &= \theta_{0j} + \frac{1}{a_D} \left[1 - \cos \left(i \frac{\pi}{2N_W} \right) \right] x_W \\ i &= 0, 1, \dots, N_W, \quad j = 0, 1, \dots, 2KN_{Dt} \end{aligned} \quad (4.31)$$

In Equation (4.31), $(x_{0j}, r_{0j}, \theta_{0j})$ are the coordinates of the points on the duct trailing edge and $2\pi a_D$ is the pitch of the helicoidal lines.

4.3.5 Hub Panelling

Each angular sector with amplitude $2\pi/K$ on the surface of the hub is discretised in N_{Hx} panels in the axial direction and $2N_{Ht}$ panels in the circumferential direction. The complete hub is discretised with a total number of $N_{Hx} \times 2KN_{Ht}$ panels. We divide the hub surface into three distinct regions: the region upstream the blades ($x_{H0} \leq x < x_{H1}$), the region between the blades ($x_{H1} \leq x \leq x_{H2}$) and the region downstream the blades ($x_{H2} < x \leq x_{H3}$). The regions upstream and downstream of the blades are discretised with N_{H1} and N_{H2} panels along the axial direction, respectively. The region between the blade leading and trailing edges is discretised with N_C panels along the axial direction.

For the hub grid, an elliptical grid generator is used, as described by Eça [41]. The approach is similar to the one incorporated in the GRAPE code, Sorensen [42]. The method solves a system of elliptic partial differential equations for the curvilinear coordinates with Dirichlet or Neumann-Dirichlet boundary conditions. In the present application to generate the surface grid on the hub, we only use the Dirichlet boundary condition option, which requires the specification of the grid nodes on the four boundaries of the domain.

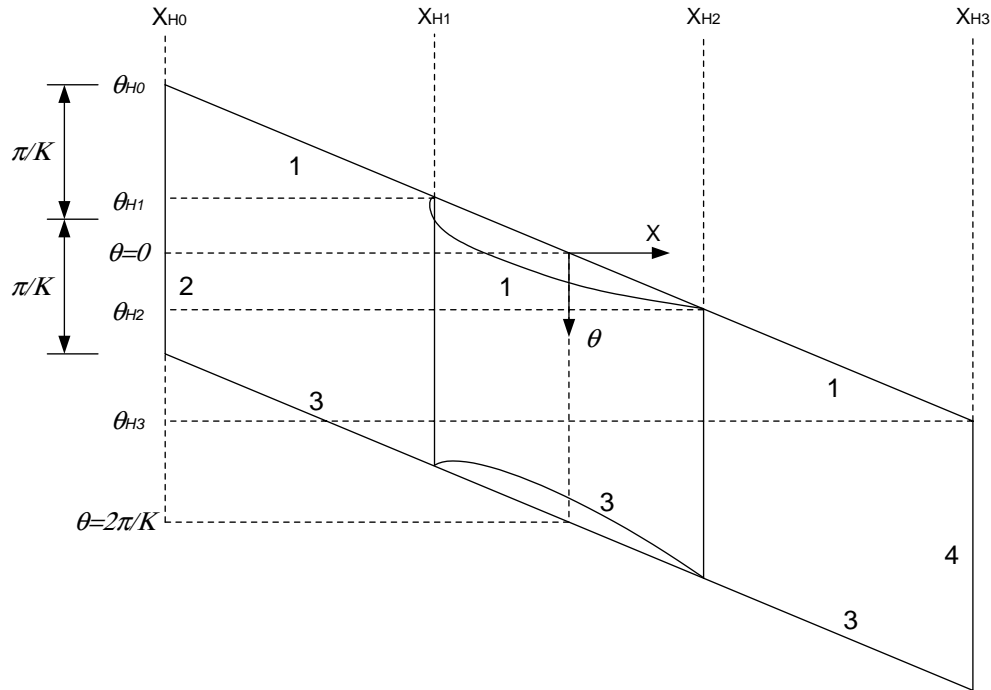


Figure 4.2: Domain for grid generation on the hub.

The four boundaries of the physical domain are shown in Figure 4.2. Boundaries 1 and 3 are lines that coincide, respectively, with the suction and the pressure side of the blades

4.3.5. Hub Panelling

on the region between the leading and trailing edges. Outside that region the boundaries are defined by lines with a linear variation of θ with the axial coordinate x (equivalent to helicoidal lines of constant pitch if the hub is cylindrical with constant radius). For the case where the wake leaves the blade root connected with the hub surface at the downstream region, it is suitable to consider the boundary lines 1 and 3 coincident with the wake boundary. In the generation of the hub grid, the two options are considered. Boundaries 2 and 4 are lines on the circular sections of the hub by $x = \text{const.}$ planes. The four boundaries are defined as follows:

Boundary 1:

$$\begin{aligned} r &= r_H(x) \\ \theta &= \theta_1(x), \end{aligned} \quad (4.32)$$

with

$$\theta_1(x) = \begin{cases} \theta_{H0} + \frac{\theta_{H1} - \theta_{H0}}{x_{H1} - x_{H0}}(x - x_{H0}) & \text{if } x_{H0} \leq x < x_{H1}, \\ \theta_B^{(+)} & \text{if } x_{H1} \leq x \leq x_{H2} \end{cases}, \quad (4.33)$$

where $\theta_B^{(+)}$ represents the angular ordinates of the blade suction side surface intersection with the hub. For the downstream $x_{H2} < x \leq x_{H3}$ part we have

$$\theta_1(x) = \begin{cases} \theta_{H2} + \frac{\theta_{H3} - \theta_{H2}}{x_{H3} - x_{H2}}(x - x_{H2}) & \text{if non-coincident with blade wake} \\ \theta_W & \text{if coincident with blade wake} \end{cases}, \quad (4.34)$$

where θ_W represents the angular ordinates of the wake surface intersection with the hub.

Boundary 2:

$$\begin{aligned} x &= x_{H0} \\ r &= r_H(x_{H0}) \\ \theta_{H0} &\leq \theta \leq \theta_{H0} + \frac{2\pi}{K} \end{aligned}. \quad (4.35)$$

Boundary 3:

$$\begin{aligned} r &= r_H(x) \\ \theta &= \theta_3(x), \end{aligned} \quad (4.36)$$

with

$$\theta_3(x) = \begin{cases} \theta_{H0} + \frac{\theta_{H1} - \theta_{H0}}{x_{H1} - x_{H0}}(x - x_{H0}) + \frac{2\pi}{K} & \text{if } x_{H0} \leq x < x_{H1}, \\ \theta_B^{(-)} & \text{if } x_{H1} \leq x \leq x_{H2} \end{cases}, \quad (4.37)$$

where $\theta_B^{(-)}$ represents the angular ordinates of the blade pressure side surface intersection with the hub. For the downstream $x_{H2} < x \leq x_{H3}$ part we have

$$\theta_3(x) = \begin{cases} \theta_{H2} + \frac{\theta_{H3} - \theta_{H2}}{x_{H3} - x_{H2}}(x - x_{H2}) + \frac{2\pi}{K} & \text{if non-coincident with blade wake} \\ \theta_W + \frac{2\pi}{K} & \text{if coincident with blade wake} \end{cases}, \quad (4.38)$$

where θ_W represents the angular ordinates of the wake surface intersection with the hub.

Boundary 4:

$$\begin{aligned} x &= x_{H3} \\ r &= r_H(x_{H3}) \\ \theta_{H3} &\leq \theta \leq \theta_{H3} + \frac{2\pi}{K} \end{aligned}. \quad (4.39)$$

The boundary point distribution in the upstream $x_{H0} \leq x < x_{H1}$ part of the hub on the boundaries 1 and 3 is given by a cosine distribution in the axial coordinate:

$$x_{i0} = \frac{1}{2}(x_{H0} + x_{H1}) + \frac{1}{2}(x_{H0} - x_{H1}) \cos\left(i \frac{\pi}{N_{H1}}\right), \quad i = 0, 1, \dots, N_{H1}. \quad (4.40)$$

Between the blade leading and trailing edges, $x_{H1} \leq x \leq x_{H2}$, the boundary point distribution coincides with the boundary point distribution on the suction and pressure side of the blade section, respectively.

The boundary point distribution in the downstream $x_{H2} < x \leq x_{H3}$ part of the hub on the boundaries 1 and 3 may be given by a cosine distribution in the axial coordinate:

$$x_{i0} = \frac{1}{2}(x_{H2} + x_{H3}) + \frac{1}{2}(x_{H2} - x_{H3}) \cos\left(i \frac{\pi}{N_{H2}}\right), \quad i = 0, 1, \dots, N_{H2}, \quad (4.41)$$

which is similar to the distribution used in the upstream part of the hub (Equation (4.40)). For the case of a coincident hub with the blade wake, we have

$$\begin{aligned} x_{i0} &= x_{W_{i0}} \\ r_{i0} &= r_H(x_{i0}) \\ \theta_{i0} &= \theta_H(x_{i0}), \quad i = 0, 1, \dots, N_{H2} \end{aligned}, \quad (4.42)$$

where $x_{W_{i0}}$ represents the axial coordinates of the wake grid points at the intersection line with the hub. The number of panels along the axial direction at the downstream region is less or equal than the number of wake panels, i.e. $N_{H2} \leq N_W$.

The boundary point distribution on the boundaries 2 and 4 follows a cosine distribution on the circumferential coordinate:

$$\theta_{0j} = \theta_{H0} + \frac{\pi}{K} \left[1 - \cos \left(j \frac{\pi}{2N_{Ht}} \right) \right], \quad j = 0, 1, \dots, 2N_{Ht}, \quad (4.43)$$

and

$$\theta_{N_{Hx},j} = \theta_{H3} + \frac{\pi}{K} \left[1 - \cos \left(j \frac{\pi}{2N_{Ht}} \right) \right], \quad j = 0, 1, \dots, 2N_{Ht}. \quad (4.44)$$

After solving the grid generation problem for the interior of the domain, the grid node index j in the circumferential direction is rearranged in order to have the first and last grid node lines as the symmetry line between blades.

4.4 Algebraic Quasi-Orthogonal Grids

In this section, a quasi-orthogonal panel arrangement is also considered for the discretisation of the wing and propeller blade surfaces. An algebraic technique is presented for the generation of quasi-orthogonal grids. Usually, the parametric coordinates of the surface definition (s_1, s_2) are used as the dependent variables of the grid generation procedure. However, an arbitrary definition of the computational domain based on the parametric coordinates of the surface definition may be difficult to achieve. In this sense, an intermediate parametric domain (I, J) is introduced in order to have the grid generation process independent of the surface definition. The parametric domain (I, J) is defined to obtain two major properties:

- The boundaries of the computational domain may be placed arbitrarily on the surface.
- A Cartesian grid in the parametric space (I, J) corresponds to a roughly equidistant grid in the physical space (x, y, z) , independent of the surface definition.

With such approach, the grid dependent variables of the two-dimensional grid generation procedure are (I, J) instead of (s_1, s_2) .

For the definition of the parametric domain (I, J) , the boundaries of the region to discretise correspond to the lines $I = 1$, $J = 1$, $I = N_T$ and $J = N_T$, where N_T is the number of nodes along each direction for the definition of the parametric domain (I, J) . The number of nodes N_T is arbitrary.

The coordinate transformation is an element-by-element bi-linear interpolation with (I, J) as the independent variables and (s_1, s_2) as the dependent variables:

$$\begin{cases} s_1 = s_1(I, J) \\ s_2 = s_2(I, J) \end{cases} . \quad (4.45)$$

The definition of s_1 and s_2 at the $N_T \times N_T$ nodes of the squared (I, J) domain requires four steps:

- Define s_1 and s_2 at the four corners of the domain to discretise. This definition is made by input variables.
- Define s_1 and s_2 along the four boundaries of the domain with an equidistant distribution between corner points.
- Generate an initial approximation for s_1 and s_2 in the interior nodes using linear transfinite interpolation,

$$\begin{aligned} s_i(I, J) = & f_1(I)s_i(1, J) + f_2(I)s_i(N_T, J) \\ & + f_1(J)s_i(I, 1) + f_2(J)s_i(I, N_T) \\ & - f_1(I)(f_1(J)s_i(1, 1) + f_2(J)s_i(1, N_T)) \\ & - f_2(I)(f_1(J)s_i(N_T, 1) + f_2(J)s_i(N_T, N_T)) \end{aligned}, \quad (4.46)$$

with

$$f_1(I) = \frac{N_T - I}{N_T - 1}, \quad f_2(I) = \frac{I - 1}{N_T - 1}, \quad f_1(J) = \frac{N_T - J}{N_T - 1}, \quad f_2(J) = \frac{J - 1}{N_T - 1}. \quad (4.47)$$

- Regularise the coordinate transformation to obtain a smooth grid in the physical space. This is accomplished sweeping the two families of grid lines $I = \text{const.}$ and $J = \text{const.}$ to obtain roughly equidistant grid lines in the physical space (x, y, z) . The sweeps applied, for instance, to the grid lines $I = \text{const.}$ include the following steps:

1. Determine one-dimensional cubic splines that represent s_1 and s_2 as a function of J .
2. Calculate the new values of s_1 and s_2 along the lines $I = \text{const.}$ that have an equidistant distribution in the physical space.

From the $N_T \times N_T$ node grid, the values of s_1 and s_2 are calculated from the parametric coordinates (I, J) by

$$s_i(I, J) = (s_i)_{i,j} \psi^1(\xi, \eta) + (s_i)_{i+1,j} \psi^2(\xi, \eta) + (s_i)_{i+1,j+1} \psi^3(\xi, \eta) + (s_i)_{i,j+1} \psi^4(\xi, \eta), \quad (4.48)$$

where

$$\begin{aligned} \psi^1 &= (1 - \xi)(1 - \eta) \\ \psi^2 &= \xi(1 - \eta) \\ \psi^3 &= \xi\eta \\ \psi^4 &= (1 - \xi)\eta \end{aligned}. \quad (4.49)$$

The indices i, j and the coordinates ξ, η are obtained from the parametric coordinates (I, J) by

$$\begin{aligned} i &= \text{INT}(I) \\ j &= \text{INT}(J) \\ \xi &= I - \text{INT}(I) \\ \eta &= J - \text{INT}(J) \end{aligned}, \quad (4.50)$$

4.4. Algebraic Quasi-Orthogonal Grids

where the INT function converts a value to integer. Since the bi-linear interpolation is applied element-by-element, it is important to use a large value for N_T in order to have a good definition of the coordinate transformation.

Finally, the coordinate transformation between the parametric domain (I, J) and the computational domain (ξ, η) corresponds to the generation of a two-dimensional grid. Different grid generation methods based on systems of partial differential equations can be used, see, for instance Eça *et al.* [43]. For the generation of quasi-orthogonal grids, an algebraic technique based on the linear transfinite interpolation is used.

In the present technique, the grid is generated specifying the boundary node distribution on the four boundaries of the domain. The interior nodes of the domain are obtained using Equation (4.46) to the variables I and J . With this technique, a quasi-orthogonal grid is obtained which reproduces in the interior the point distribution specified at the boundaries of the domain.

The method is illustrated for a wing with elliptical planform and symmetrical section NACA0010. The surface definition is given by Equations (4.6) and (4.8), and by the thickness distribution of a NACA four-digit wing section, Abbott and Doenhoff [44]. Figure 4.3 presents the conventional (left) and the quasi-orthogonal (right) panel arrangements. The grids are defined by 65×17 corner points.

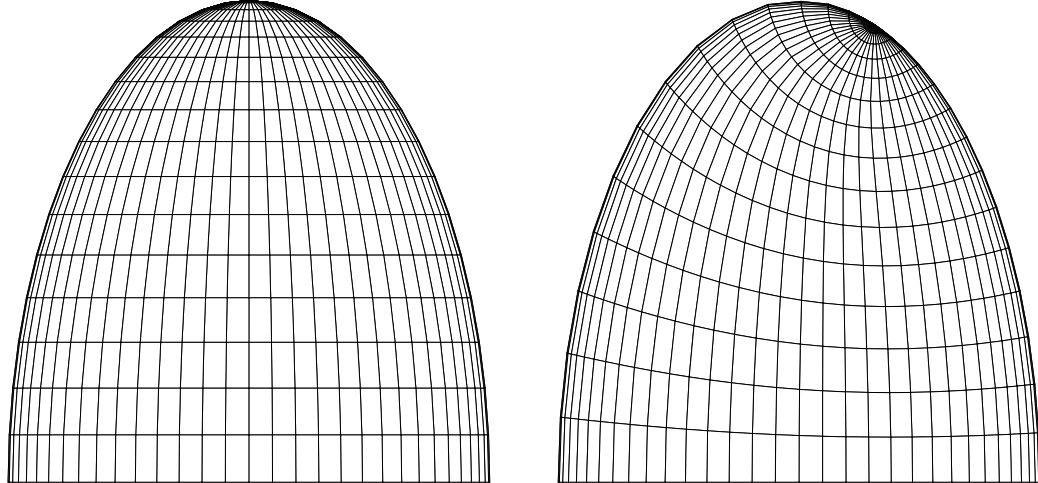


Figure 4.3: Conventional grid with $s_1 = const.$ and $s_2 = const.$ (left) and quasi-orthogonal grid with displacement of the grid singularity (right). 65×17 corner point grids for the elliptical wing.

For the conventional panel arrangement, the variables s_1 and s_2 are calculated according to a cosine distribution along the chordwise and spanwise directions. A grid singularity is present at the wing tip, which results locally in large deviations from orthogonality. In this case, the grid has a maximum deviation from orthogonality of 76.9 degrees and a mean deviation of 17.8 degrees.

The capacities of the present technique are illustrated for the quasi-orthogonal grid with displacement of the grid singularity along the trailing edge to the spanwise section $y/S = 0.95$. Cosine distributions are applied along the wing root, leading edge and trailing edge. The grid is generated using a linear transfinite interpolation for the lower and upper sides of the wing. The grid has a maximum deviation from orthogonality of 19.4 degrees and a mean deviation of 4.8 degrees.

The parametric domains (I, J) and (s_1, s_2) are shown in Figure 4.4. The intermediate coordinate transformation is defined with $N_T = 257$ nodes. The advantage of introducing the intermediate coordinate transformation is evident: the (I, J) domain corresponds to a rectangular grid; meanwhile, using the coordinates (s_1, s_2) of the geometrical description as dependent variables of the grid generation technique would be an almost impossible task.

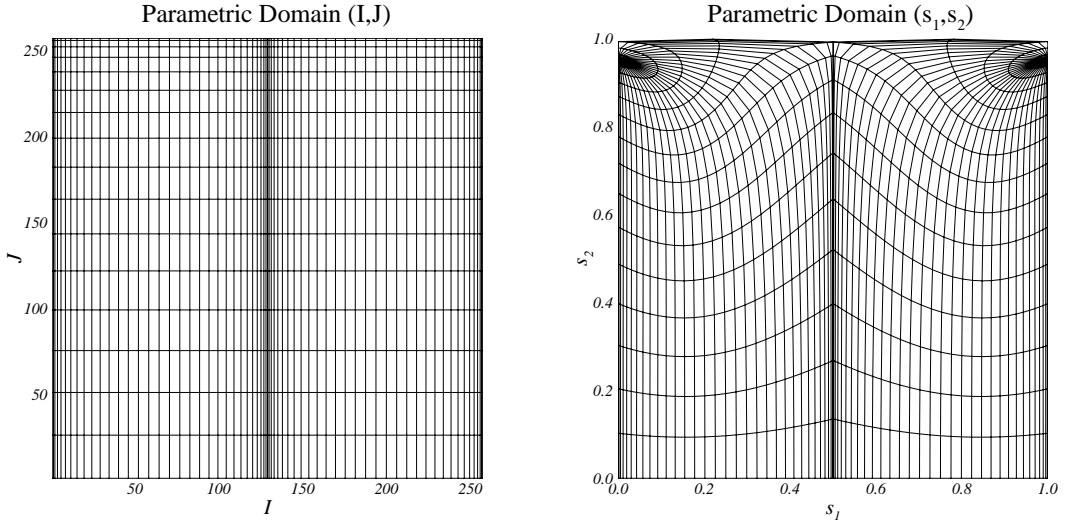


Figure 4.4: Parametric domains (I, J) and (s_1, s_2) for the algebraic quasi-orthogonal grid of the elliptical wing with 65×17 corner points.

Chapter 5

Potential Flow Calculations for Wings and Marine Propellers

5.1 Introduction

Results of the three-dimensional steady potential flow with rigid wake model and conventional panel arrangement about wings and marine propellers are presented in this chapter. Special attention is placed on the solution behaviour near the wing and blade tips. The set of results form the basis for the subsequent developments presented in this thesis.

First, calculations were carried out for wings with elliptical and rectangular planforms at an angle of attack. Grid convergence studies and comparison with experimental data, Falcão de Campos [45], have been performed.

Second, comparisons of numerical calculations with other methods and experimental measurements are presented for two open propellers: DTRC propeller P4119 and DTRC propeller P4842M. For these propellers, extensive numerical and experimental data are available from two workshops organised by the Propulsor Committee of the ITTC [15] and [46]. The convergence of the method with grid refinement is also studied.

Finally, the potential flow around a ducted propeller is considered. Results of the present method for the duct NSMB 19A and the propeller $K_a4\text{-}70$ inside duct 19A are presented. The numerical results of the duct 19A are compared with a surface vorticity method, Falcão de Campos [47], together with wind tunnel measurements, Gibson [48]. In addition, the sensitivity of the results to the position of the stagnation point on the trailing edge is investigated. The convergence of the method, and the influence of the gap and of the duct wake shedding line are studied for the ducted propeller $K_a4\text{-}70$ inside duct 19A. The numerical results are compared with experimental open-water data, Kuiper [49].

A rigid wake model with an iterative pressure Kutta condition is considered. A specified tolerance of $|\Delta C_p|_{TE} \leq 10^{-3}$ on the pressure-jump at the trailing edge control points is applied. The detailed geometries of the tested propellers can be found in the literature and are reproduced in the Appendix C for the sake of completeness.

5.2 Wings

5.2.1 Elliptical Wing

Calculations were performed for an elliptical wing with $\Lambda \simeq 2.55$ and NACA0010 section at 6 degrees incidence. Figure 5.1 shows the wing and wake grids with a detail of the panel arrangement near the tip. In the figure, the wing is discretised with 64 chordwise and 16 spanwise panels. Triangular panels are used at the wing tip. A plane wake along the bisector of the trailing edge is considered. The wake is discretised with 32 streamwise and 16 spanwise panels and has an axial length of 3 wing spans.

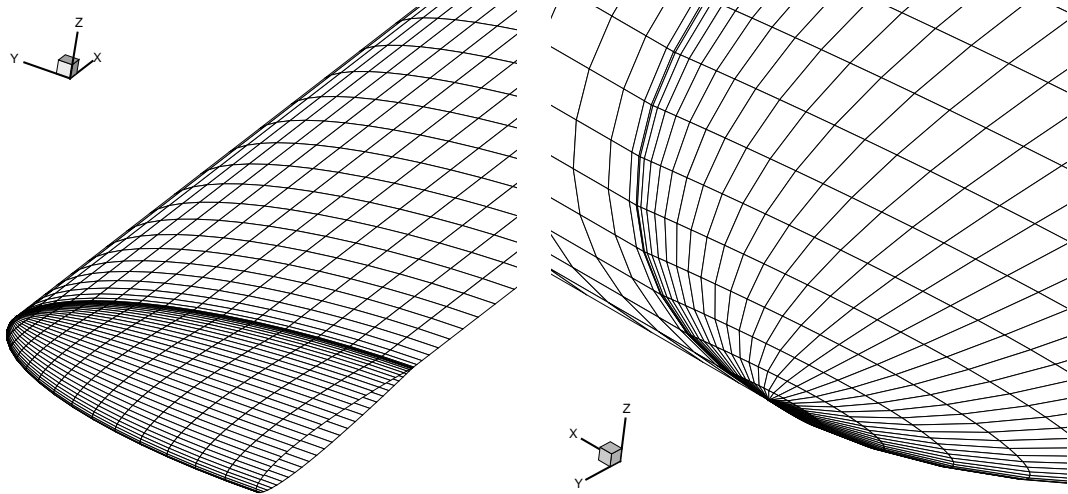


Figure 5.1: Elliptical wing panel arrangement (left). Detail of the wing tip (right). Note that only half of the wing and wake grids are shown.

The convergence of the numerical results with grid refinement is studied. The discretisations ranged from $N_{CP} \times 2N_R = 16 \times 8$ to 128×64 for the complete wing. The iterative pressure Kutta condition, in general, converged in one iteration.

The convergence of the wing circulation is presented in Figure 5.2. The circulation does not converge with grid refinement. An irregular circulation distribution is obtained near the wing tip for the finest discretisations. Table 5.1 presents the convergence of the lift and induced drag coefficients with the grid refinement. The lift and induced drag coefficients decrease with grid refinement, except for the finest grid discretisation. This behaviour is due to the irregular circulation distribution obtained near the tip when increasing the grid refinement level.

Figure 5.3 presents the convergence of the pressure distribution at spanwise sections $y/S = 0.20, 0.40, 0.60, 0.80, 0.95$ and 0.99 . The pressure distribution converges with grid refinement between sections $y/S = 0.20$ and 0.95 . At section $y/S = 0.99$ the pressure distribution does not converge with grid refinement and develops a pressure peak at the trailing edge.

Results of the present method are compared with experimental data, Falcão de Campos [45], for an elliptical wing with $\Lambda = 4$ and NACA0015 section at the angles of attack of 2 and 8 degrees. The calculations presented refer to the discretisation 64×32 . This discretisation provides a reasonably converged solution up to $y/S = 0.95$. Figures 5.4 and 5.5 present the comparison between the numerical results and the experimental data at spanwise sections $y/S = 0.20, 0.40, 0.60, 0.80$ and 0.95 for the angles of attack of 2 and 8 degrees, respectively. An overall good agreement between the numerical results and the experiments is achieved. However, some differences are observed in the region of the suction peak, which are due to viscous effects near the leading edge.

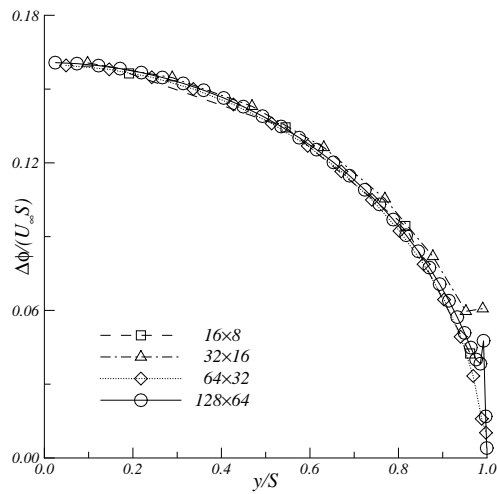


Figure 5.2: Circulation distribution. Convergence with grid refinement. Elliptical wing at 6 degrees incidence.

Grid Size (Wing+Wake)	C_L	C_{D_i}
$16 \times 8 + 8 \times 8$	0.1341	0.0053
$32 \times 16 + 16 \times 16$	0.1296	0.0050
$64 \times 32 + 32 \times 32$	0.1221	0.0046
$128 \times 64 + 64 \times 64$	0.1230	0.0048

Table 5.1: Lift and induced drag coefficients. Convergence with grid refinement. Elliptical wing at 6 degrees incidence.

5.2.1. Elliptical Wing

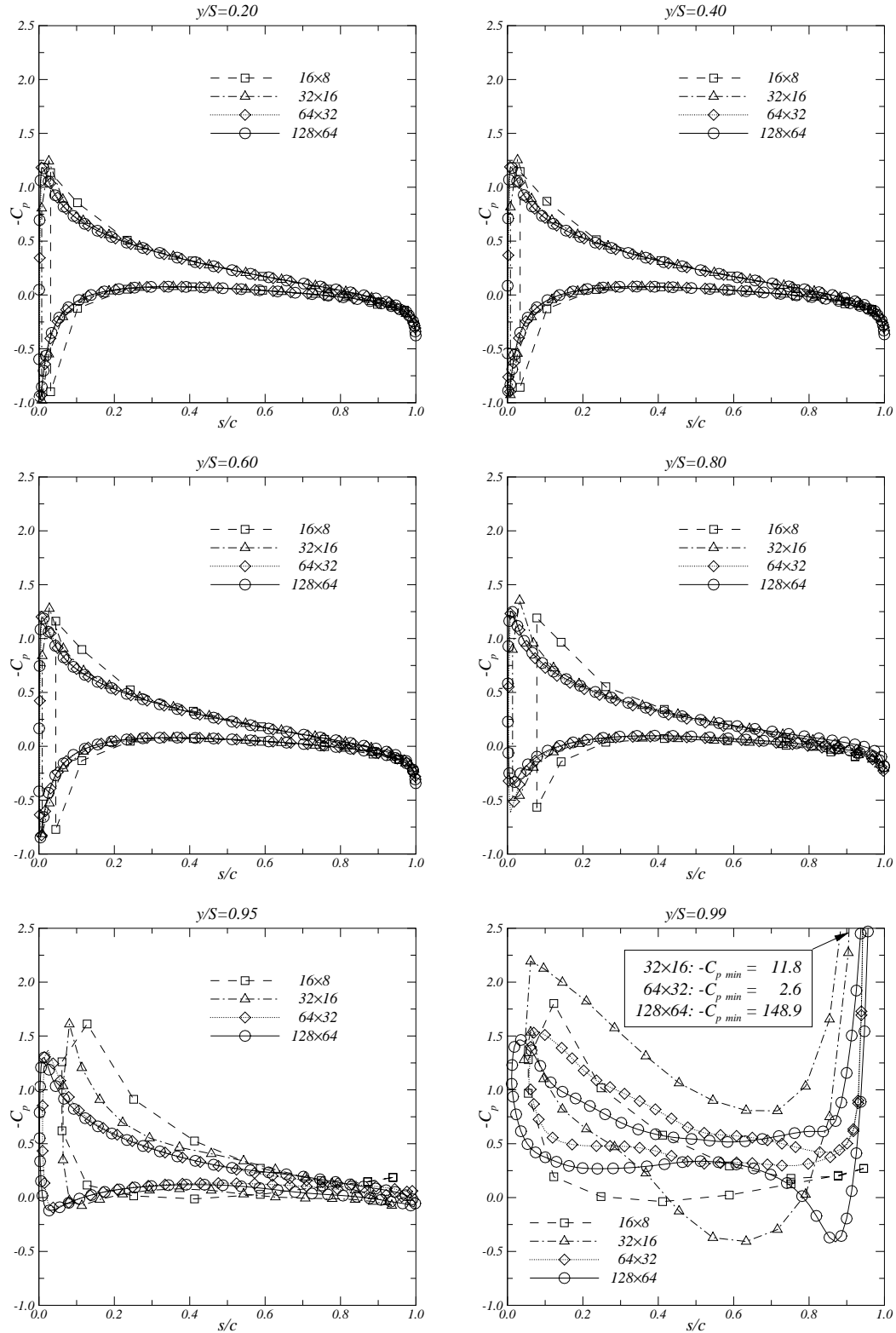


Figure 5.3: Pressure distribution at sections $y/S = 0.20, 0.40, 0.60, 0.80, 0.95$ and 0.99 . Convergence with grid refinement. Elliptical wing at 6 degrees incidence.

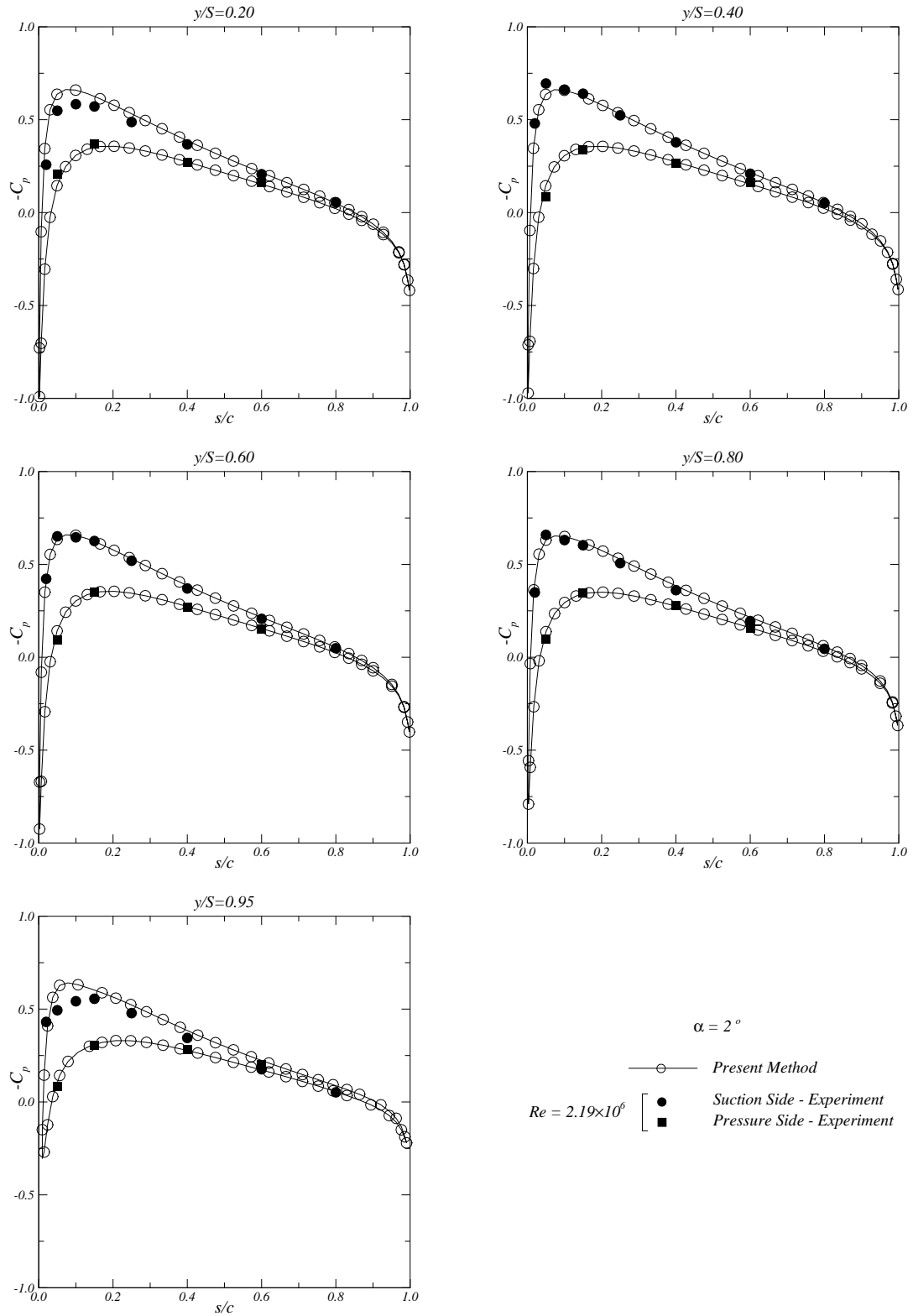


Figure 5.4: Pressure distribution at sections $y/S = 0.20, 0.40, 0.60, 0.80$ and 0.95 . Comparison with experimental data, Falcão de Campos [45]. Elliptical wing at 2 degrees incidence.

5.2.1. Elliptical Wing

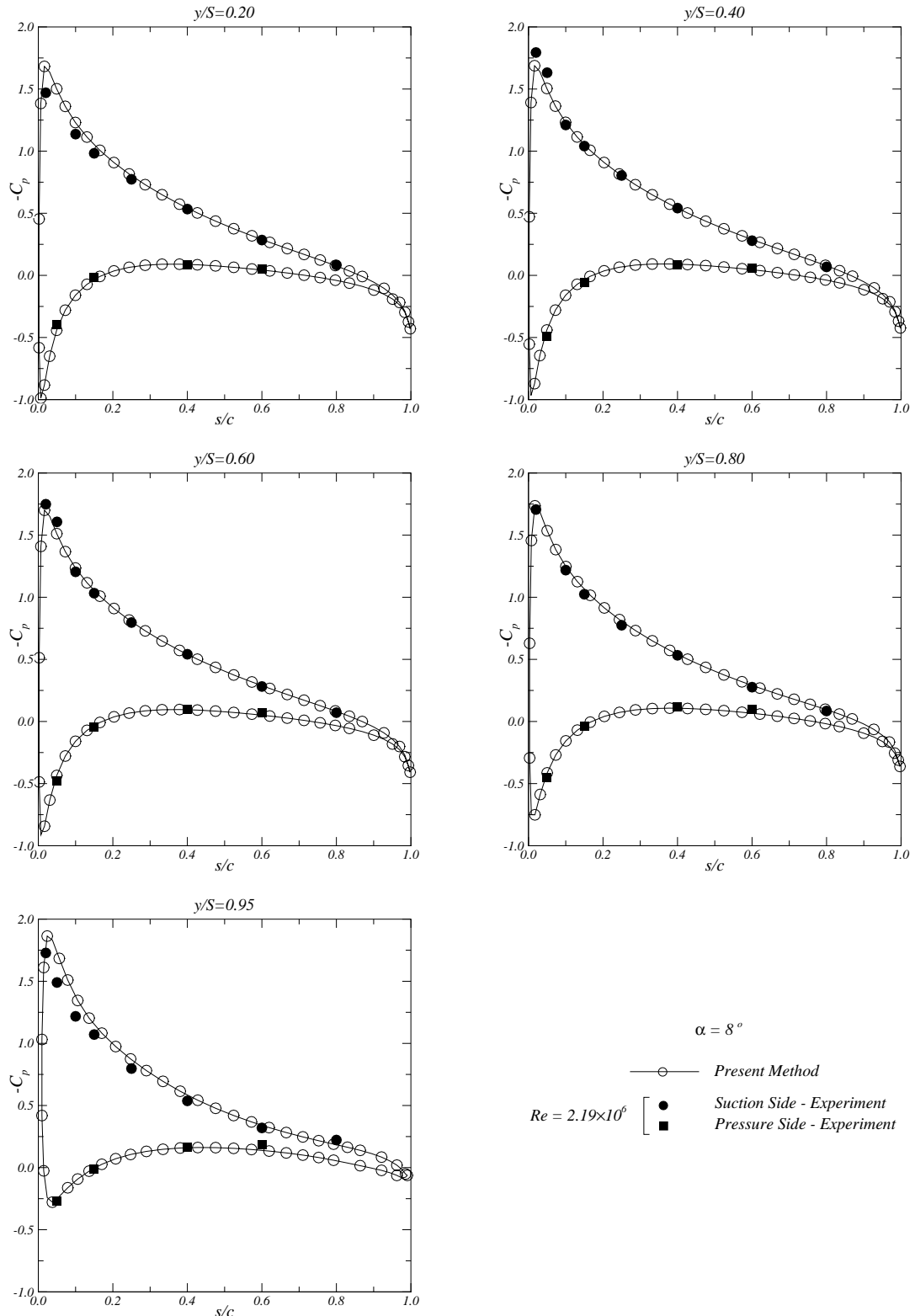


Figure 5.5: Pressure distribution at sections $y/S = 0.20, 0.40, 0.60, 0.80$ and 0.95 . Comparison with experimental data, Falcão de Campos [45]. Elliptical wing at 8 degrees incidence.

5.2.2 Rectangular Wing

Calculations have been performed for a rectangular wing with $\Lambda = 4$ and NACA0010 section at 6 degrees incidence. Figures 5.6 and 5.7 show the panel arrangement of the rectangular wing as well as the prescribed wake grid. In the figures, the wing is discretised with 64 chordwise and 17 spanwise panels. The wing tip is closed with an additional strip of panels, see Figure 5.7. A plane wake along the bisector of the trailing edge is considered. The wake is discretised with 32 streamwise and 16 spanwise panels and has an axial length of 3 wing spans. Note that only half of the wing and wake grids are shown in Figures 5.6 and 5.7.

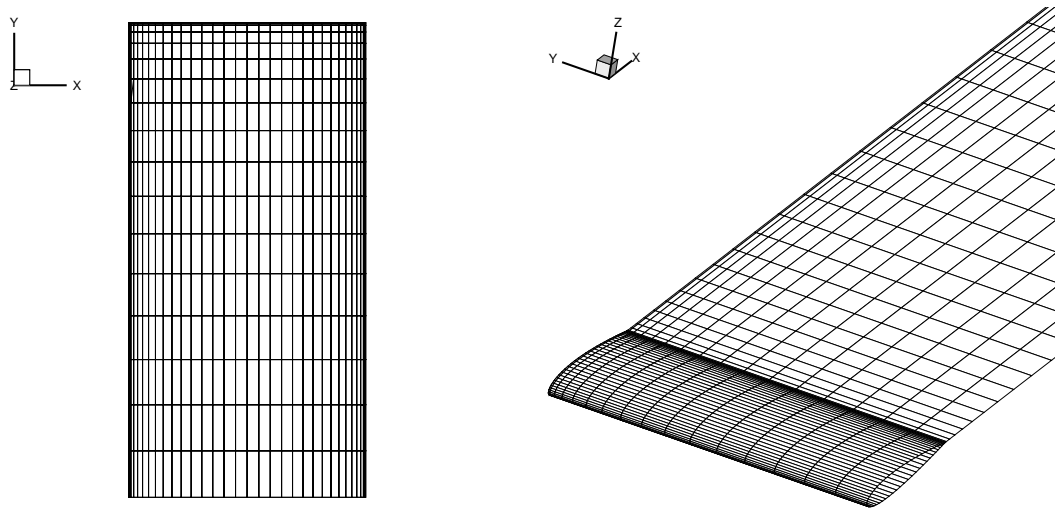


Figure 5.6: Rectangular wing panel arrangement.

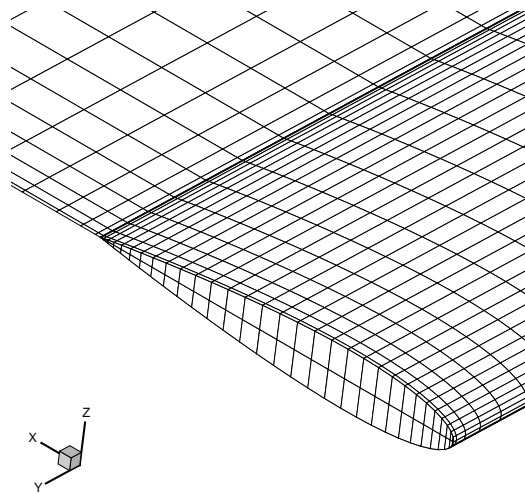


Figure 5.7: Detail of the wing tip.

5.2.2. Rectangular Wing

The convergence of the numerical results with grid refinement is studied. The discretisations ranged from $N_{CP} \times 2N_R = 16 \times 10$ to 128×66 for the complete wing. The number of panels on the wake is modified according the number of panels on the wing. The iterative pressure Kutta condition converged in one iteration.

Figure 5.8 presents the convergence of the pressure distribution at spanwise sections $y/S = 0.200, 0.400, 0.600, 0.800, 0.950$ and 0.998 . The pressure distribution converges with grid refinement between sections $y/S = 0.200$ and 0.950 . At section $y/S = 0.998$ the pressure distribution does not converge with grid refinement between mid-chord and trailing edge. In addition, a pressure peak appears at the trailing edge, which increases with grid discretisation level.

The convergence of the wing circulation is presented in Figure 5.9. The circulation distribution converges with grid refinement. Table 5.2 presents the convergence of the lift and induced drag coefficients with the grid refinement. Convergence of the lift coefficient is difficult to achieve. The lift and induced drag coefficients decrease with grid refinement.

The streamlines of the potential flow solution on the pressure and suction sides of the rectangular wing are depicted in Figure 5.10 for the discretisation 128×66 . We observe that some streamlines from the pressure side pass to the suction side flowing around the tip region. Since the tip of the rectangular wing has two sharp edges, Figure 5.7, this will produce large pressure peaks, because in potential flow theory the velocity becomes infinite at a sharp edge. The streamline pattern is consistent with the pressure distribution at spanwise section $y/S = 0.998$, where a pressure peak starting from mid-chord is seen.

The effect of the tip geometry is visible, by comparing the potential flow solutions between the elliptical and rectangular wings. No convergence of the pressure distribution is obtained in both cases. For the elliptical wing, the application of the iterative pressure Kutta condition combined with the plane wake produces pressure peaks at the trailing edge. However, for the rectangular wing the pressure peaks are due to the flow crossing the wing tip. In this case, a weaker interaction with the wake geometry is seen, since a regular circulation distribution is obtained.

Comparisons of numerical results and experimental measurements, Falcão de Campos [45], are presented for a rectangular wing with $\Lambda = 4$ and NACA0015 section at the angles of attack of 2.5 and 8.5 degrees. The results presented are for the discretisation 64×34 . Figures 5.11 and 5.12 present the comparison between the numerical results and the experimental data at spanwise sections $y/S = 0.211, 0.411, 0.611, 0.811$ and 0.961 for the angles of attack of 2.5 and 8.5 degrees, respectively. The numerical results are in overall good agreement with the experimental data for both angles of attack. However, at the wing section $y/S = 0.961$ for the case of 8.5 degrees incidence the pressure distribution calculated with the present method deviates from the experimental results, between the mid-chord and the trailing edge. This discrepancy is due to the presence of a tip vortex on the suction side, that extends downstream starting from the mid-chord and changes the flow locally.

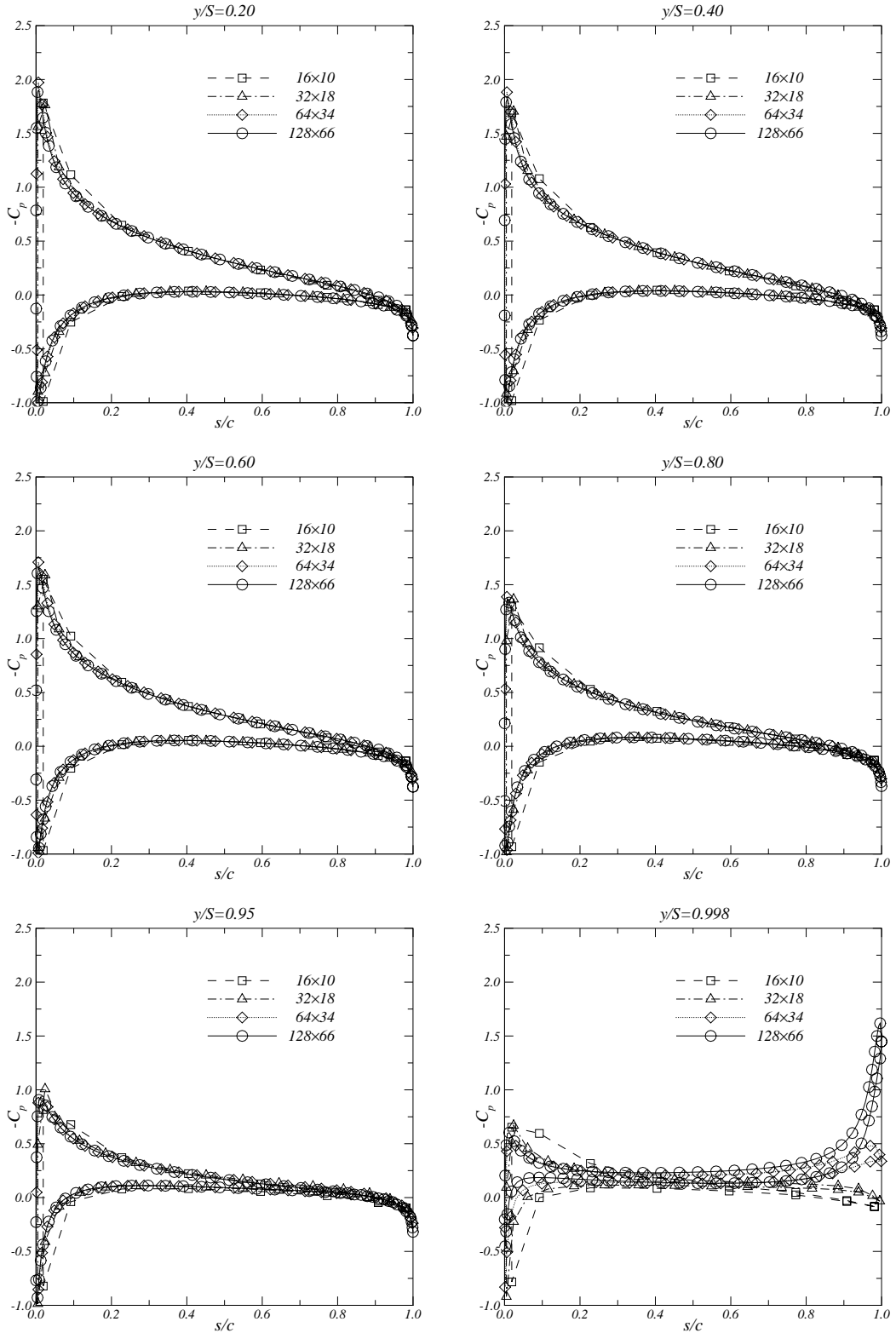


Figure 5.8: Pressure distribution at sections $y/S = 0.20, 0.40, 0.60, 0.80, 0.95$ and 0.998 . Convergence with grid refinement. Rectangular wing at 6 degrees incidence.

5.2.2. Rectangular Wing

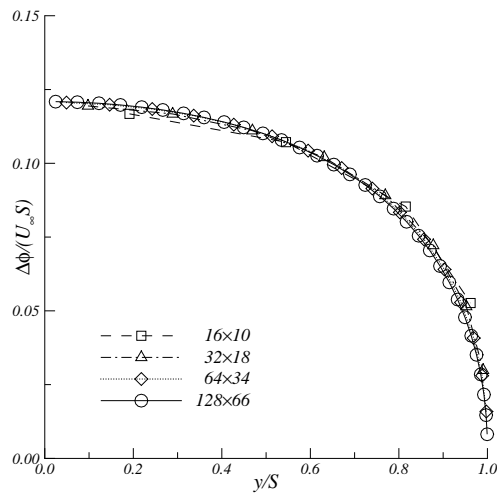


Figure 5.9: Circulation distribution. Convergence with grid refinement. Rectangular wing at 6 degrees incidence.

Grid Size (Wing+Wake)	C_L	C_{D_i}
$16 \times 10 + 8 \times 8$	0.1082	0.0039
$32 \times 18 + 16 \times 16$	0.1024	0.0034
$64 \times 34 + 32 \times 32$	0.1002	0.0032
$128 \times 66 + 64 \times 64$	0.0993	0.0031

Table 5.2: Lift and induced drag coefficients. Convergence with grid refinement. Rectangular wing at 6 degrees incidence.

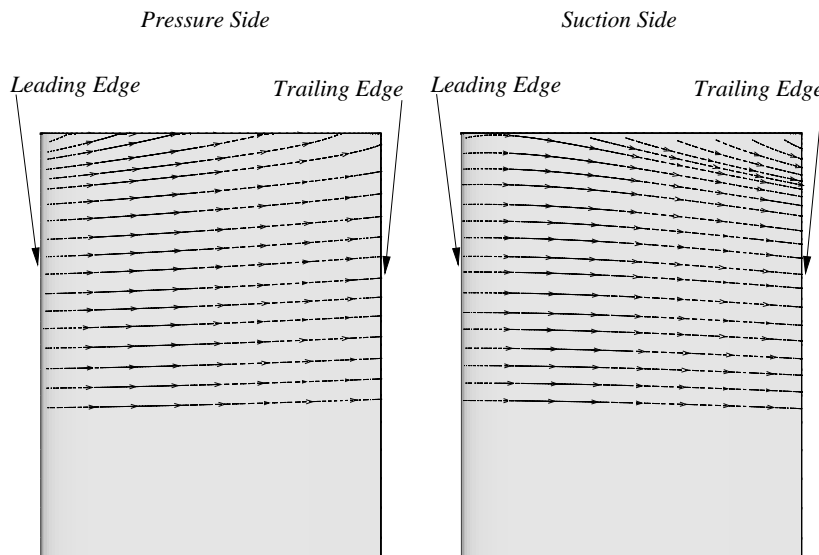


Figure 5.10: Streamlines near the tip at the pressure (left) and suction (right) sides of the rectangular wing at 6 degrees incidence. 128×66 blade grid.

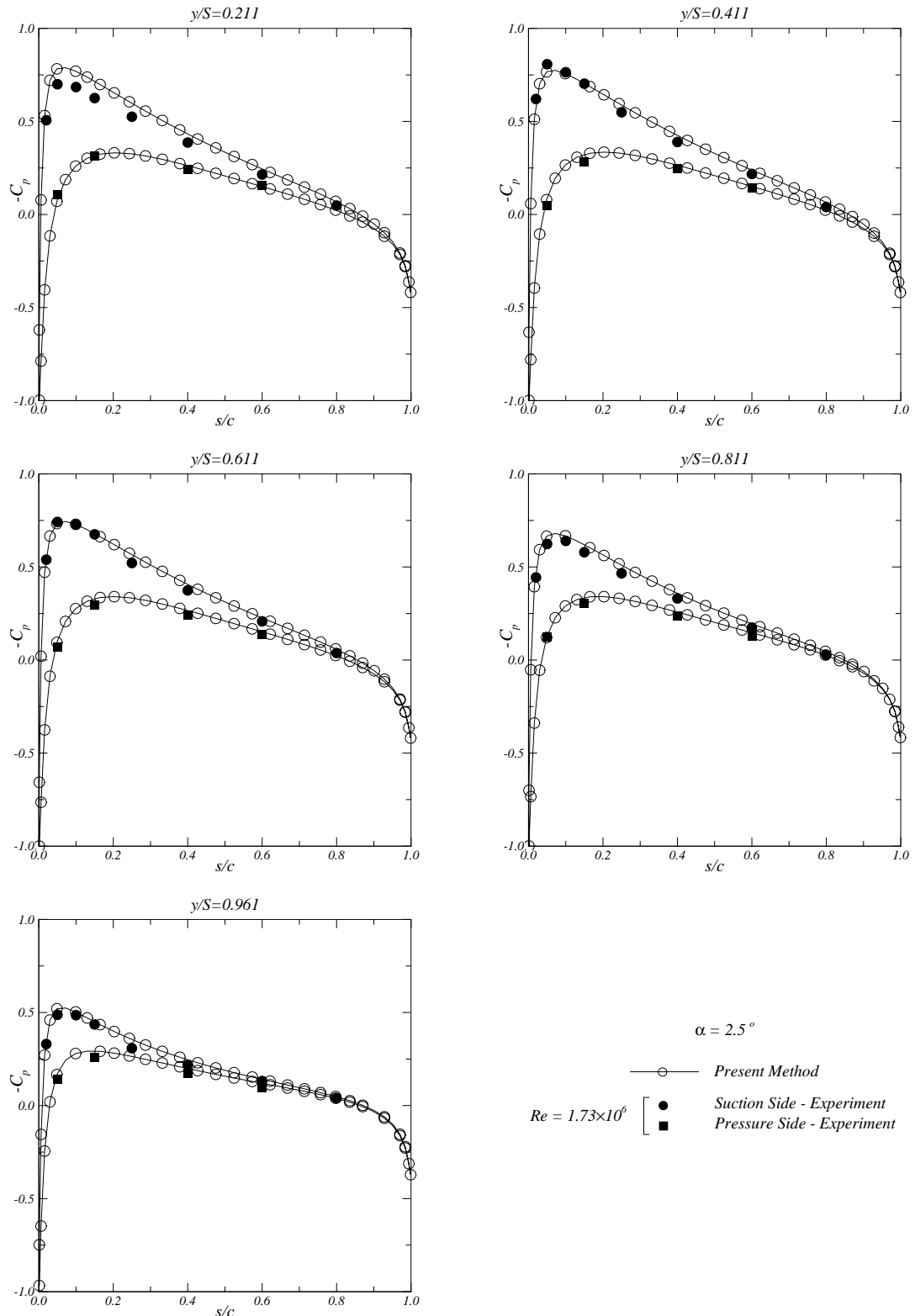


Figure 5.11: Pressure distribution at sections $y/S = 0.211, 0.411, 0.611, 0.811$ and 0.961 . Comparison with experimental data, Falcão de Campos [45]. Rectangular wing at 2.5 degrees incidence.

5.2.2. Rectangular Wing

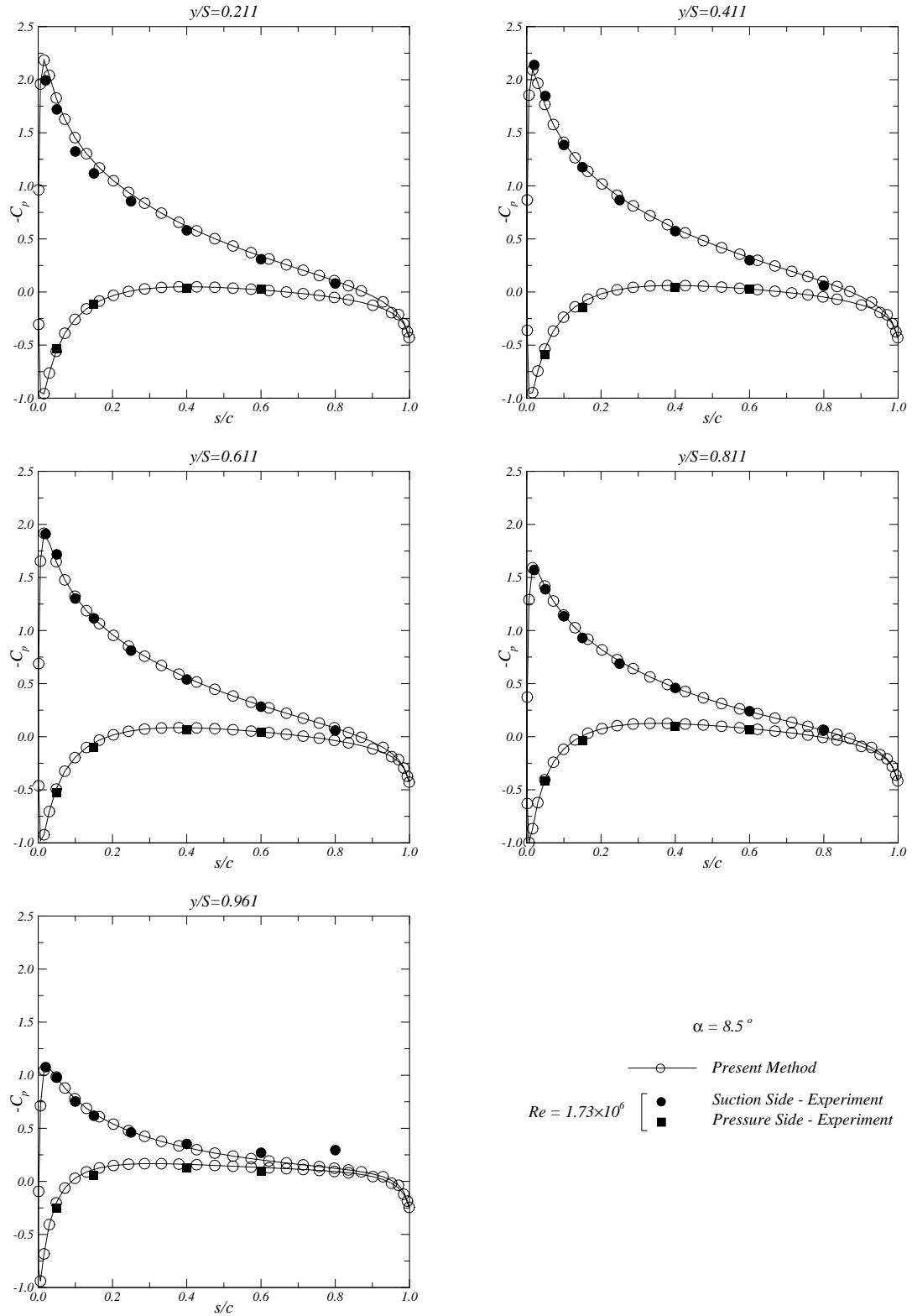


Figure 5.12: Pressure distribution at sections $y/S = 0.211, 0.411, 0.611, 0.811$ and 0.961 . Comparison with experimental data, Falcão de Campos [45]. Rectangular wing at 8.5 degrees incidence.

5.3 Open Propellers

5.3.1 DTRC P4119

The DTRC propeller P4119 is a three-bladed propeller without skew or rake. For this propeller there is an extensive experimental data set available, which has been used in the comparisons with the results of panel method calculations in the two ITTC workshops [15] and [46]. The detailed geometry of this propeller can be found in Koyama [15].

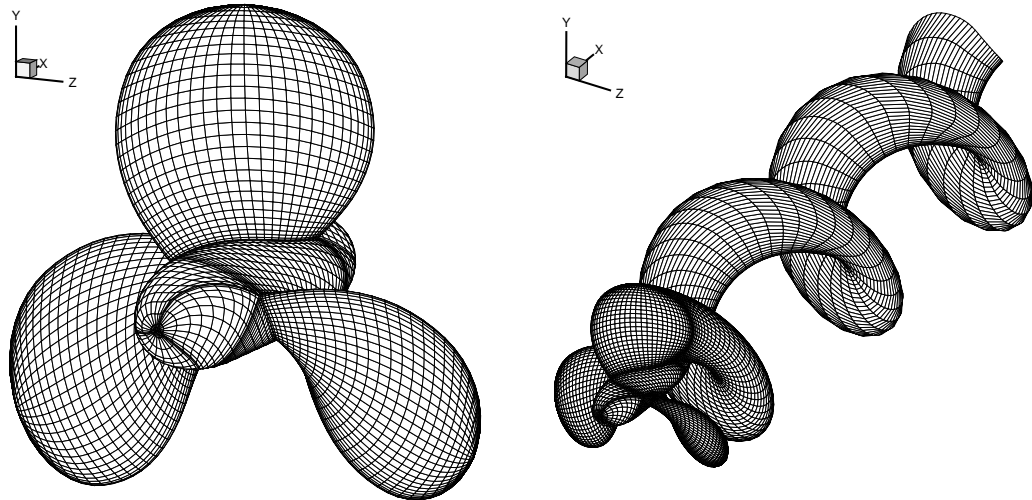


Figure 5.13: DTRC P4119 panel arrangement. Note that only one wake grid is shown.

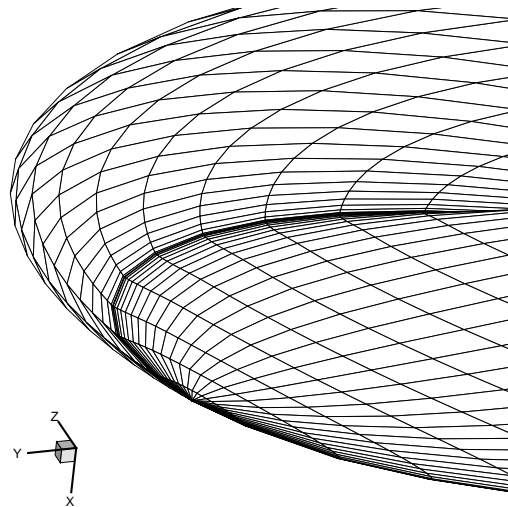


Figure 5.14: Panel arrangement at the blade tip. DTRC P4119.

5.3.1. DTRC P4119

Figure 5.13 shows a typical panel arrangement of the propeller blade as well as the prescribed wake grid. The hub recommended by the ITTC Propulsor Committee [15] is considered. In the figure, each propeller blade is discretised with 60 chordwise and 30 spanwise panels. Since the propeller has zero chord at the tip, a strip of triangular panels is introduced. Figure 5.14 shows the blade and wake panel arrangements near the tip. The wake is discretised with 90 streamwise and 30 spanwise panels and has an axial length of 3 propeller diameters. The pitch of the helicoidal lines of the wake grid is equal to the blade pitch. Contraction of the helicoidal lines is not considered. From flow symmetry considerations, the hub surface is divided into three identical sectors. Each hub sector is discretised with 54 panels along the axial direction and 12 panels along the circumferential direction.

The convergence of the numerical results with grid refinement is studied. The propeller blade discretisations ranged from $N_{CP} \times N_R = 20 \times 10$ to 80×40 . The number of panels on the hub and the wake is modified according to the number of panels on the blade. Calculations were carried out at the design condition $J = 0.833$. The iterative pressure Kutta condition converged in all cases. Figure 5.15 presents the convergence of the pressure distribution at radial sections $r/R = 0.25, 0.50, 0.75, 0.90, 0.95$ and 0.995 . It is seen that the pressure distribution at sections $r/R = 0.25, 0.50, 0.75, 0.90$ and 0.95 has practically converged for a discretisation of 40×20 . At section $r/R = 0.995$ the pressure distribution does not converge with grid refinement.

Figure 5.16 shows the convergence of the radial distribution of circulation. The circulation drops to zero at the tip. The blade circulation distribution converges with grid refinement. Table 5.3 presents the convergence of the propeller thrust and torque coefficients with the grid refinement. It is observed that the propeller thrust and torque coefficients are converged to a precision with three digits for a discretisation of 60×30 .

Results of the present method are compared with the numerical results of Hoshino [50] and experimental data, Jessup [51]. The calculations performed with the present method for the discretisation of 60×30 were selected for the comparison. The numerical results of Hoshino [50] were obtained with a discretisation of 24×12 . The experiments were carried out for a Reynolds number at radial section $r/R = 0.7$ of 10^6 .

For the design condition $J = 0.833$, calculated pressure distributions at radial sections $r/R = 0.30, 0.70$ and 0.90 are compared with the numerical results of Hoshino [50] and experimental data in Figure 5.17. Similar results are obtained between the present method and the numerical results of Hoshino [50], except near the trailing edge possible due to the use of different wake geometries. A good agreement of the numerical results and the experimental data is obtained at the radial sections $r/R = 0.70$ and 0.90 . However, some differences are observed near the leading and trailing edges, which are attributable to viscous and wake effects. At the radial section $r/R = 0.30$, some discrepancies between the calculations and the experiments are seen, although the section loading looks reasonable. This disagreement may be due to the different hub geometries considered between the numerical calculations and the experiments.

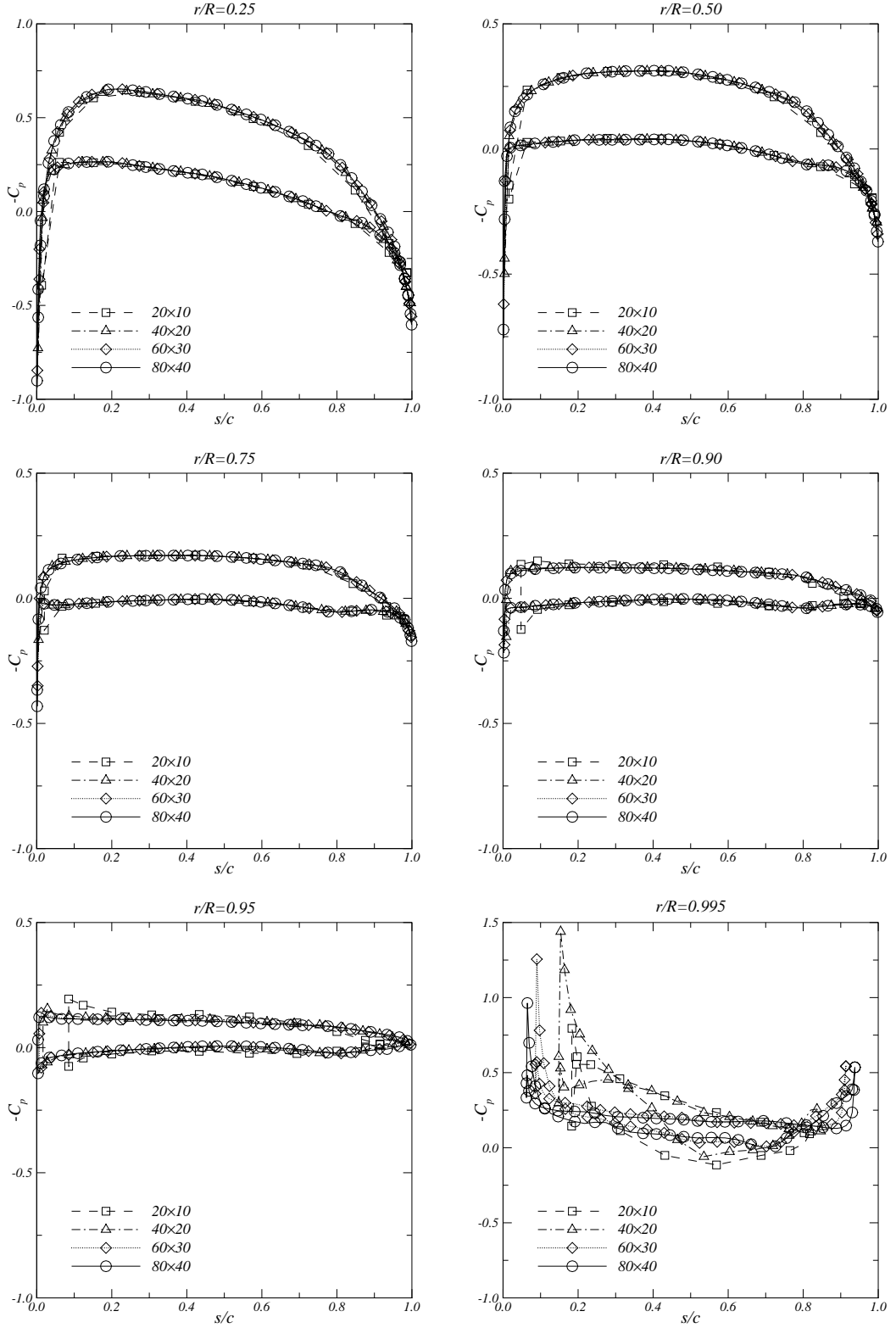


Figure 5.15: Pressure distribution at sections $r/R = 0.25, 0.50, 0.75, 0.90, 0.95$ and 0.995 . Convergence with grid refinement. $J = 0.833$. DTRC P4119.

5.3.1. DTRC P4119

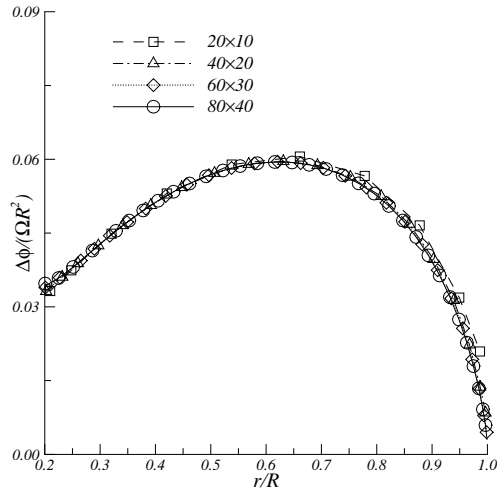


Figure 5.16: Circulation distribution. Convergence with grid refinement. $J = 0.833$. DTRC P4119.

Grid Size (Blade+Wake+Hub)	K_T	K_Q
$20 \times 10 + 30 \times 10 + 18 \times 4$	0.1622	0.0263
$40 \times 20 + 60 \times 20 + 36 \times 8$	0.1568	0.0258
$60 \times 30 + 90 \times 30 + 54 \times 12$	0.1560	0.0258
$80 \times 40 + 120 \times 40 + 72 \times 16$	0.1556	0.0258

Table 5.3: Inviscid thrust and torque coefficients for the propeller DTRC P4119. $J = 0.833$. Convergence with grid refinement.

Open-water characteristics are compared between calculations and experiments in Figure 5.18. An empirically determined formula for frictional drag was used in the force predictions of Hoshino [50]. For the thrust coefficient, a good agreement between the numerical results and the experimental data is obtained. The present method under-predicts the torque coefficient. The smaller deviations are obtained in the vicinity of the design condition $J = 0.833$. These differences may be explained by the fact that no viscous correction was applied in the thrust and torque coefficients calculated with the present method.

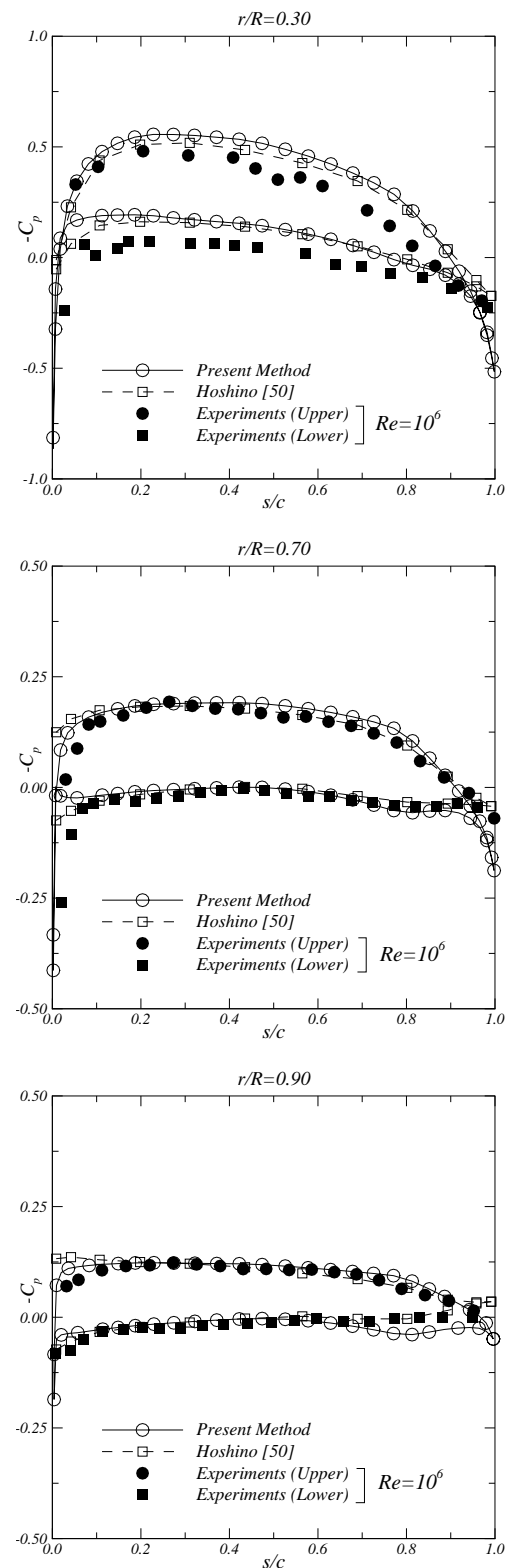


Figure 5.17: Pressure distribution at sections $r/R = 0.30$, 0.70 and 0.90 . Comparison with Hoshino [50] and experimental data, Jessup [51]. $J = 0.833$. DTRC P4119.

5.3.2. DTRC P4842M

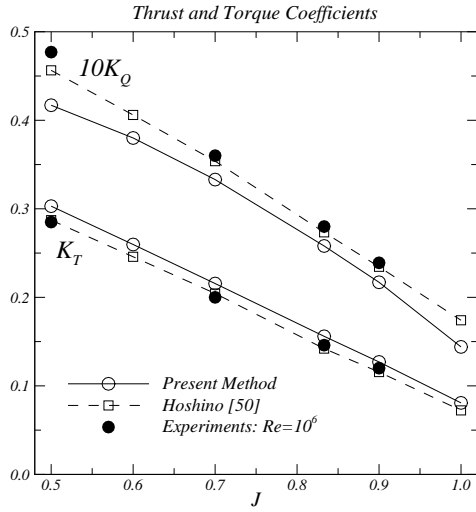


Figure 5.18: Thrust and torque coefficients for the propeller DTRC P4119. Comparison with Hoshino [50] and experimental data, Jessup [51].

5.3.2 DTRC P4842M

The DTRC propeller P4842 is a five-bladed propeller with high skew also used as a sample propeller in the 1993 ITTC workshop [15]. The modified DTRC propeller P4842, designated P4842M, was obtained from the original P4842 propeller geometry by increasing the chord length in the tip region while keeping the same mid-chord skew distribution.

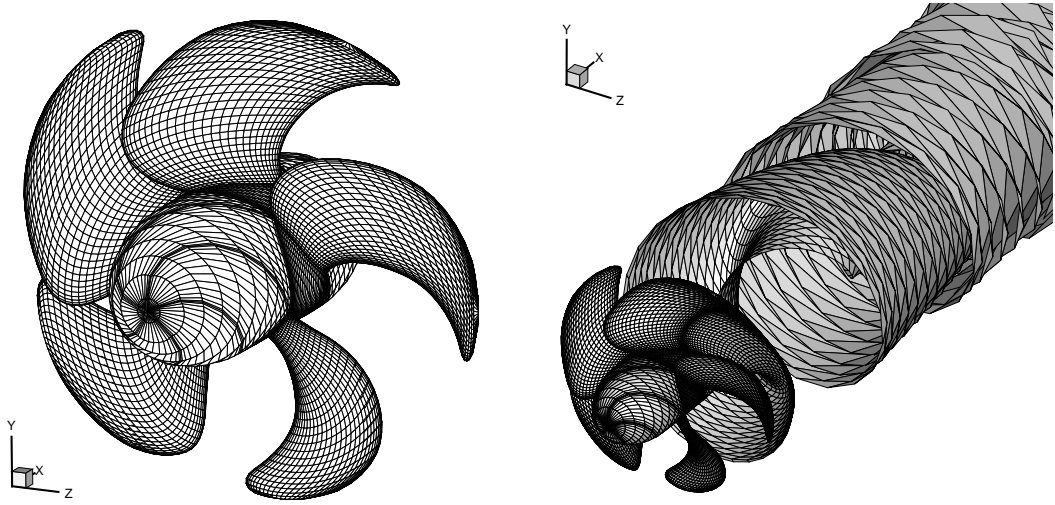


Figure 5.19: DTRC P4842M panel arrangement. Note that only one wake grid is shown.

Figure 5.19 shows a typical panel arrangement of the propeller blade as well as the prescribed wake grid. The hub recommended by the ITTC Propulsor Committee [15] is used. In the figure, each propeller blade is discretised with 60 chordwise and 30 spanwise

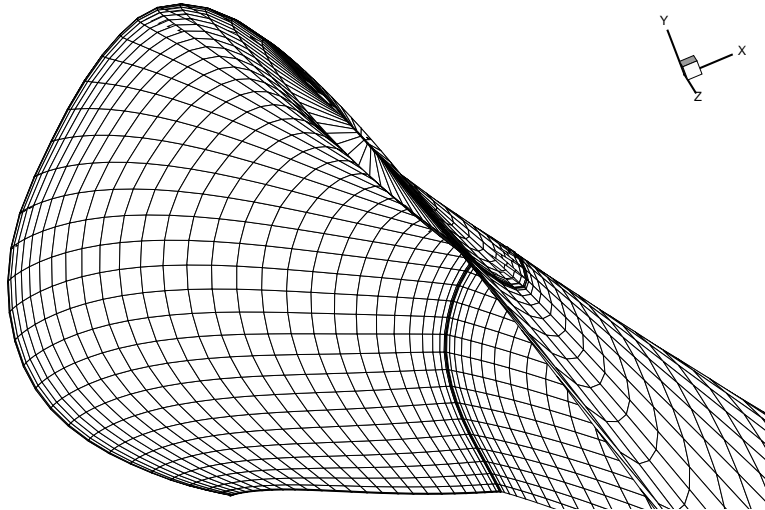


Figure 5.20: Panel arrangement at the tip. DTRC P4842M.

panels. The spanwise grid stretching parameters α_h and α_t of the blade grid were set equal to 10 degrees. The propeller has finite chord at the tip so the blade grid does not require the use of triangular panels. The blade and wake panel arrangements near the tip are depicted in Figure 5.20. The wake is discretised with 90 streamwise and 30 spanwise panels and has an axial length of 3 propeller diameters. The pitch of the helicoidal lines of the wake grid is equal to the blade pitch. Contraction of the helicoidal lines is not considered. The hub surface is divided in five identical sectors. Each hub sector is discretised with 54 panels along the axial direction and 12 panels along the circumferential direction.

Grid convergence studies were carried out at the design condition $J = 0.905$. The propeller blade discretisations ranged from 20×10 to 80×40 . The number of panels on the hub and the wake is modified according to the number of panels on the blade. Convergence of the iterative pressure Kutta condition may be difficult to achieve, especially for discretisation 60×30 . Figure 5.21 presents the convergence of the pressure distribution at radial sections $r/R = 0.40, 0.50, 0.70, 0.90, 0.95$ and 0.99 . The pressure distribution converges with grid refinement at sections $r/R = 0.40, 0.50, 0.70, 0.90$ and 0.95 . Close to the blade tip, at section $r/R = 0.99$ the solution does not converge with increasing grid refinement. The pressure distribution for the finest discretisations contains a pressure peak near the trailing edge.

Figure 5.22 presents the convergence of the blade circulation. An irregular circulation distribution is obtained near the blade tip for the case of the finest discretisations. Although convergence of the iterative pressure Kutta condition for the discretisation 60×30 is achieved, the circulation presents a peak near the blade tip. Table 5.4 shows the convergence of the propeller thrust and torque coefficients with the grid refinement. For the present discretisations convergence of the thrust and torque coefficients is not achieved.

5.3.2. DTRC P4842M

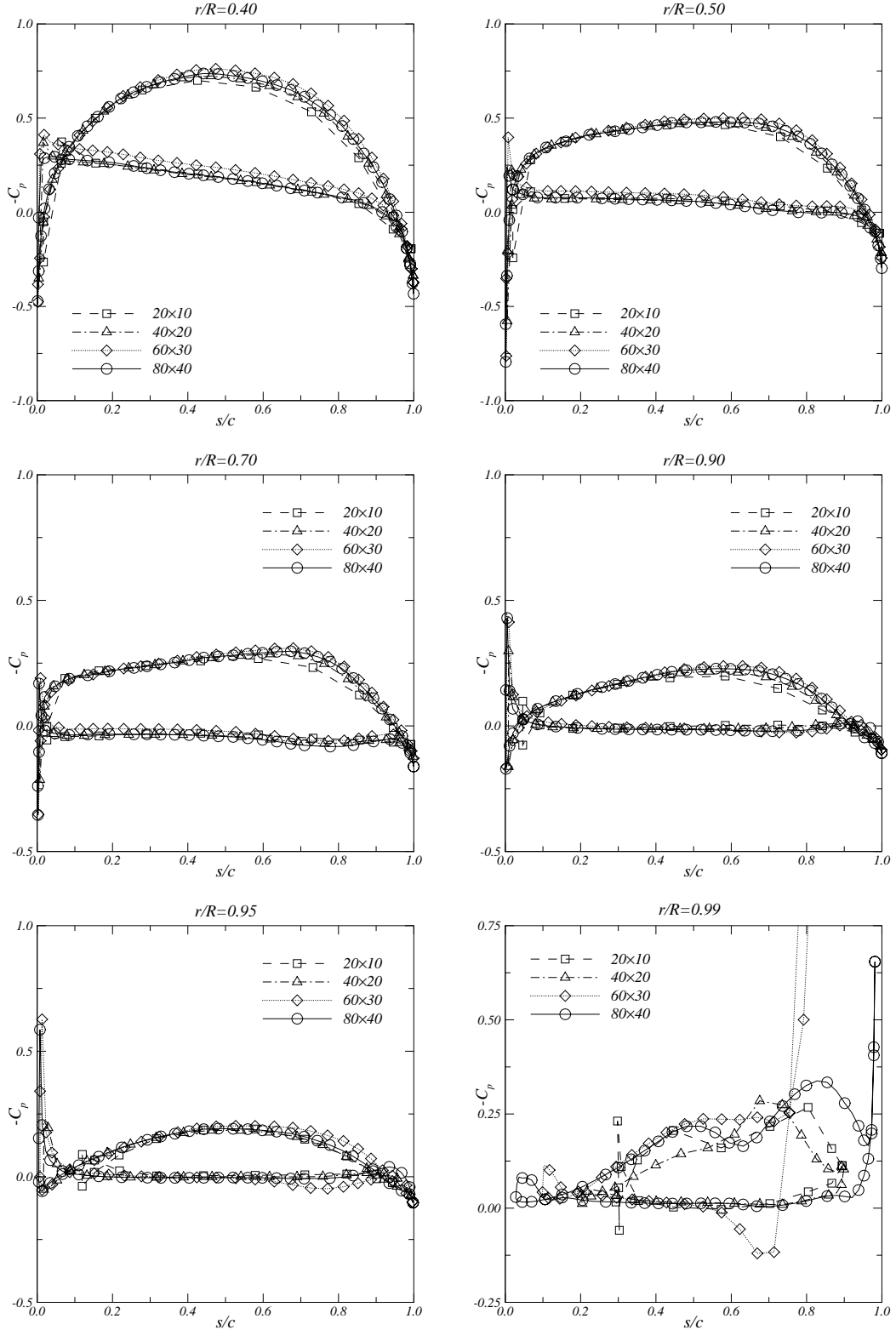


Figure 5.21: Pressure distribution at sections $r/R = 0.40, 0.50, 0.70, 0.90, 0.95$ and 0.99 . Convergence with grid refinement. $J = 0.905$. DTRC P4842M.

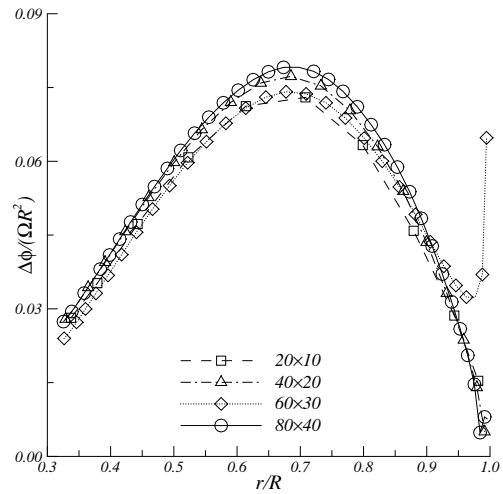


Figure 5.22: Circulation distribution. Convergence with grid refinement. $J = 0.905$. DTRC P4842M.

Grid Size (Blade+Wake+Hub)	K_T	K_Q
$20 \times 10 + 30 \times 10 + 18 \times 4$	0.2751	0.0559
$40 \times 20 + 60 \times 20 + 36 \times 8$	0.2922	0.0606
$60 \times 30 + 90 \times 30 + 54 \times 12$	0.2885	0.0657
$80 \times 40 + 120 \times 40 + 72 \times 16$	0.3021	0.0635

Table 5.4: Inviscid thrust and torque coefficients for the propeller DTRC P4842M. $J = 0.905$. Convergence with grid refinement.

5.4 Ducted Propellers

5.4.1 NSMB Duct 19A

The NSMB duct 19A has an axial cylindrical part in the inner side of the duct at the propeller location. The outer side of the duct is straight in order to simplify its manufacturing, and the trailing edge of the duct is round. This duct has a length-diameter ratio of 0.5. The duct section geometry is given by van Manen [52]. Calculations were carried out in uniform flow at zero incidence.

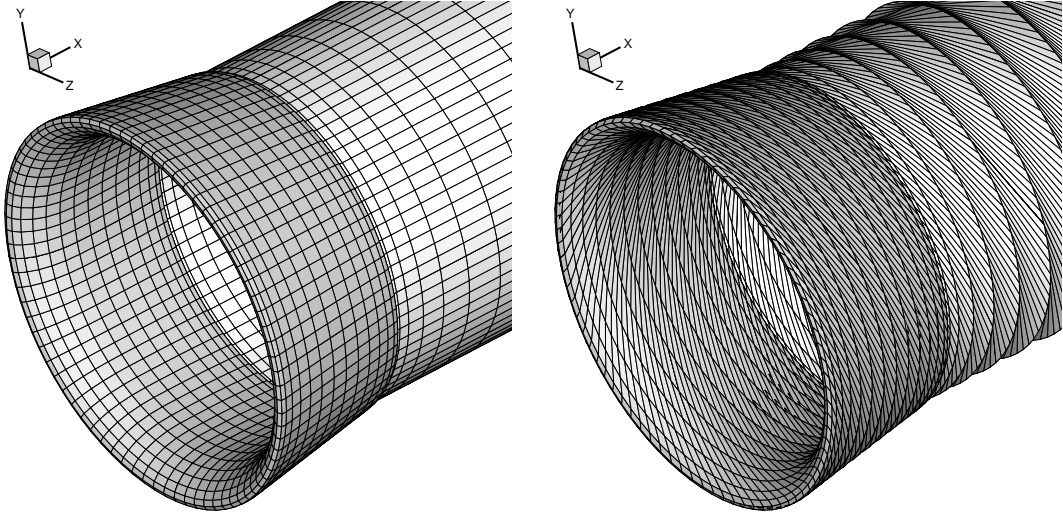


Figure 5.23: NSMB duct 19A panel grids. Cylindrical panel arrangement (left). Helical panel arrangement (right).

Two panel arrangements of the duct and wake are considered based on a cylindrical coordinate system and a helical coordinate system, Figure 5.23. The latter is adequate in the rotating coordinate system to have the most favourable match between the duct grid and the blade grid in the ducted propeller case, and is used here for comparison purposes. In the present case the pitch-diameter ratio of the helicoidal grid lines is chosen equal to 1.2. Calculations were carried out for the duct grid with 120 panels along the chordwise axial direction and with 120 along the circumferential direction. The wake is discretised with 60 panels along the streamwise direction, which corresponds to an axial length of 3 duct diameters. The duct wake leaves the trailing edge along the bisector to the angle of the inner and outer surfaces. This angle is defined by the straight parts of the duct inner and outer surfaces prior to the application of the circular trailing edge fairing. The iterative pressure Kutta condition converged in one iteration for both cases.

In Figure 5.24 the pressure coefficient and the circulation distribution are compared between the cylindrical arrangement and the helical arrangement. Similar results for the pressure distribution are obtained for the two panel arrangements. A higher suction peak is obtained with the helical panel arrangement. Small differences in the duct circulation are obtained between the cylindrical and helical panel arrangements.

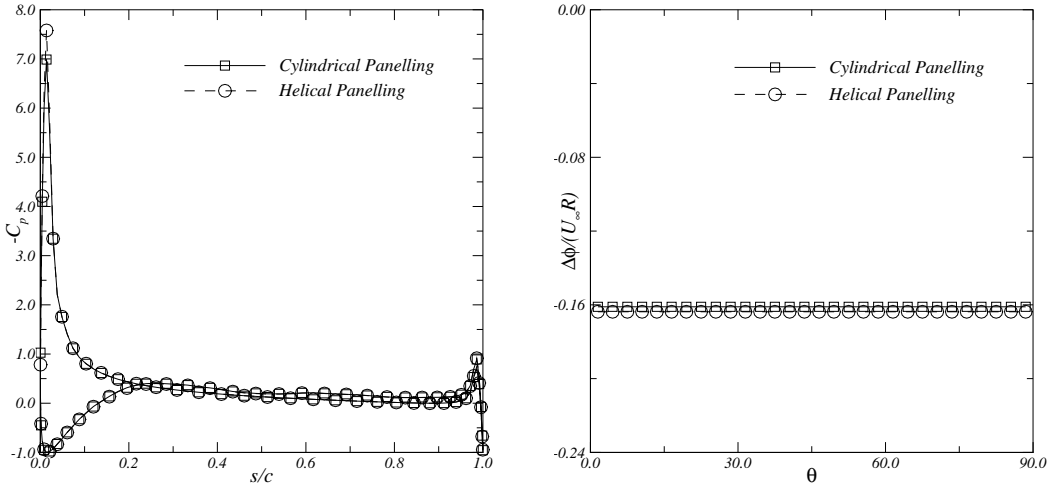


Figure 5.24: Duct pressure distribution along the chordwise direction (left). Circumferential distribution of circulation on the duct (right). Comparison between the cylindrical and helical panel arrangements.

The numerical results obtained with the helical panel arrangement are compared with a surface vorticity method, Falcão de Campos [47], together with wind tunnel measurements, Gibson [48], in Figure 5.25. It can be seen that marginal differences are obtained between the panel method and the surface vorticity method, except near the leading and trailing edges. At the leading edge a different suction peak is obtained, probably due to the different leading edge interpolated geometry in the present method and discretisation error due to the helical panel arrangement. The differences near the trailing edge are caused by the different way of fairing the trailing edge. The comparison with experiment is poor on the outer side of the duct due to the occurrence of flow separation from the leading edge followed by reattachment, as reported in Gibson [48]. The circulation is also not well predicted by the Kutta condition applied at the trailing edge and this is the cause for the discrepancy of the duct pressure level.

The sensitivity of the calculation to the position of the stagnation point on the trailing edge has also been investigated. Three different locations of the stagnation point are considered: at 99.7% on the outer side and inner side of the duct, and at the bisector of the trailing edge (100%). The helical panel arrangement is used. The results are shown in Figure 5.26 and depict an enormous change of the pressure distribution for a small variation of the stagnation point location. Note that the stagnation point is defined by the intersection of the dipole wake with the duct surface.

5.4.1. NSMB Duct 19A

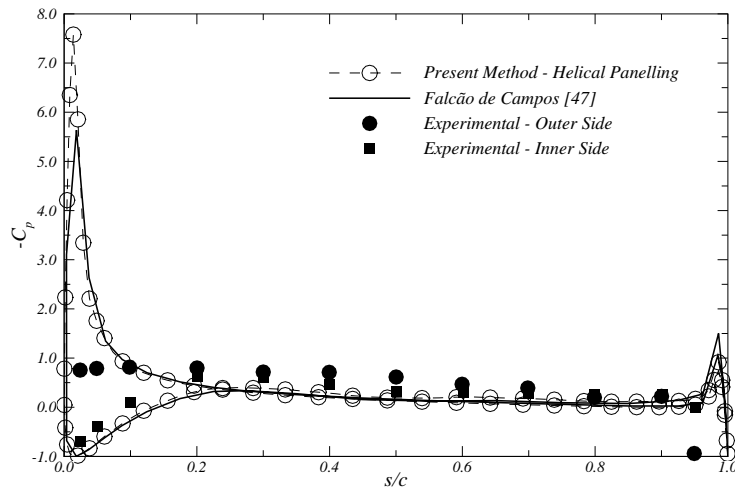


Figure 5.25: Pressure distribution on duct NSMB 19A. Comparison with Falcão de Campos [47] and experimental data, Gibson [48].

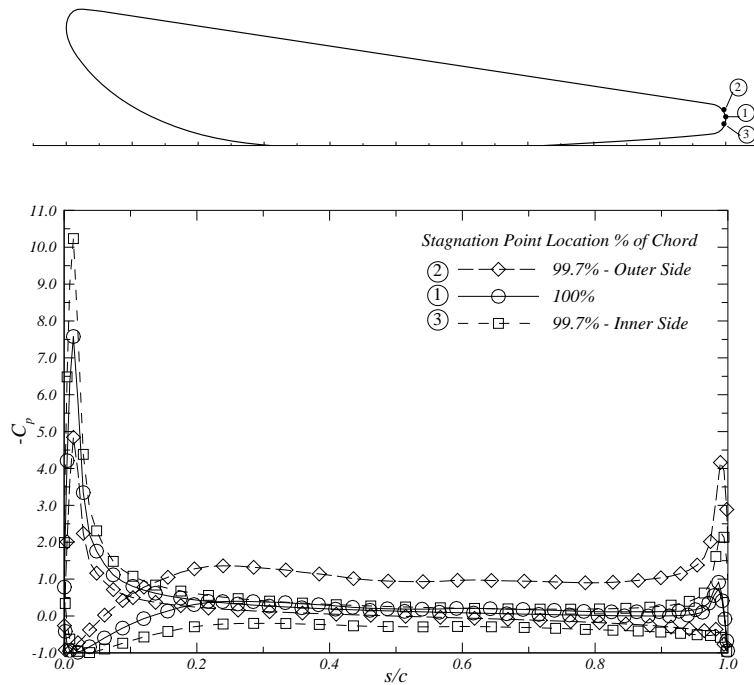


Figure 5.26: NSMB 19A duct profile with location of the stagnation points (top). Effect of the location of the stagnation point on the pressure distribution on duct NSMB 19A (bottom).

5.4.2 Propeller K_a 4-70 Inside Duct NSMB 19A

The propeller K_a 4-70 is a four-bladed propeller of the Kaplan type with a finite chord at the blade tip. The geometry of the K_a series is given in Kuiper [49]. Calculations were performed in uniform flow for the propeller K_a 4-70 in combination with duct NSMB 19A at the advance ratio $J = 0.7$. A pitch-diameter ratio of 1.2 is considered. The gap between the duct inner side and the blade tip is uniform and equal to 0.8% of the propeller radius.

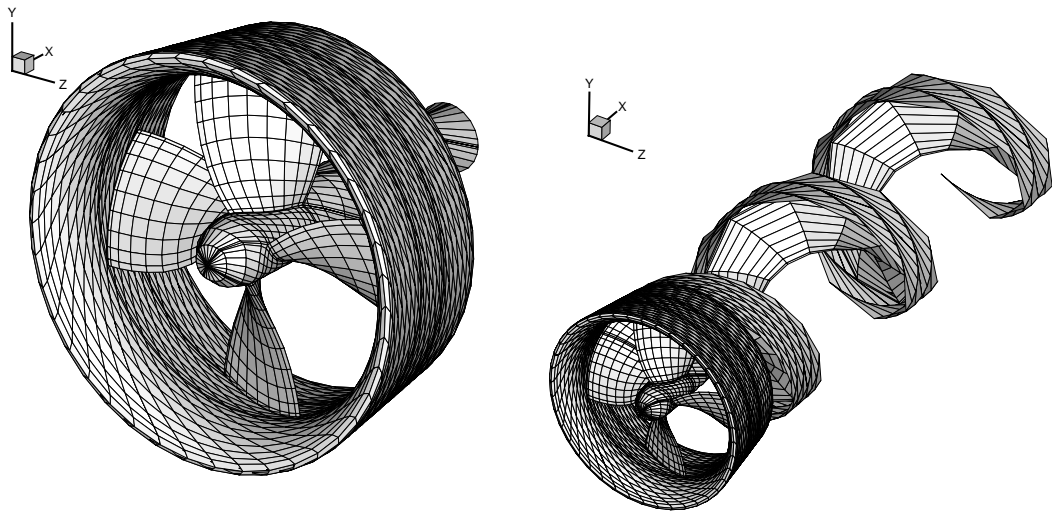


Figure 5.27: Panel arrangement for propeller K_a 4-70 inside duct 19A. Note that only one blade wake grid and one duct section grid are shown.

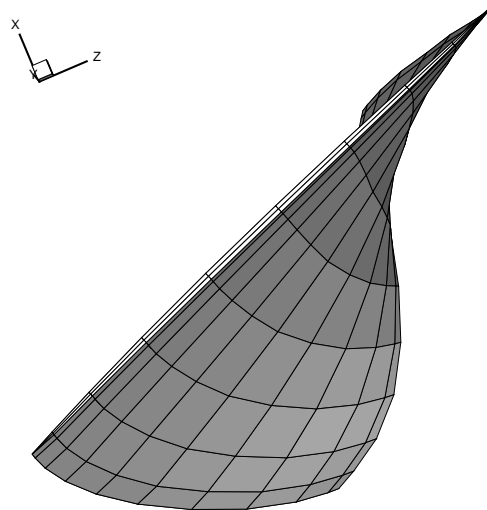


Figure 5.28: Panel arrangement at the blade tip. K_a 4-70 inside duct 19A.

Figure 5.27 shows a typical panel arrangement of the ducted propeller. In this figure, each propeller blade is discretised with 20 and 11 panels in the chordwise and radial direction, respectively. Since the blade has a finite chord with non-zero thickness at the

5.4.2. Propeller K_a 4-70 Inside Duct NSMB 19A

tip, an additional strip of panels is applied in order to close the blade tip. Figure 5.28 presents a detail of the blade tip. The blade wake is discretised with 30 panels along the streamwise direction and 10 panels along the radial direction, which corresponds to an axial length of 3 propeller diameters. The pitch of the helicoidal lines of the wake grid is equal to the blade pitch. Contraction of the helicoidal lines is not considered. From flow symmetry considerations, the duct and the hub surfaces are divided in four identical sectors. The duct is discretised with 60 panels along the chordwise direction and with 10 panels along the circumferential direction for each duct sector. The corresponding duct wake is discretised with 30 panels along the streamwise direction and with 10 panels along the circumferential direction, which also corresponds to an axial length of 3 propeller diameters. An open-water hub is considered. Each hub sector is discretised with 21 panels along the axial direction and 8 panels along the circumferential direction.

The convergence of the numerical results with grid refinement is studied. The propeller blade discretisations ranged from 20×11 to 40×21 . The number of panels on the duct, hub and wakes is modified according the number of panels on the blade. The duct wake leaves the trailing edge at the bisector. The iterative pressure Kutta condition, applied at blade and duct trailing edges, converged in all cases. Figure 5.29 shows the convergence of the blade pressure distribution at the radii $r/R = 0.50, 0.75$ and 0.99 , and of the duct pressure distribution at the circumferential positions $\theta = 0, 20$ and 40 degrees. The blade pressure distribution at the radial sections $r/R = 0.50$ and 0.75 converges with grid refinement. Nevertheless, at section $r/R = 0.99$ the blade pressure distribution is not yet converged. The duct pressure distribution converges with grid refinement, except at the suction peak near the blade tip vortex.

Figure 5.30 presents the convergence of the blade and duct circulations. The blade circulation distribution converges with grid refinement. Nevertheless, for the present discretisations the duct circulation distribution is not yet converged. Table 5.5 shows the convergence of the inviscid thrust and torque coefficients with grid refinement. Convergence to three significant digits is achieved both for the total thrust and torque coefficients. Convergence of the duct thrust coefficient is difficult to achieve.

The influence of the gap is studied. Gaps of 0.0% and 0.8% of the propeller radius are considered. Calculations were carried out for the 40×21 blade grid, 120×30 duct grid and 41×16 hub grid. The duct wake leaves the trailing edge at the bisector. Figure 5.31 shows the blade pressure distribution at $r/R = 0.99$ and the duct pressure distribution at $\theta = 40$ degrees. A smooth blade pressure distribution is obtained near the tip for both cases. The duct pressure distribution of the zero gap model does not show the suction peak, since in this case there is no blade tip vortex. Figure 5.32 presents the influence of the gap on the blade and duct circulations. The trends of the blade circulation distribution near the tip are as expected. The maximum circulation is obtained for the 0.8% gap case. The duct circulation for the zero gap model shows a discontinuity, which is very close to the value of the finite circulation at the blade tip. Decreasing the gap from 0.8% to zero greatly increases the mean circulation, as well as its circumferential variation.

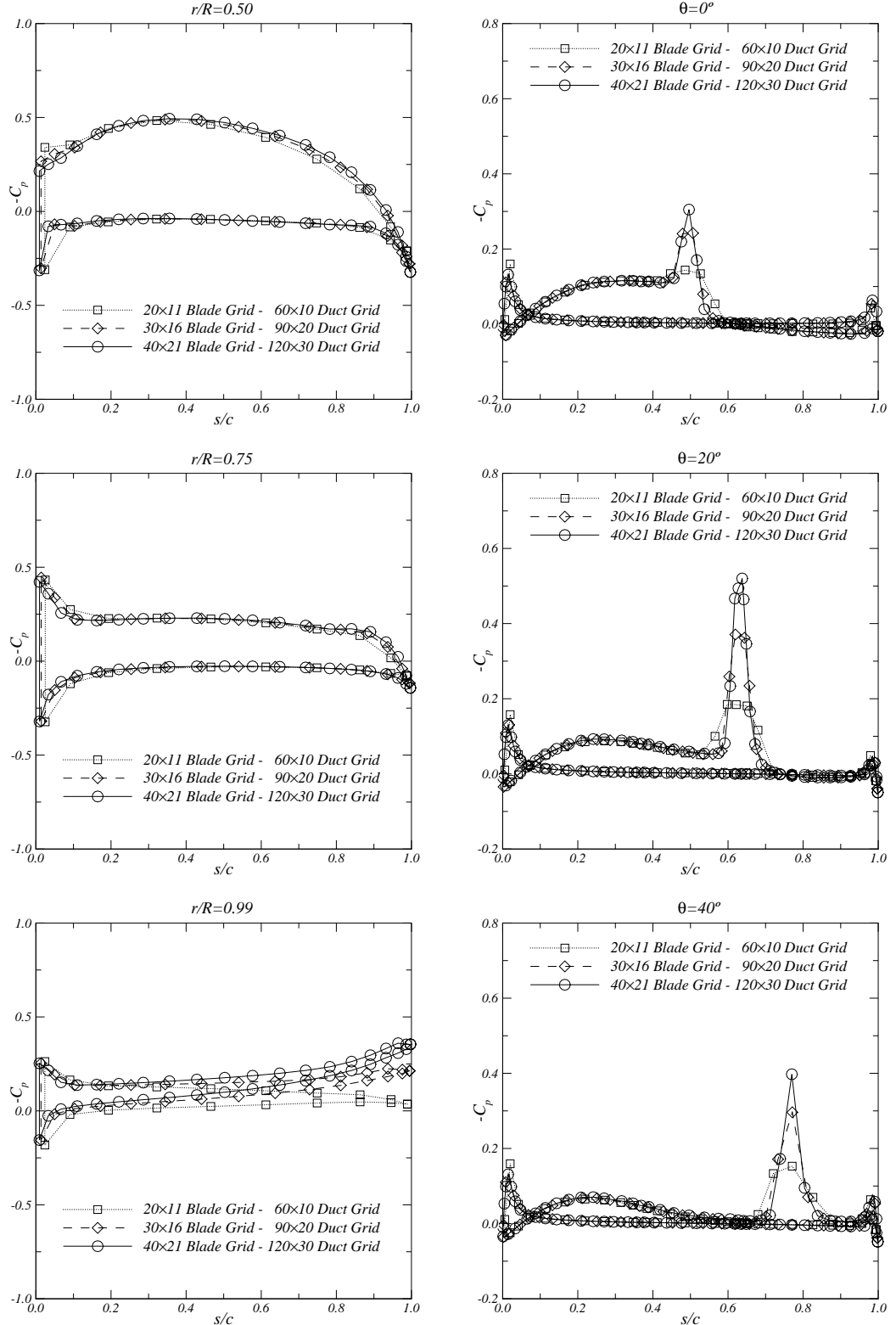


Figure 5.29: Blade pressure distribution at radial sections $r/R = 0.50$, 0.75 and 0.99 (left). Duct pressure distributions at circumferential positions $\theta = 0$, 20 and 40 degrees (right). Convergence with grid refinement. K_a 4-70 inside duct 19A at $J = 0.7$.

5.4.2. Propeller K_a 4-70 Inside Duct NSMB 19A

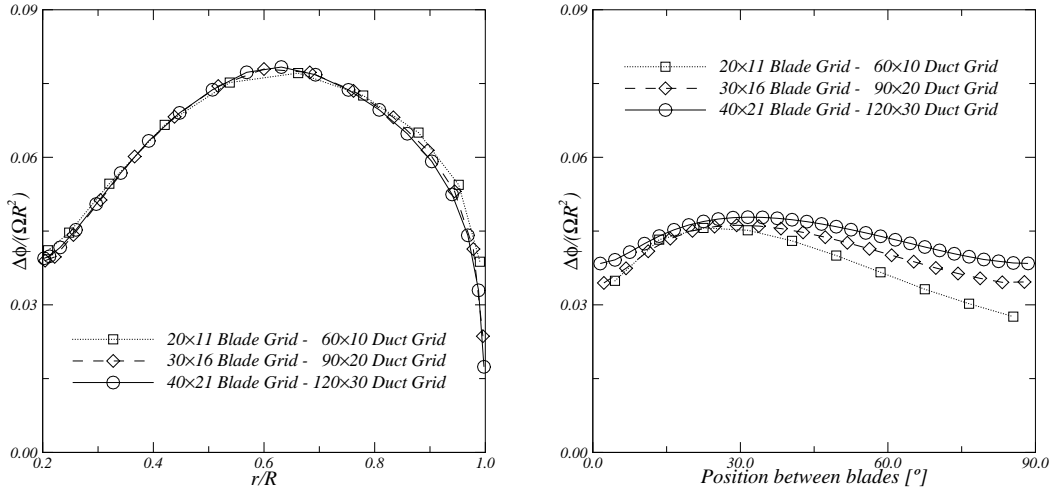


Figure 5.30: Radial distribution of circulation on the blade (left). Circumferential distribution of circulation on the duct (right). Convergence with grid refinement. K_a 4-70 inside duct 19A at $J = 0.7$.

Grid Size (Blade+Duct+Hub)	K_{T_D}	K_{T_T}	K_Q
$20 \times 11 + 60 \times 10 + 21 \times 8$	0.0194	0.3155	0.0526
$30 \times 16 + 90 \times 20 + 32 \times 12$	0.0266	0.3145	0.0515
$40 \times 21 + 120 \times 30 + 41 \times 16$	0.0287	0.3147	0.0515

Table 5.5: Inviscid thrust and torque coefficients for the propeller K_a 4-70 inside duct 19A at $J = 0.7$. Convergence with grid refinement.

The sensitivity of the calculation to the position of the wake vorticity shedding line of the duct trailing edge has also been investigated. Three different locations of the shedding line are considered: at 99.9% on the outer side and inner side of the duct, and at the bisector of the trailing edge (100%). Figure 5.33 shows the duct profile with the location of the wake vorticity shedding line. Calculations were carried out for the 40×21 blade grid, 120×30 duct grid and 41×16 hub grid. Figure 5.34 presents the pressure and circulation distributions on the propeller blade and duct. The results show large variations in the pressure and circulation distributions with the location of the shedding line.

The numerical results were compared with experimental data available from the open-water diagrams, Kuiper [49]. The duct wake vorticity shedding line is considered at the bisector of the trailing edge. Figure 5.35 presents the comparison between the computed thrust and torque coefficients and the experimental data. The present method over-predicts the total thrust and torque coefficients. The duct thrust coefficient agrees well with the experimental data around the advance ratio $J = 0.7$, while the largest discrepancies appear at low advance ratios.

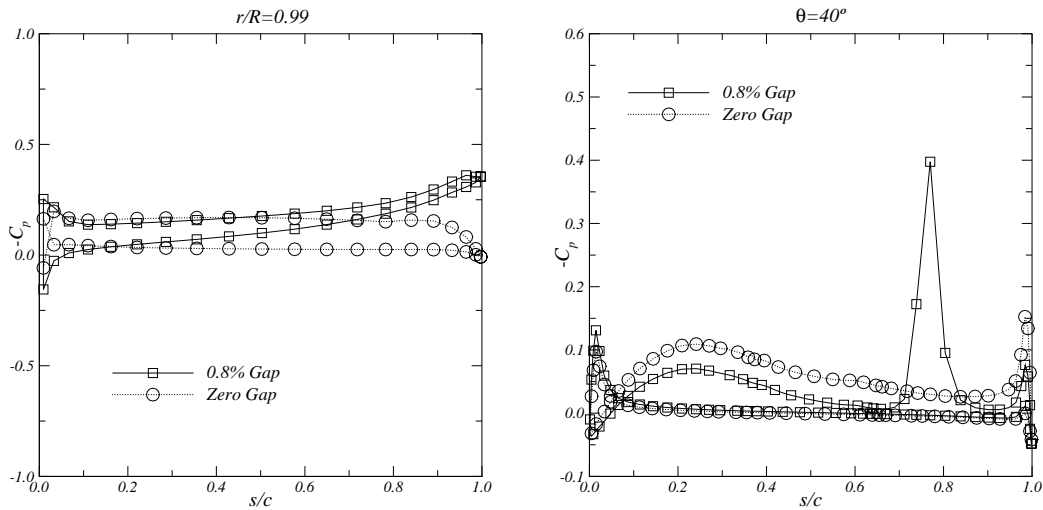


Figure 5.31: Blade pressure distribution at radial section $r/R = 0.99$ (left). Duct pressure distribution at the circumferential position $\theta = 40$ degrees (right). Influence of the gap. K_a 4-70 inside duct 19A at $J = 0.7$.

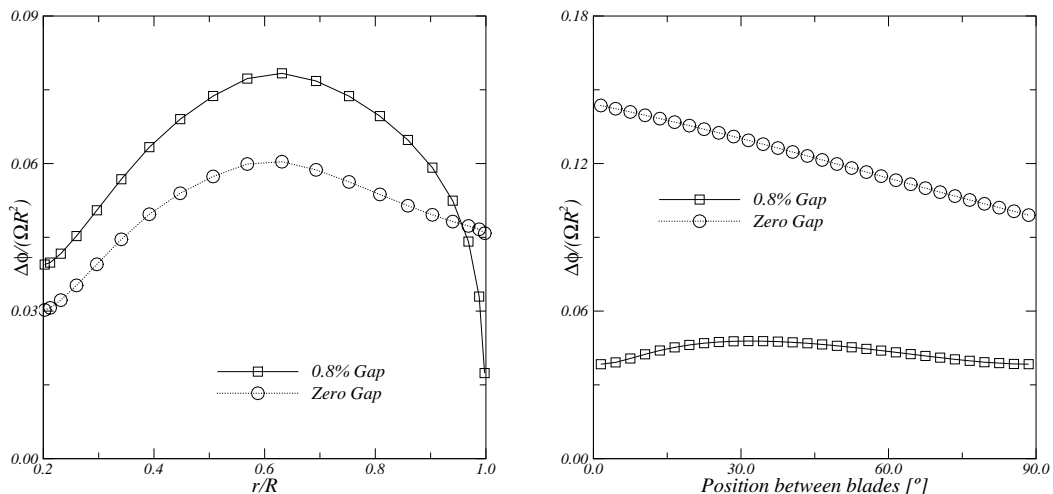


Figure 5.32: Radial distribution of circulation on the blade (left). Circumferential distribution of circulation on the duct (right). Influence of the gap. K_a 4-70 inside duct 19A at $J = 0.7$.

5.4.2. Propeller K_a 4-70 Inside Duct NSMB 19A

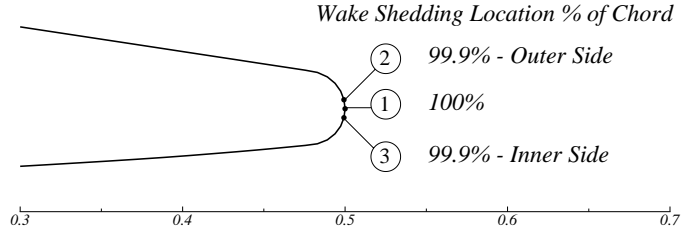


Figure 5.33: NSMB 19A duct profile with location of the shedding lines.

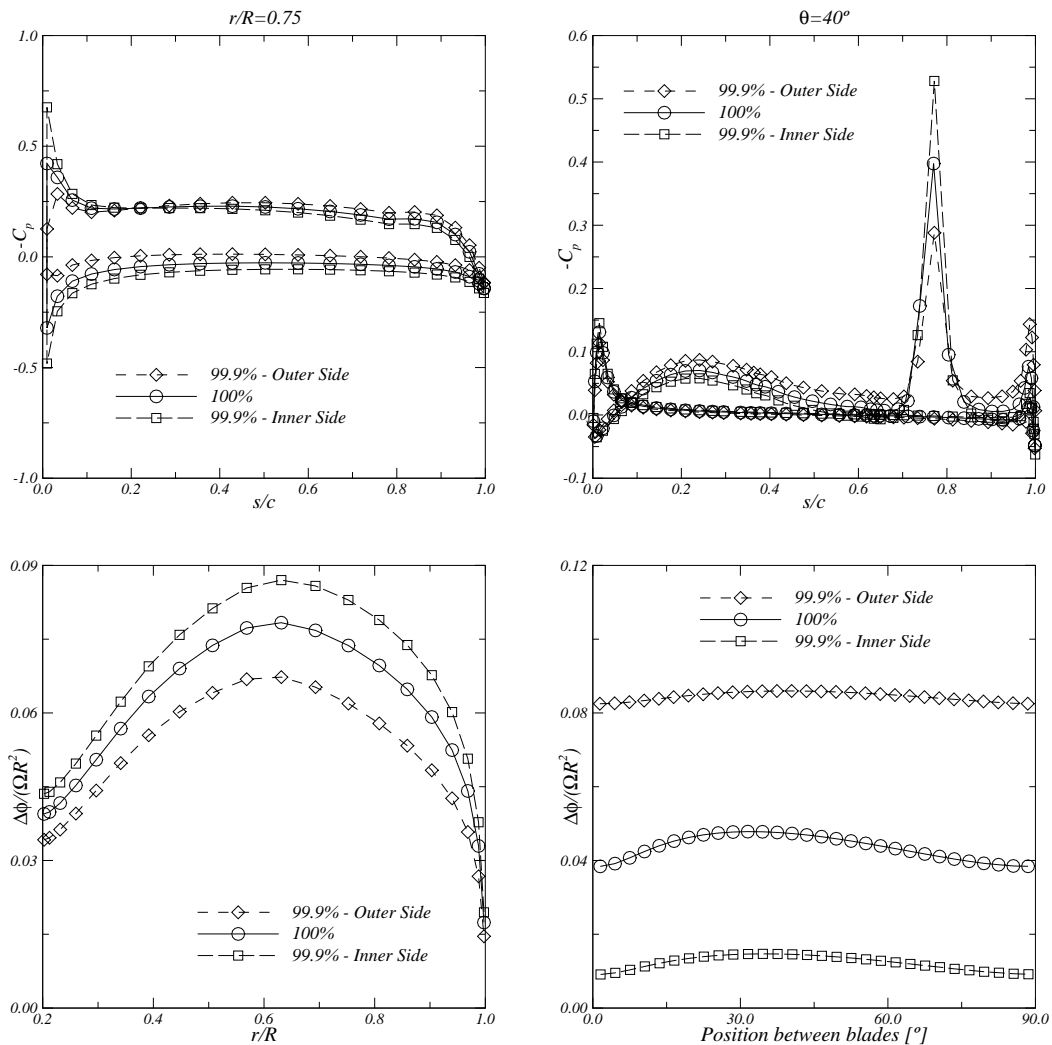


Figure 5.34: Blade pressure distribution at $r/R = 0.75$ (top-left). Duct pressure distribution at $\theta = 40$ degrees (top-right). Blade (bottom-left) and duct (bottom-right) circulation distributions. Influence of the shedding line location.

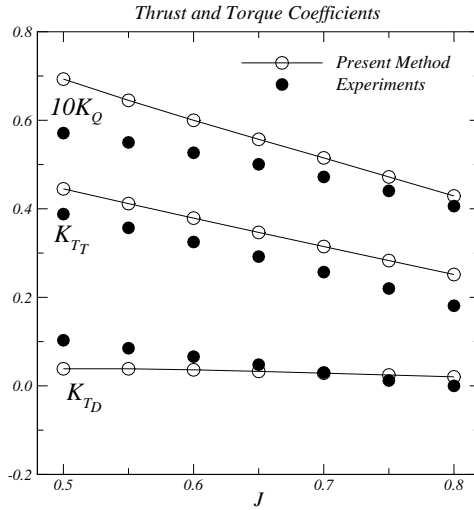


Figure 5.35: Inviscid thrust and torque coefficients for the propeller K_d4-70 inside duct 19A. Comparison with experimental data, Kuiper [49].

5.5 Discussion of the Results

Potential flow calculations were performed for wings and marine propellers. Grid convergence studies using conventional panel arrangement and comparisons with experimental data were made. A rigid wake model with an iterative pressure Kutta condition was used. From this study the following conclusions are drawn:

- Convergence of the numerical results with grid refinement is achieved, except near the tip where an irregular solution is obtained. Large pressure peaks at the trailing edge near the tip are seen. Depending on the blade and wake geometries, convergence of the iterative pressure Kutta condition may be difficult to obtain.
- An overall good agreement between the present method and the experimental measurements for the pressure distribution is achieved. For the open propellers, some differences are observed between the calculated thrust and torque coefficients and the experimental data. These differences may be explained by the fact that no viscous correction was applied in the thrust and torque coefficients calculated with the present inviscid flow method.
- For the ducted propeller, significant differences in the thrust and torque coefficients are observed when comparing the numerical results and the experimental data from the open-water diagrams, suggesting a more complex interaction between the propeller and duct. The position of the wake vorticity shedding line on the duct trailing edge strongly influences the potential flow solution of the propeller and duct. Large variations of the duct and blade circulation with small variations of the shedding line are seen.

5.5. Discussion of the Results

- The panel method is robust and fast. The influence coefficient calculation scheme proved to be efficient for the configurations presented in this Chapter. The system of equations is solved with a direct solver (LU factorisation) in order to minimise the computational time. As an example, the computer time of the results obtained for the elliptical wing with 4096 panels presented in Section 5.2.1, is 10 minutes on a Pentium IV at 3.2GHz with 2.0GB of RAM. For the ducted propeller with 840 blade panels, 656 hub panels and 3600 duct panels, presented in Section 5.4.2, the computer time is 22 minutes.

Chapter 6

Tip Flow Modelling

6.1 Introduction

Results of potential flow calculations for wings and marine propellers were presented and compared with experimental measurements in the previous Chapter. Calculations were performed with rigid wake model combined with the conventional panel arrangement. The present method is able to predict the pressure distribution with reasonable to good accuracy in comparison with experimental data. Convergence of the numerical results with grid refinement is achieved for most of the wing and propeller blade. However, there are still a number of difficulties to the prediction of the pressure distribution in the tip region. The correct prediction of the pressure distribution is important not only for the thrust and torque calculations by integration of the pressure distribution on the blade surface, but also for the cavitation inception estimation.

Grid convergence studies, Falcão de Campos and Ferreira de Sousa [53], were carried out for marine propellers using conventional and quasi-orthogonal grids. At the corresponding design conditions the solutions obtained with the conventional grids appear to converge for the major part of the propeller blade, but a non-smooth behaviour of the pressure distribution near the tip was evident. The use of quasi-orthogonal grids showed some promising results in dealing with the occurrence of pressure peaks at the trailing edge after the application of the pressure Kutta condition. However, the predicted pressure distributions close to the tip remained rather erratic and strongly influenced by the smoothness of the grid generated.

BEM computations, Baltazar [20], were carried out for an elliptical wing with conventional and quasi-orthogonal grids using a rigid wake model. Unrealistic pressure peaks at the trailing edge near the tip using the iterative pressure Kutta condition for both panel arrangements were obtained. From these studies it became clearer that the lack of wake alignment with the flow near the tip should be responsible for the occurrence of the unrealistic pressure peaks near the trailing edge.

Furthermore, studies on the accuracy of the potential flow past ellipsoids were performed with conventional and quasi-orthogonal grids by Falcão de Campos *et al.* [29] and Baltazar

6.2. Influence of the Wake Model

et al. [54]. An oscillating behaviour of the solution is observed in the conventional arrangement. The oscillations disappear as the grid approaches orthogonality. However, the application of quasi-orthogonal grids to ellipsoids produces a single pressure oscillation at mid-chord which stems from the poor geometric approximation of the surface, inherent to the shape of the grid locally at the tip.

This Chapter focusses on the numerical modelling of wing and propeller tip flows. Different techniques are tested to obtain a more reliable solution at the blade tip. First, the application of wake relaxation models in potential flow calculations for wings is investigated. Second, calculations with a new panel arrangement with “hydrodynamic tip”, similar to the flow adapted grid, Kinnas *et al.* [19], are performed for propeller blades. Finally, the effect of blade tip geometry on the potential flow solution is studied.

6.2 Influence of the Wake Model

In this section, the application of wake relaxation models for potential flow calculations to wings is studied. The focus of the investigation is on the behaviour of the pressure distribution near the wing tip. Three types of wake relaxation models are considered: rigid wake, partial wake relaxation and full wake relaxation. The rigid wake model is used in combination with a linear and an iterative pressure Kutta condition at the trailing edge. The partial wake relaxation model applies a zero-pressure-jump condition on the wake panels. The full wake relaxation model aligns the vortex lines with the local fluid velocity and makes use of the iterative pressure Kutta condition.

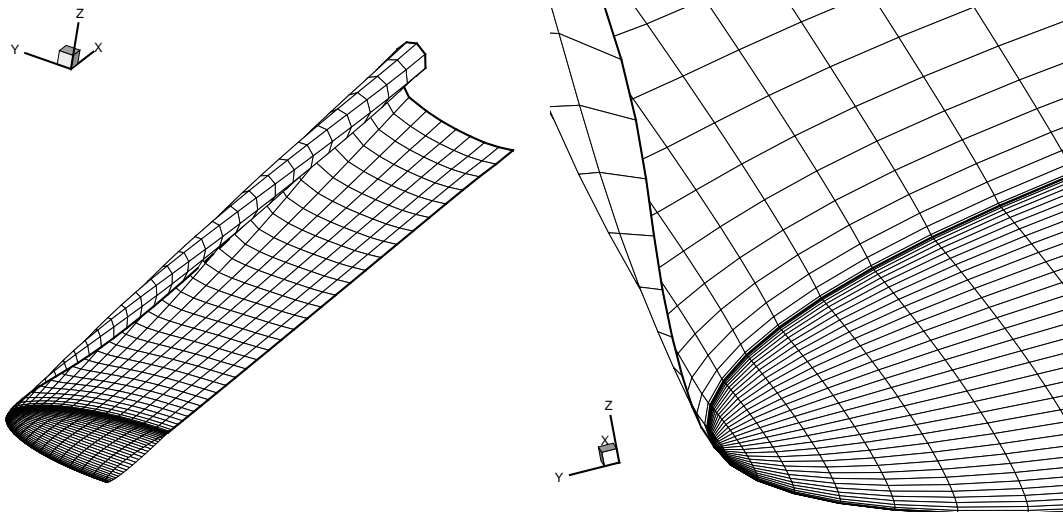


Figure 6.1: Rolled-up wake grid for the elliptical wing.

The configuration studied is a NACA0010 wing with a 2:1 elliptical planform. Calculations were performed for the elliptical wing at 6 degrees incidence using the 64×32 conventional grid. A plane wake along the bisector of the trailing edge, $z = 0$, is considered. The wake sheet is discretised with 32 streamwise and 32 spanwise panels and has an axial length

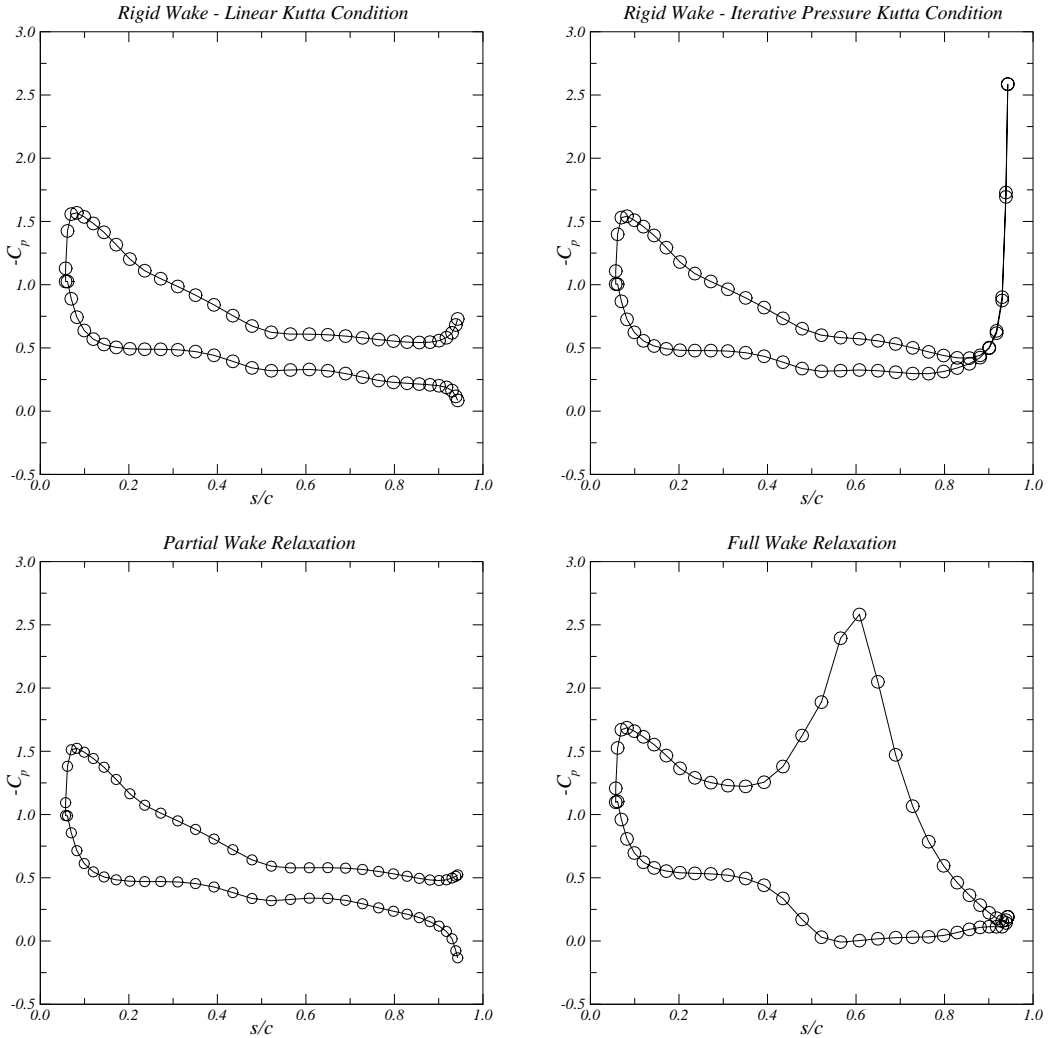


Figure 6.2: Pressure distribution at section $y/S = 0.99$. Comparison between wake models. Elliptical wing at 6 degrees incidence.

of 3 wing spans. The partial wake relaxation model and the iterative pressure Kutta condition converged in all cases to $|\Delta C_p| \leq 10^{-3}$. The rolled-up wake grid obtained with the full wake relaxation model is shown in Figure 6.1. Figure 6.2 presents the pressure distribution at section $y/S = 0.99$ obtained with the three wake relaxation models.

Similar results are obtained between the rigid wake model with linear Kutta condition and the partial wake relaxation model. This is due to the fact that no pressure condition is applied at the control points on the panels adjacent to the wing trailing edge. The application of a zero-pressure-jump condition on the wake in combination with a plane wake geometry does not change significantly the pressure distribution near the wing tip.

The application of the rigid wake model with the iterative pressure Kutta condition results in a pressure distribution with a peak at the trailing edge, which is due to the lack of wake alignment with the flow near the wing tip, Baltazar [20]. However, the use of a rolled-up

6.2. Influence of the Wake Model

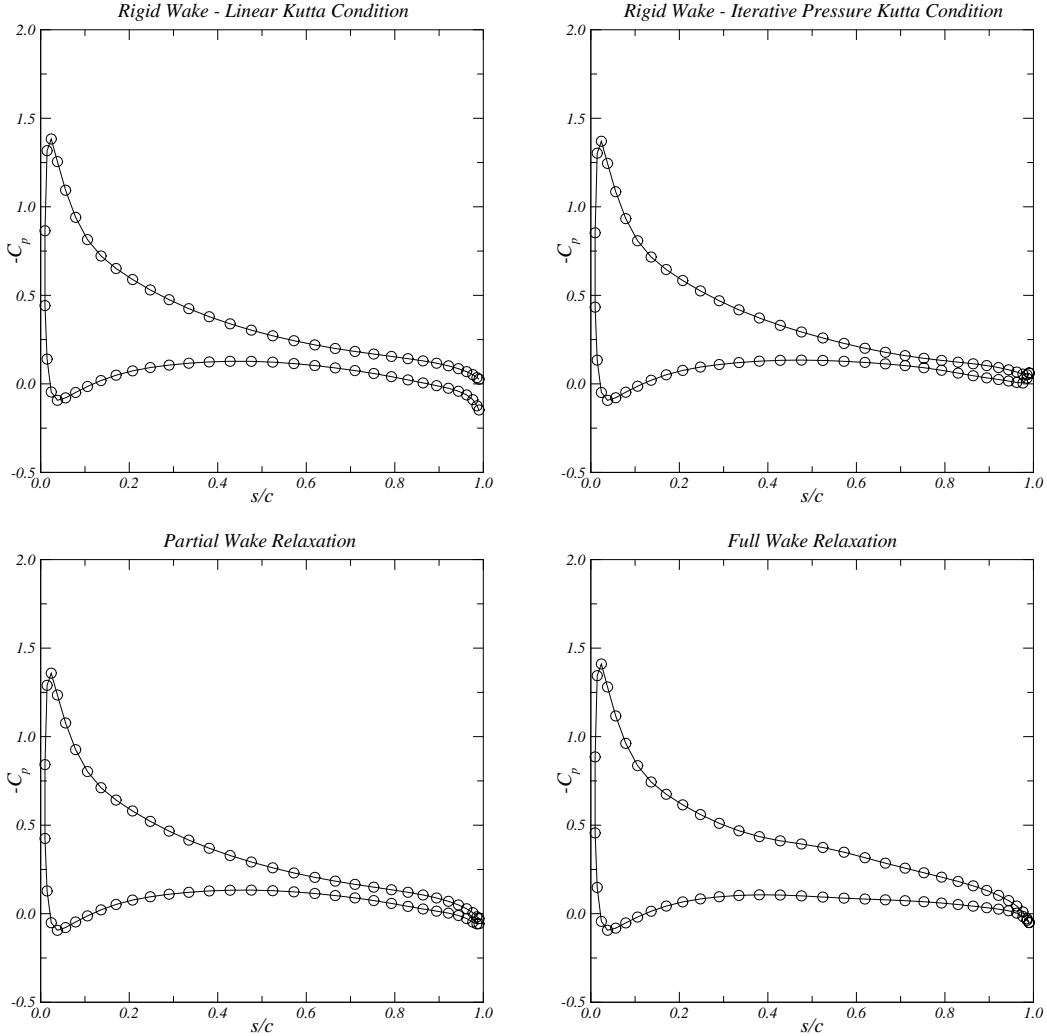


Figure 6.3: Pressure distribution at section $y/S = 0.95$. Comparison between wake models. Elliptical wing at 6 degrees incidence.

wake eliminates the pressure peak at the trailing edge when applying the iterative pressure Kutta condition. Due to the roll-up process, the wake sheet passes near the suction side of the wing, inducing a low pressure region. The results show that the wake sheet location is essential to avoid the pressure peaks at the trailing edge near the tip when applying the iterative pressure Kutta condition. The influence of the wake vortex distribution in the tip solution increases significantly by displacing the wake sheet from the plane $z = 0$.

The influence of the wake models on the pressure distribution at the spanwise section $y/S = 0.95$ is shown in Figure 6.3. Small differences are seen between the various wake models. However, zero-pressure-jump at the trailing edge is not obtained with the linear Kutta condition. Although no pressure condition is applied at the wing trailing edge with the partial wake relaxation, the pressure-jump tends to zero. No pressure peaks are obtained at the wing trailing edge after the application of the iterative pressure Kutta condition with the plane wake geometry.

6.3 Panel Arrangements With “Hydrodynamic Tip”

In this section, the location of the tip vortex position is studied. Results of BEM calculations for new panel arrangements with “hydrodynamic tip” are presented and compared with the conventional panel arrangement for the marine propellers DTRC P4119 and DTRC P4842M. The “hydrodynamic tip” is defined as the location on the trailing edge where the vortex wake ends and no longer coincides with the geometrical tip. A rigid wake model and a full wake relaxation model with roll-up are considered.

Calculations were carried out for the DTRC propeller P4119 at the design condition $J = 0.833$ using the conventional grid and the new panel arrangement with the “hydrodynamic tip” located at $r/R = 0.97$. The “hydrodynamic tip” location was selected to be comparable to the one used by Pyo [16] in his work with the flow adapted grid arrangement. The iterative pressure Kutta condition converged in all cases to $|\Delta C_p|_{TE} \leq 10^{-3}$.

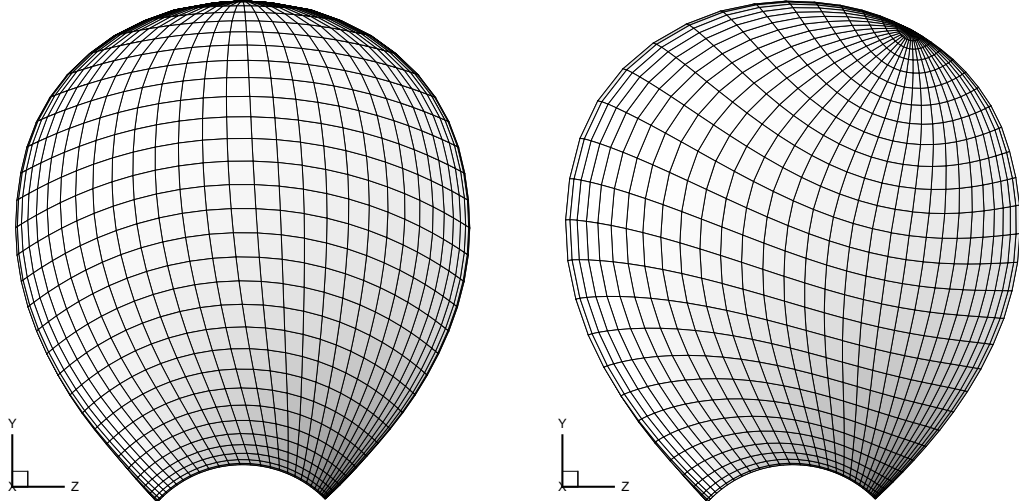


Figure 6.4: Blade back panel arrangement for the propeller P4119: conventional grid (left) and new panel arrangement with “hydrodynamic tip” (right).

Figure 6.4 shows the blade back panel arrangement with 60 chordwise and 30 spanwise panels for the conventional grid (left) and the new panel arrangement with “hydrodynamic tip” (right). For the new panel arrangement, a cosine distribution for the grid corner points is used at the boundaries. Near the propeller tip, the panels present a high aspect ratio for the conventional grid, due to the existence of a grid singularity at the tip. The maximum deviation from orthogonality is 85.3 degrees for the conventional grid and 49.8 degrees for the new panel arrangement.

Figure 6.5 presents the helicoidal wake grid with 90 streamwise and 30 chordwise panels for the conventional grid, generated using the same pitch of the propeller blade for the helicoidal lines on the wake. Figure 6.6 shows the aligned wake grid obtained with the full wake relaxation model for the conventional grid and the new panel arrangement with “hydrodynamic tip”. It can be seen that the full wake relaxation model produces a rather smooth roll-up of the vortex sheet.

6.3. Panel Arrangements With “Hydrodynamic Tip”

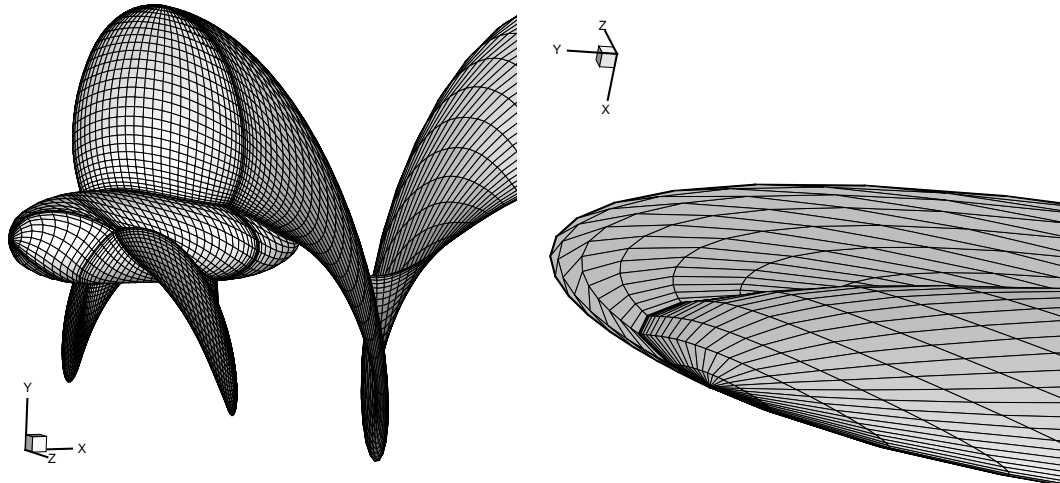


Figure 6.5: Helicoidal wake grid (left) for the propeller P4119 with a detail over the blade tip (right). Note that only one wake grid is shown.

Figure 6.7 presents the pressure distribution close to the tip at sections $r/R = 0.95$, 0.99 and 0.995 for the conventional grid (top) and for the new panel arrangement with “hydrodynamic tip” (bottom), using the rigid wake and full wake relaxation models.

From the pressure distribution obtained for the conventional grid with the rigid wake model, some oscillations and a small pressure peak at the trailing edge are observed at radial section $r/R = 0.995$. Using the full wake relaxation model, the oscillations increased significantly, due to the presence of the rolled-up wake sheet on the suction side of the blade near the tip, as we can see in Figure 6.6 (bottom-left). In this case, no pressure peak is seen at the trailing edge. Notice that section $r/R = 0.995$ is extremely close to the tip. However, at radial section $r/R = 0.99$ the oscillations are already considerably less.

For the new panel arrangement with “hydrodynamic tip”, similar pressure distributions are obtained using both wake models. The wake geometry has less influence on the pressure distribution near the blade tip, due to the more inboard position of the “hydrodynamic tip”. Pressure peaks at the trailing edge are seen at radial sections $r/R = 0.99$ and 0.995 .

From the analysis of the potential flow solution, Figure 6.8, we observe that some streamlines from the pressure side pass to the suction side flowing around the thin and sharp “leading edge” between the “hydrodynamic tip” and the geometric tip, which is located at the geometric trailing edge. Due to the shape of this “leading edge”, a pressure peak is produced since, from the theoretical point of view the pressure is singular at the sharp edge. This singularity is unavoidable for any location of the “hydrodynamic tip” on the trailing edge non-coincident with the geometric tip as, by definition, we do not allow vortex shedding outboard of the “hydrodynamic tip”.

6.3. Panel Arrangements With “Hydrodynamic Tip”

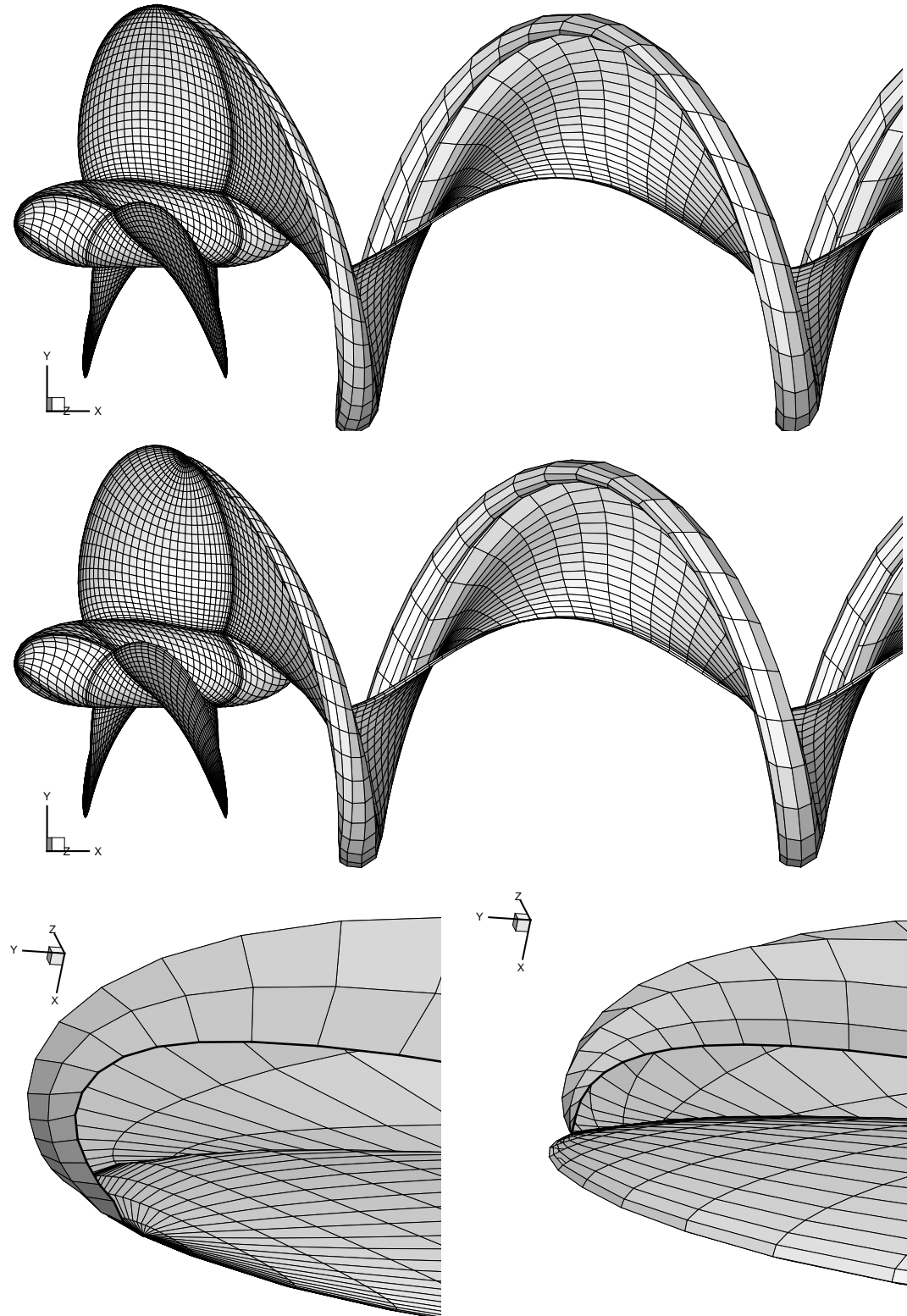


Figure 6.6: Rolled-up wake grid for the propeller P4119 obtained using the conventional grid and the new panel arrangement with “hydrodynamic tip”. Note that only one wake grid is shown.

6.3. Panel Arrangements With “Hydrodynamic Tip”

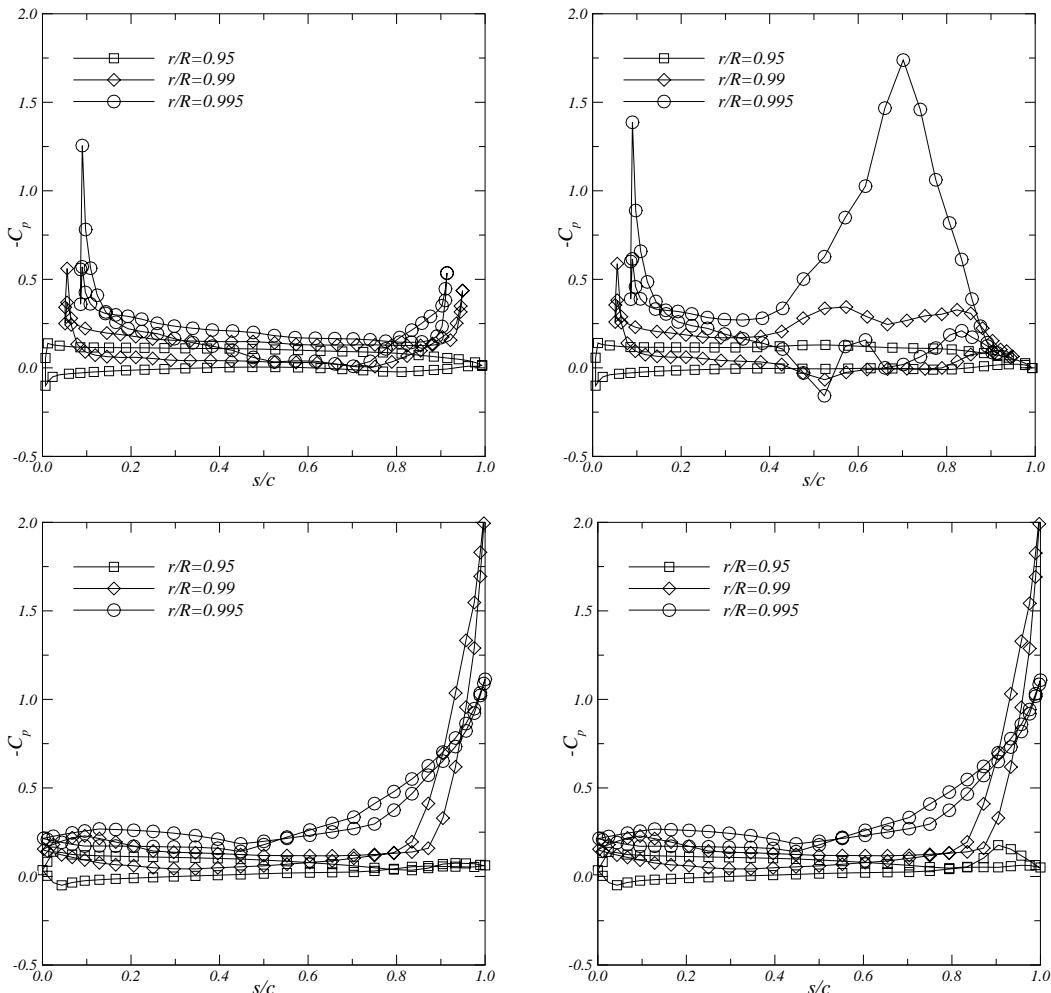


Figure 6.7: Pressure distribution on the propeller P4119 for the conventional grid using the rigid wake model (top-left) and the full wake relaxation model (top-right), and for the new panel arrangement with “hydrodynamic tip” using the rigid wake model (bottom-left) and the full wake relaxation model (bottom-right).

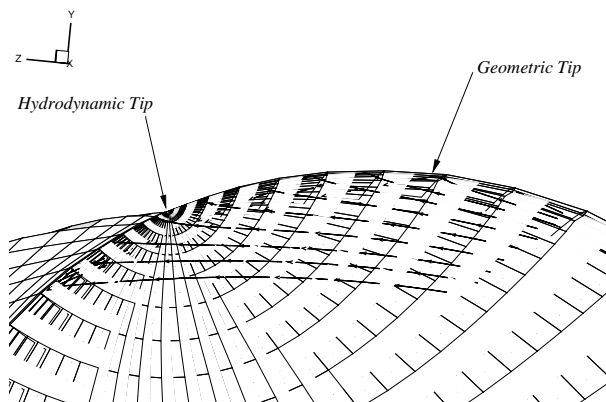


Figure 6.8: Streamlines from the pressure side around the tip region with the new panel arrangement for the propeller P4119.

6.3. Panel Arrangements With “Hydrodynamic Tip”

Calculations were carried out for the DTRC propeller P4842M at design condition $J = 0.905$ for the conventional grid and the new panel arrangement with the “hydrodynamic tip” located at $r/R = 0.973$, using the rigid wake and full wake relaxation models. The location of the “hydrodynamic tip” was selected after preliminary calculations in order to allow a smooth roll-up to occur.

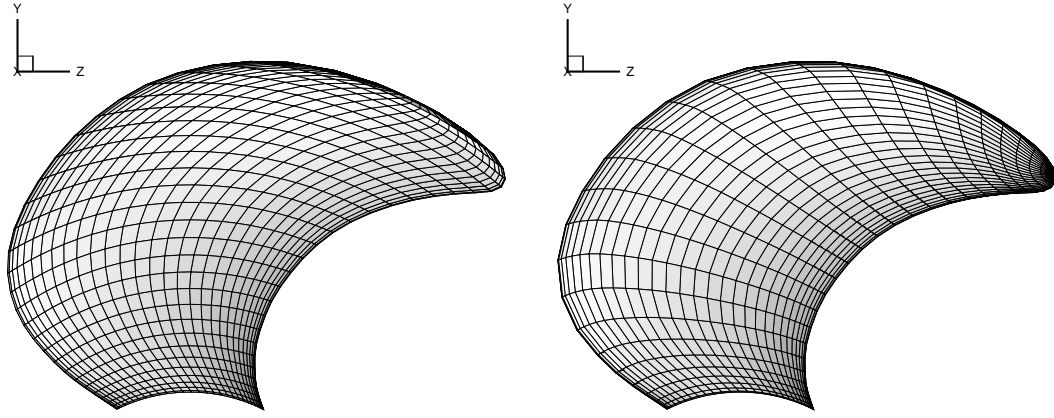


Figure 6.9: Blade back panel arrangement for propeller P4842M: conventional grid (left) and new panel arrangement with “hydrodynamic tip” (right).

Figure 6.9 shows the blade back panel arrangement with 60 chordwise and 30 spanwise panels for the conventional grid (left) and the new panel arrangement with “hydrodynamic tip” (right). The spanwise grid stretching parameters α_h and α_t of the blade grid were set equal to 2 degrees for the conventional grid, to have a larger refinement of the blade and wake geometries near the tip region for the roll-up process of the vortex sheet. For the new panel arrangement, a cosine distribution for the grid corner points was also used at the boundaries. The maximum deviation from orthogonality for the conventional grid is 84.6 degrees and for the new panel arrangement is 56.4 degrees. The wake is discretised with 90 streamwise and 30 spanwise panels.

Figure 6.10 presents the rolled-up wake grid obtained with the full wake relaxation model for the conventional grid (top) and the new panel arrangement with “hydrodynamic tip” (middle). The iterative pressure Kutta condition did not converge for the conventional grid with both wake models. Figure 6.11 presents the pressure distribution close to the tip at sections $r/R = 0.95, 0.99$ and 0.995 for the conventional grid using both wake models. Irregular oscillations and large pressure peaks are obtained close to the blade tip which explains the lack of convergence of the iterative Kutta condition.

For the new panel arrangement with “hydrodynamic tip”, the iterative pressure Kutta condition converge to $|\Delta C_p|_{TE} \leq 10^{-3}$ for both wake models. In order to avoid the problems associated with the convergence of the iterative Kutta condition in conventional grids, it was necessary to displace the “hydrodynamic tip” far from the geometric tip. In fact, preliminary calculations with the “hydrodynamic tip” located between the current position and the geometric tip showed difficulties in the convergence of the iterative pressure Kutta condition. In this case, a smoother rolled-up wake geometry is obtained.

6.3. Panel Arrangements With “Hydrodynamic Tip”

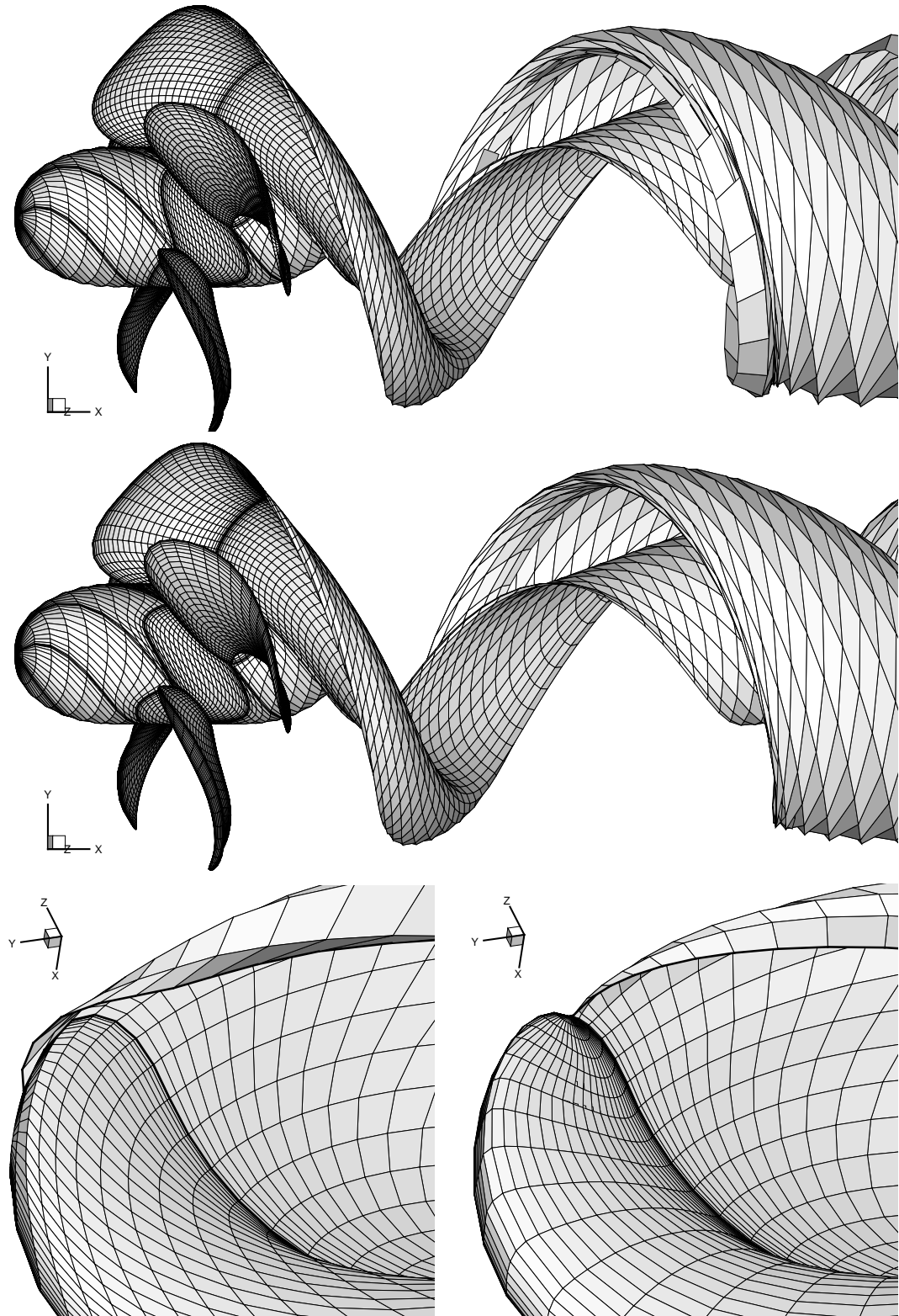


Figure 6.10: Rolled-up wake grid for the propeller P4842M obtained using the conventional grid and the new panel arrangement with “hydrodynamic tip”. Note that only one wake grid is shown.

6.3. Panel Arrangements With “Hydrodynamic Tip”

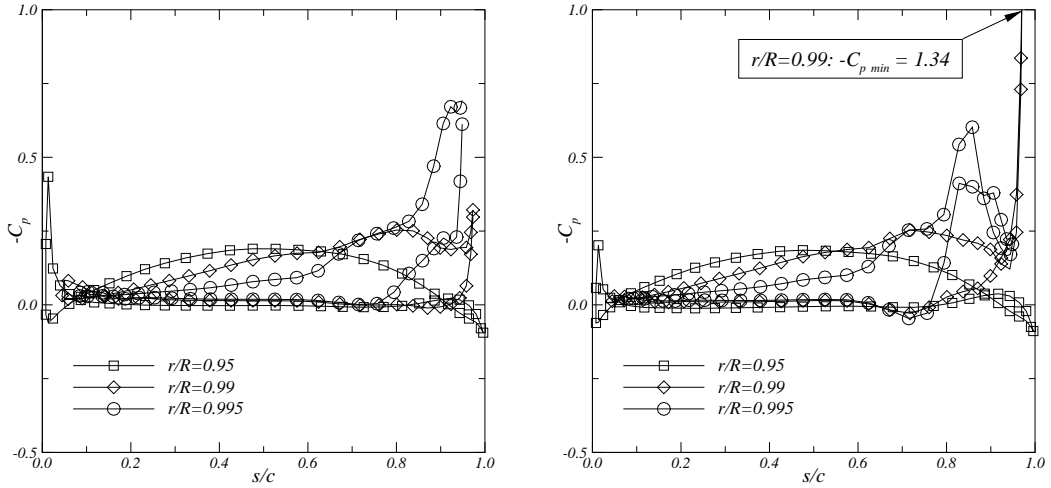


Figure 6.11: Pressure distribution on the propeller P4842M for the conventional grid using the rigid wake model (left) and the full wake relaxation model (right).

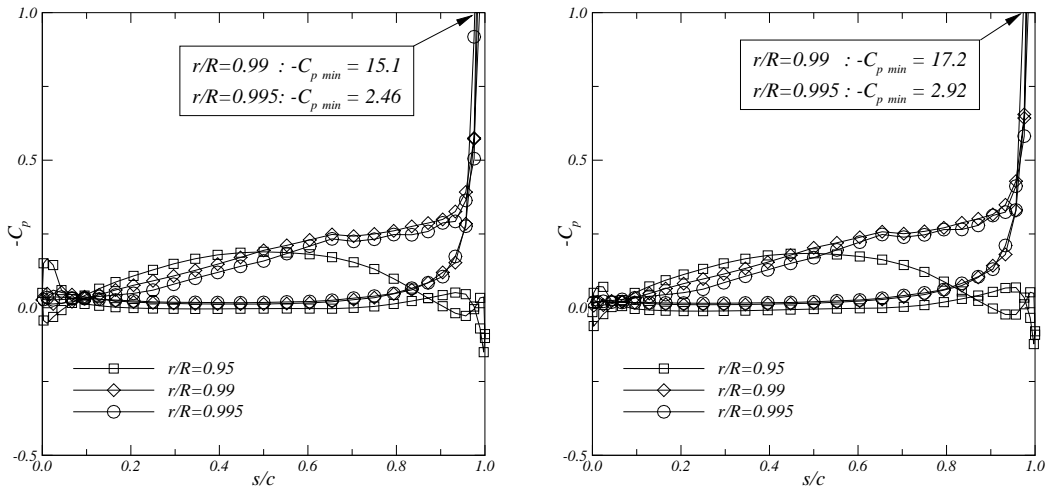


Figure 6.12: Pressure distribution on the propeller P4842M for the new panel arrangement with “hydrodynamic tip” using the rigid wake model (left) and the full wake relaxation model (right).

Figure 6.12 presents the pressure distribution close to the tip at sections $r/R = 0.95$, 0.99 and 0.995 for the new panel arrangement with “hydrodynamic tip” using both wake models. Similar pressure distributions were obtained with the rigid wake and full wake relaxation models. At section $r/R = 0.95$ the pressure distribution contains a region of negative load near the trailing edge. This pressure distribution is different from the one obtained with the conventional grid at the same radial section. At sections $r/R = 0.99$ and 0.995 there are large pressure peaks at the trailing edge. This is due to the fact that the flow passes from the pressure side to the suction side and crosses the thinner and sharp “leading edge” located in the geometric trailing edge of the propeller blade.

6.4 Sensitivity to Blade Tip Geometry

In this section, the effect of blade tip geometry on the potential flow solution is studied. Calculations were performed for the DTRC P4119 at design condition $J = 0.833$ using the 80×40 conventional grid. A rigid wake model with linear Kutta condition is used. The wake is discretised with 120 streamwise and 40 spanwise panels. The pitch of the helicoidal lines of the wake grid is equal to the blade pitch. Contraction of the helicoidal lines is not considered.

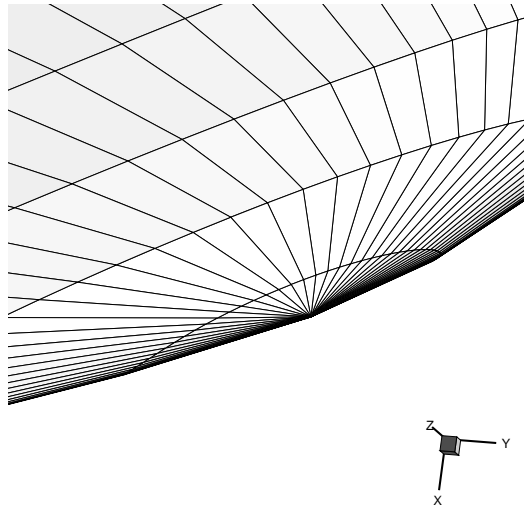


Figure 6.13: Blade grid at the tip. Conventional grid. Propeller DTRC P4119.

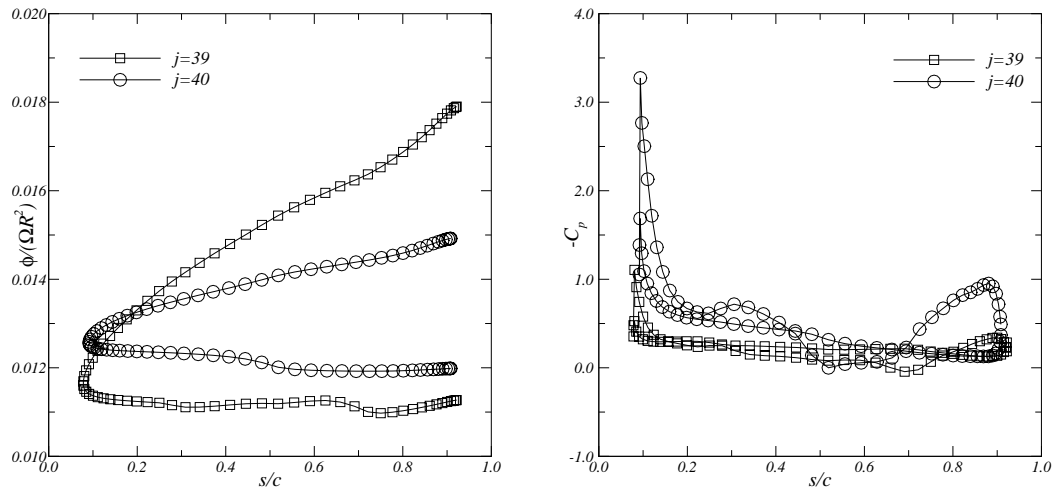


Figure 6.14: Perturbation potential (left) and pressure coefficient (right) at panel strips $j = 39$ and $j = 40$. Conventional grid.

Figure 6.13 depicts the tip geometry and the conventional panelling for the DTRC propeller P4119. Since the propeller has zero chord at the tip, a strip of triangular panels is used to close the tip. The maximum deviation from orthogonality of the blade grid is 86.0 degrees

and occurs at the last panel strip ($j = 40$) on the trailing edge. Figure 6.14 presents the perturbation potential and the pressure distribution at the most outboard panel strips, $j = 39$ and $j = 40$. The results show the existence of oscillations in the potential flow solution.

Next, different tip geometries are tested by cutting the blade at several radial positions near the tip. The tip cuts were made at the radial positions $r/R = 0.9988$, 0.9978 and 0.9970 . The tip was closed with an additional strip of panels. The maximum deviation from orthogonality is 85.2 degrees for the tip cut at $r/R = 0.9988$ and 83.2 degrees for the tip cut at $r/R = 0.9970$, and occurs at the last panel strip. The chord length increases from $c/D = 0.03$ at section $r/R = 0.9988$ to $c/D = 0.066$ at section $r/R = 0.9970$. Figure 6.15 shows the blade tip geometry for the tip cuts $r/R = 0.9988$ and $r/R = 0.9978$. Notice that the radial sections are extremely close to the tip.

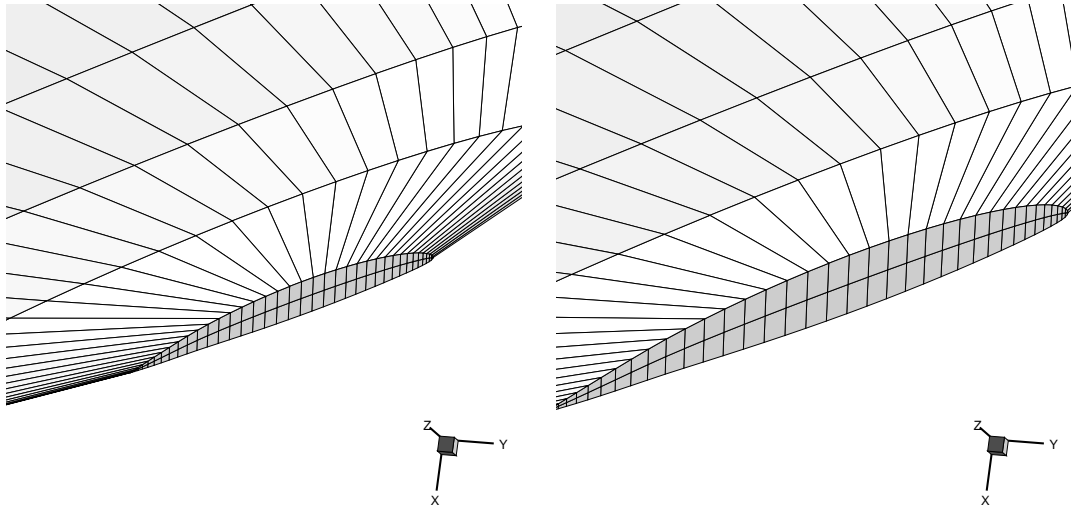


Figure 6.15: Blade grid at the tip. Tip cuts at $r/R = 0.9988$ (left) and $r/R = 0.9978$ (right). Propeller DTRC P4119.

Figure 6.16 presents the perturbation potential and the pressure distribution at the panel strips $j = 39$ and $j = 40$ for the three tip cuts. Results show the existence of oscillations in both quantities. However, by cutting the tip at more inboard positions the oscillations decrease. The suction peak presented in the last panel strip also decreases.

An alternative to the blade tip cut, is the application of a finite chord at the tip. A similar modification of the blade tip geometry was applied by Vaz [14]. Figure 6.17 presents the blade tip geometry considering a tip chord of $c/D = 0.07$ with zero and extrapolated thickness, together with the perturbation potential and pressure distribution at the panel strips $j = 39$ and $j = 40$. The maximum deviation from orthogonality is 80.3 degrees. From the comparison with the results of zero chord at tip, Figure 6.14, we observe a significantly reduction of the oscillations for both quantities. The use of a finite chord at the tip displaces the position of the tip vortex. In this sense, an improvement on the convergence of the iterative pressure Kutta condition is expected.

6.4. Sensitivity to Blade Tip Geometry

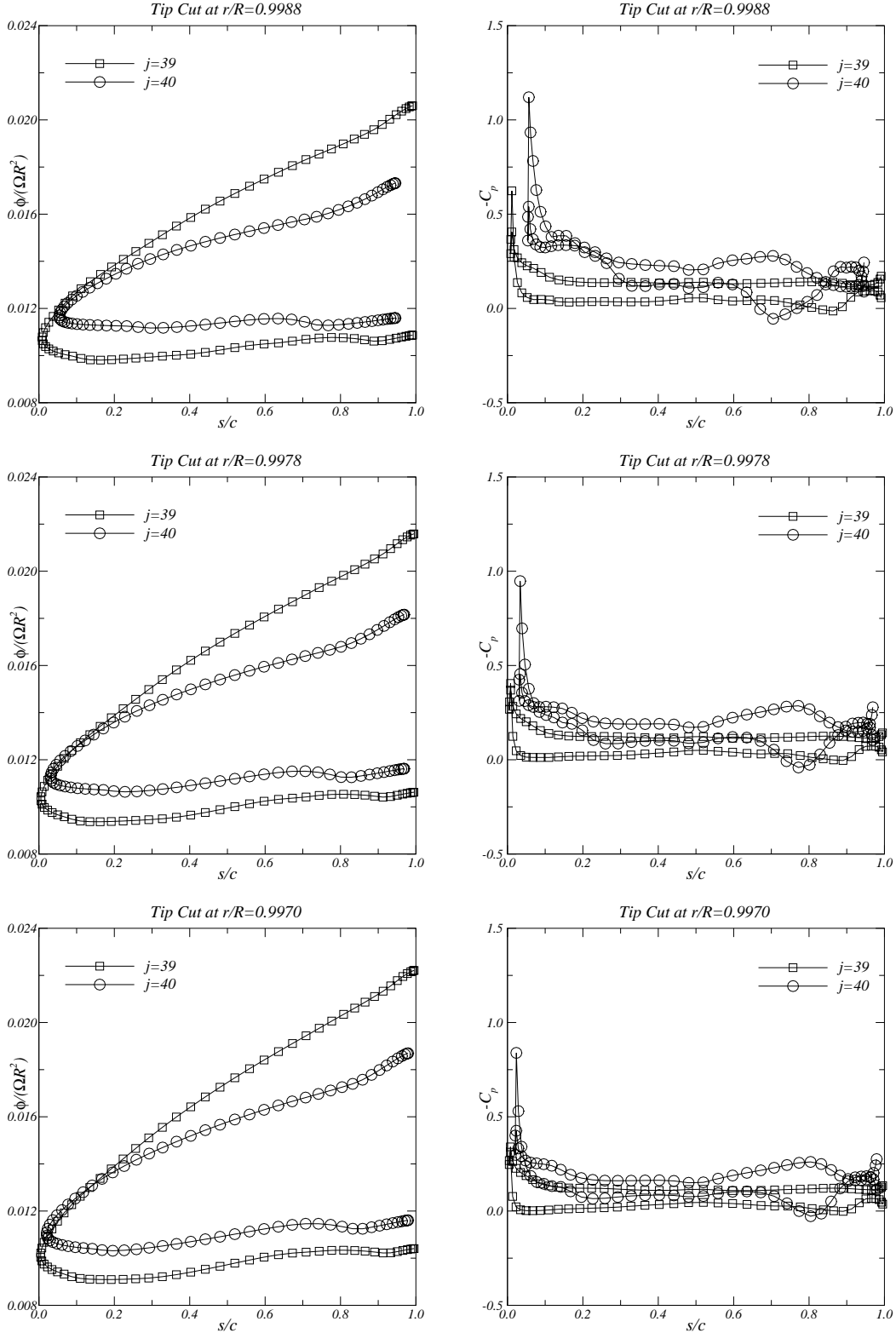


Figure 6.16: Perturbation potential (left) and pressure coefficient (right) at panel strips $j = 39$ and $j = 40$. Comparison between different tip geometries.

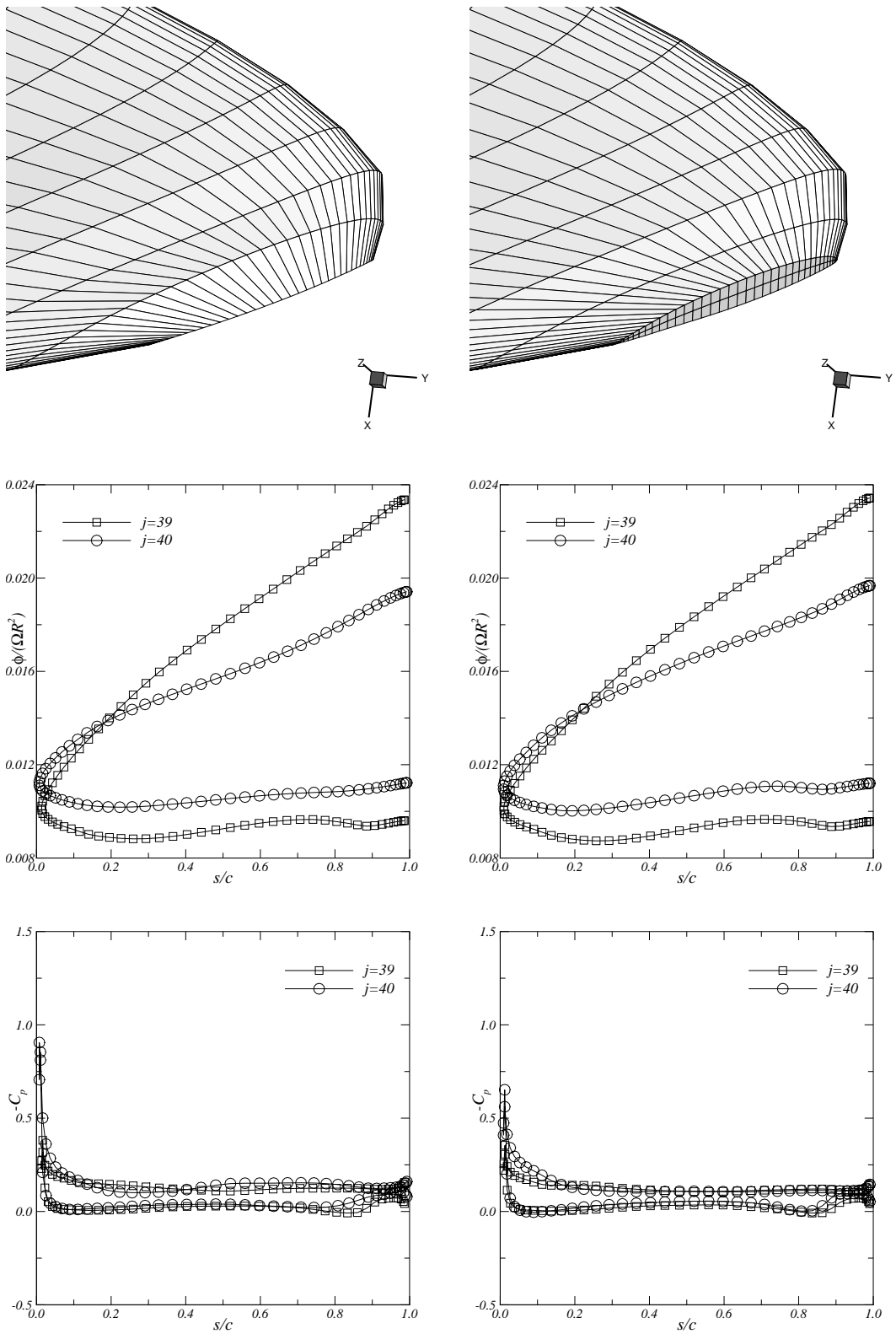


Figure 6.17: Perturbation potential and pressure coefficient at panel strips $j = 39$ and $j = 40$. Finite chord at tip.

6.5 Discussion of the Results

The performance of BEM, applied for the numerical modelling of wing and propeller tip flows, has been addressed. From previous calculations, the rigid wake model with a conventional panel arrangement has been found to be incompatible with the application of a pressure Kutta condition at the trailing edge near the tip. In this Chapter, the importance of the wake geometry together with the location of the tip vortex and the blade tip geometry and its panelling is analysed.

First, results of an evaluation of wake relaxation models for potential flow calculations about elliptical wings are presented. Three types of wake relaxation models were considered: rigid wake model, partial wake relaxation model and full wake relaxation model with roll-up. It is seen that the wake geometry is essential to avoid the pressure peaks at the trailing edge when applying the pressure Kutta condition. The use of a rolled-up wake eliminates the pressure peak at the trailing edge near the tip.

Second, results of BEM calculations for a new panel arrangement with “hydrodynamic tip” are presented and compared with the conventional arrangement for the propellers DTRC P4119 and DTRC P4842M. A rigid wake model and a full wake relaxation model with roll-up are considered. The results show that the use of the new panel arrangement reduces the pressure oscillations inboard of the “hydrodynamic tip”. At the edge, outboard of the “hydrodynamic tip”, a pressure peak occurs associated with the flow around the sharp edge from the pressure to the suction side of the blade.

The use of the present full wake relaxation model with roll-up in combination with the conventional panel arrangement introduces a region of negative load near the tip due to the proximity of the tip vortex from the blade suction surface. In addition, an irregular pressure distribution is seen. This suggests that the detailed modelling of the roll-up in the tip vortex may be required to obtain a smooth pressure distribution near the tip. With the “hydrodynamic tip” grids the rolled-up wake at the tip leaves the blade smoothly. In these cases, the effect of wake roll-up on the pressure distribution near the tip is smaller. On the other hand, the adoption of a “hydrodynamic tip” suffers from a modelling deficiency on the sharp edge of the trailing edge between the “hydrodynamic tip” and the geometric tip. It is unlikely that vortex shedding will not take place from that edge.

Finally, the effect of blade tip geometry on the behaviour of the potential flow solution at the tip is studied. Two modifications to the tip geometry of propeller DTRC P4119 are made: blade cut at several radial positions near the propeller tip and the application of finite chord at the tip. Calculations were carried out for the conventional panel arrangement using a linear Kutta condition. An oscillatory behaviour of the potential flow solution near the tip with the original blade geometry is observed. This result strongly suggests that the oscillations are related to the ill-conditioning of the grid due to the highly skewed panels when approaching the tip. However, by modifying the blade tip geometry, which reduces the panel skewness, the oscillations decrease.

Chapter 7

Vortex Sheet Separation Modelling

7.1 Introduction

When wings or propeller blades with swept leading edges are operated at a high angle of attack, the flow may separate from the leading edge forming a free shear layer. This free layer often rolls up just behind the leading edge to form a vortex sheet which passes over the lifting surface. Although viscosity is responsible for the formation of the free shear layer, potential flow methods can be used to model the vortex sheet separation.

For delta wings the problem is of the utmost importance due to the effect of the leading edge vortex on the lift characteristics of the wing. Hoeijmakers [26] developed a second-order panel method for the three-dimensional potential flow about thin delta-like wings with leading edge vortex sheet separation. The vortex core formed from the free shear layer is replaced by a discrete vortex filament, connected with the remainder vortex sheet by a feeding-sheet. The leading edge and trailing edge wake geometries are determined to have zero-pressure-jump on the vortex sheet.

This phenomenon also influences significantly the hydrodynamic characteristics of marine propellers. Greeley and Kerwin [25] introduced a leading edge vortex sheet model for marine propellers using a numerical lifting surface method. Horseshoe vortices are included along the leading edge for which flow separation is predicted to occur. The position of the horseshoe vortices are specified. A correlation between the upwash velocity at the leading edge control points and the leading edge suction force is considered and used to determine the leading edge horseshoe strengths.

In ducted propellers, a leakage vortex sheet is shed from the blade tip due to the strong gap flow induced by the pressure difference between both sides of the blade. This leakage vortex changes significantly the blade loading. Gu [27] proposed a tip leakage vortex method to model the flow through the gap between the blade tip and the duct inner surface in the case of a ducted propeller. The tip leakage vortex model is composed of horseshoe vortices placed along the blade tip. At some distance downstream from the blade, these vortices end up in a concentrated vortex. A wake alignment model is used to predict the position of the tip vortex sheet.

7.2. Leading Edge Vortex Flow About Delta Wings

In order to model the leading edge vortex separation properly with BEM it is first necessary to know where the separation occurs on the blade. In the case of a wing with sharp leading edge the problem would be relatively simple: separation would occur all along the leading edge and the Kutta condition could be imposed directly in order to determine the amount of vorticity shed into the flow from the leading edge. However, propeller blades usually have round leading edges, and in this case it is not possible to know previously where the leading edge flow separation occurs and also the amount of vorticity shed. A second problem is related to the difficulty in performing full roll-up calculation for wakes in close vicinity of the propeller blade. Therefore in a first approach to the problem, an empirical specification of the vortex sheet geometry would be acceptable.

To prepare the ground for attacking the problem to propeller blades, the leading edge flow separation modelling with BEM is first considered for delta-like wings. It is assumed that both the leading and trailing edges of the wing are sharp. Therefore, we consider that the flow separates along the entire length of the leading and trailing edges. An empirical specification of the vortex sheet geometry is considered. Results of a 76 degrees swept delta wing at incidences that ranged from 10 to 40 degrees are presented. Second, the leading edge vortex separation modelling for marine propellers is addressed. A specified leading edge vortex wake geometry with linear Kutta condition is used. Calculations are presented for the DTNSRDC propeller P4498 operating at 90% of the design advance coefficient. The leading edge vortex separation position was predicted from model scale experiments. Finally, the gap flow between the blade tip and the duct inner surface is considered. A tip leakage model with a vortex sheet shed along the chord of the blade tip is investigated. The tip leakage vortex sheet model is applied for propeller K_a 4-70 inside duct 19A.

7.2 Leading Edge Vortex Flow About Delta Wings

7.2.1 Numerical Method

Let us consider a delta wing of span $2S$ and maximum chord C_0 advancing with constant axial speed U_∞ in an incompressible fluid. In this type of flow at high angle of attack the flow separates at the leading edge, resulting in a free shear layer emanating from the leading edge. This free shear layer rolls up in a spiral fashion to form a relatively compact core with distributed vorticity.

In terms of the inviscid flow model, this shear layer can be represented by a highly rolled-up vortex sheet of infinite length. At the edge of this vortex sheet the dipole distribution is zero. Since it is quite impossible to discretise a vortex sheet of infinite length the tightly rolled-up part of the vortex sheet is replaced by a discrete vortex filament, connected to the remainder vortex sheet by a feeding-sheet. The latter enables vorticity to be transported from the outer vortex sheet to the vortex filament and vice versa which consequently changes its strength. The vortex, if of the correct strength and if positioned at the correct location, will provide the proper flow field away from the vortex filament but not near the centre of the vortex core where the velocity will be singular in the mathematical model.

The potential flow model with leading edge vortex sheet separation is presented in Figure 7.1. The geometry consists of the delta wing S_B , the leading edge vortex sheet \mathcal{S}_{LW} with a vortex filament/feeding-sheet vortex core model, the trailing edge vortex sheet \mathcal{S}_{TW} and the far wake vortex sheet \mathcal{S}_{FW} . The far wake is composed by horseshoe vortices which forms the continuation to downstream infinity of the leading edge and trailing edge wakes.

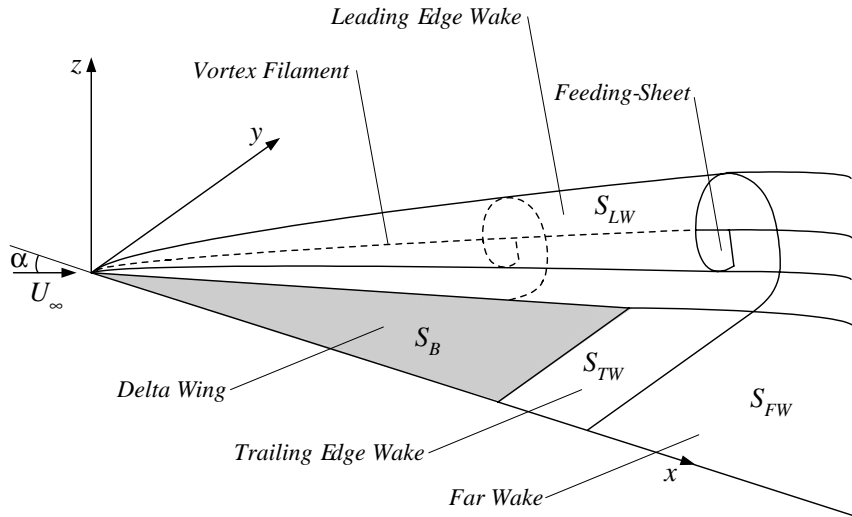


Figure 7.1: Potential flow model with leading edge vortex sheet separation.

In the present study, we will consider a partial wake relation model in which the condition of pressure equality is applied at the control points of the leading edge wake and trailing edge wake:

$$\Delta p = -\rho (\vec{V}_m \cdot \Delta \vec{V}) = 0 \text{ on } \mathcal{S}_{LW} \text{ and } \mathcal{S}_{TW}. \quad (7.1)$$

The velocity discontinuity is calculated by numerical surface differentiation of the potential-jump on the wake surface:

$$\Delta \vec{V} = \nabla_S (\Delta \phi). \quad (7.2)$$

However, the use of a central second-order scheme results in a stability problem and a biased scheme must be implemented, Hoeijmakers [26]. In the present study, a second-order backward differentiation scheme is applied. The coupling between the solution on the leading edge wake and trailing edge wake with the solution on the delta wing is made by the differentiation scheme. Therefore, on the boundaries of the wake surfaces the potential-jump is calculated by the potential difference between the upper side and the lower side of the delta wing.

The function of the feeding-sheet is only to transport the vorticity from the leading edge wake to the vortex filament. In this sense, we consider that the dipole strength on the feeding-sheet is equal to the dipole strength of the leading edge wake panel adjacent to the feeding-sheet.

7.2.1. Numerical Method

For the geometrical description of the delta wing, we introduce the following parametric coordinates,

$$\begin{aligned} s &= \frac{x}{C_0} \\ t &= \frac{y}{x} \frac{C_0}{S}, \end{aligned} \quad (7.3)$$

with $0 \leq s \leq 1$ and $0 \leq t \leq 1$. The delta wing surface \mathcal{S}_B is discretised by lines of constant spanwise coordinate $t = \text{const.}$ and lines of constant chordwise coordinate $s = \text{const.}$. To generate the grid of corner points we use an equidistant stretching function to distribute the points along the two parametric coordinates. This grid topology presents a singular point at the wing apex. The delta wing is discretised with $N_{CP} = 2 \times N_R$ chordwise and N_R spanwise panels.

The trailing edge wake \mathcal{S}_{TW} is discretised in the spanwise direction into N_R panel strips, which extend downstream from the trailing edge of the corresponding panel strips on the delta wing. Each strip is discretised with N_{TW} panels in the streamwise direction. A plane wake geometry along the bisector of the trailing edge, $z = 0$, is considered. The corner points of the trailing edge wake grid are distributed equidistantly along the streamwise direction.

The leading edge wake geometry \mathcal{S}_{LW} is specified based on similar results obtained with the method of Hoeijmakers [26]. The leading edge wake geometry has a conical appearance starting from the apex to the trailing edge. Downstream of the wing trailing edge, the leading edge wake geometry is kept constant along the streamwise direction. The leading edge wake grid is constructed with a spiral geometry and is sketched in Figure 7.2.

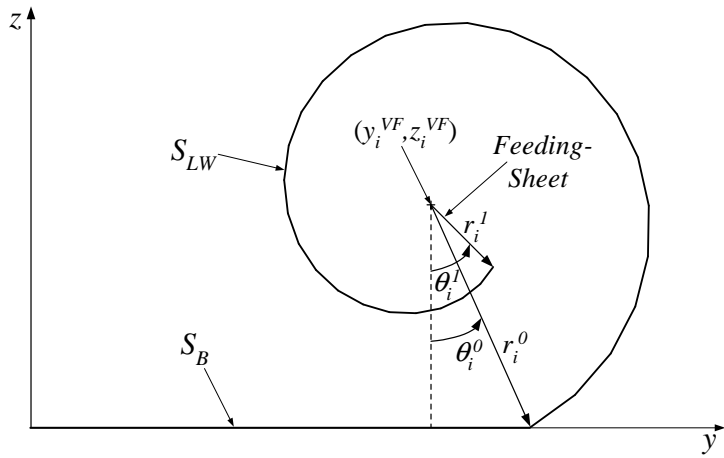


Figure 7.2: Leading edge wake geometric parameters.

The leading edge wake is discretised in the spanwise direction into N_{LR} panel strips, which extend along the spanwise direction from the leading edge of the delta wing and from the last panel strip of the trailing edge wake. Each strip is discretised with N_{LW} panels in

the streamwise direction. Note $N_{LW} = N_C + N_{TW}$. The coordinates of the panel corner points in the conical region are given by

$$\begin{aligned} x_{ij}^{LW} &= x_{i,N_R}^B \\ y_{ij}^{LW} &= y_i^{VF} + r_{ij} \sin \theta_{ij} \\ z_{ij}^{LW} &= z_i^{VF} + r_{ij} \cos \theta_{ij} \\ i &= 0, 1, \dots, N_C, j = 0, 1, \dots, N_{LR} - 1 \end{aligned} \quad . \quad (7.4)$$

x_{i,N_R}^B is the axial coordinate of the wing corner points at the leading edge and N_R and N_C are on each side of the delta wing, respectively, the number of spanwise and chordwise panels. (y_i^{VF}, z_i^{VF}) are the Cartesian coordinates of the vortex filament, which vary linearly from the apex to the trailing edge

$$\begin{aligned} y_i^{VF} &= \frac{y_0^{VF}}{C_0} x_{i1}^{LW} \\ z_i^{VF} &= \frac{z_0^{VF}}{C_0} x_{i1}^{LW} \end{aligned} \quad , \quad (7.5)$$

where (y_0^{VF}, z_0^{VF}) are the coordinates of the vortex filament at the trailing edge of the delta wing. The variables r_{ij} and θ_{ij} are given by

$$\begin{aligned} r_{ij} &= \frac{r_i^0(N_{LR} - j) + r_i^1 j}{N_{LR}} \\ \theta_{ij} &= \frac{\theta_i^0(N_{LR} - j) + (2\pi + \theta_i^1) j}{N_{LR}} \end{aligned} \quad (7.6)$$

where θ_i^0 and r_i^0 refer to the beginning of the spiral and are equal to

$$\begin{aligned} \theta_i^0 &= \tan^{-1} \left(\frac{y_{i,N_R+1}^B - y_i^{VF}}{z_i^{VF}} \right) \\ r_i^0 &= \frac{z_i^{VF}}{\cos \theta_i^0} \end{aligned} \quad . \quad (7.7)$$

The parameters θ_i^1 and r_i^1 refer to the end of the spiral and are specified. The last strip $j = N_{LR}$ corresponds to the vortex filament and the coordinates are given by Equation (7.5).

Based on the numerical results of Hoeijmakers [26], the leading edge wake geometry can be specified empirically. In the present work, the position of the vortex filament for the 76 degrees swept delta wing is expressed as a function of the angle of attack:

$$\begin{aligned} y_0^{VF}/S &= \begin{cases} -0.0014\alpha + 0.778, & 10^\circ \leq \alpha < 20^\circ \\ 0.75, & 20^\circ \leq \alpha \leq 40^\circ \end{cases} \\ z_0^{VF}/S &= \begin{cases} 0.0185\alpha + 0.008, & 10^\circ \leq \alpha < 20^\circ \\ 0.01065\alpha + 0.165, & 20^\circ \leq \alpha \leq 40^\circ \end{cases} \end{aligned} \quad . \quad (7.8)$$

7.2.2. 76 Degrees Swept Delta Wing at 20 Degrees Incidence

The parameter r_i^1 at the end of the leading edge wake spiral, also varies linearly from the apex to the trailing edge:

$$r_i^1 = \frac{r_0^1}{C_0} x_{i1}^{LW}. \quad (7.9)$$

At the trailing edge, the parameter r_0^1 is chosen to approximate the wake geometry obtained from the calculations of Hoeijmakers [26]. Therefore, the parameter r_0^1 is approximated by a polynomial expression as

$$r_0^1/S = -0.00022\alpha^2 + 0.01855\alpha - 0.01429, \quad 10 \leq \alpha \leq 40. \quad (7.10)$$

Finally, the parameter θ_i^1 is defined by:

$$\theta_i^1 = \theta_i^0 + \frac{\pi}{6}, \quad (7.11)$$

corresponding to a maximum roll-up allowed for the vortex sheet.

7.2.2 76 Degrees Swept Delta Wing at 20 Degrees Incidence

The numerical results for a delta wing with a sweep angle of 76 degrees and an ogival section composed of two circular arcs with 0.1% maximum thickness at 20 degrees incidence are presented. The calculations are compared with the numerical results of Hoeijmakers [26] performed for thin pointed delta wings with a lifting surface method without thickness effects. The partial wake relaxation model converged to a precision of $|\Delta C_p| \leq 10^{-3}$.

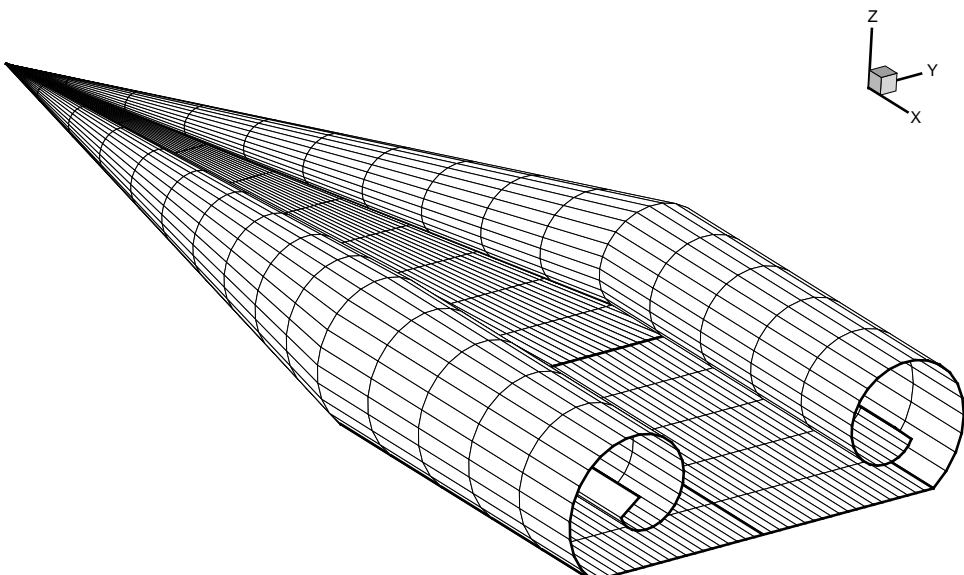


Figure 7.3: Blade and wake panel arrangement.

7.2.2. 76 Degrees Swept Delta Wing at 20 Degrees Incidence

Figure 7.3 shows the panel arrangement for the complete delta wing, leading edge wake and trailing edge wake. The delta wing is discretised using 20 panels along the chordwise direction and 20 panels along the spanwise direction. The leading edge wake is discretised with 15 panels along the streamwise direction and with 30 panels along the spanwise direction. The trailing edge wake is discretised with 5 panels along the streamwise direction and 20 panels along the spanwise direction, which corresponds to an axial length of $x_W/S = 2$.

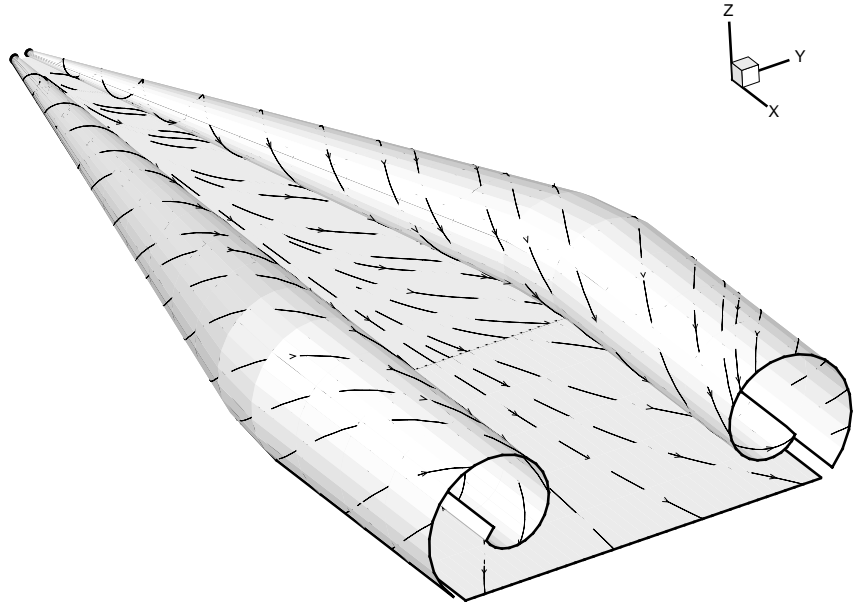


Figure 7.4: Streamlines of the potential flow solution for the 76 degrees delta wing at 20 degrees incidence.

The streamlines of the potential flow solution are depicted in Figure 7.4. Figure 7.5 shows an overview of the perturbation potential and pressure distribution on the delta wing. The contour lines of the perturbation potential on the wing suction side, which coincide with vortex lines, leave the wing almost perpendicular to the leading edge. Whence on the leading edge vortex sheet the vortex lines align with the mean velocity. The low pressure region on the wing suction side is due to the presence of the vortex filament. On the pressure side of the wing, the pressure coefficient decreases from the apex to the trailing edge.

Figure 7.6 presents the potential-jump on the panel strips along the spanwise direction. The potential-jump strength increases along the streamwise direction from the apex to the trailing edge. At the trailing edge the potential-jump distribution reaches its maximum. Then, in the near wake the potential-jump decreases from the trailing edge to the far wake. From the values of the potential-jump strength at the vortex filament, we observe that the circulation increases along the streamwise direction. This is consistent with the physical phenomenon, that the strength of the vortex core continuously grows along the downstream direction. Figure 7.7 shows the wing pressure coefficient along the span at

7.2.2. 76 Degrees Swept Delta Wing at 20 Degrees Incidence

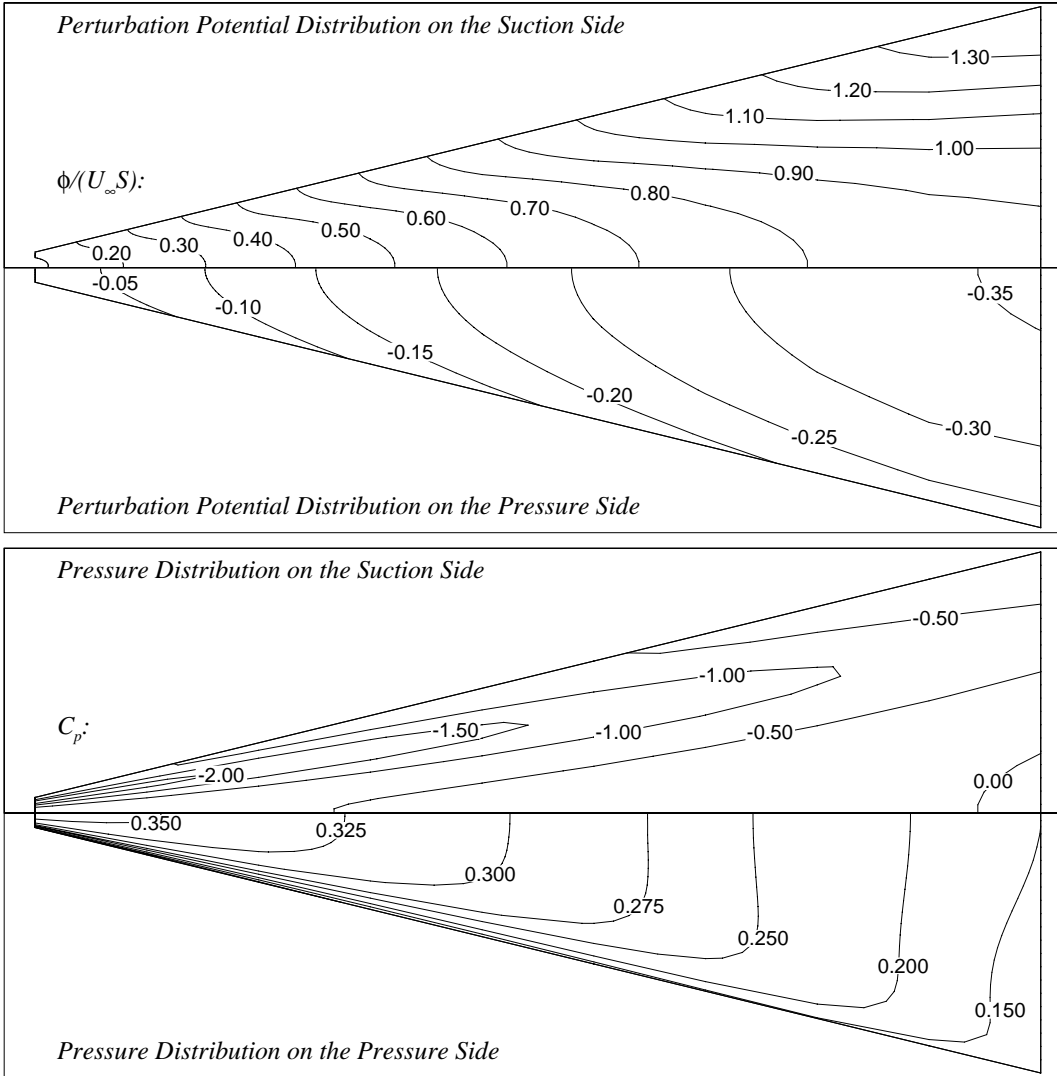


Figure 7.5: Potential flow solution over the 76 degrees delta wing at 20 degrees incidence. Perturbation potential (top) and pressure coefficient (bottom) on the suction and pressure sides.

different cross-flow planes. For the pressure coefficient, the distribution on the suction side increases along the streamwise direction from the apex to the trailing edge.

Figure 7.8 shows the comparison of the leading edge wake geometries used in the two methods. Differences are observed between the two wake geometries, which increase as we move from the trailing edge to the apex of the wing, as expected from the present empirical construction of the wake geometry. In Figures 7.9 and 7.10 the pressure distribution computed with the present method is compared with the results of Hoeijmakers [26]. A reasonable agreement is seen for the pressure distribution obtained with the present method and the numerical results of Hoeijmakers [26]. Similar locations of the suction peak at each cross-flow plane are obtained.

7.2.2. 76 Degrees Swept Delta Wing at 20 Degrees Incidence

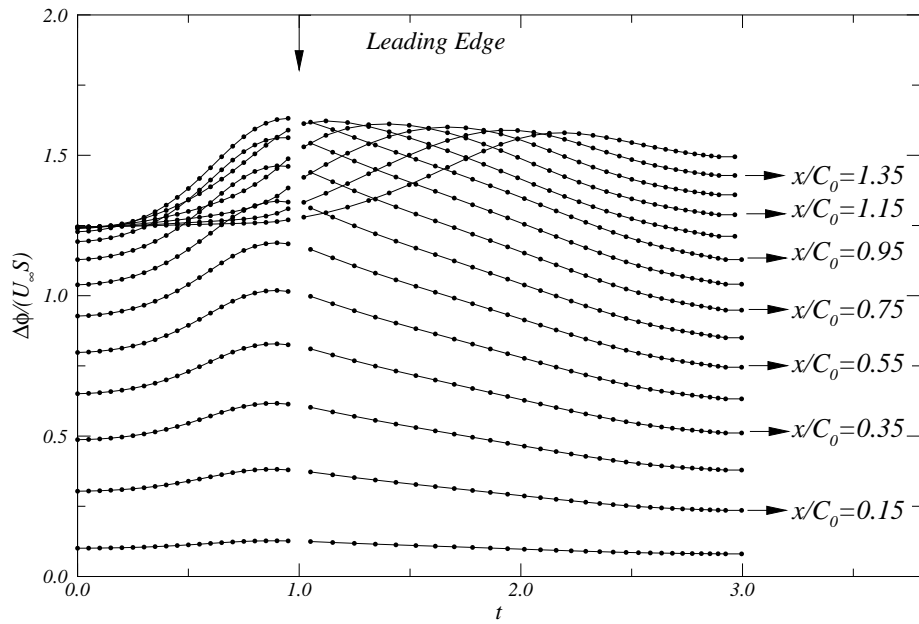


Figure 7.6: Potential-jump distribution along cross-flow planes. 76 degrees delta wing at 20 degrees incidence.

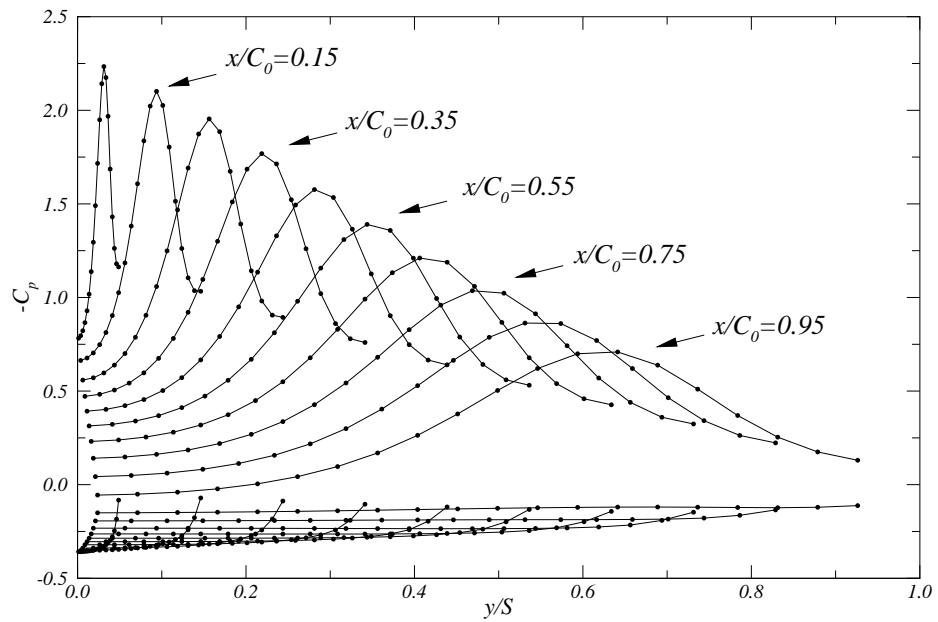


Figure 7.7: Pressure distribution along cross-flow planes. 76 degrees delta wing at 20 degrees incidence.

7.2.2. 76 Degrees Swept Delta Wing at 20 Degrees Incidence

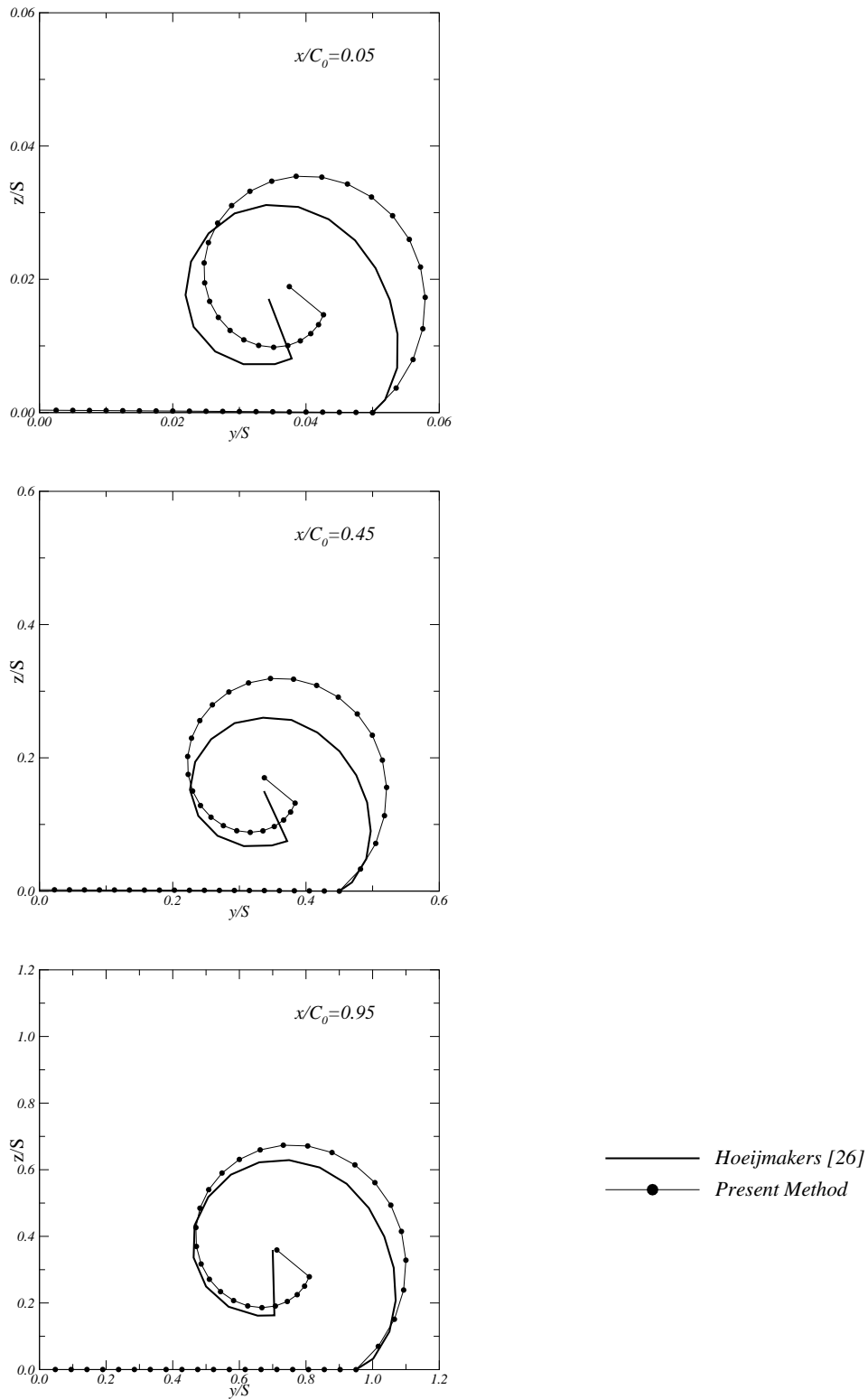


Figure 7.8: Leading edge wake geometry in cross-flow planes. Comparison with Hoeijmakers [26]. 76 degrees delta wing at 20 degrees incidence.

7.2.2. 76 Degrees Swept Delta Wing at 20 Degrees Incidence

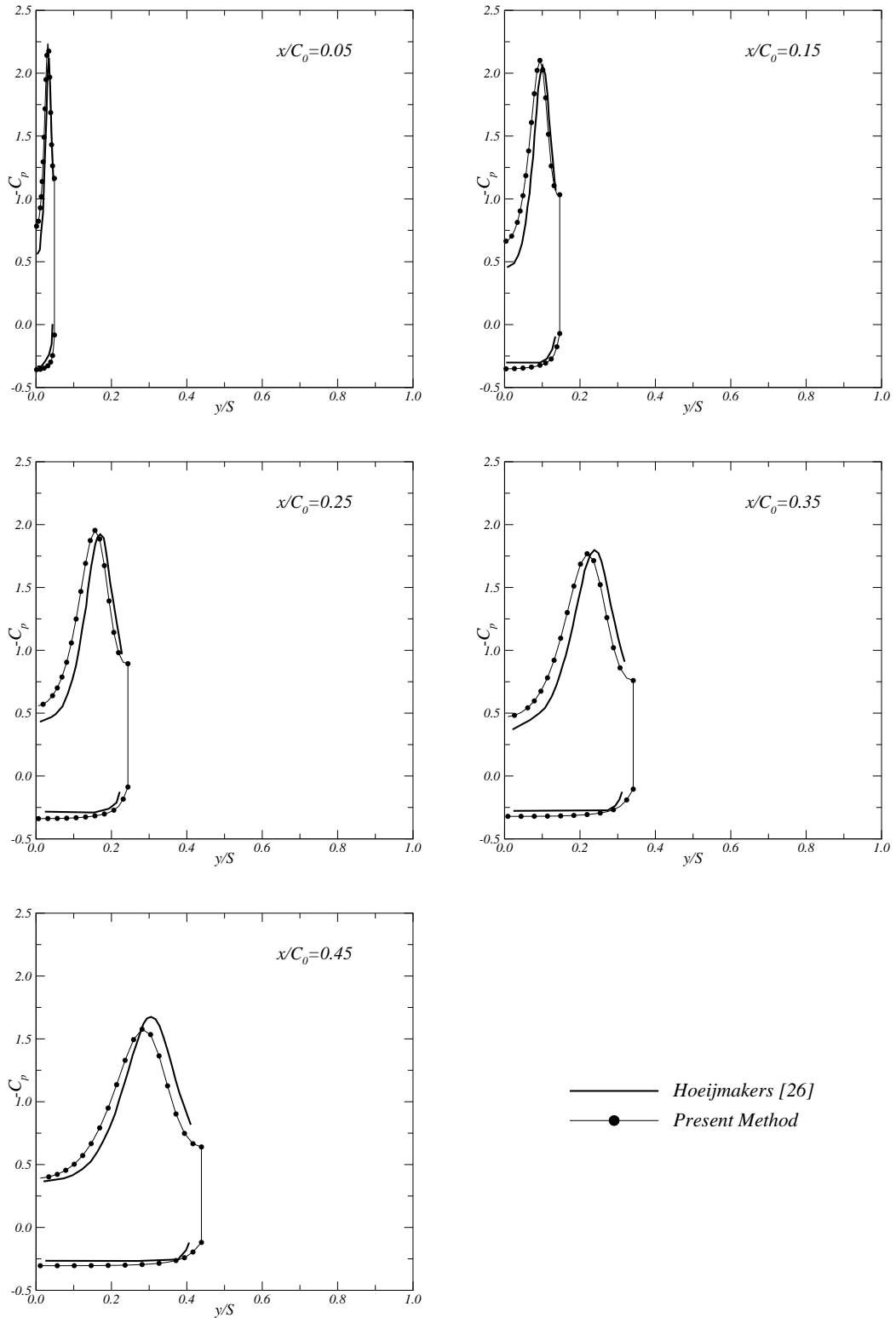


Figure 7.9: Pressure distribution along cross-flow planes. Comparison with Hoeijmakers [26]. 76 degrees delta wing at 20 degrees incidence.

7.2.2. 76 Degrees Swept Delta Wing at 20 Degrees Incidence

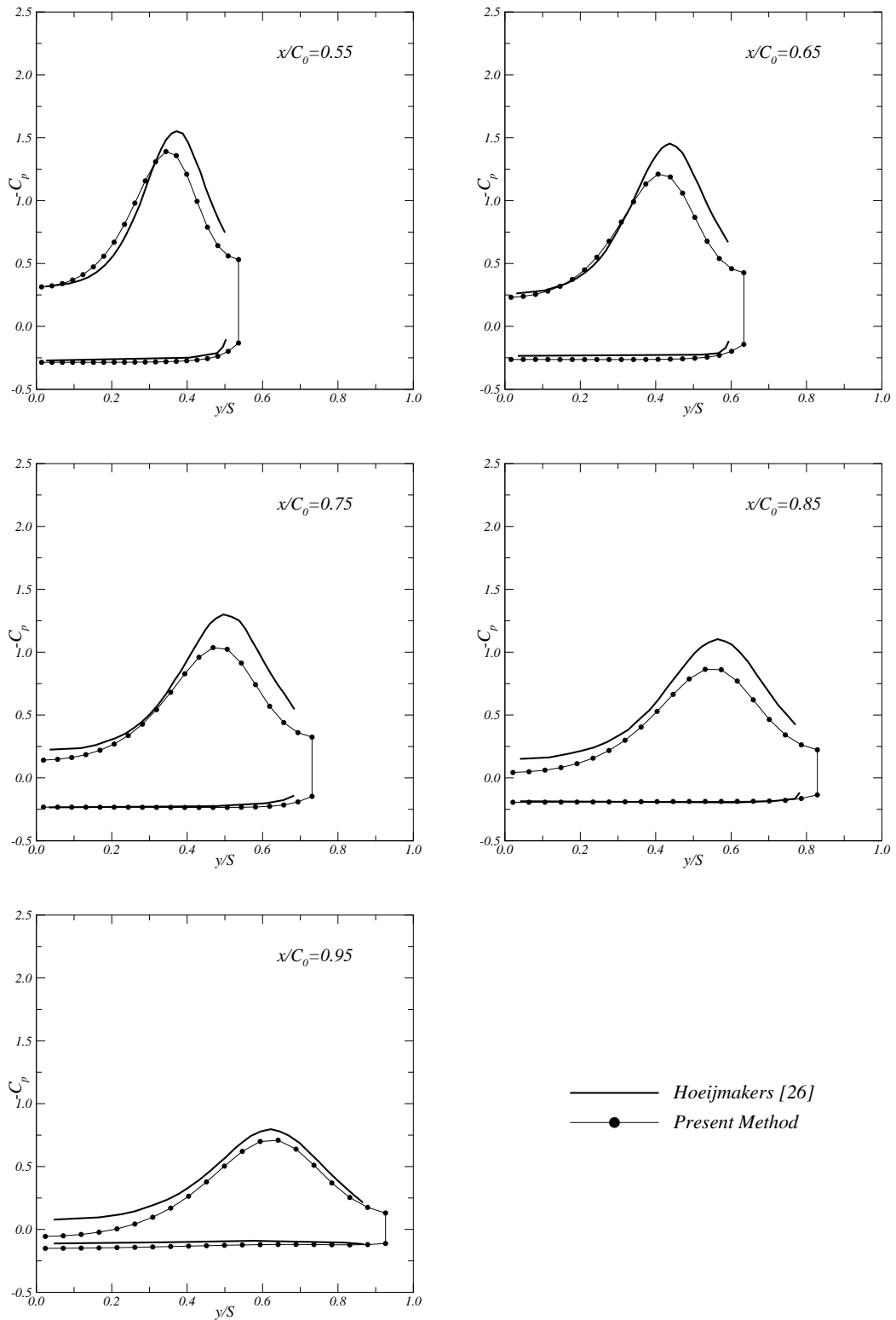


Figure 7.10: Pressure distribution along cross-flow planes. Comparison with Hoeijmakers [26]. 76 degrees delta wing at 20 degrees incidence.

7.2.3. Solution for the 76 Degrees Swept Delta Wing for Different Angles of Attack

7.2.3 Solution for the 76 Degrees Swept Delta Wing for Different Angles of Attack

Calculations of the 76 degrees swept delta wing at incidences that ranged from 10 to 40 degrees are presented and compared with the numerical results of Hoeijmakers [26]. The partial wake relaxation model converged in all cases to a precision of $|\Delta C_p| \leq 10^{-3}$.

Table 7.1 presents the comparison of the inviscid lift and induced drag coefficients obtained with the present method and the calculations by Hoeijmakers [26]. Detailed solutions for the incidences 10, 30 and 40 degrees are presented in Figures 7.11 to 7.22.

The differences between the two solutions increase with the angle of attack. The suction peak, especially near the apex, increases significantly with the angle of attack. In addition, the specified leading edge wake geometry deviates from the numerical solution of Hoeijmakers [26] as we move from the trailing edge to the wing apex. A similar behaviour of the potential flow solution is obtained for all angles of attack. The lift and induced drag coefficients are in good agreement with the results of Hoeijmakers [26]. For the pressure distribution, some differences are observed between the present method and the numerical results of Hoeijmakers [26].

α°	Present Method		Hoeijmakers [26]	
	C_L	C_{D_i}	C_L	C_{D_i}
10	0.356	0.063	0.359	0.063
15	0.577	0.154	0.587	0.157
20	0.796	0.289	0.834	0.304
25	0.999	0.460	1.065	0.497
30	1.348	0.777	1.315	0.760
35	1.538	1.076	1.520	1.065
40	1.649	1.382	1.662	1.395

Table 7.1: Inviscid lift and induced drag coefficients. 76 degrees swept delta wing for different angles of attack.

From these calculations we conclude that potential flow computations about delta wings with leading edge vortex sheet separation using the present panel method are feasible. A strong interaction between the vortex sheet geometry and the flow about the wing is observed. By providing an approximate shape of the vortex sheet geometry the method is able to realistically capture the behaviour of the leading edge vortex flow.

7.2.3. Solution for the 76 Degrees Swept Delta Wing for Different Angles of Attack

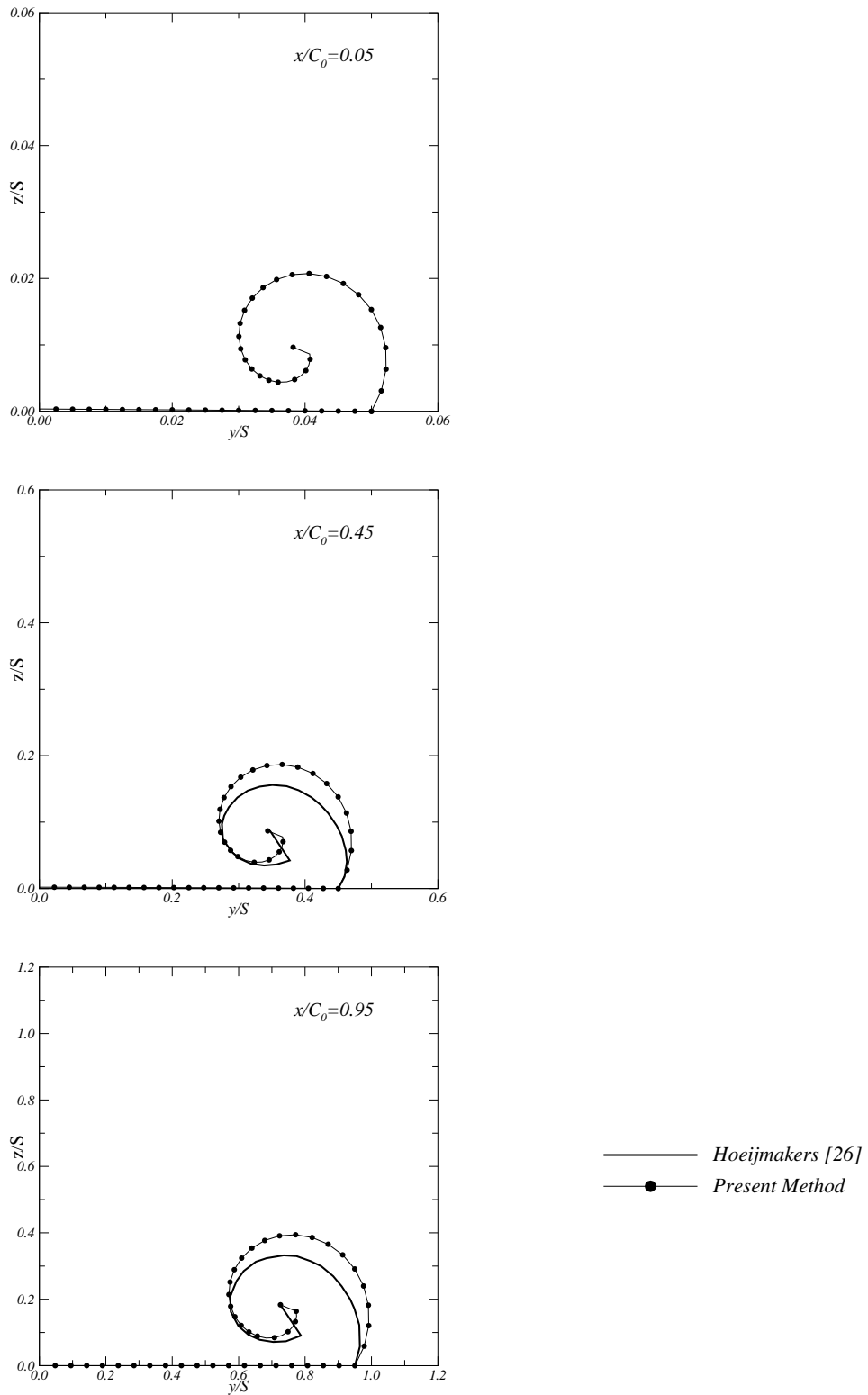


Figure 7.11: Leading edge wake geometry in cross-flow planes. Comparison with Hoeijmakers [26]. 76 degrees delta wing at 10 degrees incidence.

7.2.3. Solution for the 76 Degrees Swept Delta Wing for Different Angles of Attack

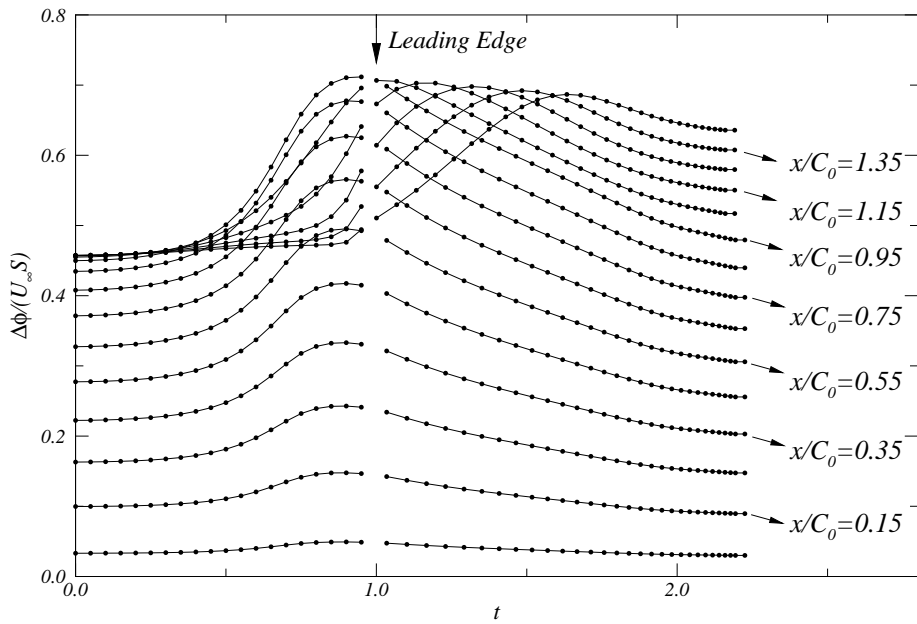


Figure 7.12: Potential-jump distribution along cross-flow planes. 76 degrees delta wing at 10 degrees incidence.

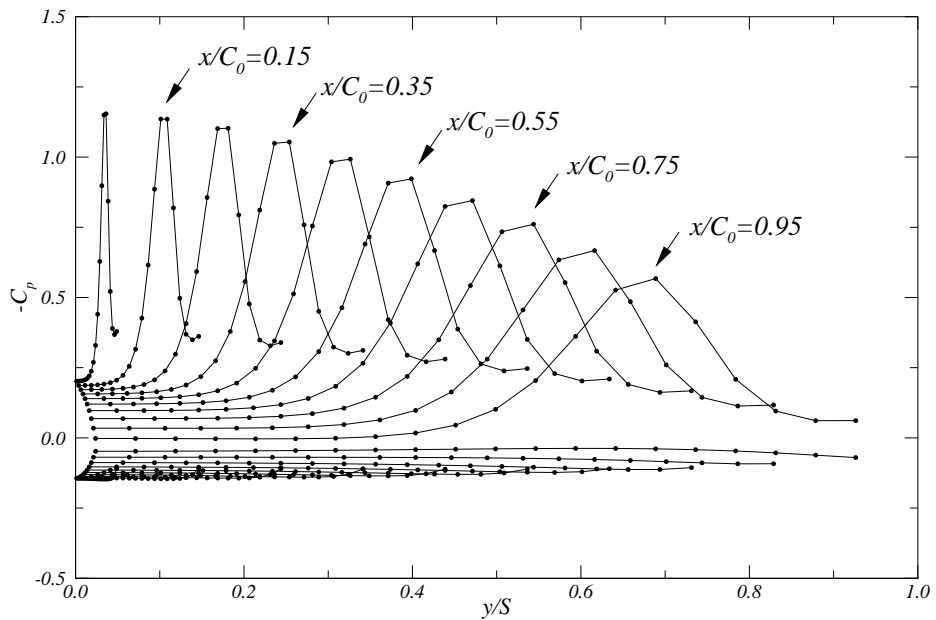


Figure 7.13: Pressure distribution along cross-flow planes. 76 degrees delta wing at 10 degrees incidence.

7.2.3. Solution for the 76 Degrees Swept Delta Wing for Different Angles of Attack

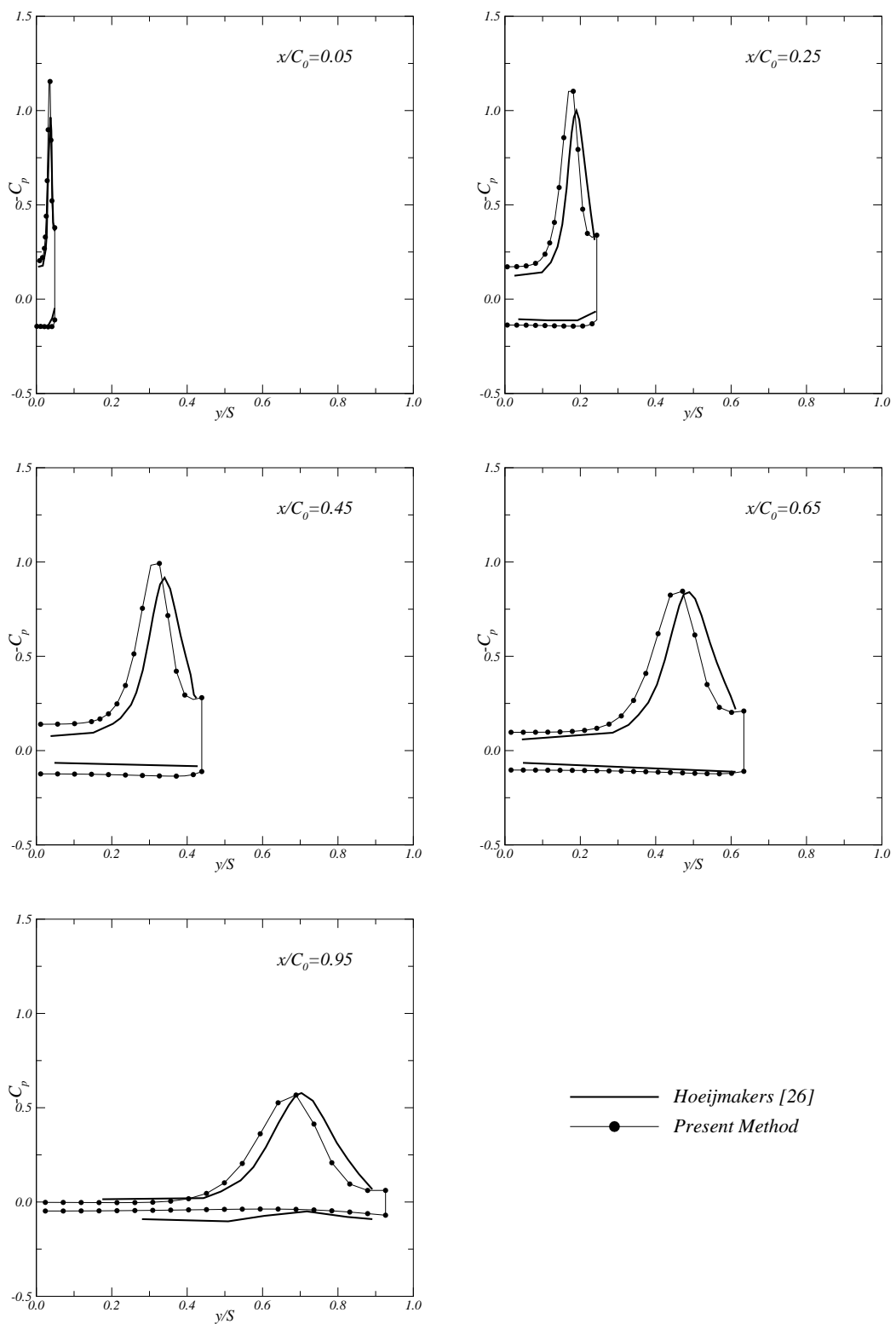


Figure 7.14: Pressure distribution along cross-flow planes. Comparison with Hoeijmakers [26]. 76 degrees delta wing at 10 degrees incidence.

7.2.3. Solution for the 76 Degrees Swept Delta Wing for Different Angles of Attack

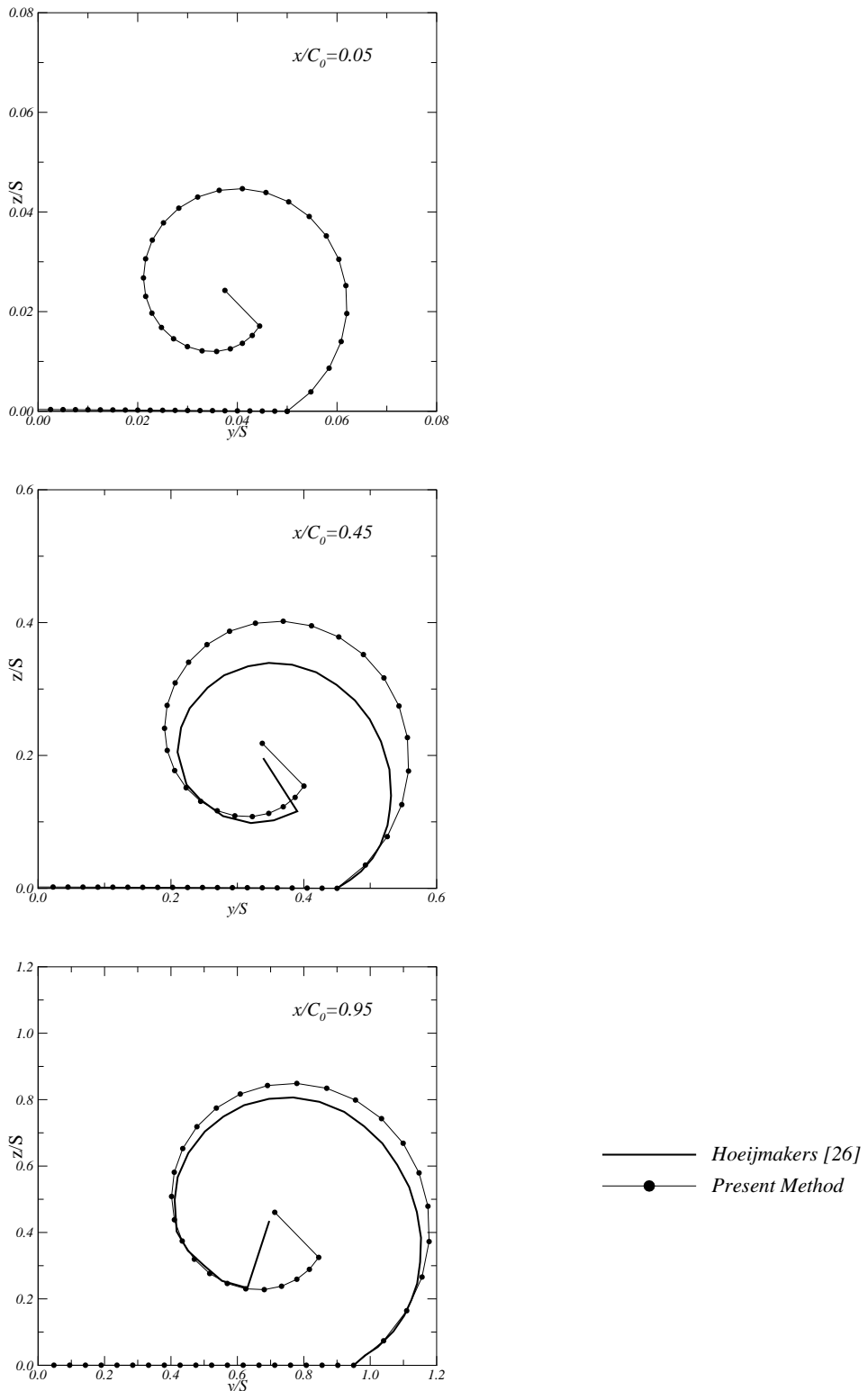


Figure 7.15: Leading edge wake geometry in cross-flow planes. Comparison with Hoeijmakers [26]. 76 degrees delta wing at 30 degrees incidence.

7.2.3. Solution for the 76 Degrees Swept Delta Wing for Different Angles of Attack

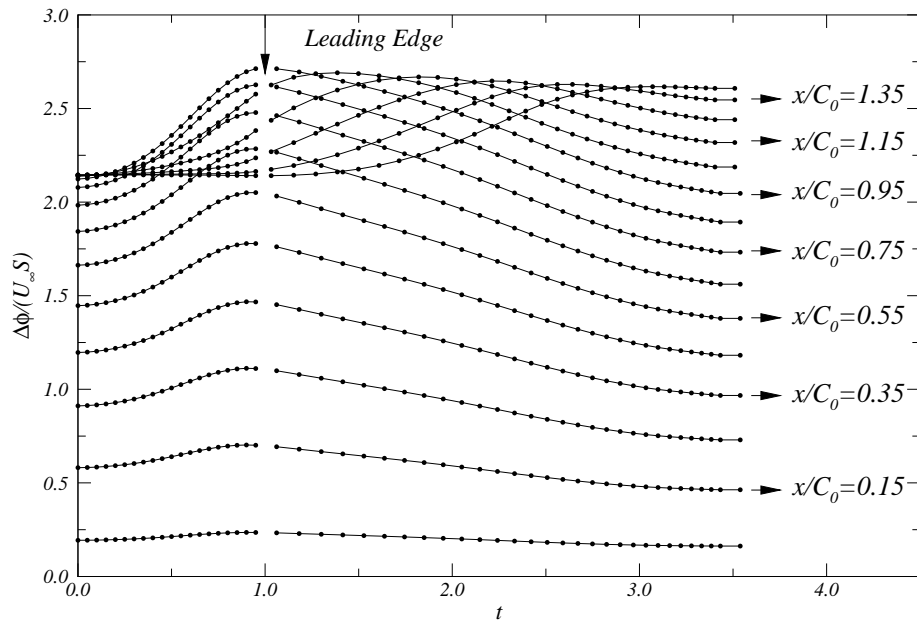


Figure 7.16: Potential-jump distribution along cross-flow planes. 76 degrees delta wing at 30 degrees incidence.

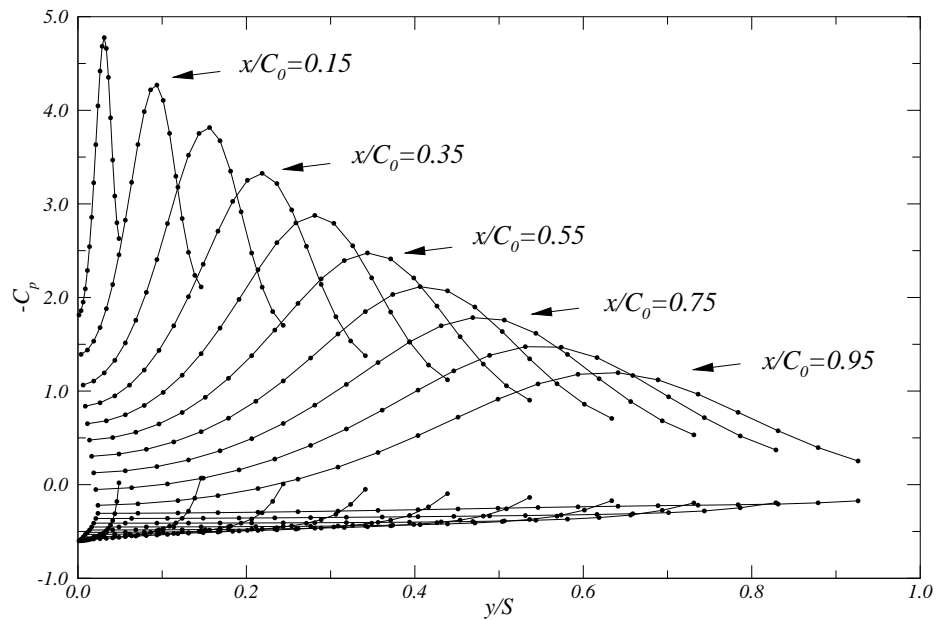


Figure 7.17: Pressure distribution along cross-flow planes. 76 degrees delta wing at 30 degrees incidence.

7.2.3. Solution for the 76 Degrees Swept Delta Wing for Different Angles of Attack

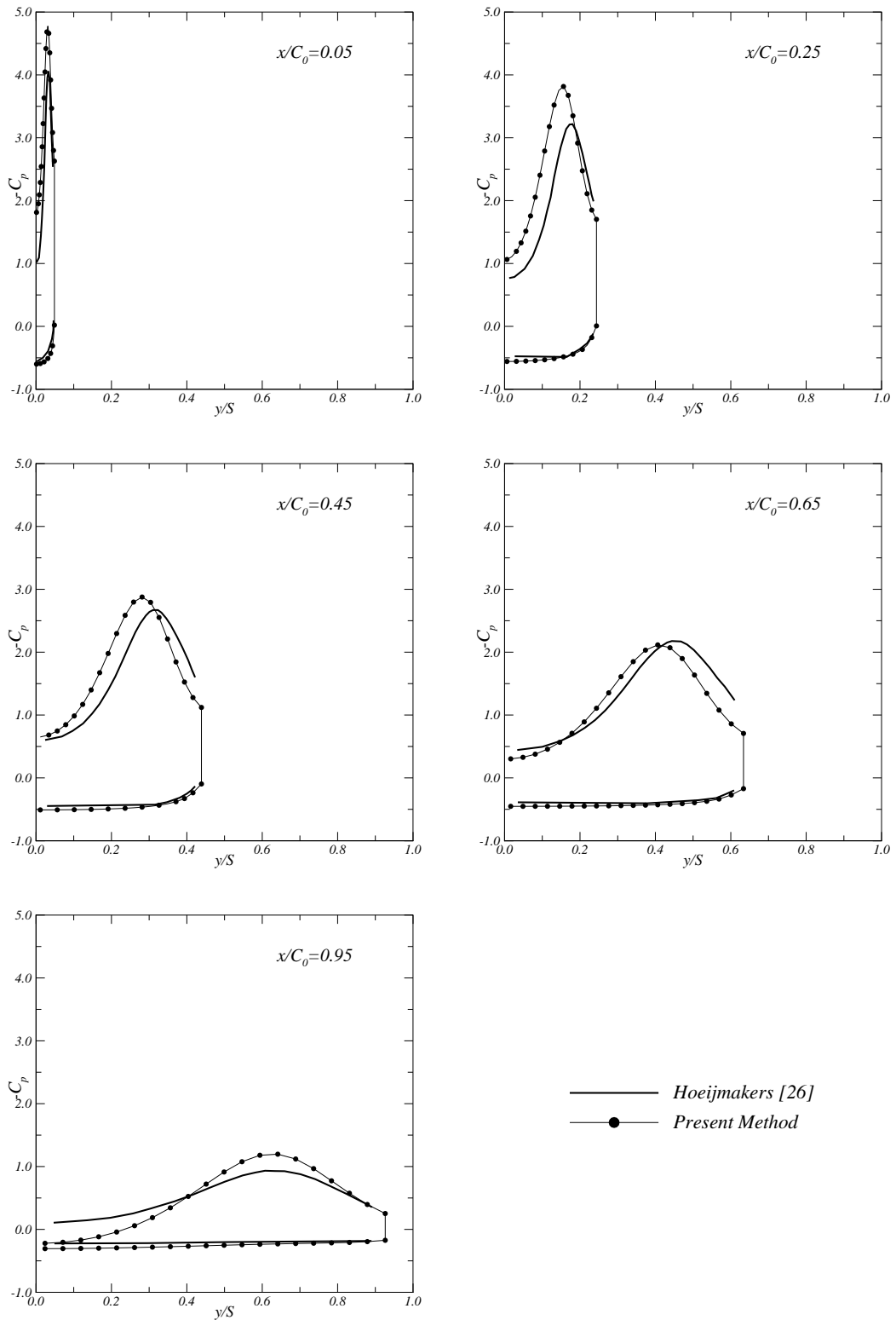


Figure 7.18: Pressure distribution along cross-flow planes. Comparison with Hoeijmakers [26]. 76 degrees delta wing at 30 degrees incidence.

7.2.3. Solution for the 76 Degrees Swept Delta Wing for Different Angles of Attack

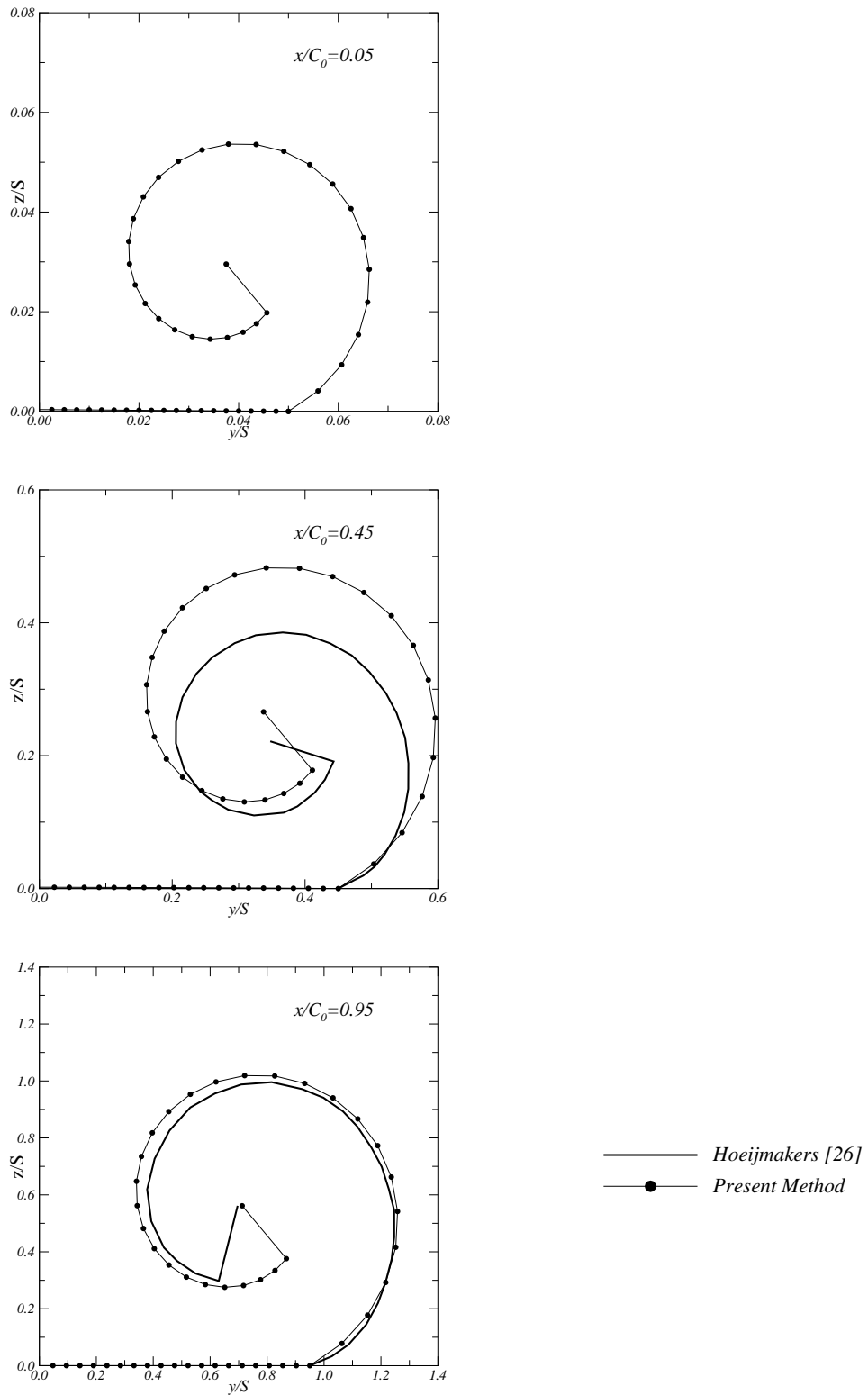


Figure 7.19: Leading edge wake geometry in cross-flow planes. Comparison with Hoeijmakers [26]. 76 degrees delta wing at 40 degrees incidence.

7.2.3. Solution for the 76 Degrees Swept Delta Wing for Different Angles of Attack

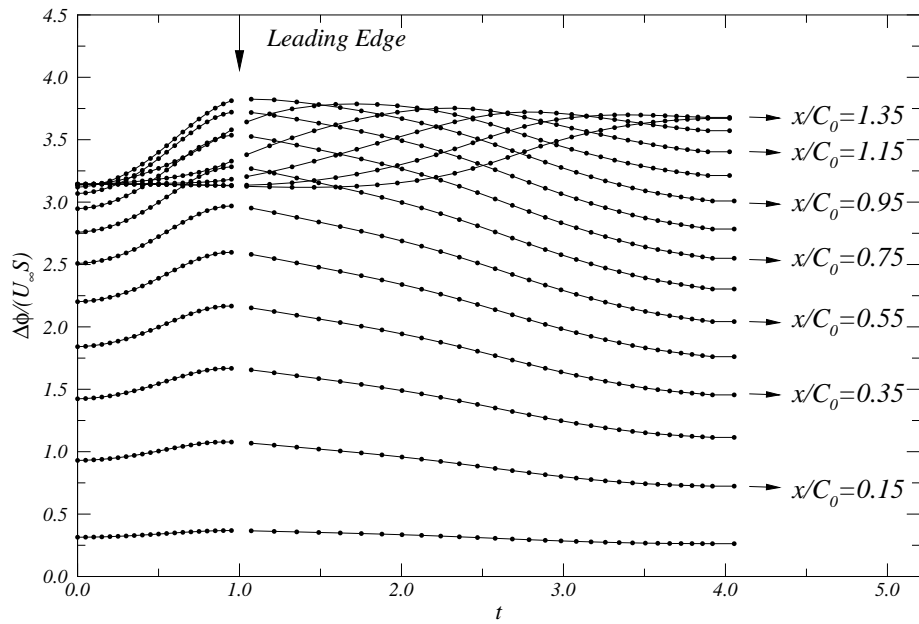


Figure 7.20: Potential-jump distribution along cross-flow planes. 76 degrees delta wing at 40 degrees incidence.

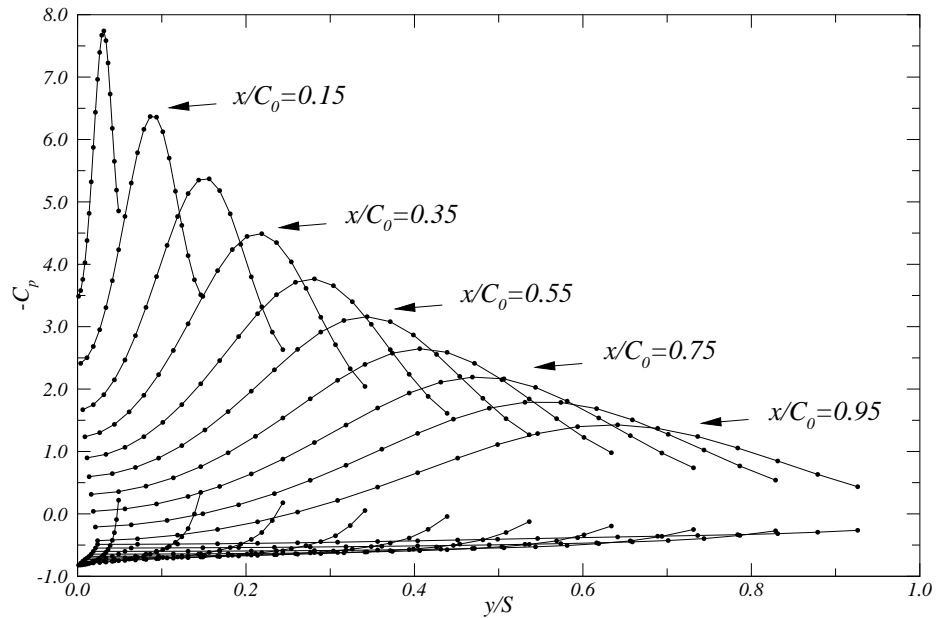


Figure 7.21: Pressure distribution along cross-flow planes. 76 degrees delta wing at 40 degrees incidence.

7.2.3. Solution for the 76 Degrees Swept Delta Wing for Different Angles of Attack

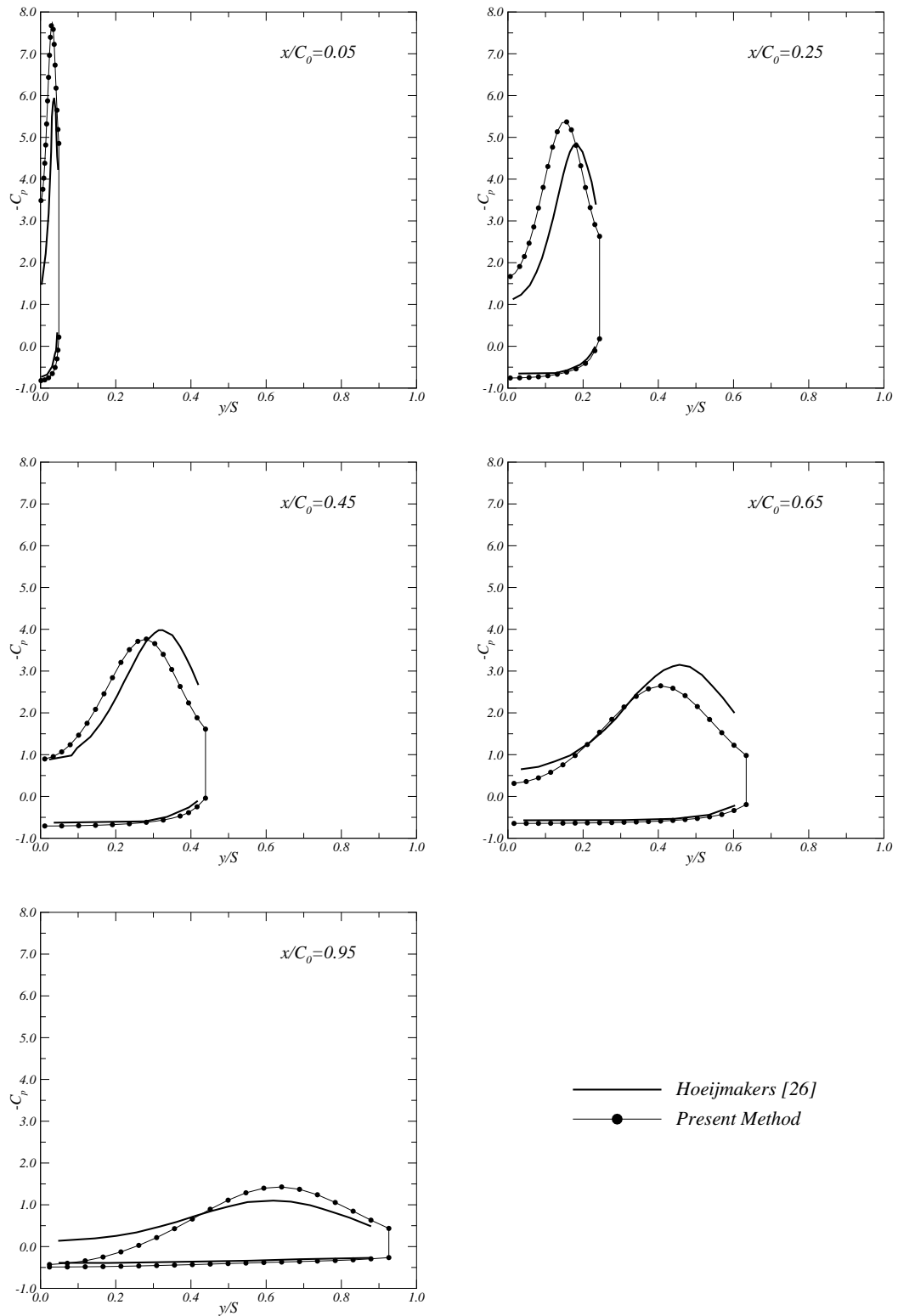


Figure 7.22: Pressure distribution along cross-flow planes. Comparison with Hoeijmakers [26]. 76 degrees delta wing at 40 degrees incidence.

7.3 Leading Edge Vortex Sheet Separation on Open Propellers

In this section, the leading edge vortex sheet separation on marine propellers is considered. When propeller blades are operated at heavy load conditions, the flow may separate from the leading edge as well as the trailing edge. This vorticity shed from the leading edge passes very close to the blade and changes the load distribution on the propeller blade.

An example of this physical phenomenon can be found in Greeley and Kerwin [25]. They presented the flow for the DTNSRDC propeller P4498 at two operation conditions. At 60% of its design loading condition, a significant vortex sheet is shed from the leading edge. However, when the propeller is operating near design condition, the leading edge vortex separation reduces significantly and only occurs near the blade tip.

In an attempt to model the effect of this phenomenon on blade loadings, Greeley and Kerwin [25] introduced a leading edge vortex sheet model for marine propellers in their numerical lifting surface method. The method was applied for the DTNSRDC propeller P4498 operating at $J = 0.800$ (design condition $J = 0.889$). A prescribed leading edge vortex sheet was implemented. A correlation between the upwash velocity at the leading edge control points and the leading edge suction force was considered and used to determine the strength of the leading edge vortices.

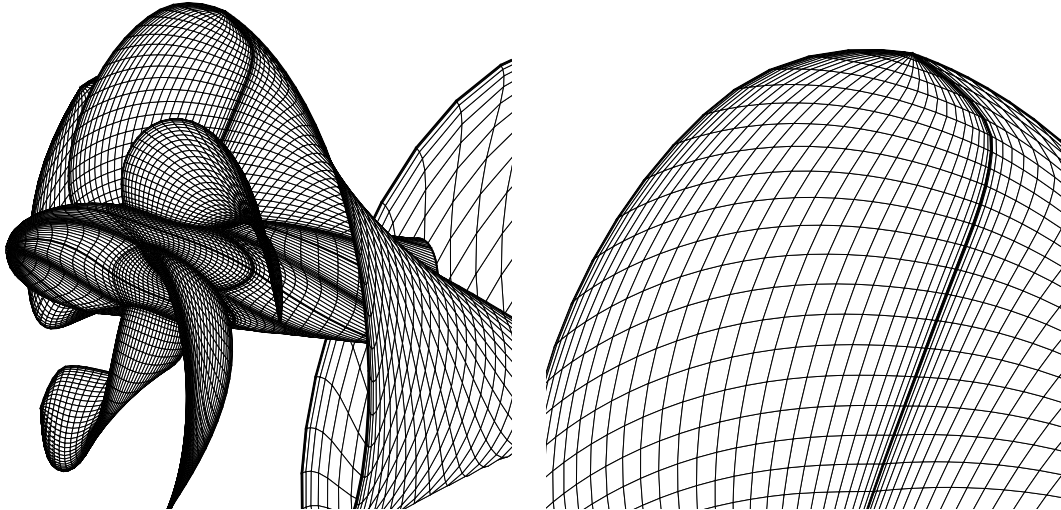


Figure 7.23: DTNSRDC P4498 panel arrangement. Note that only one wake grid is shown.

To address this problem with the present method, let us first consider the potential flow solution without leading edge vortex separation for the DTNSRDC propeller P4498 at the advance coefficients $J = 0.889$ and $J = 0.800$. The propeller P4498 is a five-bladed propeller with high skew. The detailed geometry of the this propeller can be found in the literature and is reproduced in the Appendix C. Figure 7.23 shows the panel arrangement of the propeller blade as well as the prescribed trailing edge wake grid. Each propeller

7.3. Leading Edge Vortex Sheet Separation on Open Propellers

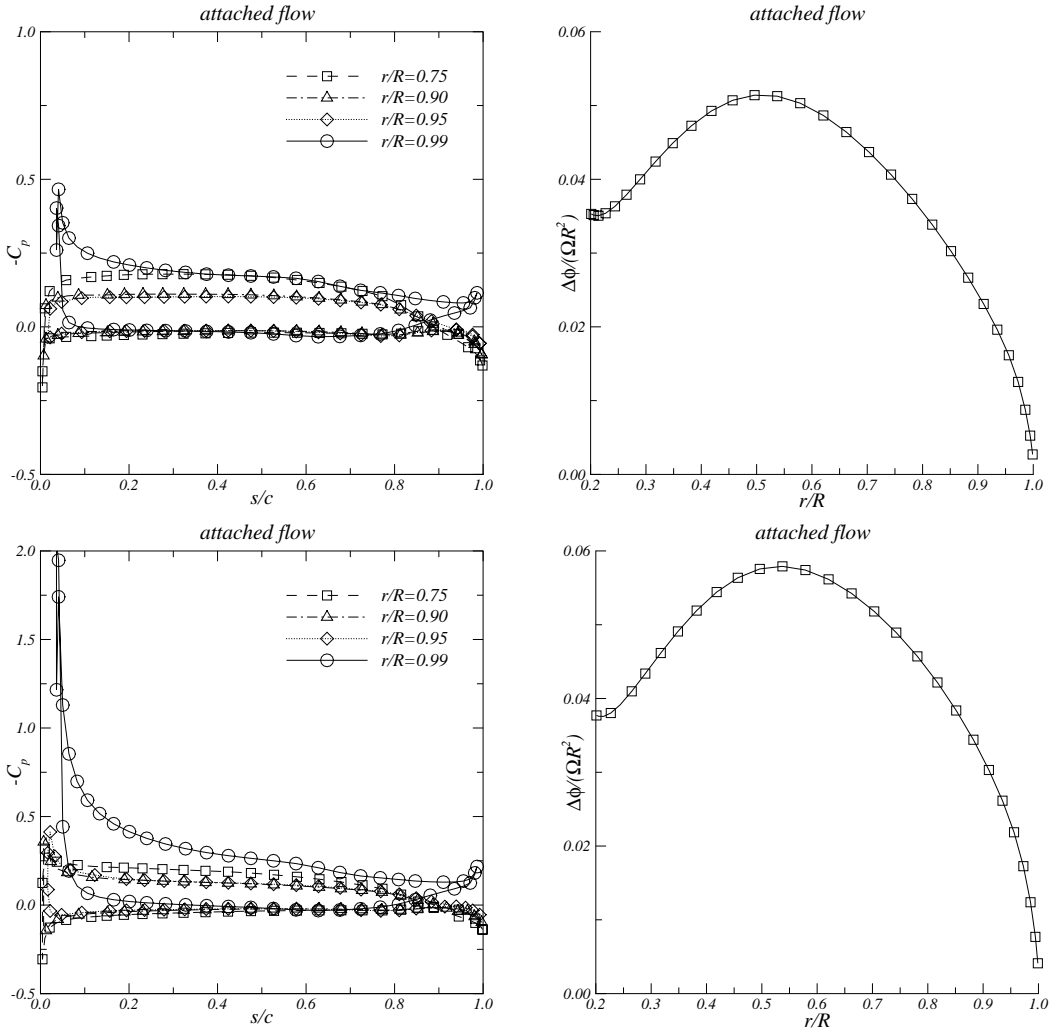


Figure 7.24: Pressure and circulation distributions at design condition $J = 0.889$ (top). Pressure and circulation distributions at condition $J = 0.800$ (bottom). DTNSRDC propeller P4498.

blade is discretised with 60 chordwise and 30 spanwise panels. Since the propeller has zero chord at the tip, a strip of triangular panels is employed. The wake is discretised with 90 streamwise and 30 spanwise panels and has an axial length of 3 propeller diameters. The pitch of the helicoidal lines of the wake grid is equal to the blade pitch. Contraction of the helicoidal lines is not considered. Each hub sector is discretised with 58 panels along the axial direction and 12 panels along the circumferential direction. An iterative pressure Kutta condition is applied at the blade trailing edge.

Figure 7.24 shows the pressure coefficient and the circulation distribution at the two advance coefficients. The predicted pressure distribution at $J = 0.889$ is typical of a design condition. It remains reasonably well behaved up to the tip with a small pressure peak at $r/R = 0.99$. At $J = 0.8$ a suction peak is present at the leading edge from $r/R = 0.81$. The presence of a large suction peak in the inviscid flow solution may be an indication of flow separation from the leading edge in viscous flow.

The present method is used to model the leading edge vortex sheet separation on marine propellers. The free shear layer emanated from the leading edge is modelled by a vortex sheet. Since the position of the separated boundary layer is unknown, the vortex sheet geometry must be specified. In the present method, the geometry of the leading edge vortex sheet is specified empirically based on observations from experiments.

The amount of vorticity shed from the leading edge of the propeller blade should be determined by the nature of the flow at the leading edge. If the leading edge is sharp it is appropriate to impose a Kutta condition to insure that the velocity at the leading edge remains bounded. However, propeller blades typically have round leading edges, so the vortex shedding rate should be a fraction of the total amount of vorticity shed in the case of a sharp edge.

The present method with leading edge vortex sheet separation is addressed for the propeller P4498 at the advance coefficient $J = 0.800$. At model scale, leading edge vortex separation was predicted to occur outboard of $r/R = 0.85$, Greeley and Kerwin [25]. The blade sections of this propeller between the radial positions $0.85 \leq r/R \leq 1.00$ have a mean maximum thickness of $t_M/c = 2.2\%$, which correspond to small leading edge radii. So, in first approximation we will assume a sharp leading edge. In this sense, the dipole strengths of the leading edge wake sheet are determined by the Morino Kutta condition, Equation (2.29).

The focus of the present study is on the behaviour of the pressure distribution on the blade due to a leading edge vortex sheet. Two leading edge wake geometries are considered: a leading edge wake with vortex lines along curves of constant radius, similar to the work of Greeley and Kerwin [25], and a leading edge wake where the vortex lines are convected outboard to the blade tip. The leading edge wake is divided in the transition wake region and ultimate wake region. The ultimate region starts at $x_u/R = 0.15$. The pitch of the vortex lines vary with the polynomial Hoshino function, Equation (4.29), in the transition region. The pitch distribution at the leading edge is chosen to allow the wake surface to pass over the suction side of the propeller blade. In the leading edge wake where the vortex lines are convected to the blade tip, the radius of the first vortex line varies from its position at the blade leading edge $r/R = 0.85$ to $r/R = 0.99$ at the ultimate section.

Figure 7.25 shows the panel arrangements for the two leading edge wake grids. The leading edge wake is discretised with 90 streamwise and 8 spanwise panels and has an axial length of 3 propeller diameters. The computed pressure coefficient over the propeller blade and the circulation distributions of the leading edge wake and trailing edge wake are also shown. A uniform pressure distribution on the suction side of the propeller blade is obtained with both wake grids. As expected, no suction peak is visible at the leading edge. The leading edge wake increases significantly the circulation distribution near the blade tip. Larger values are obtained for the leading edge wake with constant radius vortex lines. The circulation increases along the leading edge from the separation point $r/R = 0.85$ to the blade tip.

7.3. Leading Edge Vortex Sheet Separation on Open Propellers

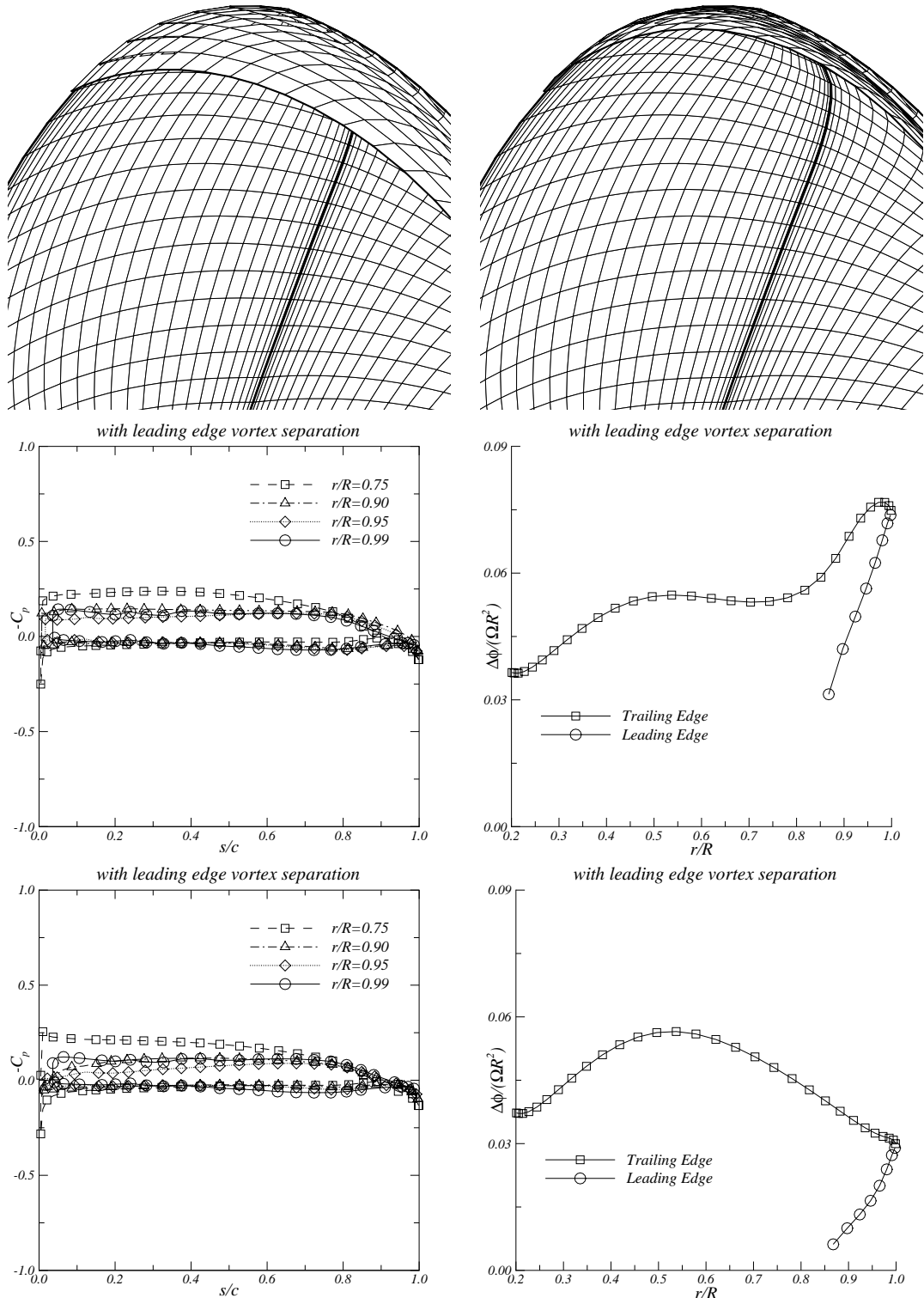


Figure 7.25: Panel arrangements of the two leading edge wakes for DTNSRDC propeller P4498 (top). Pressure and circulation distributions at the advance coefficient $J = 0.800$. Potential flow solution for the constant radius leading edge wake (middle) and for the leading edge wake with vortex lines convected to the blade tip (bottom).

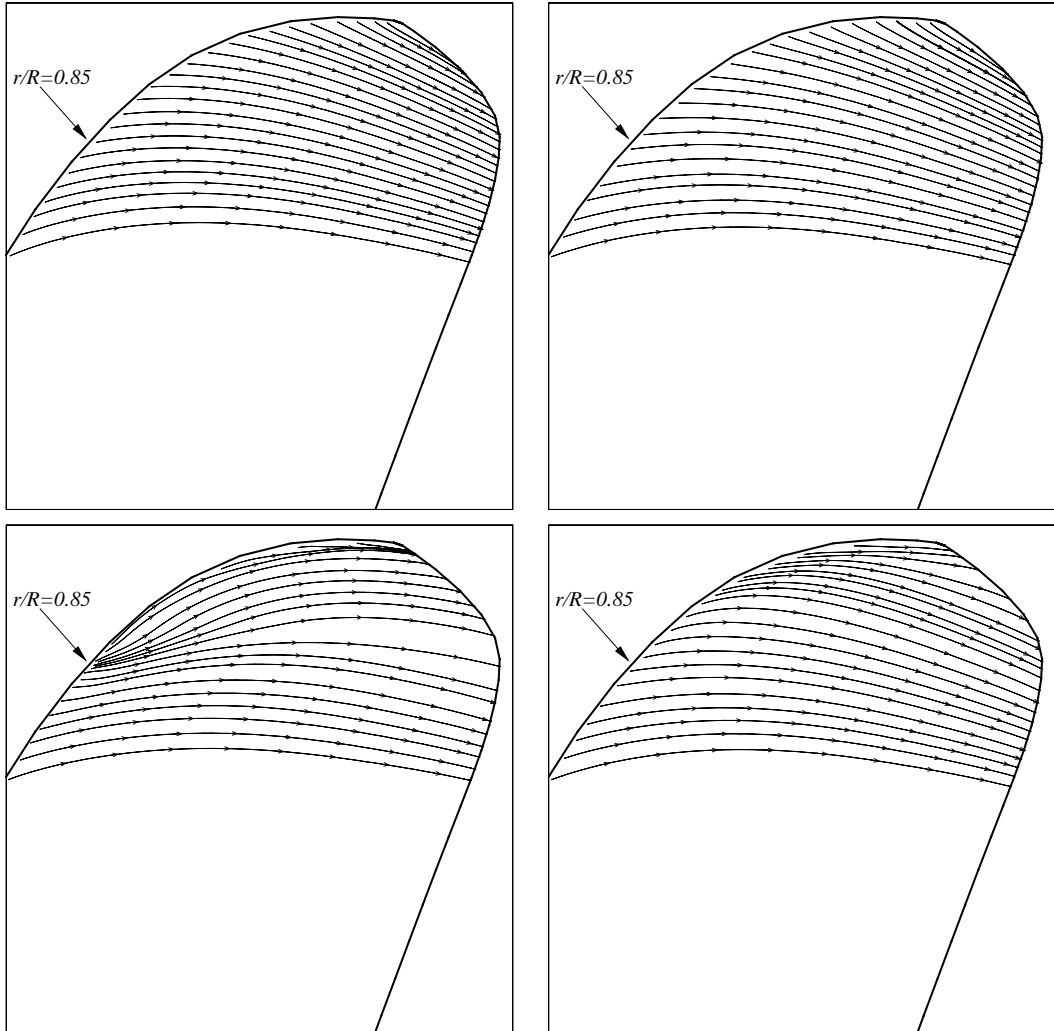


Figure 7.26: Streamlines on the suction side of the blade. Attached flow: $J = 0.889$ (top-left) and $J = 0.8$ (top-right). Leading edge vortex separation at $J = 0.8$: constant radius vortex lines (bottom-left) and vortex lines convected to the tip (bottom-right).

Model	K_T	K_Q
Attached flow	0.2463	0.0427
Constant radius vortex lines	0.2614	0.0465
Vortex lines convected to blade tip	0.2314	0.0414

Table 7.2: Inviscid thrust and torque coefficients. $J = 0.800$. DTNSRDC propeller P4498.

The streamlines on the suction side of the DTNSRDC propeller P4498 are presented in Figure 7.26 for the attached flow model and the leading edge separation model. The computed thrust and torque coefficients are given in Table 7.2. The leading edge wake with constant radius vortex lines increases the propeller loading. The streamlines become parallel to the leading edge from the separation point. This effect is smaller when applying the leading edge wake with vortex lines convected to the blade tip. In this case, a reduction in the propeller loading is obtained.

7.4 Tip Leakage Modelling in Ducted Propellers

Finally, the gap flow between the blade tip and the duct inner side is considered. The relative motion between the propeller blade and the duct inner surface, combined with the pressure difference between the pressure and suction sides of the blade, creates a leakage flow across the tip, resulting in a strongly accelerating flow through the gap. Due to this, the flow may separate from the blade tip creating a tip leakage vortex.

Different models for the potential flow in the gap region are investigated: non-zero and zero gap width and a tip leakage model with a vortex sheet shed along the chord at the tip of the propeller blade.

Calculations are presented for the ducted propeller $K_a 4\text{-}70$ with $P/D = 1.2$ inside duct NSMB 19A at the advance coefficients $J = 0.5$ and $J = 0.7$. An iterative pressure Kutta condition was applied at the blade and duct trailing edges, using a Newton-Raphson scheme to a precision of $|\Delta C_p|_{TE} \leq 10^{-3}$. Calculations were carried out for the 40×21 blade grid, 120×30 duct grid and 41×16 hub grid. The duct wake leaves the trailing edge at the bisector.

Figure 7.27 presents the panel arrangements for the three gap models. First, a gap width equal to 0.8% of the propeller radius is used. In this model, a vortex sheet leaving the blade trailing edge is presented. Second, a zero gap width is assumed. Special attention has been given to the duct panel arrangement to match the blade panelling at the tip. The stretching of the blade wake along the streamwise direction is also chosen to match the duct grid. Finally, a tip leakage model with a vortex sheet shed along the entire length of the blade tip is considered. The dipole strengths of the tip wake sheet are determined by the Morino Kutta condition, Equation (2.29). The pitch of the vortex shed from the leading edge of the blade tip is assumed to be

$$\bar{P} = \frac{1}{2} (P + P_{TW}), \quad (7.12)$$

where P is the undisturbed flow pitch at the tip and P_{TW} is the pitch of the trailing edge wake at the blade tip. A linear variation of the pitch of the vortex lines along the chord between the leading and trailing edges is assumed. The tip leakage vortex sheet is divided into a transition wake and an ultimate wake. The ultimate region starts at $x_u/R = 1.0$ and has the same pitch of the trailing edge wake. In the transition wake, the pitch of the vortex lines vary along the axial direction according to the polynomial Hoshino function, Equation (4.29), from its value at the blade tip to the ultimate wake. The tip wake is discretised with 60 panels along the streamwise direction and 20 panels along the chordwise direction.

Figures 7.28 to 7.31 present the pressure distributions over the duct surface and the blade and duct circulations calculated with the three gap models for the advance ratios of $J = 0.5$ and $J = 0.7$. The pressure distribution is presented as the mean, first and second harmonic amplitude of blade frequency. The definitions are:

$$C_p(\theta) = C_{p0} + C_{p1} \cos(K\theta - \varphi_1) + C_{p2} \cos(2K\theta - \varphi_2), \quad (7.13)$$

where

- C_{p0} = Mean value of pressure coefficient;
- C_{p1} = First harmonic amplitude of pressure coefficient;
- C_{p2} = Second harmonic amplitude of pressure coefficient;
- $\varphi_{1,2}$ = Cosine phase angles, corresponding to the maximum pressure.

It is seen that the modelling of the gap flow by assuming a tip vortex or a vortex sheet shed from the blade tip introduces a larger pressure decrease at the duct inner surface. This is particularly evident in the first and second harmonics. This pressure behaviour is absent in the zero gap model.

The gap model influences significantly the blade and duct circulations. The blade circulation distribution tends to zero when approaching the tip in the non-zero gap model. In the zero gap model, the blade circulation at the tip is equal to the duct circulation discontinuity. A finite circulation at the blade tip is also obtained in the tip leakage vortex model. Then, the circulation distribution along the chord at the blade tip decreases from its value at the trailing edge to zero at the leading edge.

Figure 7.32 shows the blade pressure distribution at the radial section $r/R = 0.99$ and the duct pressure distribution at the circumferential position $\theta = 20$ degrees. The blade pressure distribution of the non-zero gap model reduces along the chordwise direction from the leading edge to the trailing edge. No pressure peak is obtained at the trailing edge with the other gap models. For the duct pressure distribution, a suction peak is visible in the non-zero gap and tip leakage vortex models. This pressure decrease is due to the presence of the tip vortex shed from the blade trailing edge, which is close to the duct inner surface. In the tip leakage model the vorticity shed from the blade tip is distributed along the chord and reduces the suction peak. The duct pressure distribution of the zero gap width does not present the suction peak, due to the gap model which does not allow vorticity to be shed from the blade tip. Note that these results may have some grid sensitivity, due to the small distance of the panel control points on the duct inner surface to the singularity associated to the tip vortex. However, the purpose here is to show the effect of the gap model on the blade and duct pressure distributions.

Figure 7.33 exhibits the comparison of the thrust and torque coefficients with experimental data, Kuiper [49]. The non-zero gap and tip leakage vortex models over-predict the total thrust and torque coefficients. The potential flow solution obtained with these models results in a very large velocity through the gap region which will not occur in real flow. This unrealistic large velocity affects the prediction of the circulation and forces on both duct and propeller. Although the zero gap model ignores the flow between the propeller blade tip and the inner surface of the duct, a better agreement with the experimental data is obtained. These results indicate that the correct flow through the gap region is of the utmost importance for an accurate prediction of the circulation and forces on the ducted propeller.

7.4. Tip Leakage Modelling in Ducted Propellers

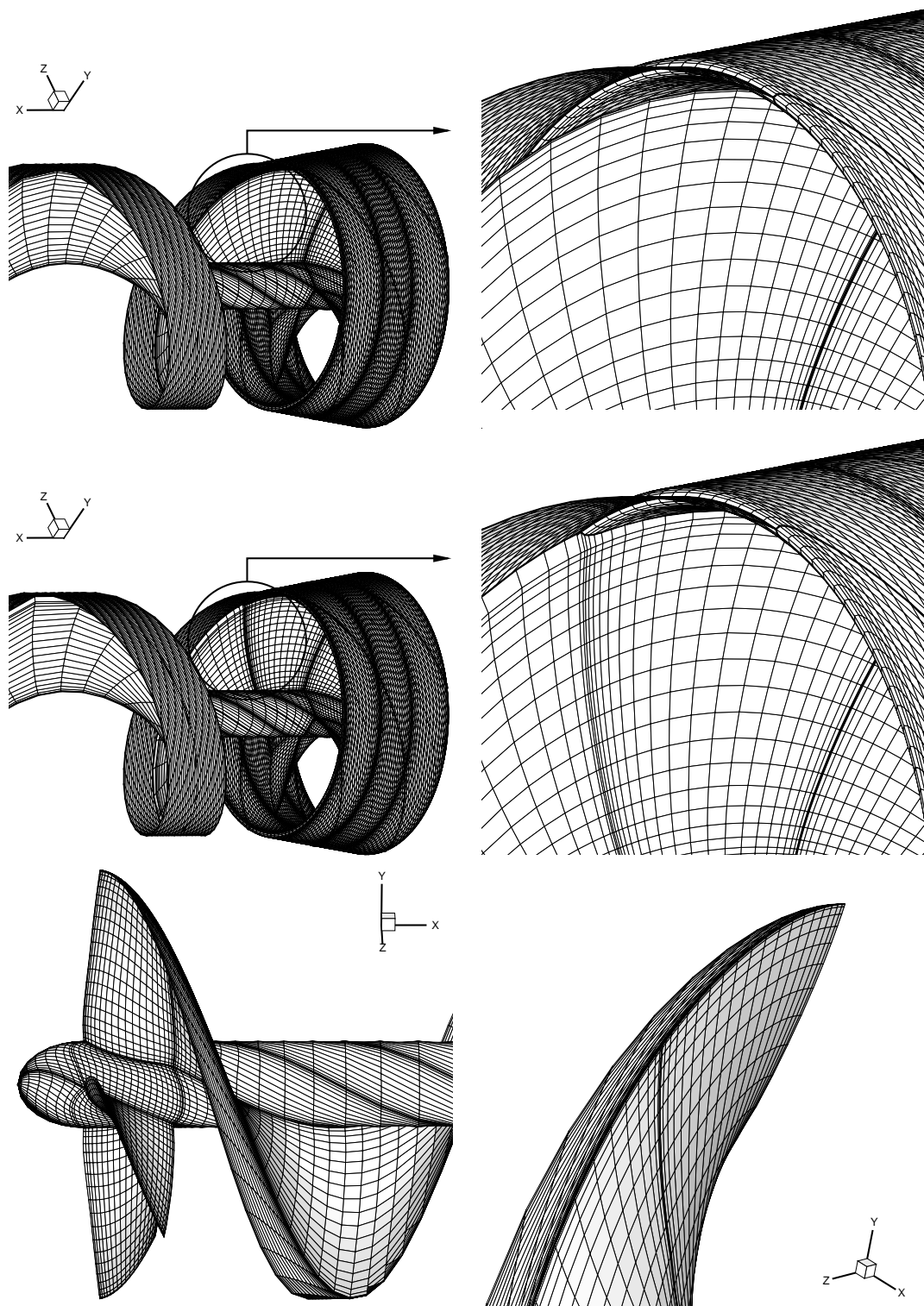


Figure 7.27: Panel arrangements for propeller K_a4-70 inside duct 19A for the three gap models. 0.8% gap (top), zero gap (middle), tip leakage vortex model (bottom). Note that only one blade wake grid and one duct sector wake grid are shown.

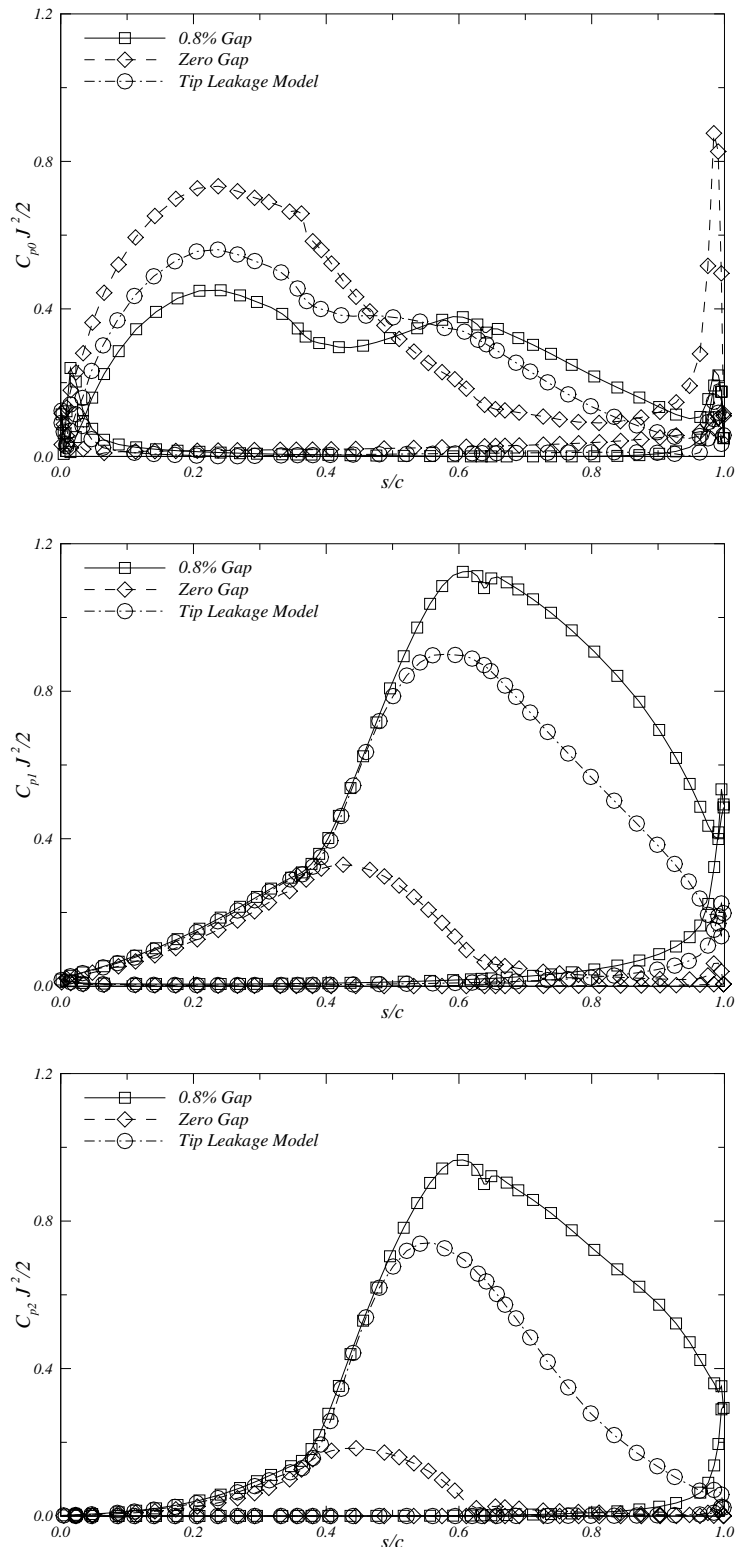


Figure 7.28: Influence of the gap model on the pressure distribution on the duct 19A at $J = 0.5$. Mean (top), first harmonic (middle) and second harmonic (bottom) amplitude of blade frequency.

7.4. Tip Leakage Modelling in Ducted Propellers

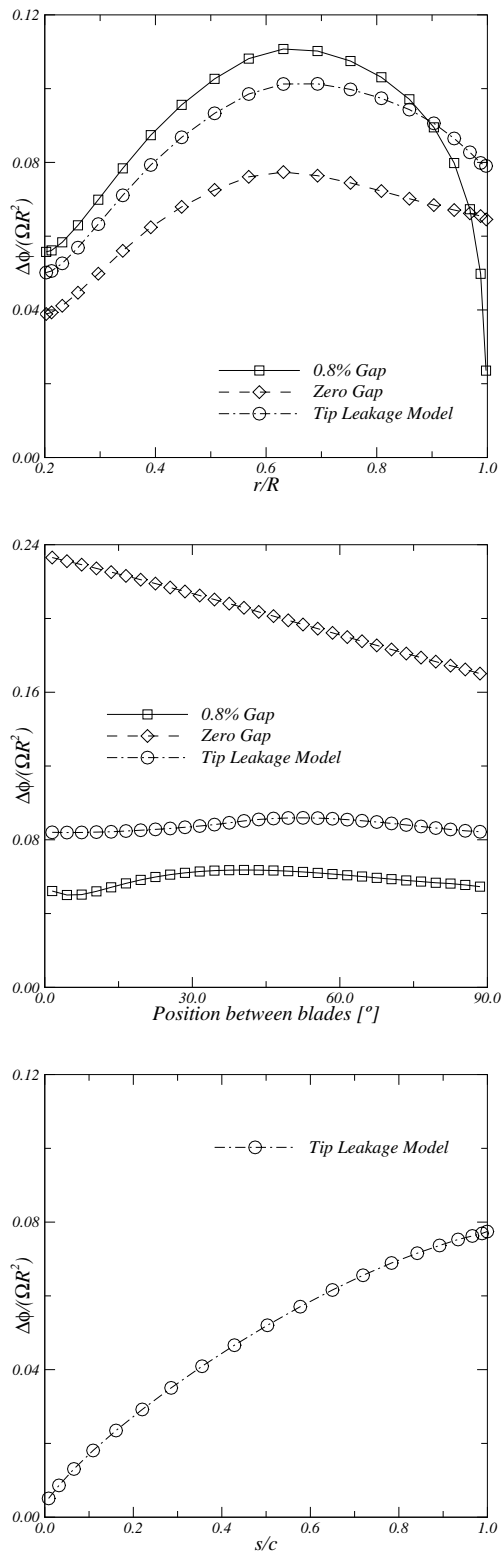


Figure 7.29: Influence of the gap model on the circulation distributions: blade circulation (top), duct circulation (middle), blade tip circulation (bottom). K_a4-70 inside duct 19A at $J = 0.5$.

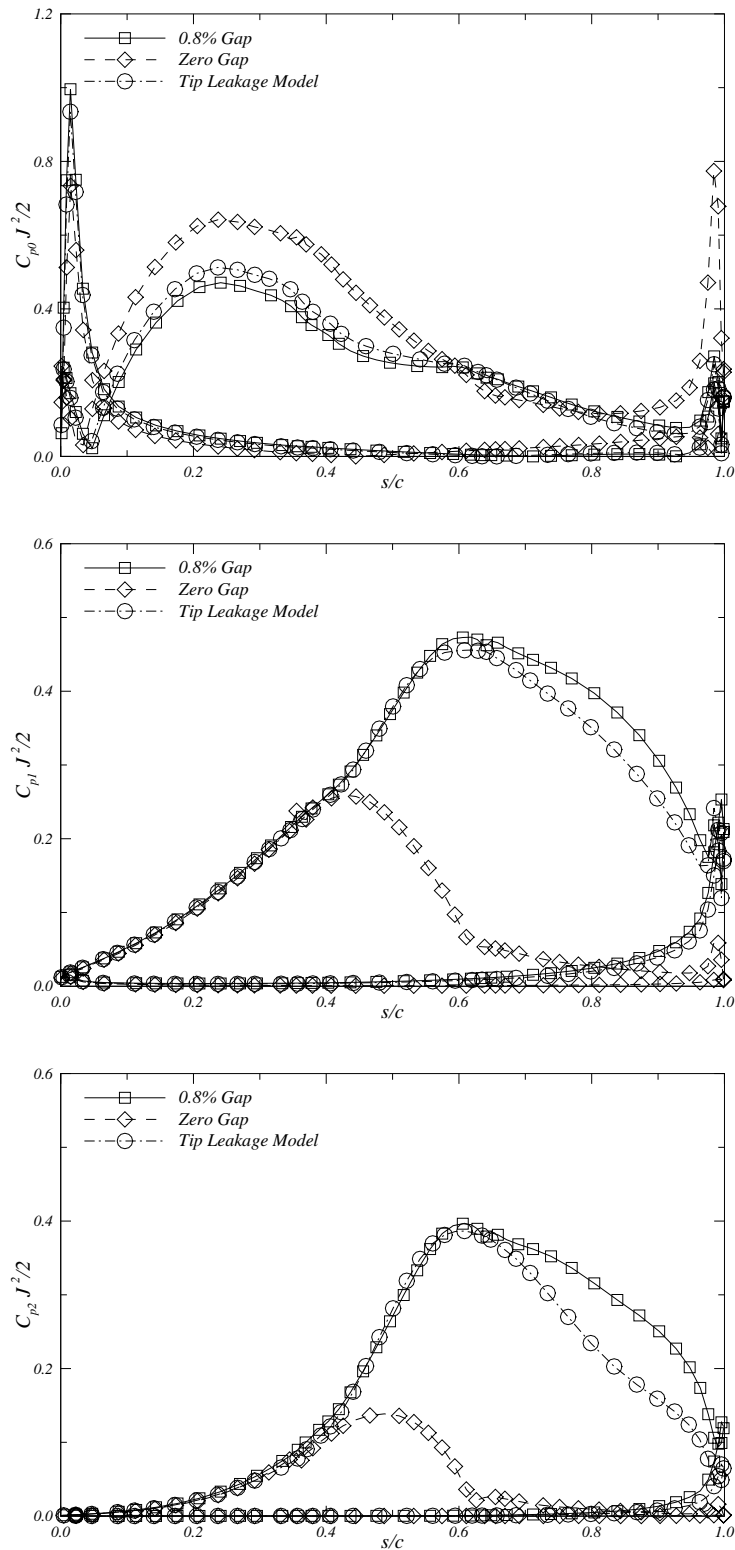


Figure 7.30: Influence of the gap model on the pressure distribution on the duct 19A at $J = 0.7$. Mean (top), first harmonic (middle) and second harmonic (bottom) amplitude of blade frequency.

7.4. Tip Leakage Modelling in Ducted Propellers

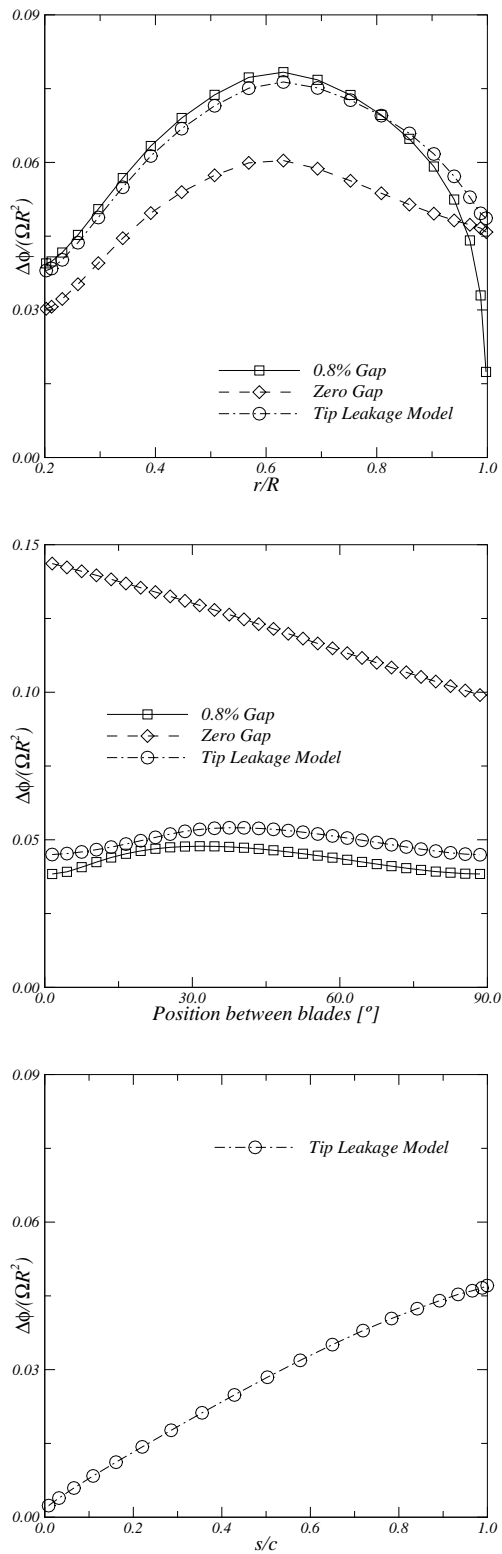


Figure 7.31: Influence of the gap model on the circulation distributions: blade circulation (top), duct circulation (middle), blade tip circulation (bottom). $K_a4\text{-}70$ inside duct 19A at $J = 0.7$.

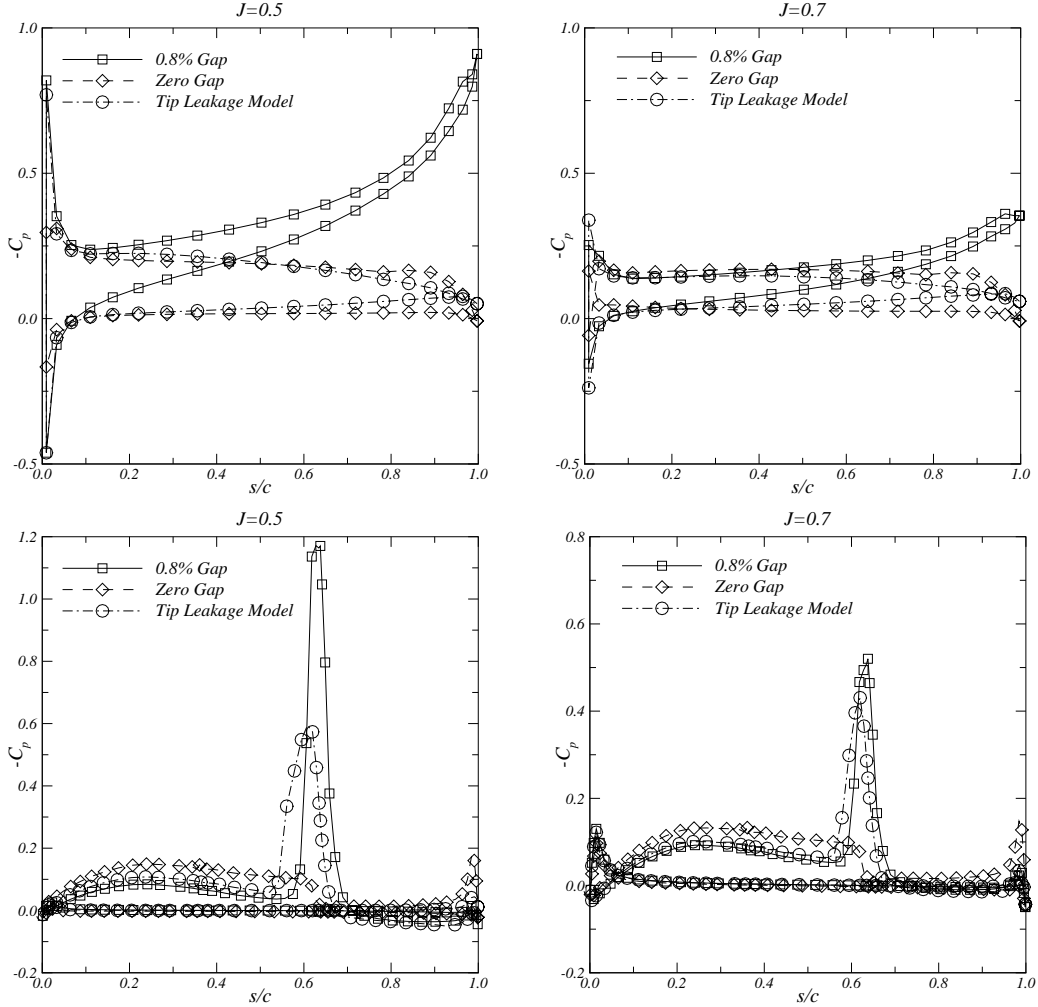


Figure 7.32: Influence of the gap model on the pressure distribution on the blade at section $r/R = 0.99$ (top) and on the duct at circumferential position $\theta = 20$ degrees (bottom).

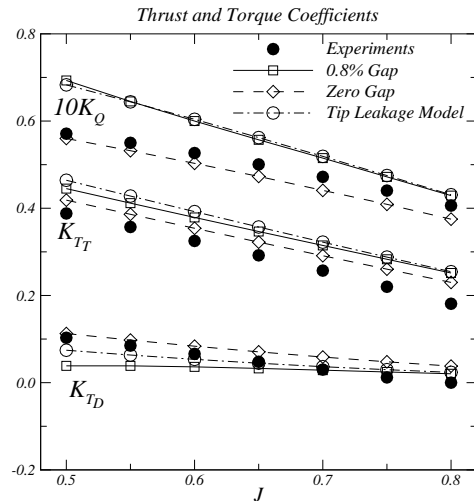


Figure 7.33: Inviscid thrust and torque coefficients for propeller K_a4-70 inside duct 19A. Comparison between gap models.

Chapter 8

Conclusions

A low-order potential-based panel method for the calculation of the incompressible potential flow around wings and marine propellers is presented. Three wake models are considered: rigid wake with linear and iterative pressure Kutta condition, partial wake relaxation and full wake relaxation with roll-up. The techniques for the generation of structured grids on the surfaces of the wing, propeller blade, duct, hub and vortex sheet are described.

Grid convergence studies using the conventional panel arrangement and comparison with other panel methods and experimental measurements are presented. Convergence of the numerical results with grid refinement is achieved, except near the tip where an irregular solution is obtained. The application of the iterative pressure Kutta condition at the trailing edge leads to pressure peaks near the tip. The predictions of the pressure distribution are generally in good agreement with the experimental data.

As a consequence of the previous results, the potential flow solution behaviour in the vicinity of the tip is studied. The application of a partial wake relaxation model does not change significantly the pressure distribution near the tip, due to the weak interaction between the trailing vortex sheet and the flow over the surface. The use of a rolled-up wake is sufficient to eliminate the pressure peaks at the trailing edge near the tip. The position of the tip vortex is studied by introducing a new panel arrangement with “hydrodynamic tip”. A smoother rolled-up wake sheet is obtained, when combined with the new panel arrangement. A more regular pressure distribution is achieved inboard of the “hydrodynamic tip”. However, outboard of the “hydrodynamic tip”, a pressure peak is seen associated to the flow around the sharp edge from the pressure to the suction side. The blade tip geometry and its panelling influence significantly the potential flow solution near the tip. The modification of the tip geometry, by reducing the panel skewness, produces a more regular potential flow solution.

The present method is applied to the modelling of separated vortex flows about wings and marine propellers. The method employs prescribed vortex sheets. A strong interaction between the separated vortex sheet and the flow over the wing or propeller blade is observed. The method is applied to delta-like wings using a partial wake relaxation

8. Conclusions

model for the leading and trailing wakes. Similar results are obtained between the present method and a second-order panel method for thin wings with leading edge vortex sheet separation. The application of a vortex sheet along the leading edge of a marine propeller alters the potential flow solution on the blade. A uniform pressure distribution over the suction side of the blade is seen. Vortex sheet separation is used to model the gap flow between the duct and the blade tip. Results are compared with non-zero and zero gap width. The results show significant variations in the potential flow solution in relation to the gap model.

The panel method for the three-dimensional flow about wings and marine propellers described in this thesis shows that a potential flow method for the modelling of attached and separated vortex flows is feasible. The potential flow solution in the vicinity of the tip needs special attention. A strong influence of the blade tip panelling and wake sheet geometry is seen. For the vortex sheet separation modelling, promising results using prescribed leading edge wake geometries are obtained. Nevertheless, further investigations should be undertaken in alternative wake models.

Bibliography

- [1] Hess, J.L., Smith, A.M.O., (1964). “Calculation of Nonlifting Potential Flow About Arbitrary Three-Dimensional Bodies”. *Journal of Ship Research*, Vol. 8, No. 2, pp. 22–44.
- [2] Hess, J.L., (1974). “The Problem of Three-Dimensional Lifting Flow and its Solution by Means of Surface Singularity Distribution”. *Computer Methods in Applied Mechanics and Engineering*, Vol. 4, pp. 283–319.
- [3] Hess, J.L., Valarezo, W.O., (1985). “Calculation of Steady Flow About Propellers Using a Surface Panel Method”. *Journal of Propulsion and Power*, Vol. 1, No. 6, pp. 470–476.
- [4] Morino, L., Kuo, C.-C., (1974). “Subsonic Potential Aerodynamics for Complex Configurations: A General Theory”. *AIAA Journal*, Vol. 12, No. 2, pp. 191–197.
- [5] Maskew, B., (1982). “Prediction of Subsonic Aerodynamic Characteristics: A Case for Low-Order Panel Methods”. *Journal of Aircraft*, Vol. 19, No. 2, pp. 157–163.
- [6] Youngren, H.H., Bouchard, E.E., Coopersmith, R.M., Miranda, L.R., (1983). “Comparison of Panel Method Formulations and its Influence on the Development of QUADPAN, an Advanced Low Order Method”. *AIAA Paper 83-1827*, AIAA Applied Aerodynamics Conference.
- [7] Kerwin, J.E., Kinnas, S., Lee, J.-T., Shih, W.-Z., (1987). “A Surface Panel Method for the Hydrodynamic Analysis of Ducted Propellers”. *SNAME Transactions*, Vol. 95, pp. 93–122.
- [8] Lee, J.-T., (1987). “A Potential Based Panel Method for the Analysis of Marine Propellers in Steady Flow”. Ph. D. Thesis, Massachusetts Institute of Technology.
- [9] Hoshino, T., (1989). “Hydrodynamic Analysis of Propellers in Steady Flow Using a Surface Panel Method”. *Journal of The Society of Naval Architects of Japan*, Vol. 165, pp. 50–70.
- [10] Kinnas, S.A., Hsin, C.-Y., Keenan, D.P., (1990). “A Potential Based Panel Method for the Unsteady Flow Around Open and Ducted Propellers”. *Proceedings of the Eighteenth Symposium on Naval Hydrodynamics*, pp. 667-685.

Bibliography

- [11] Hsin, C.-Y., (1990). "Development and Analysis of Panel Method of Propellers in Unsteady Flow". Ph. D. Thesis, Massachusetts Institute of Technology.
- [12] Hoshino, T., (1993). "Hydrodynamic Analysis of Propellers in Unsteady Flow Using a Surface Panel Method". Journal of The Society of Naval Architects of Japan, Vol. 174, pp. 71–87.
- [13] Fine, N., (1992). "Non-Linear Analysis of Cavitating Propellers in Nonuniform Flow". Ph. D. Thesis, Massachusetts Institute of Technology.
- [14] Vaz, G., (2005). "Modelling of Sheet Cavitation on Hydrofoils and Marine Propellers Using Boundary Element Methods". Ph. D. Thesis, Instituto Superior Técnico.
- [15] Koyama, K. (Ed.), (1993). "Comparative Calculations of Propellers by Surface Panel Method - Workshop organized by 20th ITTC Propulsor Committe". Papers of Ship Research Institute, Supplement No. 15.
- [16] Pyo, S., (1995). "Numerical Modelling of Propeller Tip Flows With Wake Sheet Roll-up in Three Dimensions". Ph. D. Thesis, Massachusetts Institute of Technology.
- [17] Kinnas, S.A., (1996). Theory and Numerical Methods for the Hydrodynamic Analysis of Marine Propulsors, "Advances in Marine Hydrodynamics". Ohkusu (Ed.), Computational Mechanics Publications, pp. 279–322.
- [18] Hsin, C.-Y., Kerwin, J.E., Kinnas, S.A., (1991). "A Panel Method for the Analysis of the Flow Around Highly Skewed Propellers". Proceedings of the Propellers/Shafing '91 Symposium, SNAME, Virginia Beach, pp. 1–13.
- [19] Kinnas, S.A., Pyo, S., Hsin, C.Y., Kerwin, J.E., (1994). "Numerical Modelling of Propeller Tip Flows". Proceedings of the Sixth International Conference on Numerical Ship Hydrodynamics.
- [20] Baltazar, J., (2002). "Estudo Numérico do Escoamento Potencial na Extremidade de Asas Elípticas com um Método de Elementos de Fronteira". Master's Thesis, Instituto Superior Técnico. (in Portuguese).
- [21] Maitre, T.A., Rowe, A.R., (1991). "Modeling of Flow Around a Marine Propeller Using a Potential-Based Method". Journal of Ship Research, Vol. 35, No. 2, pp. 114–126.
- [22] Takinaci, A.C., (1996). "A Wake Rollup Model for Heavily Loaded Marine Propellers". International Shipbuilding Progress, Vol. 43, No. 435, pp. 247–272.
- [23] Dang, J., (2001). "Numerical Simulation of Unsteady Partial Cavity Flows". Ph. D. Thesis, Delft University of Technology.
- [24] Lee, H., (2002). "Modeling of Unsteady Wake Alignment and Developed Tip Vortex Cavitation". Ph. D. Thesis, The University of Texas at Austin.

- [25] Greeley, D.S, Kerwin, J.E., (1982). “Numerical Methods for Propeller Design and Analysis in Steady Flow”. SNAME Transactions, Vol. 90, pp. 415–453.
- [26] Hoeijmakers, H.W.M., (1989). “Computational Aerodynamics of Ordered Vortex Flows”. Ph. D. Thesis, Technical University of Delft.
- [27] Gu, H., (2006). “Numerical Modeling of Flow Around Ducted Propellers”. Ph. D. Thesis, The University of Texas at Austin.
- [28] Falcão de Campos, J.A.C., (1996). “Formulação de um Método de Elementos de Fronteira Para o Cálculo do Escoamento Potential Incompressível em Hélices Propulsores”. MARETEC/DEM Relatório Técnico P1-1. (in Portuguese).
- [29] Falcão de Campos, J.A.C., Ferreira de Sousa, P.J.A., Bosschers, J., (2006). “A Verification Study on Low-Order Three-Dimensional Potential-Based Panel Codes”. Computer & Fluids 35, pp.61–73.
- [30] Saffman, P.G., (1992). “Vortex Dynamics”. Cambridge University Press.
- [31] Morino, L., (1993). “Boundary Integral Equations in Aerodynamics”. Applied Mechanics Reviews, Vol. 46, No. 8, pp. 445–466.
- [32] Batchelor, G.K., (1967). “An Introduction to Fluid Dynamics”. Cambridge University Press.
- [33] Hoeijmakers, H.W.M., (1991). “Panel Methods for Aerodynamic Analysis and Design”. AGARD-R-783, Special Course on Engineering Methods in Aerodynamic Analysis and Design of Aircraft, Paper 5.
- [34] Morino, L., Chen, L.-T., Suciu, E.O., (1975). “Steady and Oscillatory Subsonic and Supersonic Aerodynamics Around Complex Configurations”. AIAA Journal, Vol. 13, No. 3, pp. 368–374.
- [35] Newman, J.N., (1986). “Distributions of Sources and Normal Dipoles Over a Quadrilateral Panel”. Journal of Engineering Mathematics, Vol. 20, pp. 113–126.
- [36] Katz, J., Plotkin, A., (1991). “Low-Speed Aerodynamics. From Wing Theory to Panel Methods”. McGraw-Hill.
- [37] Pina, H., (1995). “Métodos Numéricos”. McGraw-Hill. (in Portuguese).
- [38] Eça, L., (2001). “Practical Tools for 2-D, 3-D and Surface Grid Generation”. IST Technical Report D72-10.
- [39] Vinokur, M., (1983). “On One-Dimensional Stretching Functions for Finite-Difference Calculations”. Journal of Computational Physics, Vol. 50, pp. 215–234.

Bibliography

- [40] Hoshino, T., (1989). "Hydrodynamic Analysis of Propellers in Steady Flow Using a Surface Panel Method. 2nd Report: Flow Field Around Propeller". Journal of The Society of Naval Architects of Japan, Vol. 166, pp. 79–92.
- [41] Eça, L., (1994). "Grid Generation With a System of Elliptical Partial Differential Equations". IST Technical Report D10-2.
- [42] Sorensen, R.L., (1986). "Three-Dimensional Elliptic Grid Generation About Fighter Aircraft for Zonal Finite-Difference Computations". AIAA-86-0429, AIAA 24th Aerospace Sciences Conference, Reno, NV.
- [43] Eça, L., Hoekstra, M., Windt, J., (2002). "Practical Grid Generation Tools With Application to Ship Hydrodynamics". 8th International Conference on Numerical Grid Generation in Computational Field Simulations, Honolulu, USA, pp. 317–328.
- [44] Abbott, I.H., Doenhoff, A.E.V., (1959). "Theory of Wing Sections". Dover Publications.
- [45] Falcão de Campos, J.A.C., (1990). "Calculation of the Tip Vortex Flow Behind Wings Using an Inviscid Vortex Wake Roll-Up Model". MARIN Report No. 50920-2-RF.
- [46] Gindroz, B., Hoshino, T., Pylkkänen, J.V. (Eds.), (1998). "22nd ITTC Propulsion Committee Propeller RANS/Panel Method Workshop". Grenoble, France.
- [47] Falcão de Campos, J.A.C., (1983). "On the Calculation of Ducted Propeller Performance in Axisymmetric Flows". Ph. D. Thesis, Delft University of Technology.
- [48] Gibson, I.S., (1972). "Application of Vortex Singularities to Ducted Propellers". Ph. D. Thesis, University of Newcastle upon Tyne.
- [49] Kuiper, G., (1992). "The Wageningen Propeller Series". MARIN Publication 92-001.
- [50] Hoshino, T., (1998). "Comparative Calculations of Propeller Performance in Steady and Unsteady Flows Using a Surface Panel Method". 22nd ITTC Propulsion Committee Propeller RANS/Panel Method Workshop, Grenoble, France, pp. 329–342.
- [51] Jessup, S.D., (1989). "An Experimental Investigation of Viscous Flow Aspects of Propeller Blade Flow". Ph. D. Thesis, The Catholic University of America.
- [52] van Manen, J.D., (1962). "Effect of Radial Load Distribution on the Performance of Shrouded Propellers". International Shipbuilding Progress, Vol. 9, No. 93.
- [53] Falcão de Campos, J.A.C., Ferreira de Sousa, P, (2001). "Grid Convergence Studies for Propellers DTRC P4119 and P4842M With the Panel Code PROPAN". IST/MARETEC Technical Report D087-5.

- [54] Baltazar, J., Falcão de Campos, J.A.C., Bosschers, J., (2004). “A Study on the Accuracy of Low and Higher Order BEM in Three Dimensional Potential Flows Past Ellipsoids”. Advances in Boundary Element Techniques V, Lisbon, Portugal, pp. 71–76.
- [55] Brockett, T., (1966). “Minimum Pressure Envelopes for Modified NACA-66 Sections With NACA $a=0.8$ Camber and Buships Type I and Type II Sections”. DTMB Report No. 1780.
- [56] Kerwin, J.E., Lee, C.-S., (1978). “Prediction of Steady and Unsteady Marine Propeller Performance by Numerical Lifting-Surface Theory”. SNAME Transactions, Vol. 86, pp. 218–253.

Appendix A

Dynamic Boundary Condition on the Wake

The zero-pressure-jump boundary condition on the wake, Equation (2.11), writes

$$\vec{V}_m \cdot \Delta \vec{V} = 0, \quad (\text{A.1})$$

where

$$\vec{V}_m = \frac{1}{2}(\vec{V}^+ + \vec{V}^-) \quad (\text{A.2})$$

denotes the mean velocity and

$$\Delta \vec{V} = \vec{V}^+ - \vec{V}^- \quad (\text{A.3})$$

the velocity discontinuity across the wake surface. The velocity discontinuity may be evaluated from the limiting values of the potential gradient on each side of the vortex sheet

$$\vec{V}^\pm = \lim_{\vec{x} \rightarrow \mathcal{S}_w^\pm} \nabla \phi \equiv \nabla \phi^\pm. \quad (\text{A.4})$$

The gradient on each side of the sheet is decomposed into a normal and a tangential component to the surface in the form

$$\nabla \phi = \vec{n}(\vec{n} \cdot \nabla \phi) - \vec{n} \times (\vec{n} \times \nabla \phi). \quad (\text{A.5})$$

Evaluating the previous equation on each side of the sheet and subtracting, we obtain

$$\nabla \phi^+ - \nabla \phi^- = \vec{n}(\vec{n} \cdot \nabla \phi^+ - \vec{n} \cdot \nabla \phi^-) - \vec{n} \times (\vec{n} \times (\nabla \phi^+ - \nabla \phi^-)). \quad (\text{A.6})$$

From the kinematic boundary condition, Equation (2.10), the normal velocity component is continuous across the sheet and Equation (A.6) becomes

A. Dynamic Boundary Condition on the Wake

$$\nabla\phi^+ - \nabla\phi^- = -\vec{n} \times [\vec{n} \times (\nabla\phi^+ - \nabla\phi^-)]. \quad (\text{A.7})$$

Denoting the surface gradient operator by

$$\nabla_S \equiv -\vec{n} \times (\vec{n} \times \nabla) \quad (\text{A.8})$$

and with Equation (A.4), we obtain for the velocity discontinuity across the surface

$$\Delta\vec{V} = \nabla_S(\Delta\phi). \quad (\text{A.9})$$

The boundary condition on the wake, Equation (A.1), finally gives

$$\vec{V}_m \cdot \nabla_S(\Delta\phi) = 0. \quad (\text{A.10})$$

Appendix B

Iterative Solution of the System of Equations With Pressure Kutta Condition

Consider the algebraic system of equations:

$$[A] \{\phi\} - [W] \{\Delta\phi\} = \{B\}, \quad (\text{B.1})$$

where $[A]$ is a $N \times N$ matrix with elements

$$A_{ij} = \delta_{ij} - D_{ij}, \quad i, j = 1, \dots, N, \quad (\text{B.2})$$

$[W]$ is a $N \times N_K$ matrix and $\{B\}$ is a N vector with elements

$$B_i = \sum_{j=1}^N S_{ij} (\vec{n} \cdot \vec{U}_\infty), \quad i = 1, \dots, N. \quad (\text{B.3})$$

D_{ij} , W_{ij} and S_{ij} are the influence coefficients. $\{\phi\}$ is the vector of N unknowns and $\{\Delta\phi\}$ is the vector of N_K wake dipole strengths. In the rigid wake model, the wake dipole strength vector corresponds to the N_R dipole strengths of the streamwise wake strips. In the partial wake model, the wake dipole strength vector corresponds to the $N_R \times N_W$ dipole strengths of the near wake.

Suppose that the solution $\{\phi^{(n)}\}$ and the wake dipole strength vector $\{\Delta\phi^{(n)}\}$ are known at the iteration level (n) . The pressure-jump vector $\{(\Delta C_p)^{(n)}\}$ is also known from the solution at the iteration level (n) . According to the method of Newton-Raphson the values at the iteration level $(n+1)$ of the wake dipole strength vector can be obtained from the solution of the system of equations

$$[P^{(n)}] \left\{ \delta (\Delta\phi)^{(n+1)} \right\} = - \left\{ (\Delta C_p)^{(n)} \right\}, \quad (\text{B.4})$$

B. Iterative Solution of the System of Equations With Pressure Kutta Condition

where

$$\delta(\Delta\phi_j)^{(n+1)} = (\Delta\phi_j)^{(n+1)} - (\Delta\phi_j)^{(n)}, \quad j = 1, \dots, N_K, \quad (\text{B.5})$$

and $[P^{(n)}]$ is the Jacobian matrix at the iteration level (n) .

A correction to the solution at the iteration level (n) is obtained by solving the equation

$$[A] \{ \delta\phi^{(n+1)} \} = [W] \left\{ \delta(\Delta\phi)^{(n+1)} \right\}, \quad (\text{B.6})$$

where

$$\delta\phi_j^{(n+1)} = \phi_j^{(n+1)} - \phi_j^{(n)}, \quad j = 1, \dots, N. \quad (\text{B.7})$$

With the solution vector $\{\phi^{(n+1)}\}$ the pressure jump vector at the trailing edge $\{(\Delta C_p)^{(n+1)}\}$ is evaluated and a new iteration cycle can be initiated.

To solve (B.4) the Jacobian matrix $[P^{(n)}]$ needs to be evaluated at each iteration level. The Jacobian matrix is defined by

$$P_{ij} = \frac{\partial(\Delta C_p)_i}{\partial(\Delta\phi)_j}, \quad i, j = 1, \dots, N_K. \quad (\text{B.8})$$

The Jacobian matrix P_{ij} is a non-linear function of the strength of the dipole strips $\Delta\phi_j$ and is not known at the outset. In a first approximation we may adopt a modified Newton-Raphson scheme and assume that the Jacobian matrix will not vary much with the iteration level. In this case, we write

$$P_{ij}^{(n)} \cong P_{ij}^{(\beta)} = \frac{(\Delta C_p)_i^{(\beta)} - (\Delta C_p)_i^{(0)}}{\Delta\phi_j^{(\beta)} - \Delta\phi_j^{(0)}}, \quad i, j = 1, \dots, N_K, \quad (\text{B.9})$$

where $(\Delta C_p)_i^{(\beta)}$ is the pressure difference obtained at the trailing edge for a disturbed strength of the dipole strips in the wake

$$\Delta\phi_j^{(\beta)} = (1 + \beta) \Delta\phi_j^{(0)}, \quad j = 1, \dots, N_K \quad (\text{B.10})$$

and β is a small parameter.

From (B.1) we may write for the first approximation

$$[A] \{ \phi^{(0)} \} = \{ B \} + [W] \{ \Delta\phi^{(0)} \}. \quad (\text{B.11})$$

For the disturbed solution we have

B. Iterative Solution of the System of Equations With Pressure Kutta Condition

$$[A] \{ \phi^{(\beta)} \} = \{ B \} + [W] \{ \Delta \phi^{(\beta)} \}. \quad (\text{B.12})$$

Subtracting (B.12) from (B.11), we obtain

$$[A] \{ \delta \phi^{(\beta)} \} = \beta [W] \{ \Delta \phi^{(0)} \}, \quad (\text{B.13})$$

where

$$\delta \phi_j^{(\beta)} = \phi_j^{(\beta)} - \phi_j^{(0)}, \quad j = 1, \dots, N. \quad (\text{B.14})$$

Once the pressure difference at the trailing edge corresponding to the disturbed solution $\phi^{(\beta)}$ becomes known from a simple calculation, the Jacobian matrix is calculated from

$$P_{ij}^{(\beta)} = \frac{(\Delta C_p)_i^{(\beta)} - (\Delta C_p)_i^{(0)}}{\beta \Delta \phi_j^{(0)}}, \quad i, j = 1, \dots, N_K. \quad (\text{B.15})$$

In a second approximation we may refine the calculation of the Jacobian matrix by disturbing the solution obtained at the iteration level (n). In this case, we have

$$\Delta \phi_j^{(\beta)} = (1 + \beta) \Delta \phi_j^{(n)}, \quad j = 1, \dots, N_K, \quad (\text{B.16})$$

and we solve

$$[A] \{ \delta \phi^{(\beta)} \} = \beta [W] \{ \Delta \phi^{(n)} \}, \quad (\text{B.17})$$

with

$$\delta \phi_j^{(\beta)} = \phi_j^{(\beta)} - \phi_j^{(n)}, \quad j = 1, \dots, N, \quad (\text{B.18})$$

to obtain

$$P_{ij}^{(\beta)} = \frac{(\Delta C_p)_i^{(\beta)} - (\Delta C_p)_i^{(n)}}{\beta \Delta \phi_j^{(n)}}, \quad i, j = 1, \dots, N_K. \quad (\text{B.19})$$

Appendix C

Propeller Geometries

C.1 DTRC Propeller P4119

The DTRC propeller P4119 is a three-bladed propeller without skew or rake. The geometry of this propeller is given in Table C.1, Koyama [15]. The blade sections are built from the NACA $a = 0.8$ meanline and the NACA 66 thickness form (DTRC modified). The thickness and meanline distributions are given in Table C.2, Brockett [55]. The hub geometry for this propeller is given in Figure C.1, Koyama [15].

r/R	c/D	P/D	$\theta_s(\text{deg.})$	i_T/D	t_M/c	f_M/c
0.200	0.32000	1.10500	0.0	0.0	0.20550	0.01429
0.250	0.34200	1.10370	0.0	0.0	0.17870	0.01985
0.300	0.36250	1.10220	0.0	0.0	0.15530	0.02318
0.400	0.40480	1.09830	0.0	0.0	0.11800	0.02303
0.500	0.43920	1.09320	0.0	0.0	0.09016	0.02182
0.600	0.46100	1.08790	0.0	0.0	0.06960	0.02072
0.700	0.46220	1.08390	0.0	0.0	0.05418	0.02003
0.800	0.43470	1.08110	0.0	0.0	0.04206	0.01967
0.900	0.36130	1.07850	0.0	0.0	0.03321	0.01817
0.925	0.32621	1.07779	0.0	0.0	0.03252	0.01744
0.950	0.27750	1.07700	0.0	0.0	0.03228	0.01631
0.975	0.20449	1.07609	0.0	0.0	0.03211	0.01450
0.990	0.13276	1.07546	0.0	0.0	0.03187	0.01298
0.995	0.09479	1.07523	0.0	0.0	0.03175	0.01239
1.000	0.00000	1.07500	0.0	0.0	0.03160	0.01175

Table C.1: Geometry of DTRC propeller P4119.

x/c	t/t_M	f/f_M
0.0000	0.0000	0.0000
0.0050	0.1330	0.0423
0.0075	0.1624	0.0595
0.0125	0.2088	0.0907
0.0250	0.2932	0.1586
0.0500	0.4132	0.2712
0.0750	0.5050	0.3657
0.1000	0.5814	0.4482
0.1500	0.7042	0.5869
0.2000	0.8000	0.6993
0.2500	0.8726	0.7905
0.3000	0.9274	0.8635
0.3500	0.9664	0.9202
0.4000	0.9904	0.9615
0.4500	1.0000	0.9881
0.5000	0.9924	1.0000
0.5500	0.9692	0.9971
0.6000	0.9306	0.9786
0.6500	0.8766	0.9434
0.7000	0.8070	0.8892
0.7500	0.7224	0.8121
0.8000	0.6220	0.7027
0.8500	0.5064	0.5425
0.9000	0.3754	0.3586
0.9500	0.2286	0.1713
0.9750	0.1496	0.0823
1.0000	0.0666	0.0000

Table C.2: Thickness and camber distributions of DTRC propeller P4119.

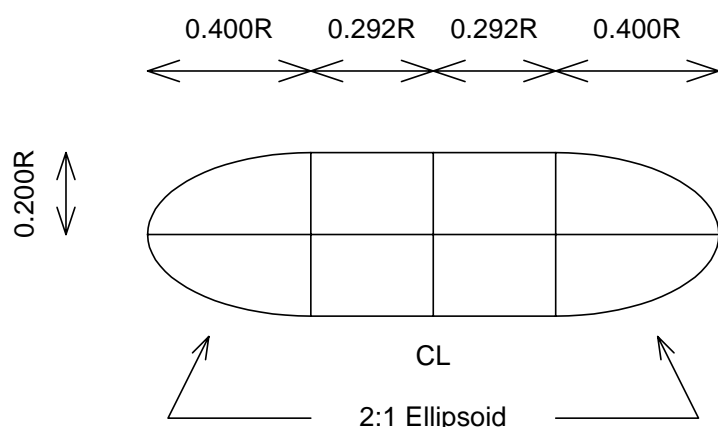


Figure C.1: Hub geometry for DTRC propeller P4119.

C.2 DTRC Propeller P4842M

The DTRC propeller P4842M is a five-bladed propeller with high skew obtained from the original P4842 propeller geometry, Koyama [15], by increasing the chord length in the tip region while keeping the same mid-chord skew distribution. The geometry of the P4842M propeller is given in Table C.3¹. Notice that, in contrast with the original propeller DTRC P4842, the maximum camber and thickness of this propeller are set to zero at the tip. The thickness distribution of the blade sections (NACA 66 DTRC modified) and the meanline distribution are given in Table C.4. The hub geometry for this propeller is given in Figure C.2, Koyama [15].

Number of blades: 5 Hub-diameter ratio: 0.323 Expanded area ratio: 0.537 Section thickness form: NACA 66 (DTRC modified) Section meanline form: specified (see Table C.4)						
r/R	c/D	P/D	$\theta_s(\text{deg.})$	i_T/D	t_M/c	f_M/c
0.323	0.201501	0.932101	0.380	0.001036	0.217896	0.010000
0.350	0.218101	1.078999	-3.070	-0.009002	0.187102	0.015802
0.400	0.249400	1.236099	-6.820	-0.022887	0.141496	0.025296
0.500	0.311299	1.419400	-9.020	-0.037003	0.085403	0.036496
0.600	0.366400	1.489201	-7.570	-0.032533	0.058102	0.038997
0.700	0.403099	1.488001	-3.240	-0.013603	0.044403	0.037102
0.800	0.408999	1.328999	4.340	0.016423	0.037902	0.031903
0.900	0.398171	1.075900	13.750	0.042323	0.035601	0.026399
0.925	0.389561	0.992801	16.420	0.047053	0.033253	0.025421
0.950	0.362120	0.901200	19.250	0.050909	0.036300	0.024703
0.975	0.301318	0.802499	22.250	0.053928	0.052098	0.024313
0.990	0.235136	0.740460	24.130	0.055340	0.070755	0.024245
0.995	0.191283	0.719370	24.770	0.055746	0.078861	0.024276
1.000	0.070000	0.698101	25.420	0.056133	0.000000	0.000000

Table C.3: Geometry of DTRC propeller P4842M.

¹The geometry is taken from the geometry IGES file supplied by MARIN.

x/c	t/t_M	f/f_M
0.0000	0.0000	0.0000
0.0125	0.2088	0.0875
0.0250	0.2932	0.1530
0.0500	0.4132	0.2625
0.0750	0.5050	0.3585
0.1000	0.5814	0.4415
0.1500	0.7042	0.5803
0.2000	0.8000	0.6955
0.3000	0.9274	0.8630
0.4000	0.9904	0.9630
0.4500	1.0000	0.9907
0.5000	0.9924	1.0000
0.6000	0.9306	0.9750
0.7000	0.8070	0.8777
0.8000	0.6220	0.6760
0.9000	0.3754	0.3613
0.9500	0.2286	0.1785
1.0000	0.0666	0.0000

Table C.4: Thickness and camber distributions of DTRC propeller P4842M.

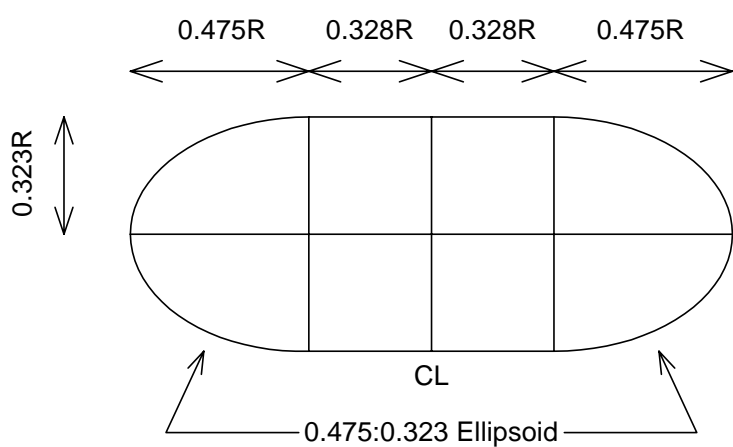


Figure C.2: Hub geometry for DTRC propeller P4842M.

C.3 NSMB Duct 19A

The section geometry of NSMB duct 19A is given in van Manen [52]. This is a duct with a cylindrical inner side. The outside of the duct is straight to simplify its manufacturing, and the trailing edge is round. The length-diameter ratio of the duct is 0.5. The profile of NSMB duct 19A is given in Figure C.3. The geometry of this duct is given in Table C.5 in percentages of the duct length L . The straight part in the outer contour of the duct is indicated with s .

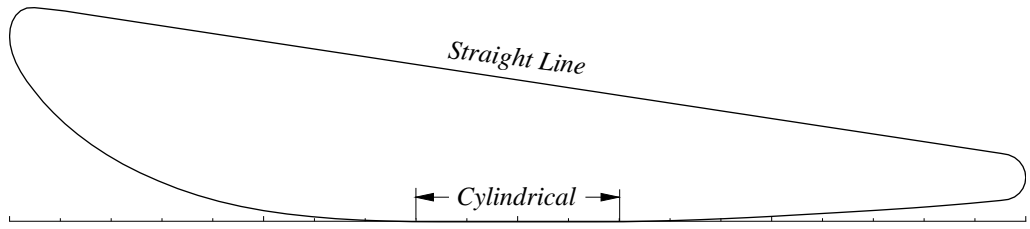


Figure C.3: Geometry of NSMB duct 19A.

x/L	y_{inner}/L	y_{outer}/L
0.00	18.25	18.25
1.25	14.66	20.72
2.50	12.80	21.07
5.00	10.07	20.80
7.50	8.00	s
10.00	6.34	s
15.00	3.87	s
20.00	2.17	s
25.00	1.10	s
30.00	0.48	s
40.00	0.00	s
50.00	0.00	s
60.00	0.00	s
70.00	0.29	s
80.00	0.82	s
90.00	1.45	s
95.00	1.86	s
100.00	2.36	6.36

Table C.5: Ordinates of NSMB duct 19A.

C.4 NSMB Propeller $K_a4\text{-}70$

The NSMB propeller $K_a4\text{-}70$ is a four-bladed propeller without rake. The blade geometry is of Kaplan type with a finite chord at the blade tip. The hub geometry used for the calculations with this propeller is given in Figure C.4. The geometry of this propeller is presented in Table C.6, Kuiper [49]. The blade section ordinates are given in Table C.7.

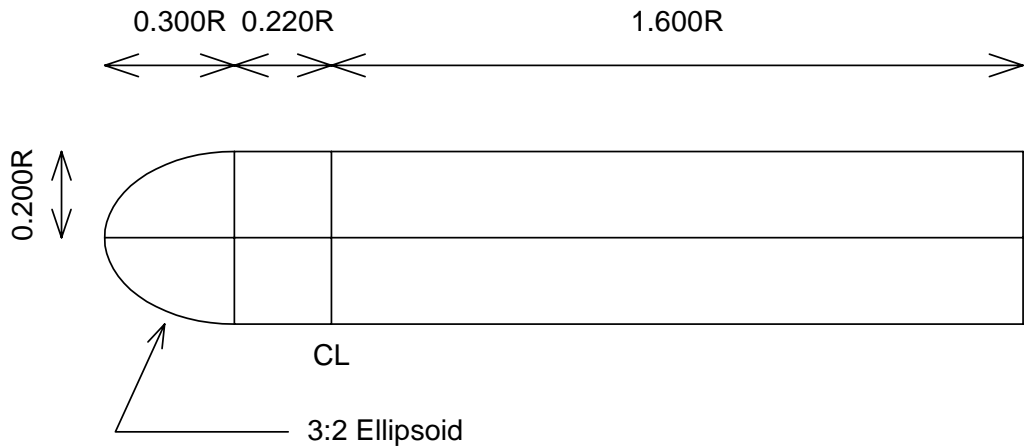


Figure C.4: Hub geometry for propeller $K_a4\text{-}70$.

	r/R	0.2	0.3	0.4	0.5	0.6	0.7	0.8	0.9	1.0
Chord of the blade sections in percentages of the diameter	23.14	26.39	29.35	32.04	34.48	36.47	37.92	38.82	38.83	
Skew of the blade sections in percentages of the chord	5.00	2.80	1.30	0.60	0.00	0.00	0.00	0.00	0.00	0.00
Maximum blade thickness in percentages of the diameter	4.00	3.52	3.00	2.45	1.90	1.38	0.92	0.61	0.50	
Distance of maximum thickness from leading edge in percentages of the length of the sections	34.98	39.76	46.02	49.13	49.98	—	—	—	—	
Maximum camber in percentages of the diameter	0.85	1.12	1.16	1.05	0.95	0.69	0.46	0.31	0.25	

 Table C.6: Dimensions of the propeller $K_a 4-70$.

r/R	From maximum thickness to trailing edge				From maximum thickness to leading edge						
	100%	80%	60%	40%	20%	40%	60%	80%	90%	95%	100%
0.2	—	38.23	63.65	82.40	95.00	97.92	90.83	77.19	55.00	38.75	27.40
0.3	—	39.05	66.63	84.14	95.86	97.63	90.06	75.62	53.02	37.87	27.57
0.4	—	40.56	66.94	85.69	96.25	97.22	88.89	73.61	50.00	34.72	25.83
0.5	—	41.77	68.59	86.42	96.60	96.77	87.10	70.46	45.84	30.22	22.24
0.6	—	43.58	68.26	85.89	96.47	96.47	85.89	68.26	43.58	28.59	20.44
0.7	—	45.31	69.24	86.33	96.58	96.58	86.33	69.24	45.31	30.79	22.88
0.8	—	48.16	70.84	87.04	96.76	96.76	87.04	70.84	48.16	34.39	26.90
0.9	—	51.75	72.94	88.09	97.17	97.17	88.09	72.94	51.75	38.87	31.87
1.0	—	52.00	73.00	88.00	97.00	97.00	88.00	73.00	52.00	39.25	32.31
					Ordinates for the face						
0.2	20.21	7.29	1.77	0.1	—	0.21	1.46	4.37	10.52	16.04	20.62
0.3	13.85	4.62	1.07	—	—	0.12	0.83	2.72	6.15	8.28	10.30
0.4	9.17	2.36	0.56	—	—	0.42	1.39	2.92	1.02	4.44	13.47
0.5	6.62	0.68	0.17	—	—	0.17	0.51	1.36	1.53	7.81	

 Table C.7: Table of the ordinates of the propeller $K_a 4-70$.

C.5 DTNSRDC Propeller P4498

The DTNSRDC propeller P4498 is a five-bladed propeller without rake. The geometry of this propeller is given in Table C.8, Kerwin and Lee [56]. The blade sections are built from the NACA $a = 0.8$ meanline and the NACA 66 thickness form (DTRC modified). The thickness and meanline distributions are given in Table C.2. The hub geometry for this propeller is given in Figure C.5.

Number of blades: 5 Hub-diameter ratio: 0.20 Expanded area ratio: 0.725 Section thickness form: NACA 66 (DTRC modified) Section meanline form: NACA, $a = 0.8$						
r/R	c/D	P/D	$\theta_s(\text{deg.})$	i_T/D	t_M/c	f_M/c
0.200	0.174	1.5660	0.000	0.0	0.249425	0.0402
0.250	0.202	1.5390	4.647	0.0	0.196040	0.0408
0.300	0.229	1.5124	9.293	0.0	0.156332	0.0407
0.400	0.275	1.4598	18.816	0.0	0.106909	0.0385
0.500	0.312	1.3860	27.991	0.0	0.076923	0.0342
0.600	0.337	1.2968	36.770	0.0	0.056677	0.0281
0.700	0.347	1.1986	45.453	0.0	0.042075	0.0230
0.800	0.334	1.0969	54.245	0.0	0.031437	0.0189
0.900	0.280	0.9965	63.102	0.0	0.023929	0.0159
0.950	0.210	0.9450	67.531	0.0	0.022857	0.0168
1.000	0.000	0.8950	72.000	0.0	0.021786	0.0177

Table C.8: Geometry of DTNSRDC propeller P4498.

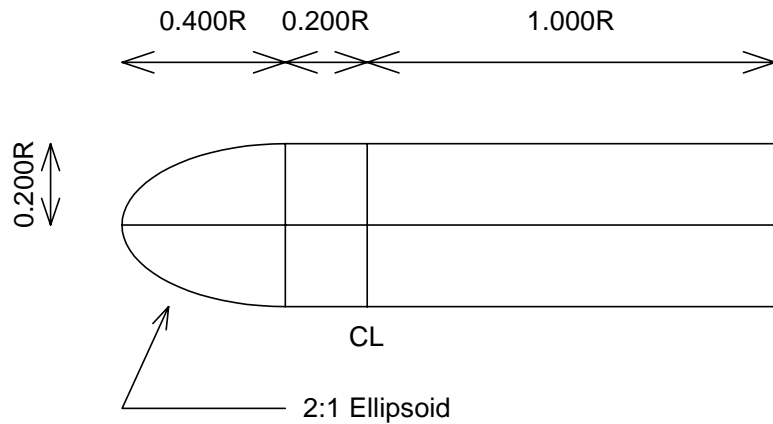


Figure C.5: Hub geometry for DTNSRDC propeller P4498.

List of Figures

2.1	Coordinate reference systems for propeller and wing.	7
2.2	Partial wake relaxation - force on wake.	13
3.1	Definition of a hyperboloidal panel.	23
4.1	Definitions of regions for the panel discretisation of a duct sector surface.	39
4.2	Domain for grid generation on the hub.	43
4.3	Conventional grid with $s_1 = \text{const.}$ and $s_2 = \text{const.}$ (left) and quasi-orthogonal grid with displacement of the grid singularity (right). 65×17 corner point grids for the elliptical wing.	48
4.4	Parametric domains (I, J) and (s_1, s_2) for the algebraic quasi-orthogonal grid of the elliptical wing with 65×17 corner points.	49
5.1	Elliptical wing panel arrangement (left). Detail of the wing tip (right). Note that only half of the wing and wake grids are shown.	52
5.2	Circulation distribution. Convergence with grid refinement. Elliptical wing at 6 degrees incidence.	53
5.3	Pressure distribution at sections $y/S = 0.20, 0.40, 0.60, 0.80, 0.95$ and 0.99 . Convergence with grid refinement. Elliptical wing at 6 degrees incidence.	54
5.4	Pressure distribution at sections $y/S = 0.20, 0.40, 0.60, 0.80$ and 0.95 . Comparison with experimental data, Falcão de Campos [45]. Elliptical wing at 2 degrees incidence.	55
5.5	Pressure distribution at sections $y/S = 0.20, 0.40, 0.60, 0.80$ and 0.95 . Comparison with experimental data, Falcão de Campos [45]. Elliptical wing at 8 degrees incidence.	56
5.6	Rectangular wing panel arrangement.	57
5.7	Detail of the wing tip.	57
5.8	Pressure distribution at sections $y/S = 0.20, 0.40, 0.60, 0.80, 0.95$ and 0.998 . Convergence with grid refinement. Rectangular wing at 6 degrees incidence.	59
5.9	Circulation distribution. Convergence with grid refinement. Rectangular wing at 6 degrees incidence.	60
5.10	Streamlines near the tip at the pressure (left) and suction (right) sides of the rectangular wing at 6 degrees incidence. 128×66 blade grid.	60

5.11 Pressure distribution at sections $y/S = 0.211, 0.411, 0.611, 0.811$ and 0.961 . Comparison with experimental data, Falcão de Campos [45]. Rectangular wing at 2.5 degrees incidence.	61
5.12 Pressure distribution at sections $y/S = 0.211, 0.411, 0.611, 0.811$ and 0.961 . Comparison with experimental data, Falcão de Campos [45]. Rectangular wing at 8.5 degrees incidence.	62
5.13 DTRC P4119 panel arrangement. Note that only one wake grid is shown.	63
5.14 Panel arrangement at the blade tip. DTRC P4119.	63
5.15 Pressure distribution at sections $r/R = 0.25, 0.50, 0.75, 0.90, 0.95$ and 0.995 . Convergence with grid refinement. $J = 0.833$. DTRC P4119.	65
5.16 Circulation distribution. Convergence with grid refinement. $J = 0.833$. DTRC P4119.	66
5.17 Pressure distribution at sections $r/R = 0.30, 0.70$ and 0.90 . Comparison with Hoshino [50] and experimental data, Jessup [51]. $J = 0.833$. DTRC P4119.	67
5.18 Thrust and torque coefficients for the propeller DTRC P4119. Comparison with Hoshino [50] and experimental data, Jessup [51].	68
5.19 DTRC P4842M panel arrangement. Note that only one wake grid is shown.	68
5.20 Panel arrangement at the tip. DTRC P4842M.	69
5.21 Pressure distribution at sections $r/R = 0.40, 0.50, 0.70, 0.90, 0.95$ and 0.99 . Convergence with grid refinement. $J = 0.905$. DTRC P4842M.	70
5.22 Circulation distribution. Convergence with grid refinement. $J = 0.905$. DTRC P4842M.	71
5.23 NSMB duct 19A panel grids. Cylindrical panel arrangement (left). Helical panel arrangement (right).	72
5.24 Duct pressure distribution along the chordwise direction (left). Circumferential distribution of circulation on the duct (right). Comparison between the cylindrical and helical panel arrangements.	73
5.25 Pressure distribution on duct NSMB 19A. Comparison with Falcão de Campos [47] and experimental data, Gibson [48].	74
5.26 NSMB 19A duct profile with location of the stagnation points (top). Effect of the location of the stagnation point on the pressure distribution on duct NSMB 19A (bottom).	74
5.27 Panel arrangement for propeller K_a4-70 inside duct 19A. Note that only one blade wake grid and one duct section grid are shown.	75
5.28 Panel arrangement at the blade tip. K_a4-70 inside duct 19A.	75
5.29 Blade pressure distribution at radial sections $r/R = 0.50, 0.75$ and 0.99 (left). Duct pressure distributions at circumferential positions $\theta = 0, 20$ and 40 degrees (right). Convergence with grid refinement. K_a4-70 inside duct 19A at $J = 0.7$	77
5.30 Radial distribution of circulation on the blade (left). Circumferential distribution of circulation on the duct (right). Convergence with grid refinement. K_a4-70 inside duct 19A at $J = 0.7$	78

5.31 Blade pressure distribution at radial section $r/R = 0.99$ (left). Duct pressure distribution at the circumferential position $\theta = 40$ degrees (right). Influence of the gap. K_a4-70 inside duct 19A at $J = 0.7$	79
5.32 Radial distribution of circulation on the blade (left). Circumferential distribution of circulation on the duct (right). Influence of the gap. K_a4-70 inside duct 19A at $J = 0.7$	79
5.33 NSMB 19A duct profile with location of the shedding lines.	80
5.34 Blade pressure distribution at $r/R = 0.75$ (top-left). Duct pressure distribution at $\theta = 40$ degrees (top-right). Blade (bottom-left) and duct (bottom-right) circulation distributions. Influence of the shedding line location.	80
5.35 Inviscid thrust and torque coefficients for the propeller K_a4-70 inside duct 19A. Comparison with experimental data, Kuiper [49].	81
6.1 Rolled-up wake grid for the elliptical wing.	84
6.2 Pressure distribution at section $y/S = 0.99$. Comparison between wake models. Elliptical wing at 6 degrees incidence.	85
6.3 Pressure distribution at section $y/S = 0.95$. Comparison between wake models. Elliptical wing at 6 degrees incidence.	86
6.4 Blade back panel arrangement for the propeller P4119: conventional grid (left) and new panel arrangement with “hydrodynamic tip” (right).	87
6.5 Helicoidal wake grid (left) for the propeller P4119 with a detail over the blade tip (right). Note that only one wake grid is shown.	88
6.6 Rolled-up wake grid for the propeller P4119 obtained using the conventional grid and the new panel arrangement with “hydrodynamic tip”. Note that only one wake grid is shown.	89
6.7 Pressure distribution on the propeller P4119 for the conventional grid using the rigid wake model (top-left) and the full wake relaxation model (top-right), and for the new panel arrangement with “hydrodynamic tip” using the rigid wake model (bottom-left) and the full wake relaxation model (bottom-right).	90
6.8 Streamlines from the pressure side around the tip region with the new panel arrangement for the propeller P4119.	90
6.9 Blade back panel arrangement for propeller P4842M: conventional grid (left) and new panel arrangement with “hydrodynamic tip” (right).	91
6.10 Rolled-up wake grid for the propeller P4842M obtained using the conventional grid and the new panel arrangement with “hydrodynamic tip”. Note that only one wake grid is shown.	92
6.11 Pressure distribution on the propeller P4842M for the conventional grid using the rigid wake model (left) and the full wake relaxation model (right).	93
6.12 Pressure distribution on the propeller P4842M for the new panel arrangement with “hydrodynamic tip” using the rigid wake model (left) and the full wake relaxation model (right).	93
6.13 Blade grid at the tip. Conventional grid. Propeller DTRC P4119.	94
6.14 Perturbation potential (left) and pressure coefficient (right) at panel strips $j = 39$ and $j = 40$. Conventional grid.	94

6.15	Blade grid at the tip. Tip cuts at $r/R = 0.9988$ (left) and $r/R = 0.9978$ (right). Propeller DTRC P4119.	95
6.16	Perturbation potential (left) and pressure coefficient (right) at panel strips $j = 39$ and $j = 40$. Comparison between different tip geometries.	96
6.17	Perturbation potential and pressure coefficient at panel strips $j = 39$ and $j = 40$. Finite chord at tip.	97
7.1	Potential flow model with leading edge vortex sheet separation.	101
7.2	Leading edge wake geometric parameters.	102
7.3	Blade and wake panel arrangement.	104
7.4	Streamlines of the potential flow solution for the 76 degrees delta wing at 20 degrees incidence.	105
7.5	Potential flow solution over the 76 degrees delta wing at 20 degrees incidence. Perturbation potential (top) and pressure coefficient (bottom) on the suction and pressure sides.	106
7.6	Potential-jump distribution along cross-flow planes. 76 degrees delta wing at 20 degrees incidence.	107
7.7	Pressure distribution along cross-flow planes. 76 degrees delta wing at 20 degrees incidence.	107
7.8	Leading edge wake geometry in cross-flow planes. Comparison with Hoeijmakers [26]. 76 degrees delta wing at 20 degrees incidence.	108
7.9	Pressure distribution along cross-flow planes. Comparison with Hoeijmakers [26]. 76 degrees delta wing at 20 degrees incidence.	109
7.10	Pressure distribution along cross-flow planes. Comparison with Hoeijmakers [26]. 76 degrees delta wing at 20 degrees incidence.	110
7.11	Leading edge wake geometry in cross-flow planes. Comparison with Hoeijmakers [26]. 76 degrees delta wing at 10 degrees incidence.	112
7.12	Potential-jump distribution along cross-flow planes. 76 degrees delta wing at 10 degrees incidence.	113
7.13	Pressure distribution along cross-flow planes. 76 degrees delta wing at 10 degrees incidence.	113
7.14	Pressure distribution along cross-flow planes. Comparison with Hoeijmakers [26]. 76 degrees delta wing at 10 degrees incidence.	114
7.15	Leading edge wake geometry in cross-flow planes. Comparison with Hoeijmakers [26]. 76 degrees delta wing at 30 degrees incidence.	115
7.16	Potential-jump distribution along cross-flow planes. 76 degrees delta wing at 30 degrees incidence.	116
7.17	Pressure distribution along cross-flow planes. 76 degrees delta wing at 30 degrees incidence.	116
7.18	Pressure distribution along cross-flow planes. Comparison with Hoeijmakers [26]. 76 degrees delta wing at 30 degrees incidence.	117
7.19	Leading edge wake geometry in cross-flow planes. Comparison with Hoeijmakers [26]. 76 degrees delta wing at 40 degrees incidence.	118
7.20	Potential-jump distribution along cross-flow planes. 76 degrees delta wing at 40 degrees incidence.	119

7.21	Pressure distribution along cross-flow planes. 76 degrees delta wing at 40 degrees incidence.	119
7.22	Pressure distribution along cross-flow planes. Comparison with Hoeijmakers [26]. 76 degrees delta wing at 40 degrees incidence.	120
7.23	DTNSRDC P4498 panel arrangement. Note that only one wake grid is shown.	121
7.24	Pressure and circulation distributions at design condition $J = 0.889$ (top). Pressure and circulation distributions at condition $J = 0.800$ (bottom). DTNSRDC propeller P4498.	122
7.25	Panel arrangements of the two leading edge wakes for DTNSRDC propeller P4498 (top). Pressure and circulation distributions at the advance coefficient $J = 0.800$. Potential flow solution for the constant radius leading edge wake (middle) and for the leading edge wake with vortex lines convected to the blade tip (bottom).	124
7.26	Streamlines on the suction side of the blade. Attached flow: $J = 0.889$ (top-left) and $J = 0.8$ (top-right). Leading edge vortex separation at $J = 0.8$: constant radius vortex lines (bottom-left) and vortex lines convected to the tip (bottom-right).	125
7.27	Panel arrangements for propeller K_a4-70 inside duct 19A for the three gap models. 0.8% gap (top), zero gap (middle), tip leakage vortex model (bottom). Note that only one blade wake grid and one duct sector wake grid are shown.	128
7.28	Influence of the gap model on the pressure distribution on the duct 19A at $J = 0.5$. Mean (top), first harmonic (middle) and second harmonic (bottom) amplitude of blade frequency.	129
7.29	Influence of the gap model on the circulation distributions: blade circulation (top), duct circulation (middle), blade tip circulation (bottom). K_a4-70 inside duct 19A at $J = 0.5$	130
7.30	Influence of the gap model on the pressure distribution on the duct 19A at $J = 0.7$. Mean (top), first harmonic (middle) and second harmonic (bottom) amplitude of blade frequency.	131
7.31	Influence of the gap model on the circulation distributions: blade circulation (top), duct circulation (middle), blade tip circulation (bottom). K_a4-70 inside duct 19A at $J = 0.7$	132
7.32	Influence of the gap model on the pressure distribution on the blade at section $r/R = 0.99$ (top) and on the duct at circumferential position $\theta = 20$ degrees (bottom).	133
7.33	Inviscid thrust and torque coefficients for propeller K_a4-70 inside duct 19A. Comparison between gap models.	133
C.1	Hub geometry for DTRC propeller P4119.	150
C.2	Hub geometry for DTRC propeller P4842M.	152
C.3	Geometry of NSMB duct 19A.	153
C.4	Hub geometry for propeller K_a4-70	154
C.5	Hub geometry for DTNSRDC propeller P4498.	156

List of Tables

5.1	Lift and induced drag coefficients. Convergence with grid refinement. Elliptical wing at 6 degrees incidence.	53
5.2	Lift and induced drag coefficients. Convergence with grid refinement. Rectangular wing at 6 degrees incidence.	60
5.3	Inviscid thrust and torque coefficients for the propeller DTRC P4119. $J = 0.833$. Convergence with grid refinement.	66
5.4	Inviscid thrust and torque coefficients for the propeller DTRC P4842M. $J = 0.905$. Convergence with grid refinement.	71
5.5	Inviscid thrust and torque coefficients for the propeller K_a4-70 inside duct 19A at $J = 0.7$. Convergence with grid refinement.	78
7.1	Inviscid lift and induced drag coefficients. 76 degrees swept delta wing for different angles of attack.	111
7.2	Inviscid thrust and torque coefficients. $J = 0.800$. DTNSRDC propeller P4498.	125
C.1	Geometry of DTRC propeller P4119.	149
C.2	Thickness and camber distributions of DTRC propeller P4119.	150
C.3	Geometry of DTRC propeller P4842M.	151
C.4	Thickness and camber distributions of DTRC propeller P4842M.	152
C.5	Ordinates of NSMB duct 19A.	153
C.6	Dimensions of the propeller K_a4-70	155
C.7	Table of the ordinates of the propeller K_a4-70	155
C.8	Geometry of DTNSRDC propeller P4498.	156